Ultrafast spin transport through oxide and nitride barriers measured by inverse spin Hall effect

Dissertation

zur Erlangung des Doktorgrades der Naturwissenschaften
(Dr. rer. nat.)

der Naturwissenschaftlichen Fakultät II
- Chemie, Physik und Mathematik

Der Martin-Luther-Universität Halle-Wittenberg

Vorgelegt von Herrn

Mohamed Amine Wahada

Gutachter:

Prof. Dr. Stuart. S. P. Parkin
Prof. Dr. Georg Woltersdorf
Prof. Dr. Markus Münzenberg

Tag der öffentlichen Verteidigung:
19.06.2023

Contents

List of Figures

List of Tables

List of Abbreviations

AF	Antiferromagnet
AFM	Atomic force microscopy
AHE	Amomalous Hall effect
ANE	Amomalous Nernst effect
BL	Bilayer
DMI	Dzyaloshinskii–Moriya interaction
FM	Ferromagnet
GMR	Giant magnetoresistance
HM	Heavy metal
ISHE	Inverse Spin Hall effect
LFO	$LaFeO_3$
LSMO	$La_{0.67}Sr_{0.33}MnO_3$
MgO	Magnesium oxide
ML	Monolayer
MOKE	Magneto-optical Kerr effect
MRAM	Magnetoresistive random access memory
MTJ	Magnetic tunnel junction
NM	Normal metal
S2C	Spin to charge
SC	Spin current
SDL	Spin diffusion length
SDSE	Spin-dependent Seebeck effect
SHE	Spin Hall effect
SML	Spin-memory loss
SOT	Spin-orbit torque
SOI	Spin-orbit interaction
SOC	Spin-orbit coupling
STO	Strontium Titanate, $SrTiO_3$
SQUID	Superconducting quantum interference device
SSE	Spin Seebeck effect
STT	Spin transfer torque
TEM	Transmission electron microscopy
TM	Transition metal
TMR	Tunnel magnetoresistance

VSM	Vibration sample magnetometry
XRD	X-ray diffraction

Abstract

A femtosecond laser pulse triggers an ultrafast spin current pulse in a transition metal ferromagnet/heavy metal bilayer. The heavy metal acts as a spin detector with the ability, owing to the inverse Spin Hall effect, to convert the spin current into a transient charge current. This charge current radiates a THz pulse, making this simple bilayer an efficient spintronic THz emitter. In this thesis, we are able to measure such currents electrically on-chip. We then probe the spin current transport in thin film fabricated heterostructures where a specific layer is inserted between the ferromagnet and the heavy metal.

First, we consider the spin current transport in magnesium oxide(MgO) layer and demonstrate a short spin diffusion length of 2Å. Surprisingly, we show that heavy metal 5d elements with less than half filled d shell hinder significantly the spin current transmission due to magnetic moment reduction of the transition metal ferromagnetic layer at the interface. Based on theoretical calculations, we prove that this effect is due to 3d-5d orbital hybridization effects and can be eliminated with the insertion of thin oxide MgO or tantalum nitride (TaN). Furthermore, we fabricated a multilayer where MgO is used to decouple multiple spintronic THz emitters. For a specific number of repeats, we show that its on-chip performance is almost doubled and significantly exceeds its free space radiation output.

In contrast to the short spin dissipation in MgO, we demonstrate a spin diffusion length of $\sim$4nm in antiferromagnetic insulator $LaFeO_3$. We confirm the long distance spin transport in oxides with antiferromagnetic order.

Zusammenfassung

Ein Femtosekunden-Laserpuls löst einen ultraschnellen Spinstrompuls in einem Übergangsmetall-Ferromagnet/Schwermetall-Doppelschichtsystem aus. Das Schwermetall fungiert als Spin- Detektor, der aufgrund des inversen Spin-Hall-Effekts in der Lage ist, den Spinstrom in einen transienten Ladungsstrom umzuwandeln. Dieser Ladungsstrom strahlt einen THz-Puls ab, was diese einfache Doppelschicht zu einem effizienten spintronischen THz-Emitter macht. In dieser Arbeit sind wir in der Lage, solche Ströme elektrisch auf dem Chip zu messen. Anschließend untersuchen wir den Spinstromtransport in dünnschichtgefertigten Heterostrukturen, bei denen eine spezielle Schicht zwischen dem Ferromagneten und dem Schwermetall eingefügt ist.

Zunächst betrachten wir den Spinstromtransport in einer Magnesiumoxid(MgO)-Schicht und zeigen eine kurze Spindiffusionslänge von 2Å. Überraschenderweise zeigen wir, dass 5d-Schwermetallelemente mit einer weniger als halb gefüllten d-Schale die Spinstromübertragung aufgrund der Verringerung des magnetischen Moments der ferromagnetischen Schicht des Übergangsmetalls an der Grenzfläche erheblich behindern. Auf der Grundlage theoretischer Berechnungen weisen wir nach, dass dieser Effekt auf 3d-5d-Orbital-Hybridisierungseffekte zurückzuführen ist und durch das Einfügen von dünnem Oxid MgO oder Tantalnitrid (TaN) beseitigt werden kann. Außerdem haben wir eine Multischicht hergestellt, bei der MgO zur Entkopplung mehrerer spintronischer THz-Emitter verwendet wird. Für eine bestimmte Anzahl von Wiederholungen zeigen wir, dass die Leistung auf dem Chip fast verdoppelt wird und die Strahlungsleistung im freien Raum deutlich übertrifft.

Im Gegensatz zur kurzen Spindissipation in MgO zeigen wir eine Spindiffusionslänge von $\sim$4nm im antiferromagnetischen Isolator $LaFeO_3$. Wir bestätigen den Langstrecken-Spintransport in Oxiden mit antiferromagnetischer Ordnung.

Chapter 1

Lead In

Shining an ultrashort laser pulse on a magnetic material can lead to a transient magnetic quenching on the subpicosecond time scale(1). This discovery, dating from 1996, triggered the fascinating field of femtomagnetism. This simple loss of the magnetic moment has been under investigation since then, triggering an endless stream of controversies and different views to answer the question: where does the spin angular momentum go? The complexity of this question lies in the fact that at this ultrashort time scale, all relevant subsystems: electrons, phonons, magnons and spins are coupled.

Yet, after almost 25 years, there has been still no definite answer but progress has been made. One recent breakthrough(2) showed the transfer of the magnetic moment from the electrons directly to the rotational degree of freedom of the atoms, creating circularly polarized phonons, which in turn result in the ultrafast Einstein de Haas effect(3).

Another interesting non local mechanism that has been suggested and demonstrated, is the superdiffusive spin transport model(4). This model claims that the magnetic moment is carried away from the excited region by extremely mobile electrons. Therefore, in a magnetic material, ultrafast transport properties of electrons depend on their spin polarization which yields ultrafast spin currents enabling spintronic THz emitters(5). Another way to generate spin currents in a certain material is through microwaves. When the ferromagnet is at ferromagnetic resonance, it pumps a spin current to an adjascent layer.

The aim of this thesis is to investigate spin transport in different regimes and in different materials. A typical structure consists of a ferromagnet, an interlayer and a heavy metal. The ferromagnet serves as a spin current generator. This spin current is partly converted to a measurable charge current in the heavy metal layer, effect referred to as inverse spin Hall effect. By inserting an interlayer in-between, one can monitor the subsequent behaviour of the spin current.

The thesis is organized as follows:

In Chapter 2, some fundamental concepts of condensed matter physics and spintronics are briefly introduced. In the next Chapter 3, most relevant experimental techniques and instruments are presented. Then come four results chapters:

Chapter 4: we consider a ferromagnet(FM)/5d heavy metal(HM) bilayer, where the FM is CoFeB and the HM is either platinum(Pt) or tantalum (Ta). We insert magnesium oxide(MgO)

in between the FM and the HM and we investigate the ultrafast spin current injection for different MgO thicknesses. The spin current decays and is suppressed after 1nm of MgO in both cases. However, in the case where Ta is used as a HM, the signal appears to be enhanced for very thin MgO with an effective thickness of one monolayer. We demonstrate through ab-initio density functional theory combined with transport calculations that the Ta layer suppresses the magnetic moment of the adjacent transition metal ferromagnet which affects the spin polarization at the interface and therefore the spin injection efficiency.

Chapter 5: We fabricate a multilayer composed of multiple spintronic THz emitters, each being a typical CoFeB/Pt bilayer, separated by thin layers of MgO and demonstrate its optimized on-chip performance in contrast to a limited free space radiation output.

Chapter 6: We investigate the ultrafast spin transport in tantalum nitride (TaN). We also show that thin TaN can be used to decouple the Ta from the CoFeB and therefore enhance the spin current injection efficiency through the interface.

Chapter 7: We demonstrate ultrafast spin current generation in ferromagnetic half metal $La_{0.67}Sr_{0.33}MnO_3$(LSMO)/Pt bilayer and investigate the spin current transport in the antiferromagnetic insulator $LaFeO_3$(LFO) used here as an interlayer. A spin diffusion length of around 4nm is extracted demonstrating the long distance of spin transport in insulating antiferromagnets.

Finally, in Chapter 8 we draw general conclusions and outlooks are given.

Chapter 2

Theoretical Background

2.1 Fundamental concepts in condensed matter physics

[1]

2.1.1 Electrons in solids

In the quantum mechanical picture, electrons are described by a wavefunction and thus are treated as waves. In the free electron model, the wavefunction of the electron is unbound and oscillatory defining a specific energy and momentum for the electon.

This model fails in the description of electrons in real systems specfically in a solid. This translates into a many body problem where one single electron feels the interaction of the local atoms distributed in the lattice as well as the other electrons. Owing to the extremely astronomical numbers of interactions (order of 10^{23}), other methods have to be considered to solve this. In the independent electron approximation, all the interactions can be viewed as an external potential $U(\mathbf{r})$.

Bloch states Considering a periodic lattice of atoms, the Coulomb interaction originating from each atom can be described as a periodic potential. The Hamiltonian of an electron is then written as :

$$H = -\hbar^2 \nabla^2 / 2m + U(\mathbf{r}) \tag{2.1}$$

Where $U(\mathbf{r+R}) = U(\mathbf{r})$ for all $\mathbf{R}$ in the Bravais lattice. The peridocity of the potential U leads to significant consequences on the wavefunction of the electron. This is stated in Bloch's theorem[9]:

$$\psi_{n\mathbf{k}}(\mathbf{r}) = e^{i\mathbf{k}\cdot\mathbf{r}} u_{n\mathbf{k}}(\mathbf{r}) \tag{2.2}$$

Where $u_{n\mathbf{k}}(\mathbf{r+R}) = u_{n\mathbf{k}}(\mathbf{r})$ and n,k are two quantum numbers and usually thought of as an energy level number and a wavevector respectively. k is not a real wavevector and is called crystal momentum of the electron. For each quantum number n, one can construct the electron energy $\epsilon_{n\mathbf{k}} = \hbar^2 k^2 / 2m^*$ depending on the momentum k, refered to as bands. The whole set of $\epsilon_{n\mathbf{k}}$ constitute the band structure of the solid. Above, m^* is the effective mass of the electron

---

[1]References from (6; 7; 8; 9; 10) are used throughout this section.

and depends on the band structure. In this picture, the ground state of N Bloch electrons can be realized by just occupying all the "one electron" states $\epsilon_{n\mathbf{k}}$ respecting the Pauli exclusion principle. The energy level seperating the occupied states from the unoccupied ones is referred to as the Fermi level ϵ_F. Since the electrons are fermions, they obey the Fermi Dirac distribution statistics:

$$f(\epsilon, \mu, T) = (1 + exp[(e - \mu)/k_B T])^{-1} \tag{2.3}$$

Here ϵ is the energy, μ is the chemical potential, k_B is the Boltzmann constant and T is the temperature.

2.1.2 Angular momentum and magnetic moments

Orbital angular momentum

In the classical picture, angular momentum $\mathbf{l}$ of a particule is defined as the cross product of its position $\mathbf{r}$ and its momentum $\mathbf{p}$:

$$\mathbf{l} = \mathbf{r} \times \mathbf{p} \tag{2.4}$$

This definition can be extented to the quantum mechanical world where the definition takes a mathematical form of:

$$\mathbf{L} = -i\hbar \mathbf{r} \times \nabla \tag{2.5}$$

This implies certain properties on the angular momentum which would be defined as follows:

$$[\mathbf{L}_i, \mathbf{L}_j] = i\hbar \epsilon_{ijk} \mathbf{L}_k \tag{2.6}$$

Based on the quantum mechnical formalism, this infers that it is impossible for a given precision to measure all components of the angular momentum which is a consequence of the Heisenberg uncertainty priciple. Nonetheless, it is possible to have a common basis for $\mathbf{L}_i$ with $\mathbf{L}^2$ since $[\mathbf{L}^2, \mathbf{L}_i] = 0$. Usually, the z axis is chosen as the quantization axis (i.e. $\mathbf{L}_z$ is considered) . The eigenvalues are then defined based on two quantum integer numbers l and m_l :

$$\mathbf{L}^2 |\psi_{lm_l}> = \hbar^2 l(l+1)|\psi_{lm_l}>$$
$$\mathbf{L}_z |\psi_{lm_l}> = \hbar m_l |\psi_{lm_l}> \tag{2.7}$$

where for a given l, m_l satisfies the condition $-l \leq m_l \leq l$. These two quantum numbers define the orbital state of the electon.

Spin angular momentum

In addition to its orbital angular momentum, the electron holds an additional intrinsic angular momentum called spin. Unlike its orbital counterpart, the spin of the electron doesn't have a classical analogue and it's solely a quantum mechanical property. Its discovery came to light from the Stern Gerlach experiment in 1921 and its quantum mechanical derivation arose from the generalized Schrodinger equation after taking into account relativistic terms. It is then called the Dirac equation where the solutions are called spinors. The spin operator $\mathbf{s}$ is a set of $\mathbf{s_x}, \mathbf{s_y}, \mathbf{s_z}$ 2×2 matrices. $\mathbf{s_z}$ is chosen to be diagonal with two eigenvalues corresponding to

$m_s\hbar$ with $m_s = \pm\frac{1}{2}$. These two states are called spin up and spin down for plus and minus respectively.

Magnetic moment

Both angular momenta give rise to a magnetic moment depending on their expectation values:

$$m = -\frac{\mu_B}{\hbar}(g < \mathbf{s}_z > + < \mathbf{l}_z >) \tag{2.8}$$

Where $g = 2.0023$ is the electron g-factor and $\mu_B = \frac{e\hbar}{2m_e}$ is the Bohr magnetron. Given an external magnetic field, the electron's magnetic moment experiences a magnetic energy of the form :

$$\epsilon = -\mu_0 H \cdot m \tag{2.9}$$

This easily now accounts for the two dots seen in the Stern Gerlach experiment corresponding of the two eignevalues of the latter energy term.

2.1.3 Magnetic ordering

A single electron has at least a net magnetic moment arising from its spin angular momentum. Nonethless, in an atom, the total magnetic moment is proportional to the total angular momentum of the whole ensemble of electrons:

$$\mu = \gamma\hbar = -g\mu_B \mathbf{J} \tag{2.10}$$

Unlike the case of a single electron, the expectation value of $\mathbf{J}$ can vanish and this is due to the Pauli's exclusion principle which dictates that two electrons cannot occupy the same orbital unless they have opposite spins. In addition to the spin-orbit coupling, the orbital occupancy is determined by Hund's rule. In a case where the total angular momentum is zero, the magnetic response of the atom or the susceptibility is determined by Lenz's law and has a negative value.[2] This is called diamganetism. If the expectation value is nonzero, then a nonzero magnetic moment dominates the magnetic response. In this case, we have paramagnetism and its susceptibity is much larger than the diamagnetic one $\chi^{para} \sim 10^{-2} \gg \chi^{dia} \sim -10^{-4}$. In a solid, the paramagnetic and diamagnetic contributions persist and their corresponding magnetic responses vanish when the external magnetic field is omitted. On the other hand, another class of material can hold a magnetic order where a non zero spontaneous magnetization arises and persists even at zero field. These are ferromagnetic materials.

Ferromagnetism and Stoner model

As we have seen, each atom carries a magnetic moment arising from the total spin and orbital contributions of the electrons provided Hund's rules are satisfied. In the case of a paramagnetic material, all the atomic magnetic moments are randomized and the overall magnetization is zero. Only when an external magnetic field is applied, the atomic moments would favor to align with the external field overcoming the thermal fluctuations responsible for their randomization.

---

[2]The atom creates a magnetic field that opposes the external field.
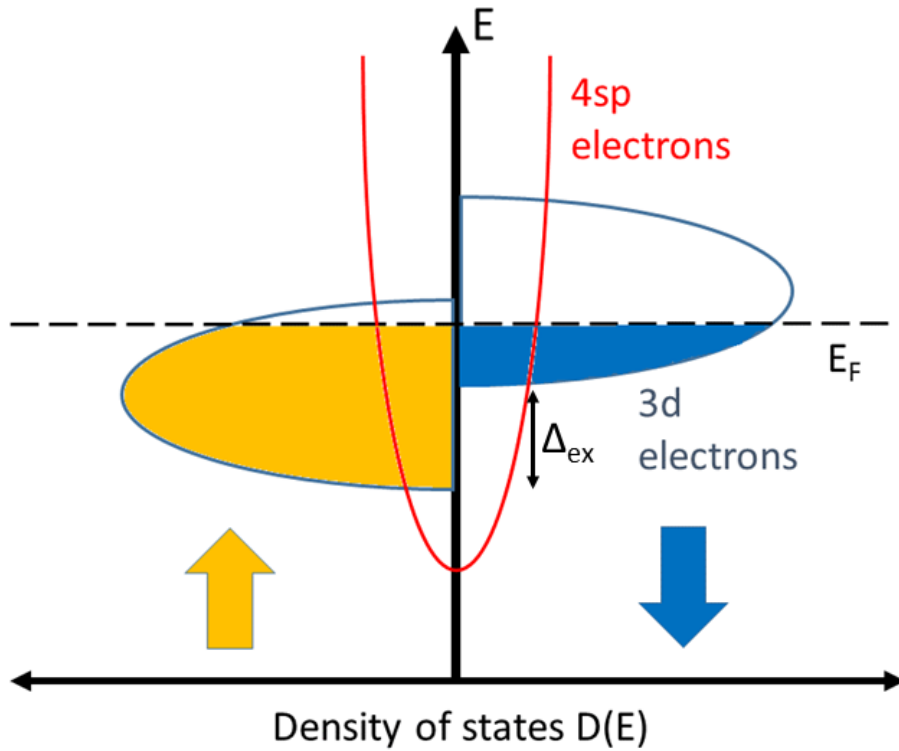
Figure 2.1: Schematic illustration of the Stoner-band model of ferromagnetism for TM ferromagnets. The 3d density of states are exchange split with an exchange splitting energy Δ_{ex}. The Fermi level crosses the band resulting in an imbalance of occupied states for majority and minority spin channels.

In a ferromagnet however, a spontaneous magnetization is formed below a certain temperature called Curie temperature, T_C. In a similar fashion to the paramagnet, a ferromagnet could be understood from a mean field theory approach where the "external field" is replaced by an internal field arising from the magnetic moments. This theory is called the Weiss mean field theory(11). Nonetheless, a certain interaction is required to account for this intrinsic internal field. This interaction is called the exchange interaction and has solely an electrostatic origin reflecting the Coulomb repulsion between two electrons in conjunction with the Pauli's exclusion principle. As an example, let's consider a molecule consisting of two hydrogen atoms. The wavefunction of the two electrons of both atoms should be antisymmetric with respect to the exchange of the two electrons[3]. This implies that either its spatial part or the spin part is antisymmetric. This entails that two states are formed with a total spin $S = 0$ called singlet state and $S = 1$ called triplet state. Their names reflect respectively their degeneracies. The energy difference between these two levels is written:

$$E^S - E^T = 2J \tag{2.11}$$

---

[3]This is due to the fermionic nature of electrons.

Here J is the exchange constant and is expressed with integrals of the overlapping of the wavefunctions of the electrons and the so called exchange integral[4].

In conjuction with his work on the helium atom He, Heisenberg generalized this problem to interacting spins and established in 1928 the Heisenberg exchange interaction with the following Hamiltonian:

$$H_{EX} = -2JS_1 \cdot S_2 \tag{2.12}$$

Where S_1 and S_2 are two spin operators. In this picture, a positive value of J would result in a parallel alignment and therefore a ferromagnetic coupling and negative value in antiparallel alignment, i.e. antiferromagnetic coupling. It is indeed this interaction that accounts for the internal mean field giving rise to the sponstaneous magnetization in solids. Nonetheless, in this picture, the magnetic moments are only treated as they are localized and with wavefunctions overlapping between the neighbouring atoms resulting in the exchange interaction. This model is called the Heisenberg model explains well certain ferromagnetism, for example in rare earth elements which is due to the high localization of the inert f shell. However, it fails to account totally for the magnetism of the early transition metals(TM) in which we will focus on in this thesis. For example, in rare earth elements, adding all the atomic magnetic moments together in the localized picture would account for, to a good agreement, the overall magnetic moment of the material. However, in the case of TMs, the disagreement is very large.[5] Therefore, another picture is needed to explain this discrepancy which brings us to the picture of band magnetism and the Stoner model of itinerant ferromagnetism(12). As indicated in the name, itinerant refers to "travelling". In this case, it is inferred that conduction electrons or delocalized electrons play an important role. Indeed, we need to consider a typical density of states of an early TM. Before that, let's go back to a free electron gas in three dimensions. The density of states has a parabolic dependence on the energy and is spin degenerate. The filling of states is done according to the Fermi Dirac distribution and defines the Fermi energy ϵ_F and we have $N_\uparrow = N_\downarrow = N/2$. Once we apply a magnetic field, neglecting for the sake of the argument the orbital contribution, the degeneracy is lifted and the energy landscape is shifted for both spin channels giving:

$$
\begin{aligned}
N_\uparrow &= \frac{N}{2} + \frac{1}{2}N(\epsilon_F)\mu_0\mu_B H \\
N_\downarrow &= \frac{N}{2} - \frac{1}{2}N(\epsilon_F)\mu_0\mu_B H
\end{aligned}
\tag{2.13}
$$

This imbalance in the number of electrons for both spin channels is a consequence of the Fermi Dirac distribution and for this new energy landscape favours the alignment of the spin parallel to the external field. This is called Pauli's paramagnetism with a typical magnetic susceptibily $\chi^{Pauli} \sim 10^{-6}$. The net resulting magnetization is $M = (N_\uparrow - N_\downarrow)\mu_B = N(\epsilon_F)\mu_0\mu_B^2 H$. Once the magnetic field is zero, the magnetization vanishes. It is the Pauli's exclusion principle that hinders the parallel alignment associated with favorable potential energy. In other terms

---

[4]depending on the overlap of the wavefunctions, the favorable state would have a bonding or antibonding character which historically contributed to the quantum mechanical understanding of chemical bonding

[5]Considering a real TM solid with a certain crystal structure, crystal fields would lift the degeneracies of the d subshell. This results in a locking of the orbital spatial configuration by the electric fields of the neighbouring nuclei. This energy exceeds largely the magnetic splitting energy of the levels due to an external magnetic field which results in a vanishing contribution of the orbital magnetic moment. This is referred to as the quenching of the orbital angular momentum. Nonetheless, taking this into consideration doesn't help to account for the gap between the total magnetic moment and the sum of the atomic magnetic moments.

the increase in kinetic energy associated with occupying higher states outweighs the potential energy. In TMs however, considering the band structure effects and the exchange energy, the parallel spin alignment can counter the kinetic term only in a certain considition expressed by Stoner as :

$$IN(\epsilon_F) > 1 \tag{2.14}$$

This is known as the Stoner criterion(13) and expresses a sufficient condition for itinerant ferromagnetism. I here known as the Stoner parameter is material dependent and reflects the localization of the wavefunctions around the Fermi level. In another intuituve picture, it captures the strength of exchange per electron. Another important point, is that a large density of states is needed which to a certain approximation scales inversely with the bandwidth. This is well achieved for an almost filled $3d$ shell giving a large density of states at the Fermi level and a more localized character compared to, for example $4d$ or $5d$ shells. The Stoner criterion is therefore only verified for three TMs which are Fe, Co and Ni which will be considered in this thesis[6]. In Fig. 2.1, we show a typical density of states of a TM ferromagnet in the Stoner-band model. One more interaction contributes to the long range ordering of the itinerant ferromagnetism is the s-d exchange interaction which is a coupling between a more 'delocalized'(compared to the d electron) sp electron with the d electron. This adds another mediator between neighbouring d electrons.

2.1.4 Magnetic anisotropy

Magnetic anisotropy(14) is a property inherent or induced in a certain material that lowers the magnetic free energy of the system in a certain direction or plane. There are various types of magnetic anisotropies. Namely the shape anisotropy, magnetoelastic anisotropy, surface anisotropy and magnetocrystalline anisotropy.

- **Shape anisotropy** Taking a finite sized material with a spontaneous magnetization induces changes in its magnetic energy due the magnetic poles that form on the surfaces(15). This energy is also called magnetostatic energy and arises from the dipole dipole interaction between all the magnetic dipoles considered in the material preferably orienting them head to tails. This results in a field opposing the magnetization M, called the demagnetizing field H_d:

$$H_d = -N \cdot M \tag{2.15}$$

  Where N is the demagnetizing factor and depends on the geometry of the sample. Therefore the magnetization within the material is reduced by the demagnetizing field. The more anisotropy there is in N, the more it is impinged on the magnetization. When the seperation between the extremities of the material gets larger, the farther are magnetic poles from each other and the less is the shape anisotropy felt. In the thin film limit for unpatterned samples, the main contribution arises from the out of plane direction.

- **Magnetocrystalline anisotropy** This type of anisotropy(16) is intrinsic to the crystal structure of the material itself owing to the combined action of spin-orbit coupling

---

[6]The Stoner criterion successfully explains the ferromagnetic ordering of TMs but fails within the model itself to give a correct estimate of the Curie temperature.

and electostatic crystal fields. Depending on the crystal order of a particular system, anisotropic crystal fields are formed and act on the electron orbital degree of freedom. This shapes the electron orbitals and bonding charge distribution in a more energetically favourable way. Due to spin-orbit coupling, the spin degree of freedom feels the changes to the electron orbitals. This opens a correlation channel between the spin and the lattice which favours certain directions easier for the spins to orient along. Such a direction is called an *easy axis*. Depending of the symmetry of the crystal, an easy plane can be formed. The direction where the magnetic energy is rather increased is called a *hard axis*.

2.1.5 Spin-orbit interaction

Spin-orbit interaction(SOI) is an interaction term coupling the spin and the orbital momenta of an electron. This coupling term appears as a relativistic correction in Schrodinger equation. To have an intuitive understanding of it in a semiclassical way, let's consider an electron moving in a uniform electric field $\mathbf{E}$ without any external magnetic field in the Laboratory frame of reference. However, applying the Lorentz transformation to the equation of motion of the electron, the latter experience in its own frame of reference a non vanishing magnetic field $\mathbf{B} = -\gamma \frac{\mathbf{V} \times \mathbf{E}}{c^2}$, where $\gamma = \frac{1}{\sqrt{1-(\frac{v}{c})^2}}$ is the Lorentz factor. Nonetheless, the Spin-orbit coupling (SOC) is a purely relativistic term and can be dereived from fully relativistic Dirac equation:

$$H\psi(r) = i\hbar \frac{\partial}{\partial t}\psi(r)$$
$$H = -eV(r) + \beta mc^2 + \alpha.[c\mathbf{p} + e\mathbf{A}(r)] \tag{2.16}$$

Where H is the hamiltonian for an electron in an external scalar potential $V(r)$ and vector potential $A(r)$. α is a vector of 4×4 matrices expressed with Pauli spin matrices. β is a 4×4 matrix.

$$\alpha = \begin{pmatrix} 0 & \sigma \\ \sigma & 0 \end{pmatrix}, \beta = \begin{pmatrix} I_2 & 0 \\ 0 & -I_2 \end{pmatrix}, \Psi = \begin{pmatrix} \psi_1 \\ \psi_2 \end{pmatrix} \tag{2.17}$$

where I_2 is a 2×2 unit matrix. Ψ is a spinor containing two component vectors ψ_1 describing the two spin electron and ψ_2 is the component arising from relativistic effects. One can then derive the so called Pauli equation. By eliminating the vector potential in non magnetic media and for non relativistic limit with $v \ll c$, the Pauli equation reduces to the Schrodinger equation with the following additional term:

$$H_{SOC} \propto \sigma.[\nabla V(r) \times \mathbf{p}] \tag{2.18}$$

which can be further reduced considering the following expension $V(r) = \frac{1}{r}\frac{dV}{dr}\mathbf{r}$ [7], $\mathbf{S} = \sigma/2$ and $\mathbf{L} = \mathbf{r} \times \mathbf{p}$

$$H_{SOC} = \xi(r)\mathbf{L} \cdot \mathbf{S} \tag{2.19}$$

In principle the spin-orbit term originates from the potential felt from all the other electrons in the atom as well as the nuclear field. The most preponderent contribution is the nucleus and therefore $|\xi(r)| \propto \frac{1}{r}\frac{dV}{dr} \sim \frac{Ze}{r^3}$ in the vicinity of the nucleus core. This makes spin-orbit coupling

---

[7]This expension is valid if $V(\mathbf{r}) = V(r)$ is spherical symmetric

term scale with the atomic number and therefore it is considerable for heavy elements. As we will see in later sections, SOC in heavy elements is responsible for fundamental phenomena inheretent to the field of Spintronics notably the Spin Hall effect. Also the SOC is responsible for spin relaxation in the bulk and can act differently in inversion symmetric compound leading to Elliot Yafet scattering and inversion symmetry breaking compounds giving rise to Dyakonov Perel type of scattering, both of which will be discussed throughly in later sections.

2.2   Spintronics: an overview

Spintronics is the generic term for spin electronics. In contrast to conventional eletronics where the information vector is the charge of electron, in Spintronics, the degree of freedom of interest is the spin of the electron. Attempts are made to utilize and control the spin momentum of the electron. The first effect that brought interest in magnetism with electronic current is known as Magnetoresistance. It was discovered by Lord Kelvin even 40 years before the discovery of the electron itself. Magnetoresistance is a phenomena responsible for an asymmetry in the resistivity of the material under an external magnetic field depending on its relative orientation with the current. This is called Ordinary Magnetoresitance (OMR) and its value is less than 1% for field as high as 1 Tesla. When extended to metals having an intrinsic magnetization, i.e. ferromagnetic metals, this is called Anisotropic Magnetoresistance (AMR)(17) where the material shows high resistivity value when current and magnetization are parallel and lower value when they are perpendicular to each other(18). AMR can reach values up to 1-2%. Later on, in the late 1980s, another magnetoresistance effect has been discovered and with it came the advent of the field of Spintronics. This effect is called the Giant Magnetoresistance(20; 21).

Owing to the development of atomic deposition techniques, multilayers with thicknesses as small as 1nm have been enabled. Heterostructures with single atomic elements with certain defined interfaces can be realized. In particular, having two (or more) magnetic layers seperated by non magnetic metallic spacer can induce in special cases an antiparallel alignment of the magnetization. This device structure is called a spin valve. To achieve an antiparallel magnetization orientation configuration, various methods can be implemented. One is via the interlayer exchange coupling which oscillates between ferromagnetic and antiferromagnetic exchange depending on the spacer layer's thickness(22). This form of interaction is called the RKKY interaction. Another way is two have two magnetic materials with two different coercive fields and finally a pinned layer through exchange bias with an antiferromagnetic layer or a synthetic antiferromagnet. Historically, the GMR effect has been observed in 1988 in Fe/Cr multilayers in Fert's group (see Fig. 2.2(a)) and in Fe/Cr/Fe trilayer in Grunberg's group. When a current is passed throough the structure, the registered resistance drops from its highest value at zero field (i.e. antiparallel configuration) to its lowest value for higher magnetic field values where the both magnetizations are parallel. Contrary to OMR or AMR, GMR can reach high values up to 200%. Despite the fundamental interest in this effect, it has enabled a tremendous technological development of magnetic sensors and memory devices(23; 24; 25; 26) notably hard disc drives(HDD) (See Fig. 2.2(c)and (d)). Two types of geometrical configurations are used. Historically, current-in-plane(CIP) devices have been made where the contacts to the heterostructure is made on the sides making the electrical current flow in plane. This
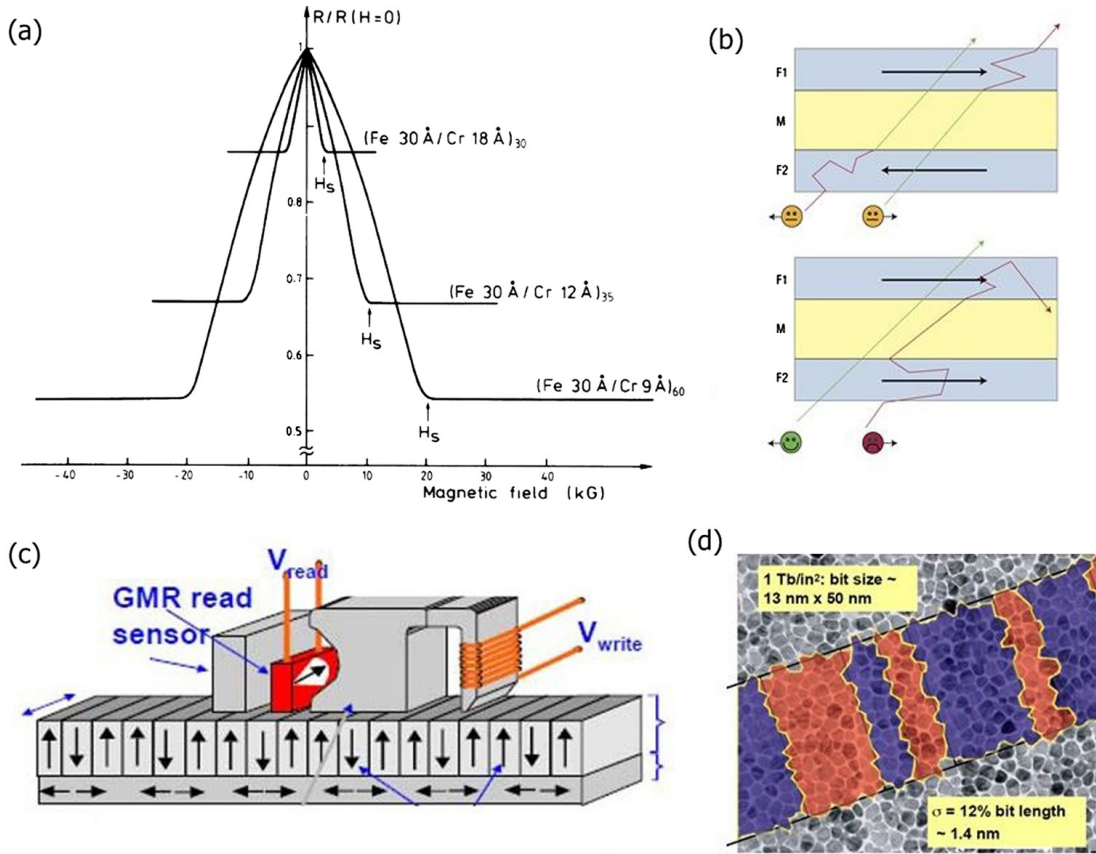
Figure 2.2: **GMR concept** (a) GMR result in Fe(3nm)/Cr(0.9nm) multilayers. (b) Schematic illustration of the mechanism of GMR. In the upper panel, the two magnetizations are anit-parallel which hinders the spin transport of a specific spin channel in one layer or another, therefore enhancing the resistance of the stack. In lower panel, the parallel configuration of the magnetizations enables a more efficient spin transport for the majority spin channel in both layers, whereas increased scattering states are available for the minority one. The transport of the majority spin channel shortcuts the minority one which results in a reduced resistance compared to antiparallel configuration. (c) Schematic representation of a GMR head in hard disk drives (HDD). (d) Micrograph stored magnetic bits in a HDD. (Taken from (19)).

measurement techinique holds an advantage of accessing a sizeable and measureable resistance of the device, yet display lower values compared to the current-perpendicular to-plane(CPP) counterpart. In this latter geometry(27), contacts are made from top to bottom, the current is flowing perpendicular to the interfaces and the resistance is measured between these contacts. The challenge has been yet to access the resistance of the device made small compared to the Ohmic resistances of the contacts. First experiments for example implemented superconducting contacts(28; 29; 30; 31). Nonetheless, with this geometry, GMR has reached values as high as 220% in Fe/Cr.

The GMR effect occurs due to the spin dependent scattering in the multilayer(32). In other words, the conductivities of both spin channels are different(see Fig. 2.2(b)). This can be qualitatively explained using Mott's picture(33; 34) where two itinerant independent[8] spin

---

[8]No spin mixing is considered for the relevant travelling distances in metal thin films, therefore these two spin up and spin down channels can be independently treated as two conductivities organized in parallel.

channels for up spin and down spin are considered. These spins are carried by the sp conduction electrons and their scattering rates is modulated by the density of states in the 3d channel. Due to the fact that the 3d densities are exchange split, the available states are different, therefore the scattering rates for both spin channels are different.

To illustrate this, one needs to consider a typical band structure of a 3d ferromagnetic element. As the bands are exchange split, the Fermi level usually lies somewhere in the minority d band. Usually the majority spin d band can be fully occupied (e.g. Co) or slightly partially occupied like in the case of Fe. One now needs to evaluate the scattering rates for both sp conducting spin channels which is dependent on the available density of states at the Fermi level roughly inversily proportional to the Fermi velocity. This adds a correlation between the scattering lifetime and the Fermi velocity. The mean free path and thus the resistivity will be then be spin dependent. For example, for Co/Cu/Co, the majority d band of Co is fully occupied and the conduction of majority spin channel is carried by the very mobile and delocalized sp electrons despite the reduced density of states whereas the minority spin electrons experience a strong sp-d hybridization and get a localized and low mobility character which enhances their resistivity. In the case of Fe/Cr/Fe however, although the resistivity of the majority spin channel is slightly higher than the majority one, it is actually the minority spin channel that is responsible for the conduction.

Indeed, another important factor comes into play which is the band matching at the interface between the elements. In the case of Co/Cu, the band structure of Cu and Co are similar for the majority spin channel of Co and in the case of Fe/Cr, the band matching happens for the minority spin channel. Hence, a spin down electron doesn't feel a potential difference entring Cr whereas a spin up electron feels a potential step which yields strong scattering and therefore large interfacial resistance. Taking all these points into account, when the magnetizations are parallel in a GMR spin valve device, the conductive spin channel in the first layer would still experimence minimal scattering in the second layer + interface contrary to the other spin channel that is hindered in both layers and interfaces. Consequently the total conductance is given by the conductive chennel. In the antiparallel case, the conductive spin channel in the first layer would experience large scattering in the second layer + interface and the other way around for the second spin channel. In this case, both spin channels experience contribute to a large resistance. This asymmetry accounts for the GMR effect.

Another important MR effect further stretched the possibilities and fundamentals of Spintronics. This is called Tunneling Magnetoresistance(TMR) and in contrast to its GMR analogue, the device rather contains a non magnetic insulator spacer layer and is called a Magnetic Tunnel Junction(MTJ). Similar to GMR, TMR exhibit an analogue low and high resistivity state for parallel and antiparallel magnetizations configuratiosn respectively. The origins of TMR go back to 1975 -which is even earlier than the GMR effect- where it was reported by Julliere in Fe/Ge-O/Co(36). Yet, due to the difficulty to reproduce the results, further development and investigations were lacking. Nevertheless, due to discovery of GMR and inauguration of the hunt for large MR ratios, TMR has regained more interest in the following years. One key year was in 1995 where Miyazaki and Moodera (37; 38)reported MR ratios of 18% at room temperature using 3d ferromagnet and amorphous Aluminium oxide as a tunnel barrier. This boosted further the focus on TMR where optimizations further increased the MR ratios.
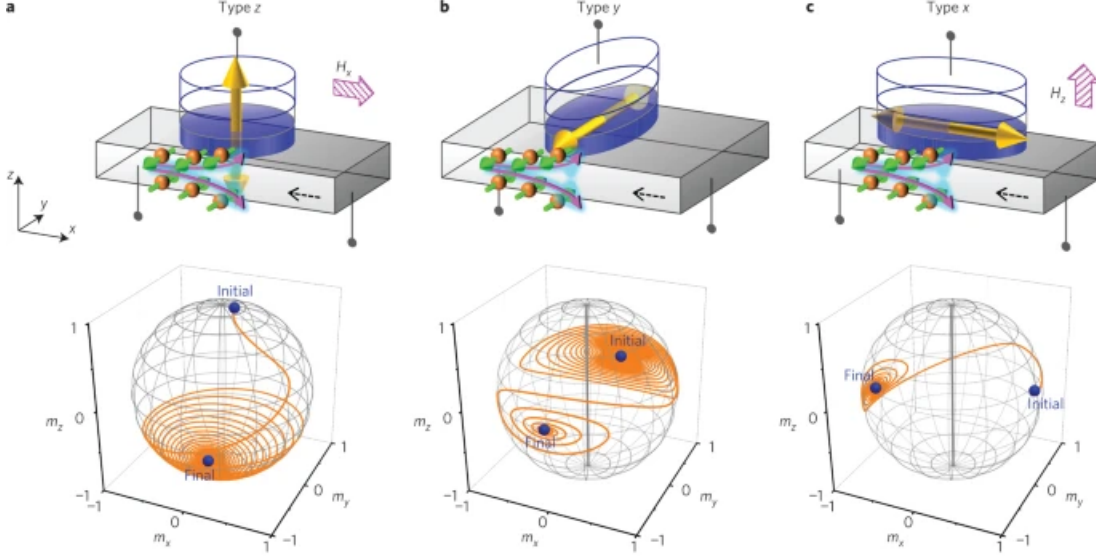
Figure 2.3: **SOT magnetization switching in different geometries.** (a) The magnetization is directed out of plane due to a perpendicular magnetic anisotropy. A current is passed in the heavy metal (Ta) layer to create a spin current acting on the magnetization via SOT. The switching is assisted with an external in plane magnetic field needed to break the symmetry. Simulation results of the macrospin dynamics during the switching is shown. (b) In this configuration the magnetization is pointing in the plane of the film and perpendicular to the applied current direction. Corresponding simulation results are shown in the bottom panel.(c) The magnetization is pointing in the same direction as the applied charge current. Deterministic bipolar switching is enable with the assistance of an external magnetic field directed along the z direction. Corresponding simulation results are shown in the bottom panel. (Taken from (35)).

One more key important milestone is the implementation of crystalline insulating barriers where MR ratios even reaching values of around 200% were obtained at room temperature with crystalline MgO based MTJs(39; 40; 41). The key physics of TMR is a symmetry filtering(42; 43) which will be discussed for crystalline insulating barriers. Indeed, the states of the bands in the ferromagnet need to couple to the evanescent tunneling states of the barrier(44; 45; 46; 42) in order to reach the second ferromagnet and their decay length depends entirely on their symmetry. In 3d ferromagnets like Fe and Co, the spd hybridized state called Δ_1 state, which displays a high spin polarization, can tunnel through MgO and recouple through the Δ_1 states in the second ferromagnet electrode in the parallel alignment case. Other states can tunnel but their decay length is much smaller than the one of Δ_1. In the antiparallel case, the Δ_1 doesn't tunnel efficiently anymore and is almost fully suppressed. Yet, a resonant tunneling occurs due to interface resonant states which reduces the effective total spin polarization and in consequence the MR ratio.

Spintronics offers more prowesses and discoveries that popped up one after the other. One important effect is called the spin transfer torque or STT. This phenomena has been predicted beforehand by Slowenski(48) and Berger(49) who argued that in magnetic/non magnetic multilayers, a spin polarized current injected from a ferromagnet could transfer its spin momentum to a second ferromagnet(50; 51; 52; 53; 54; 55). Under the influence of the exchange interaction, the incoming spin polarized current would align to the local magnetization which will acquire
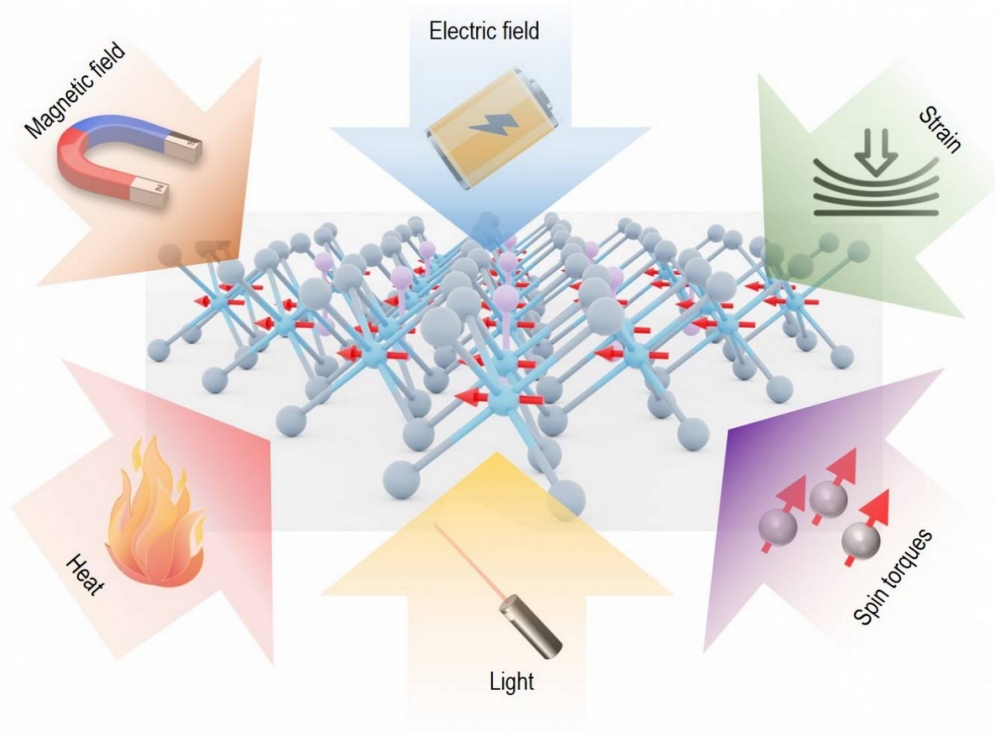
Figure 2.4: Schematic showing possible ways of interacting with the spin degree of freedom.(Taken from (47)).

its transverse component. This results in a torque acting on the magnetization. This result is remarquable as it enabled the control of magnetization without the use of external magnetic fields. As a consequence, in a well defined nanopillar device, a spin polarized current can be used to even switch a magnetization(56) or cause its precession which generated microwave osciallators called spin transfer oscillators(57; 58).

One big step for Spintronics is to enable the field free control of magnetization without the use of external magnetic fields but through spin momentum transfer. More possibilities emerged in this direction where it was possible to generate pure spin currents. One way is use spin-orbit interaction. Indeed, a material with strong spin-orbit interaction like a 5d heavy metal such as Pt,Ta or W is endowed with the ability to convert a charge current into a pure spin current flowing in the perpendicular direction, effect referred to as the Spin Hall Effect(SHE)[9](59; 60). This discovery marked a tremendous breakthrough in the field and inaugurated a new subfield called spin-Orbitronics. Similar to the prowess of STT, a Spin Hall material attached to a magnet could in principle inject pure spin current though the interface, thus acting on the magnetization through torques. This is called spin-orbit torque (SOT) and it offers less power consumption than the STT. Usually the switching requires the assistance of a field to break the symmetry. This could be achieved with external magnetic field (such a process is illustrated in Fig. 2.3), an exchange bias or an interlayer exchange.

Other spin-orbitronics mechanisms of spin to charge conversion can even live at interfaces.

---

[9]First evidence was observed in semiconductor GaAs and GaAsIn films as well as p-n junctions.

This is the case for Rashba Edelstein effect(61) where the interface acts as a 2D electron gas, under broken inversion symmetry. This leads to spin momentum locking responsible for an interfacial spin-orbit field called Rashba field(62; 63). It is also worth to mention another class of materials that possess spin to charge conversion property, called topological insulators(64). These materials are insulating in the bulk but conducting on the surface. Due to topologically protected electronic states at the surface exhibiting spin momentum locking, passing an electrical current yields a spin accumulation. Spintronics offers a whole playground involving different intercoupled phenomena that can interact directly or indirectly with the spin degree of freedom as shown schematically in Fig. 3.4. These external tools involve magnetic fields, electric fields, strain, spin torques and light. Light is of particular interest for it boosted the dynamics to femtosecond(fs) regime. Indeed, magnetization control has been achieved optically through intense fs laser pulses. Subsequently to such a laser pulse, the magnetization experiences ultrafast quenching in the subpicosend time scale(1). With this, came about the birth of the field of femtomagnetism offering a lot of complexity and rich unexplored physics. In some cases, the ultrafast demagnetization could lead to the complete reversal of the magnetization. This is called all optical switching which gained a lot of attention due to the potential technological prospects it can offer. As will be discussed in more details in a later section, this ultrafast quenching process is accompanied by superdiffusive spin currents(4) which enabled ultrabroadband THz generation(5) and therefore a means of probing the local magnetization(65).

2.3 Spin transport and spin dynamics

2.3.1 Spin to charge conversion

As pointed out briefly in section 2.2, new effects emerged yielding pure spin current generation without the need for external magnetic field or ferromagnets. Due to spin-orbit coupling, it is possible to convert longitudinal electric currents into spin currents in the bulk of certain materials due to SHE and at interfaces due to REE. SHE is extensively used throughout this thesis. Before we point out the mechanisms responsible for such an effect, we need to review the principles and fundamentals of Hall voltages.

Anomalous Hall effect

The first discovered Hall effect(66) refers to the production of a transverse voltage accross a finite conducting material under a flow of longitudinal current, placed in an external magnetic field. This transverse voltage arises due to the external magnetic field and scales with it. This Hall effect can be explained by the classical Drude model and has its origin in the Lorentz force exerted on the conduction electrons deflecting them from their trajectories in a similar fashion thus creating an imbalance on the transversial sides of the material. This Hall effect is known as the ordinary Hall effect(OHE) in contrast to its anomalous counter part. What came to be known as the anomalous Hall effect (AHE)(67) is the same effect seen in ferromagnetic materials where the transverse voltage has an additional dependence on the magnetization and

can be expressed[10] empirically by:

$$\rho_H = -\rho_{xy} = R_0 H + R_s 4\pi M_z \tag{2.20}$$

Where the first part of the right hand side is the OHE as it scales linearly with the external magnetic field H and the second part stems from the AHE where the dependence of the Hall voltage can show non linear behaviour before saturation of the magnetization. After saturation, the OHE is dominant. This means that even without an external field the electrons gain a transverse velocity and its origin cannot be explained by the intrinsic magnetic field of the ferromagnet. Indeed, it would require a field with a strength ranging around a hundred Tesla. The mechanisms responsible for the AHE can be of two kinds which are denoted intrinsic and extrinsic contributions. Interestingly, the intrinsic contribution arises solely from the band structure, whereas the extrinsic contributions refer to deflections due to scattering events on impurities, defects or phonons in the solid. The first theoretical consideration to account for a free scattering contribution was done by Karplus and Lutttiker(68) who considered the interference between the electron Bloch states, taking spin-orbit interaction into consideration, in the perturbative approximation. This gives an anomalous velocity to the electron responsible for its deflection. Later on, the formalism has been revised under the concept of Berry phase(69) or Berry curvature in which the derivation of the electron's velocity straightforwardly pinpoints to a Hall term :

$$v_n(\mathbf{k}) = \frac{\partial \epsilon_n(\mathbf{k})}{\hbar \partial \mathbf{k}} - \frac{e}{\hbar} \mathbf{E} \times \Omega_n(\mathbf{k}) \tag{2.21}$$

The first term is the normal velocity term for an electron with a crystal momentum $\mathbf{k}$ in the nth band. The second term is always perpendicular to the external electric field $\mathbf{E}$. This gives rise to a Hall term as long as $\Omega_n(\mathbf{k})$ is non zero. $\Omega_n(\mathbf{k})$ is called Berry Curvature of the nth band. In this perspective, by simply writing down the Hall conductivity using Kubo's formalism(70) for a Hamiltonian describing non-interacting Bloch electrons with $|n, \mathbf{k}>$ eigenstates:

$$\sigma_{xy} = -\frac{e^2}{\hbar} \sum_n \int_{BZ} \frac{d\mathbf{k}}{(2\pi)^3} f(\epsilon_n(\mathbf{k})) \Omega_n(\mathbf{k}) \tag{2.22}$$

where $f(\epsilon)$ is the Fermi Dirac distribution. The Berry curvature $\Omega_n(\mathbf{k})$ is related to the Berry phase $a_n(\mathbf{k})$ via:

$$\Omega_n(\mathbf{k}) = \nabla_{\mathbf{k}} \times a_n(\mathbf{k}) \tag{2.23}$$

As can be seen from the formula, the intrinsic contribution of the AHE is the integration of the Berry curvature through the whole Fermi sea. Interestingly, AHE has its intrinsic contribution depending entirely on the *Topology* of the band structure. Equivalently, the AHE conductivity has a finite value as soon as the Berry curvature is non zero. Based on symmetry considerations, the Berry curvature satisfies the following conditions for inversion invariant and time reversal invariant systems respectively:

$$\Omega_n(\mathbf{k}) = \Omega_n(-\mathbf{k})$$
$$\Omega_n(\mathbf{k}) = -\Omega_n(-\mathbf{k}) \tag{2.24}$$

---

[10]The transverse resistivity is considered here and defined as the ratio between the transverse voltage by the longitudinal current, $\rho_{xy} = \frac{V_{yy}}{j_{xx}}$

In the case where both are preserved, it is straightforward that the Berry curvature vanishes

a) Intrinsic deflection

Interband coherence induced by an external electric field gives rise to a velocity contribution perpendicular to the field direction. These currents do not sum to zero in ferromagnets.

$$\frac{d\langle \vec{r} \rangle}{dt} = \frac{\partial E}{\hbar \partial \vec{k}} + \frac{e}{\hbar} E \times b_n$$

Electrons have an anomalous velocity perpendicular to the electric field related to their Berry's phase curvature

b) Side jump

The electron velocity is deflected in opposite directions by the opposite electric fields experienced upon approaching and leaving an impurity. The time-integrated velocity deflection is the side jump.

c) Skew scattering

Asymmetric scattering due to the effective spin-orbit coupling of the electron or the impurity.

Figure 2.5: The three essential mechansims responsible for AHE shown in cartoons illustrating the delfection of electrons to the perpendicular direction to the applied electric field E, depending on the direction of their spins. (Taken from (71)).

and so does the AHE. The AHE arising in magnetic materials is due to the time reversal symmetry breaking due to the presence of the magnetic order. It is also worth noting the essential role of SOC as it is responsible for the multiband effect, band crossings(i.e. magnetic monopoles) and gives the band their non trivial topological feature leading to non zero Berry curvature contributions(72). Besides the intrinsic contribution, two extrinsic contributions are considered. They are separated according to their dependence on the transport lifetime τ or equivalently on the longitudinal resistivity ρ_{xx}:

1. **Skew scattering**: This type of scattering has been proposed by Smit(73; 74) as the main source for AHE. The origin of the formalism is traced back to Mott. Indeed it formulates that in the presence of SOC, scattering due impurities could deflect electrons in transverse directions. Usually, the transition probability between two Bloch states is symmetric or equivalent in the Fermi's golden rule approximation. In higher order terms of the perturbation field, the symmetry between the two reciprocal transitions is broken due to the presence of the magnetization. Pictorially, this gives rise to a finite scattering probability for the electron to scatter to a new state with an additional momentum perpendicular to the incident momentum direction and the magnetization. Both then longitudinal and Hall conductivities scale with the lifetime τ.

2. **Side jump scattering**: This mechanism has been identified first by Smit(74) and later on reinforced by Berger (1964)(75) where he considered a Gaussian Bloch wavepacket scattering off a spherical impurity in the presence of SOC. It is fundamentally different from the skew scattering as it doesn't involve transitions between two Bloch states. This scattering generates a transverse contribution independent of the lifetime τ and falls in the same category as the intrinsic contribution.

Spin Hall effect

Similar to the previous case of AHE, applying a longitudinal electric current in a conducting material endowed with SOC, the SHE creates an imbalance of electron populations in the transverse direction according to the direction of their spin, making spin up and spin down electons deflect in opposite directions. This mechanism creates a pure spin current resulting in a spin accumulation at the edge of the material with opposite spin polarizations. The spin polarization is perpendicular to both incident and deflected direction[11]. Illustration of the process is depicted in Fig. 2.6. For a certain charge current $\mathbf{j}_c$, the transverse spin current can be expressed as follows:

$$\mathbf{j}_s = \theta_{SH}\mathbf{j}_c \times \boldsymbol{\sigma} \tag{2.25}$$

θ_{SH} is called the spin Hall angle and quantifies the efficiency of the conversion. Similar to AHE, the SHE has an intrinsic contribution and both extrinsic contributions(77; 78).

1. **Intrinsic contribution**(79; 60; 80; 81): stems from the topology of band structure where SOC is again an essential ingredient responsible for creating anticrossings and magnetic monopoles in the reciprocal space. These hot spots possess a non zero spin Berry curvature which acts as a fictitious magnetic field in k-space and therefore due to the SOC, acts as an effective "Lorentz" force deflecting electrons in opposite directions according to their spin polarization direction.

2. **Extrinsic contributions**(59): The same concepts derived for the AHE apply to SHE. Indeed, the skew scattering contributes to the Spin Hall but in this case the magnetization is replaced by the spin polarization of the electron, therefore deflecting opposite spins in opposite directions. The side jump is a scattering process between an incoming Gaussian Bloch wavepacket and a spherical impurity. If the wavepacket contains a spin-orbit coupled term scattering a scalar impurity potential, we refer to this scattering as the intrinsic side jump. If on the other hand, the wavepacket scatters off a spin-orbit coupled impurity, it is called extrinsic side jump. In both cases, SOC is the responsible agent for deflecting electrons in the transverse direction according to their spin polarization.

2.3.2 Spin relaxation processes

Bloch-Torrey equations

A non equilibrium spin polarization in a solid is brought back to equilibrium through certain mechanisms refered to as spin relaxation and dephasing mechanisms. Historically, two relevant

---

[11]Spin-orbit coupling induced charge current scattering into a spin current was already predicted by D'yakonov-Perel but the term SHE was coined as such by Hirsch(76) later on.
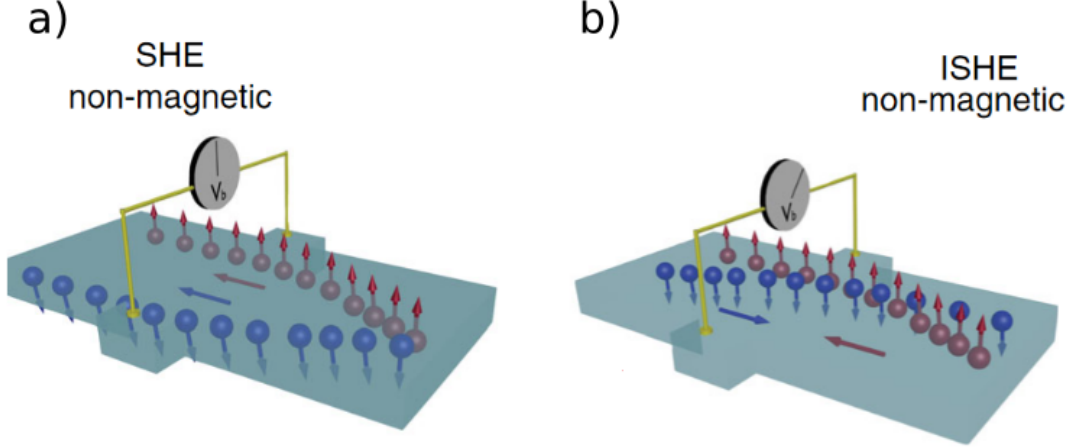
Figure 2.6: (a) Illustrartion of the Spin Hall effect: A charge current $J_{\mathbf{c}}$ gives rise to a spin current $J_{\mathbf{s}}$ in the perpendicular direction. The spin polarization of the electrons is orthogonal to both charge and spin current directions. (b) Illustration of the inverse Spin Hall effect where a spin current is converted to a charge current. The same symmetries as in the SHE are respected. (Modified from (82)).

relevant relaxation times T_1 and T_2 have been defined. They account for spin lattice relaxation time and spin decoherence time respectively. These definitions date from electron spin resonance (ESR) experiments and describe phenomenologically well the magnetization dynamics under the influence of an external magnetic field $\mathbf{B(t)}$ within the Bloch-Torrey formalism(83; 84):

$$
\begin{aligned}
\frac{dM_x(t)}{dt} &= \gamma(\mathbf{M}(t) \times \mathbf{B}(t))_x - \frac{M_x(t)}{T_2} \\
\frac{dM_y(t)}{dt} &= \gamma(\mathbf{M}(t) \times \mathbf{B}(t))_y - \frac{M_y(t)}{T_2} \\
\frac{dM_z(t)}{dt} &= \gamma(\mathbf{M}(t) \times \mathbf{B}(t))_z - \frac{M_z(t) - M_0}{T_1}
\end{aligned}
\tag{2.26}
$$

Where γ is the gyromagnetic ratio. If one considers a static magnetic field along the z direction with an time oscillating transverse component $\mathbf{B(t)} = B_0\mathbf{z} + \mathbf{b}_\perp$, the longitudinal component M_z would precess around the static magnetic field until reaching its equilibrium position $M = M_0\mathbf{z}$ within T_1 time scale. This relaxation happens via momentum scattering where the spin transfers energy to the lattice mediated by spin phonon coupling. Therefore T_1 is known as the relaxation time. The transverse magnetization components precessing in phase around the static field with the Larmor frequency $\omega_0 = \gamma B_0$ will lose their phase due spin-spin interactions within the T_2 time scale and therefore T_2 is denoted as the dephasing or decoherence time. For conduction electrons in solids, one can average these dynamics over the thermal distribution of electrons. In this case, one can have $T_1 = T_2$(85; 86). This is due to what is called motional narrowing(87). To illustrate this, let's consider a random dephasing field $\mathbf{B}$ associated with an average Larmor

frequency ω[12]. The randomization time of this field is given by τ_c called correlation time. Given the condition $\omega \ll \frac{1}{\tau_c}$, T_1 and T_2 become equal. In solids, the time constant τ_c can be approximated with momentum scattering time τ_p which is typically smaller than a ps. Even for fields up to hundreds of Tesla, the condition $\omega \ll \frac{1}{\tau_p}$ holds and could be considered in the case of metals. This means that an electron precessing at a frequency ω would experience a dephasing within the period of time τ_p. On average, the phases acquired after certain time t cancel out since it can be equivalently positive or negative but its root-mean-square is $(\omega\tau_p)^2(t/\tau_p)^{1/2}$. The time at which this expression reaches unity governs the dephasing dynamics and defines the new relaxation time experienced by all components of the magnetization :

$$T_1 = T_2 = \frac{1}{\omega^2\tau_p} \tag{2.27}$$

Consequently, for conduction electrons in semiconductors and metals, one can consider one single quantity for spin relaxation time also refered to spin lifetime. In the following sections we will focus in more detail on the most prominent spin relaxation mechanisms in metals mainly the Elliott-Yafet and D'yakonov Perel mechanisms.

Elliott-Yafet mechanism
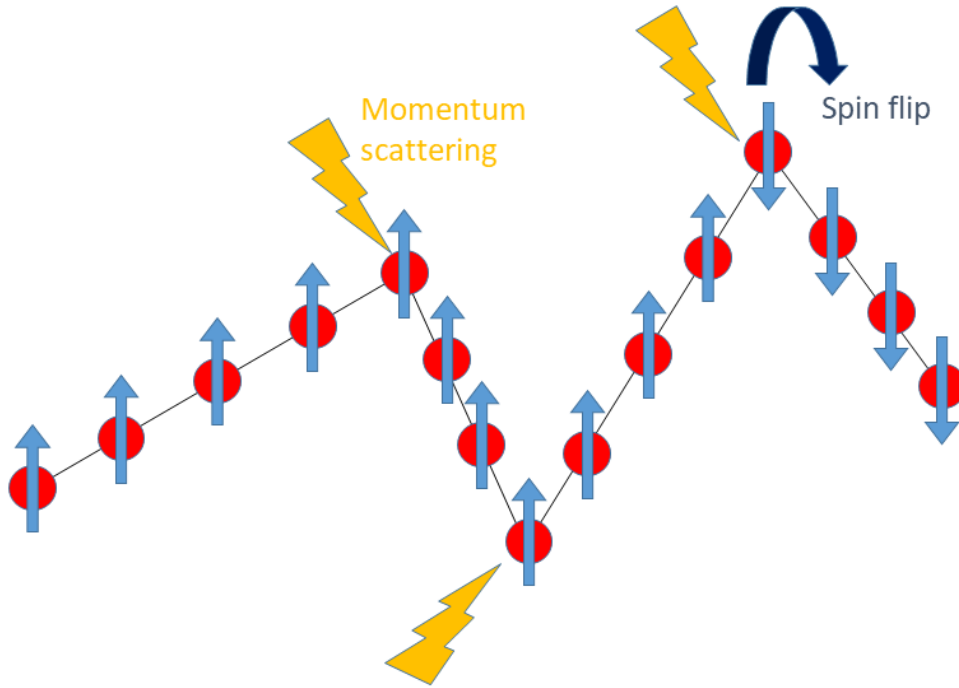
Figure 2.7: Cartoon illustrating the Elliot-Yafet spin scattering mechanism. The electron holds its spin between each momentum scattering with a small but finite probability of flipping it at a momentum scattering event.

---

[12]$\omega = \gamma|\bar{\mathbf{B}}|$.

By considering the combined action of SOC and momentum scattering off a phonon or an impurity, Elliot proved that this can lead to spin flips. First, one needs to include SOC which couples the spin of the electron Bloch wavefunction to the scalar potential of the lattice. To explain the mechanism, at least two bands need to be considered (i.e. a conduction band and an addional one nearby). Considering the typical magnitude of SOC and the energy distance between the bands, the single electron Bloch wavefunction contains a mixture of both spin up and spin down states. For electrons with the quantum numbers n and $\mathbf{k}$ in an inversion symmetrical solid, the wavefunction is written as :

$$\Psi_{n\mathbf{k}\uparrow}(\mathbf{r}) = [a_{n\mathbf{k}}(\mathbf{r})|\uparrow> + b_{n\mathbf{k}}(\mathbf{r})|\downarrow>]e^{i\mathbf{kr}}$$
$$\Psi_{n\mathbf{k}\downarrow}(\mathbf{r}) = [a^*_{n-\mathbf{k}}(\mathbf{r})|\downarrow> - b^*_{n-\mathbf{k}}(\mathbf{r})|\uparrow>]e^{i\mathbf{kr}}$$

(2.28)

Where $\frac{|b|}{|a|} \approx \frac{\lambda}{\Delta} \ll 1$. λ is the strength of the SOC and Δ is the energy distance between the two bands. Taking into account this ratio, one can still refer to $\Psi_{n\mathbf{k}\uparrow}$ and $\Psi_{n\mathbf{k}\downarrow}$ as spin "up" and spin "down" respectively. In this picture, there is a finite but small probability coming from the b^{13} term that would flip a spin "up" in band n with crystal momentum $\mathbf{k}$ to a spin "down" in the other band n' with the crystal momentum $\mathbf{k'}$. We have then the following relation :

$$|<\Psi_{n\mathbf{k}\uparrow}|V|\Psi_{n'\mathbf{k'}\downarrow}>|^2 \approx |b|^2 |<\Psi_{n\mathbf{k}\uparrow}|V|\Psi_{n'\mathbf{k'}\uparrow}>|^2$$

(2.29)

where V is the momentum scattering potential. Translating this relation into relaxation rate terms yields the Elliott relation(88) displaying the proportionality between the momentum scattering rate $1/\tau_p$ to the spin relaxation rate $1/\tau_s$:

$$1/\tau_s \approx |b|^2/\tau_p$$
$$1/\tau_s \approx (\Delta g)^2/\tau_p$$

(2.30)

Here Δg is the shift of the electron's g factor from the free electron value $g_0 = 2.0023$ and would arise from the orbital momentum of the Bloch wavefunction which is non zero when the SOC is present, leading to $\Delta g \approx |b|$. Consequently, as depicted in Fig. 2.7, after certain scattering events, there is a probablity that the electron flips its spin while conserving it in between the events. Elliott's relation shows roughly the proportionality between the two τ_s and τ_p which depends strongly on the scatterer itself and therefore certain deviations from this simple relation can happen. For example, at low temperatures, scattering by impurities dominates whereas at higher temperatures scattering by phonons takes over. Due to the relation $1/\tau_p \sim \rho(T)$ and band structure considerations, Yafet(89) established the following relation in centrosymmetric solids :

$$1/\tau_s(T) \propto \rho(T)$$

(2.31)

Yafet's relation combined with Elliott's gives a more consistance picture of spin phonon scattering.
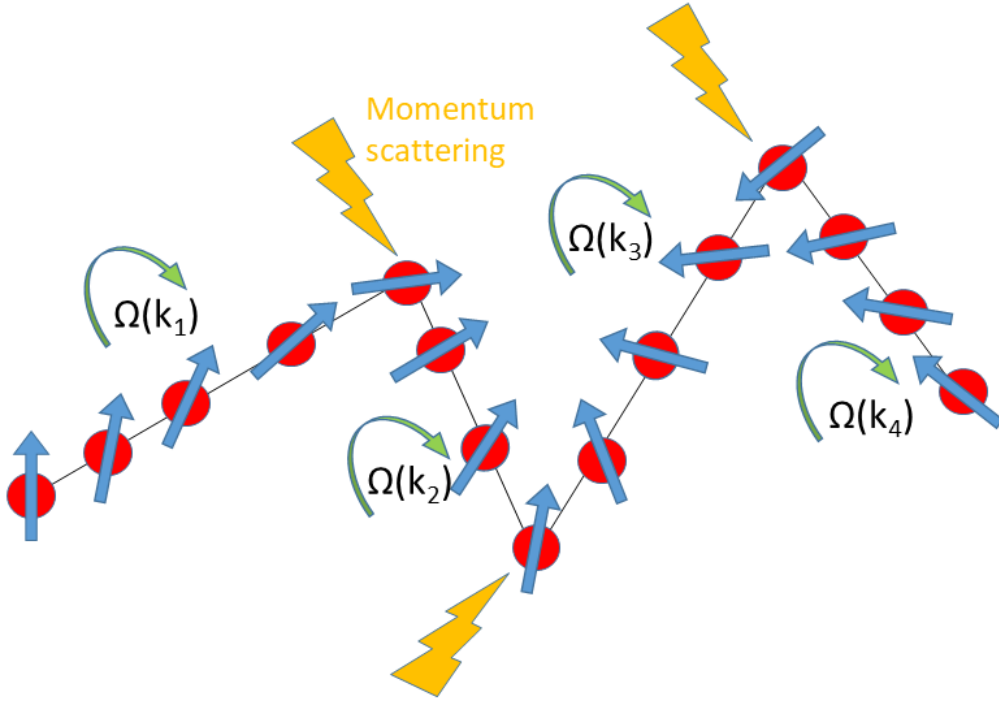
Figure 2.8: Cartoon illustration of the D'ykonov Perel spin scattering: The electron spin experiences a momentum dependant spin-orbit field leading to its precession with a $\Omega(\mathbf{k})$ frequency. At each momentum scattering event, the field is randomized and the spin's phase experiences a random walk which leads to the loss of the spin information and consequenctly its relaxation.

Dyakonov-Perel mechanism

This mechanism(90; 91) requires also SOC and additionally inversion symmetry breaking. This causes the non degeneracy of the momentum states of spin up and spin down in one band[14]. This spin splitting can be translated into a magnetic-like field also called spin-orbit field $\mathbf{B}_{so}(\mathbf{k})$, with a Hamiltonian written in the following form:

$$H(\mathbf{k}) = \frac{1}{2}\hbar\sigma.\Omega(\mathbf{k}) \tag{2.32}$$

Where $\Omega(\mathbf{k}) = \frac{eg_e}{2m_e}\mathbf{B}_{so}(\mathbf{k})$ is a frequency term equivalent to the Larmor frequency. This field is entirely derived from the band structure and is $\mathbf{k}$ dependent. Its Hamiltonian displays a Zeemann-like interaction hence the connotation of "magnetic field" though it doesn't create any spin polarization. Nevertheless, the electrons experience a precession around it with the Larmor frequency $\Omega(\mathbf{k})$. This field acts as a random fluctuating field that randomizes after each scattering event time τ_p. In the regime where $\Omega_{av}\tau_p < 1$, the dephasing is inhibited due to motional narrowing as seen in the earlier section. As illustrated in Fig. 2.8, the electron precesses around each random field within the time τ_p. Equivalently, the spin phase is in the

---

[13]From here on, let's consider $|a|$ to be in the order of unity for simplicity.

[14]Unlike Eliott-Yafet formalism, one band here is sufficient to derive the relaxation process.

random walk regime which would result in a spin relaxation time :

$$1/\tau_s^{DP} = \Omega_{av}^2 \tau_p \tag{2.33}$$

Interestingly, D'yakonov Perel and Elliott Yafet relaxation times have a very distinct dependences on the momentum scattering times. While for the former, the spin phase is randomized between the scattering events due to a k dependent precession frequency, for the latter the spin phase is conserved in between the scattering events and experiences a flip finite probability during the collision.

2.3.3 Electrical spin injection and detection
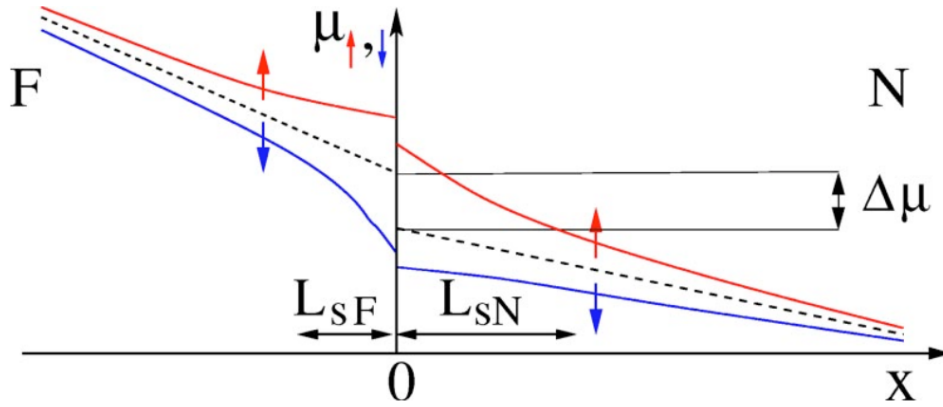
Figure 2.9: Illustration of the spin injection at a FM/NM interface. When a non equilibrium spin polarization is created at the interface, the chemical potentials for spin up and spin down near the interface are split. The difference is the spin accumulation which drives the spin current. The averaged chemical potential of the two materials would equal each other once the spin current is dissipated in both layers with their respective spin diffusion lengths. (Taken from (92).)

One important goal in the field of Spintronics is to generate a non equilibrium spin polarization and use it as a vector to vehiculate and manipulate magnetic information. To transport and process spin information in a particular thin film material, three fundamental conditions have to be met which consist of a spin generator, spin detector and a spin transport channel. Spin polarization generation can be achieved using the spin filtering effect in a ferromagnet or as stated earlier via spin galvanic effects such as SHE in materials endowed with SOC. In this case, the spin source is usually used as a contact and will be interfaced with another material of interest. One major aspect of spintronics is to complement the semiconductor technologies by interfacing spintronic components with current CMOS technologies aiming at substituting the charge with spin degree of freedom. In this case, a ferromagnetic contact is usually used to inject non equilibrium spin polarization in the semiconductor. In SOT-MRAM technologies, the use of spin-orbitornics interface a ferromagnet with a large spin to charge conversion material(93; 94; 95). In this case, via spin galvanic effects such as SHE, the SOC material is the spin source which injects a non equilibrium spin polarization in the ferromagnet

through the interface. Let's consider the spin injection from a ferromagnet to a non magnetic material(96; 97; 98; 99; 100; 101) which will be focused on later in this thesis. In the Stoner picture, the bands for both spin channels in a ferromagnet are split. The consequent magnetization is the result of this imbalance of the number of occupied carriers for both spin channels, i.e. $M \propto (n_\uparrow - n_\downarrow)$. Spin transport depends on the excitation process involved of the non equilibrium spin polarization. In steady state electric transport, the energy scale of interest is within the Fermi level. The spin dependent density of states at the Fermi level leads to spin dependent conductivities $\sigma_{\uparrow\downarrow}$and for a diffusive system can be written using Einstein's relation:

$$\sigma_{\uparrow\downarrow} = e^2 \rho_{\uparrow\downarrow}(E_F) D_{\uparrow\downarrow} \tag{2.34}$$

Where $\rho_{\uparrow\downarrow}$ is the density of states at the Fermi level and $D_{\uparrow\downarrow}$ is the diffusion constants for either spin channel. The transport is carried by the net spin polarization P defined as :

$$P = \frac{\sigma_\uparrow - \sigma_\downarrow}{\sigma_\uparrow + \sigma_\downarrow} \tag{2.35}$$

Since the spin scattering time is much longer than other scattering processes, chemical potentials may be defined as $\mu_\uparrow$ and $\mu_\downarrow$ for spin up and spin down channels respectively. If a current is flowing in the structure, given the different conductivities for both spin channels and Ohm's law, the chemical potentials split near the interface. This results in a non equilibrium spin polarization defined as a spin accumulation μ_s equal to the non equilibrium chemical potential difference between the two spin channels at the interface.[15]. As depicted in Fig. 2.9, the average chemical potential difference $\Delta\mu$ is the driving froce for the chemical potential splitting. In the steady state, this spin accumulation, therefore the spin current, diffuses in the NM and can be treated with the spin diffusion equation(100; 99; 101; 102):

$$\frac{d\mu_s}{dt} = D\nabla^2 \mu_s - \frac{\mu_s}{\tau_s} = 0 \tag{2.37}$$

Where D is the diffusion constant and τ_s is the spin relaxation time. It follows that the spin accumulation decays exponentially to its zero equilibrium value with a characteristic length constant called the spin diffusion length l_d in the non magnetic material defined as $l_d = \sqrt{D\tau_s}$. Ideally, generating a net non equilibrium spin polarization of 100% in the NM is the ultimate efficient spin injection. For example, attempting to use a half metal where only states of one spin channel lie at the Fermi level could within this simple framework lead to a maximum spin polarization. Yet, it is hindered by interface impedence mismatch. In a normal metallic ferromagnet as well, the efficiency of the spin polarization transmission is reduced. Many factors are responsible for such a reduction. We will further briefly introduce the impedence mismatch, the interface reflectivity and the spin-memory loss.

---

[15]The spin current is defined as follows :

$$j_s = j_\uparrow - j_\downarrow = \sigma_s \nabla\mu + \sigma \nabla\mu_s \tag{2.36}$$

where $\sigma_s = \sigma_\uparrow - \sigma_\downarrow$, $\mu = (\mu_\uparrow - \mu_\downarrow)/2$ and $\sigma = \sigma_\uparrow + \sigma_\downarrow$. In the case of the NM, $\sigma_s = 0$ so the spin current is entirely defined by the non equilibrium spin accumulation.

Impedence mismatch

By considering the previous FM/NM system and define the interface region as "C" for contact[16]. Here, we assume that the there is no spin scattering mechanism at the interface in other words spin current is not lost[17]. Following the the spin current continuity equations in all three regions as illustrated in more details in these relevant studies(99; 103; 104; 105), we obtain :

$$P_i = \frac{R_F P_F + R_I P_C}{R_F + R_I + R_N} \tag{2.38}$$

Where R_F, R_C and R_N[18] are the effective resistances of the ferromagnet, interface and NM respectively. P_F and P_I are the spin polarizations of the FM and interface respectively. P_i measures the average spin polarization in all regions and therefore the efficiency of the spin injection. Depending on the relative strengths of the resistances, we can point to two distinct regimes:

1. Tunneling contact: In this regime, we have the condition:$R_C \gg R_F, R_N$ which results in $P_i = P_C$. This is a very interesting case since the P_C can dependent on symmetry consideration of tunneling states from the FM to the NM. This is the case in tunnel junctions for example where large spin polarizations can be selected as mentioned in Section 2.2 for Fe/MgO/Fe.

2. Transparent interface: This regime is characterized by the condition $R_C \ll R_F, R_N$. In this case, the P_i reduces to :

$$P_i = \frac{R_F P_F}{R_F + R_N} \tag{2.39}$$

   From here on, the resultant polarization would depend on the relative strength between R_F and R_N. If $R_F \ll R_N$, then $P_i = \frac{R_F}{R_N} P_F \ll P_F$. As a result of this large impedence mismatch, the spin injection efficiency is poor and this is one of the fundamental obstacle of spin injection from a ferromagnet into semiconductors. In the case where $R_F \sim R_N$, which is usually the case for normal metals, then the spin polarization is on the order of the polarization of the FM, $P_i \sim P_F$. This case corresponds to the 3d ferromagnet interfaced with a 5d heavy metal studied further in this thesis.

When we consider a system with a good impedence matching, the interface between the FM and the NM can still electronically hinder the transmission of the spin current depending on the band matching between both materials resulting in a reduced transmission. This is called interface reflectivity and will be discussed in a Landauer approach in the following section.

Interface reflectivity and Landauer Büttiker transport formalism

The Landauer Büttiker (LB)(106; 107) approach determines the current transported through a non interacting quantum system also called scattering region[19]. It is therefore used in the single electron approximation and band theory taking into account only elastic scattering. The

---

[16]The contact could be simply the interface or a junction between the two regions such as a tunneling junction

[17]This is not the case when we consider the spin-memory loss which would be explained in a later section

[18]$R_F = \frac{l_d^F}{\sigma_F}$, $R_N = \frac{l_d^N}{\sigma_N}$ and $R_C = \frac{\Sigma}{4\Sigma_\uparrow \Sigma_\downarrow}$ where Σ is the conductivity of the contact.

[19]It can also be extended to the mesoscopic scale.

Figure 2.10: Schematic illustration of the Landauer Büttiker approach. The scattering region "S" is connected through leads to reservoirs, here L for left and R for right, with well defined chemical potentials, temperatures.

scattering region could be atomic layers, a tunnel barrier or a simple interface. A general illustration of the LB approach is depicted in Fig. 2.10. Two reservoirs are connected to the scattering region "S" through two leads which we will refer to as "L" and "R" for left and right respectively. The two reservoir are in equilibrium and incoherent in a way that any electron enters the reservoir, it thermalizes with the electronic system losing its phase information. However, the leads have well defined modes related to the Bloch wavefunctions of the electrons. One more approximation is that the lead/reservoir interface is reflectionless. As a result, right propagating in the $+k$ direction[20] states in the scattering region are occupied by electrons coming from the lead "L" and vice versa. Applying a voltage V between the two leads yields a shift in their chemical potentials, i.e. $eV = \mu_L - \mu_R$. The LB formula gives the current:

$$I(V) = \frac{e}{h} \int_{-\infty}^{\infty} T(E, V)[f_L(E + eV) - f_R(E)]dE \qquad (2.40)$$

Where $f(E)$ is the Fermi Dirac distribution and $T(E, V) = Tr(tt^\dagger) = \sum_{\alpha\beta} |t_{\alpha\beta}|^2$. t is called the transmission matrix and its element $t_{\alpha\beta}$ describes the transmission probability between a Bloch state α in the left lead to be transmitted to a Bloch state β in the right lead. The total probability of the transmission is summed over all the states in the bias voltage window defined by the voltage V around the Fermi level. This constitutes the main result of this approach linking the resistance of an object to the probability of the transmission of electronic states through it. In this thesis, the FM/NM interface is considered as the scattering region and spin resolved currents can be calculated which equivalently determines the spin interfacial transparency.

---
[20]This direction is defined from left to right.

Spin-memory loss

As been stated earlier, spin is not a conserved quantity and describing its transport through a material require a spin flip process giving a certain spin diffusion length which is nominally a bulk property. In a picture where non conserving spin scattering occurs at the interface, the interface can be defined its own resistance and spin flip parameter. This spin flipping parameter is referred to as Spin-memory loss (SML) and describes the non conservation of a spin through the interface. It is generally quantified by the parameter δ. To make sense of δ, let's assume the interface to be a bulk material with a certain spin diffusion length l^I and thickness t_I, then by shrinking the thickness down to zero, δ is then written:

$$\delta = \lim_{t^I \to 0} \frac{t^I}{l_I} \tag{2.41}$$

SML parameter δ measures therefore the probability of an electron spin to flip its direction once it traverses the interface. The probability reads :

$$P = 1 - e^{-\delta} \tag{2.42}$$

SML has been originally characterized in CPP magnetorisistance measurements and little is known about its origin. It will be considered in Chapter4.

2.3.4   Spin precession and Landau Lifshitz Gilbert equation
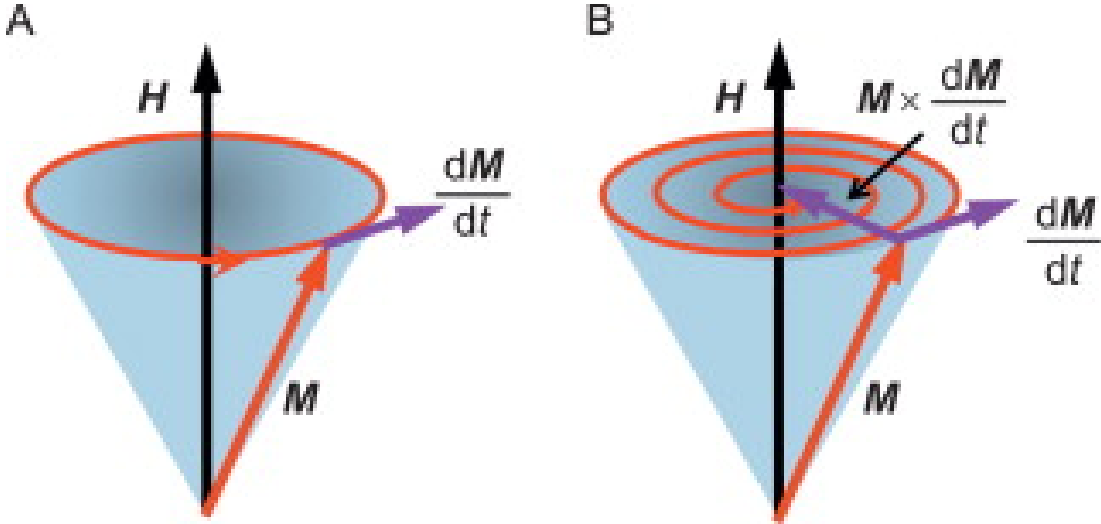
Figure 2.11: Magnetization dynamics in a ferromagnet. (A) Case of magnetization dynamics without damping: precessional motion of the magnetization vector around the effective field H with a constant cone angle. (B) Case of magnetization dynamics with damping: the magnetization spiral around the effective field **H** until its complete relaxation bringing it to its equilibrium position parallel to **H**. (Taken from (108)).

Similar to the Block-Torrey equations, the magnetization dynamics driven by an external magnetic field $\mathbf{H}_{eff}$ can be evaluated through the phenomenological Landau Lifshitz Gilbert

(LLG)(109; 110) equation:

$$\frac{d\mathbf{m}}{dt} = -\gamma \mathbf{m} \times \mathbf{H}_{eff} + \alpha \mathbf{m} \times \frac{d\mathbf{m}}{dt} \tag{2.43}$$

Where $|\mathbf{m(t)}| = |\mathbf{M(t)}|/M_s$, $\mathbf{M(t)}$ being the instantaneous microscopic magnetization and M_s is the saturation magnetization. The first term on the right hand side describes the precessional motion of the magnetization around H_{eff}, which is the driving effective magnetic field of the dynamics through energy conserving interactions. H_{eff} can be extracted from the free energy density functional of the system or the Hamiltonian $H(M)$ via $H_{eff} = -\frac{1}{\mu_0 M_s} \frac{\delta H}{\delta \mathbf{m}}$. This gives different contributions where the most prominent ones are the exchange field, Zeemann field, magnetoanisotropic field, demagnetizing field and any other external sources (e.g. microwave field, laser field...). This term is energy conserving and induces a precessional motion of the magnetization with a constant cone angle around the driving field with a frequency $\gamma |H_{eff}|$. On the other hand, the second term which was phenomenologically added by Gilbert is the damping term and describes the dissipation of the energy relaxing the magnetization to an equilibrium position along $\mathbf{H}_{eff}$. The constant quantifying this dissipation or damping is α and is called the Gilbert damping constant. This damping term originates from the coupling of the magnetization to the phonon bath through the SOC where the dissipated energy is transfered as angular momentum to the lattice. The LLG equation can be extended by adding a term taking into account the interaction between the local magnetization and the spin of a moving electron (such as a spin polarized current). This term(48; 49) is called the Slonczewski spin transfer torque and reads:

$$\tau_{STT}(\mathbf{r}) \propto (\mathbf{j}.\nabla)\mathbf{m} + \beta \mathbf{m} \times (\mathbf{j}.\nabla)\mathbf{m} \tag{2.44}$$

Where the first term is refered to as the field like term and the second as the damping like term. This nomenclature is evidenced by the symmetry of the torques. The field like torque can contribute to the driving precessing force in contrast to the other that can be added to the Gilbert damping term. Interestingly, depending on the polarization direction of the current, the damping like torque can in fact cancel the damping like torque and outcome it which enables Spin torque nano oscillators as well as magnetization switching in nanodevices. As a spin current induces changes in the magnetization dynamics through the action of a torque, a precessing magnetization can transfer angular momentum to a free electron in a non magnetic layer N through an interface in a FM/NM bilayer. This creates a spin accumulation at the interface. This is called spin pumping and will be discussed in detail in the next section.

2.3.5 Spin pumping and Ferromagnetic resonance

Ferromagnetic resonance (FMR)

Before discussing the spin pumping mechanism, we will discuss the concept of ferromagnetic resonance(FMR) enabling a coherent precession of the magnetization. To illustrate the principle of the FMR, a generic example of magnetic resonance will be presented. Let's consider an ion with a magnetic moment $\mathbf{m}$ and an electronic angular momentum $\hbar \mathbf{S}$. These two are related via $\mathbf{m} = \gamma \hbar \mathbf{S}$. When it is subject to external magnetic field $\mathbf{H}$ along the z direction, the levels
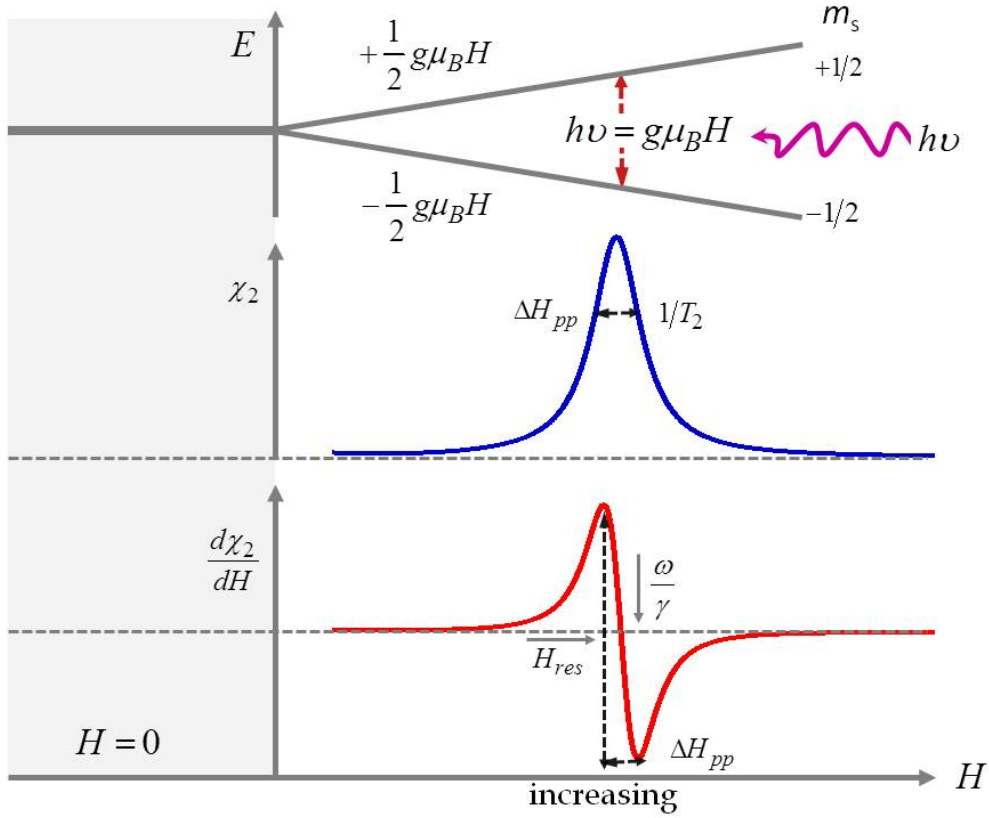
Figure 2.12: Illustration of the magnetic resonance condition for a free electron. Upper panel: The Zeemann field is responsible for a splitting of the energy band with a spacing proportional to the external magnetic field. An electromagnetic radiation with a frequency ν excites the system resonantly between the states $m_s = -1/2$ and $m_s = 1/2$. Middel and bottom panels: Magnetic susceptibility and absorption profile with respect to the external field at resonance. (Taken from (111))

become non degenrate according to the Zeemann splitting. The Zeemann Hamiltonian reads:

$$H_z = -\mathbf{m}.\mathbf{H} = -\gamma\hbar H S_z \tag{2.45}$$

Where the Eigenvalues ϵ_i are equally spaced:

$$\epsilon_i = -\gamma\hbar H m_s$$
$$m_s = -S, -(S-1), ..., S \tag{2.46}$$

m_s is the magnetic quantum number. This gives an energy spacing of $\Delta\epsilon = \gamma\hbar B_0$. Therefore, magnetic dipole transitions can be excited with a radiation of angular frequency ω_0 giving the resonance condition (10):

$$\omega_0 = \gamma H \tag{2.47}$$

This is a general condition of magnetic resonance. To achieve this, usually an AC magnetic field is applied in a direction in the plane perpendicular to the z direction. This adds non zero diagonal terms to the Zeemann Hamiltonian and therefore mixes states with the dipole

selection rule $\Delta m_s = \pm 1$ at resonance. This condition is general to magnetic resonance and can be called differently for different systems. For system of ions with unpaired electron spin, it is called electron parametric resonance(EPR) or electron spin resonance (ESR)(112). For nuclear spin, it is called nuclear magnetic resonance (NMR) and for a system with exchange coupled magnetic moments such as in a ferromagnet, it is referred to as ferromagnetic resonance.

As a next step, let's consider a ferromagnetic material at the FMR condition and derive its magnetic susceptibility. We can consider again the LLG equation. As stated earlier, besides the external DC field H_0 we drive the resonance with an ac magnetic field. The dynamics of the magnetization $\mathbf{M(t)}$ are governed by the Larmor frequency $\gamma |H_{eff}|$ which falls in the GHz regime. Therefore, applying an external radio frequency (rf) field h_{rf} provided the condition $|h_{rf}| \ll |H_0|$, results in the following expressions:

$$
\begin{aligned}
H_{ext} &= H_0 + h_{rf} \\
M(t) &\approx M_s + m(t)
\end{aligned}
\tag{2.48}
$$

Where $\mathbf{M}_s$ is the static magnetization at equilibrium and $\mathbf{m}(t)$ is the dynamic component driven by the rf field with $|\mathbf{m}| \ll M_s$. So the magnetization component along $\mathbf{z}$ can be assumed to be equal to $\mathbf{Mz}$ and $\mathbf{m}$ is in the x-y plane. Assuming $m(t) \propto e^{i\omega t}$ and following the linearized Landau Lifshitz approach[21] derived by Heinrich et.al.(113; 114), one can derive from the dynamics of transverse magnetization averaged per unit area in the film the two following equations:

$$
\begin{aligned}
-i\frac{\omega}{\gamma}\mathcal{M}_x + [\mathcal{B} - \frac{\alpha}{\gamma M_s}\frac{i\omega}{\gamma}\mathcal{M}_y] &= 0 \\
[\mathcal{H} - i\frac{\omega}{\gamma}\frac{\alpha}{\gamma M_s}]\mathcal{M}_x + i\frac{\omega}{\gamma}\mathcal{M}_y &= M_s dh_0
\end{aligned}
\tag{2.49}
$$

Where all the added parameters are expressed as follows:

$$
\begin{aligned}
\mathcal{B} &= H_0 + 4\pi M_{eff} + \frac{K_1^{eff}}{2M_s}(3 + cos(4\theta)) \\
\mathcal{H} &= H_0 + \frac{2K_1^{eff}}{M_s}cos(4\theta) \\
4\pi M_{eff} &= 4\pi D_z M_s - \frac{2K_u^{eff}}{M_s}
\end{aligned}
\tag{2.50}
$$

Where θ is the in plane angle between the external magnetic field and the magnetization, D_z is the demagnetizing factor, $2K_1^{eff}$ and $2K_u^{eff}$ are effective constants for surface in plane four fold and uniaxial anisotropies respectively. The rf response characterized by the susceptibility χ is :

$$
\chi = \frac{\mathcal{M}_y}{h_0} \frac{M_s d[\mathcal{B} - i\frac{\omega}{\gamma}(\frac{\alpha}{\gamma M_s})]}{[\mathcal{B} - i\frac{\omega}{\gamma}(\frac{\alpha}{\gamma M_s})][\mathcal{H} - i\frac{\omega}{\gamma}(\frac{\alpha}{\gamma M_s})] - (\frac{\omega}{\gamma})^2}
\tag{2.51}
$$

---

[21]For simplicity, the Gilbert damping term is omitted.

After seperating the real and imaginary part of $\chi = \chi\prime + \chi\prime\prime$, we obtain:

$$\chi\prime \propto \frac{H_0 - H_{FMR}}{\Delta H^2 + (H_0 - H_{FMR})^2}$$
$$\chi\prime\prime \propto \frac{\Delta H}{\Delta H^2 + (H_0 - H_{FMR})^2}$$

(2.52)

With $\Delta H = \frac{\alpha\omega}{\gamma}$ is the effective damping of the magnetic material and scales linearly with the frequency of the rf field. H_{FMR} is the resonance field. The absorption signal depends is proportional to $\chi\prime\prime$ and therefore at the resonance condition $H_0 = H_{FMR}$, $\chi\prime\prime$ is maximized and has a Lorenzian shape with a half width at half maximum (HWHM) equals to ΔH. Setting the Gilbert damping α to zero, H_{FMR} is the solution of the following equation :

$$\mathcal{B}\mathcal{H} = (\frac{\omega}{\gamma})^2$$

(2.53)

Let's consider the case where the external field is parallel to the equilibrium magnetization(i.e. $\theta = 0$), we find then the Kittel formula(115) :

$$(\frac{\omega}{\gamma})^2 = [H_{FMR} + 4\pi M_{eff} + \frac{2K_1^{eff}}{M_s}][H_{FMR} + \frac{K_1^{eff}}{2M_s}]$$

(2.54)

The resonance field therefore shifts with the anisotropies of the sample and the linewidth depends on the damping through:

$$\Delta H = \frac{\alpha\omega}{\gamma}$$

(2.55)

These are the two relevant parameters extracted from an FMR experiment. We will discuss later in secrtion3.2 in more details the experimental implementation of the FMR and the extraction of the relevant quantities.

FMR driven Spin pumping

We have seen that a spin current can transfer angular momentum to the local magnetization via a torque inducing its precession. Reciprocally, it has been argued that a precessing magnetization loses angular momentum by emitting a spin current. Historically, such a relation has been suspected. For example, Janossy and Monod and Silsbee et.al. claimed a coupling between a dynamical magnetization and spin accumulation in adjacent normal metals(117). It was only until the work of Tserkovnyak that the formalism of spin pumping(118; 119; 120) was developed, using the same matrix scattering formalism developped earlier by Brouwer for parametric charge pumping in a quantum dot(121). Hence the name. A precessing magnetization in a ferromagnet can be assumed to be in the adiabatic regime considering the momentum scattering rates in metals. In order for the spin pumping to take place, a channel for the vehiculation of the spin current has to open and this is done by interfacing the ferromagnet with a normal metal. Spin pumping occurs strictly at the interface and builds a spin accumulation in the normal metal that as we saw in an earlier section decay through a diffusion process in the normal metal. The latter can then act as a reservoir or a spin sink. The interaction between conduction electrons at the interface with the magnetization results in a transfer of angular momentum directed from the ferromagnet to the normal metal in a form of a pure spin current
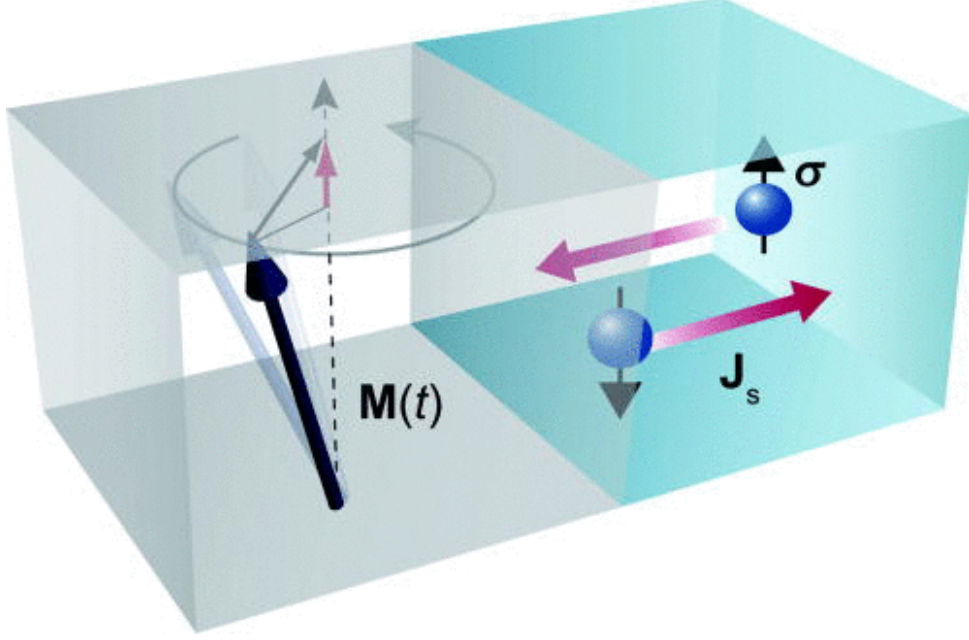
Figure 2.13: Illustration of the FMR Spin pumping: The precessing magnetization of a ferromagnet, adjascent to a normal metal layer, pumps a pure spin current $\mathbf{J}_s$ in the normal metal. (Taken from (116)).

expressed as:

$$I_s^{pump} = \frac{\hbar}{4\pi}(A_r\mathbf{m} \times \frac{d\mathbf{m}}{dt} - A_i\frac{d\mathbf{m}}{dt}) \qquad (2.56)$$

Where A_r and A_i are related to the scattering matrix elements which characterize the interface conductance. We have :

$$A_r = \frac{1}{2}\sum_{mn}|r_{mn}^{\uparrow} - r_{mn}^{\downarrow}|^2 + |t_{mn}'^{\uparrow} - t_{mn}'^{\downarrow}|^2$$
$$A_i = Im[\sum_{mn} r_{mn}^{\uparrow}(r_{mn}^{\downarrow})^* + t_{mn}'^{\uparrow}(t_{mn}'^{\downarrow})^*] \qquad (2.57)$$

Where $r_{mn}^{\uparrow}(r_{mn}^{\downarrow})$ is the interface reflection coefficient in the normal metal for spin up (spin down) from an transverse mode m to a mode n at the Fermi level. $t_{mn}'^{\uparrow}(t_{mn}'^{\downarrow})$ is the transmission coefficient into the normal metal (from another lead or layer interfaced with the ferromagnet) for spin up (spin down) from a transverse mode m to a mode n at the Fermi level. To quantify the efficiency of the transmission of the spin current through the interface, another parameter is defined as the interface DC conductance matrix and called the spin mixing conductance (SMC) $g^{\sigma\sigma'}$. It is related to the reflection matrix through :

$$g^{\sigma\sigma'} = \sum_{mn}(\delta_{mn} - r_{mn}^{\sigma}(r'^{\sigma'}_{mn})^*) \qquad (2.58)$$

This gives the relation $A_r + iA_i = g^{\uparrow\downarrow} - t^{\uparrow\downarrow}$ with $t^{\uparrow\downarrow} = t_{mn}'^{\uparrow}(t_{mn}'^{\downarrow})^*$. For ferromagnets thicker than the coherence length[22] $\lambda_{fc} = \pi/(k_{\uparrow} - k_{\downarrow})$ with $k_{\uparrow}(k_{\downarrow})$ being the spin up (spin down) Fermi

_____

[22]For transition metals, this characteristic length is equal to few monolayers.

wavevector. In this case, the transmitted states interfere coherently at the interface leading to $t^{\uparrow\downarrow} = 0$. It is also demonstrated that A_i can be neglected for ballistic and diffusive contacts(122) which leaves only the relation $A_r \approx g^{\uparrow\downarrow}$ leading to :

$$I_s^{pump} = \frac{\hbar}{4\pi} g^{\uparrow\downarrow} \mathbf{m} \times \frac{d\mathbf{m}}{dt} \qquad (2.59)$$

This gives a clear important feature of the spin pumping which is the fact that the spin current depends entirely on the interface conductance properties. As can be seen from equation (1.59), the spin current has the same symmetry as the Gilbert damping and this constitutes the main consequence of the spin pumping mechanism : The loss of the angular momentum due to the precession is transported away as a current which results in an enhanced damping of the ferromagnetic material. Therefore, this spin pumping induced damping augments effectively the intrinsic damping α_0 of the ferromagnet. We can define the total effective damping as the intrinsic damping with the additional damping due to the spin pumping process :

$$\alpha_{F/N} = \alpha_0 + \frac{g\mu_B g^{\uparrow\downarrow}}{4\pi M_s t_F} \qquad (2.60)$$

Where g is the Lande factor and t_F is the thickness of the ferromagnet. This means that one can access the interface properties through frequency dependent linewidths measurements of the FMR spectrum. It is worth to mention that similarly to a charge battery, owing to spin pumping, a ferromagnet/normal metal interface can be viewed conceptually as a spin battery(123) when the ferromagnet is driven at resonance. A spin voltage (i.e. spin accumulation) is built dragging a maximum spin current that is expressed by the equation (1.59). Nonetheless, this case has limitations. Due to spin-orbit scattering the normal metal is so far assumed to be a perfect spin sink and dissipates the total spin current injected. However, when the spin flip rate is slower than the spin injection rate, the spin accumulation at the interface induces a backflow of spin current into the ferromagnet. In general, only the component of μ_s perpendicular to $\mathbf{m}$ is responsible for this since the parallel component is cancelled by an opposite flow from the ferromagnet[23]. The backflow spin current is then :

$$I_s^{Backflow} = -\frac{g^{\uparrow\downarrow}}{4\pi} \mathbf{m} \times \mu_s \times \mathbf{m} \qquad (2.61)$$

To feel the effect of this current on the spin mixing conductance (i.e. additional Gilbert damping), we define $\epsilon = \frac{\tau_p}{\tau_{sf}}$ the ratio between the momentum scattering rate and the spin flip rate. The diffusive model for the spin accumulation in the normal metal holds as long as $\epsilon \ll 1$. The modified Gilbert damping then reads:

$$\alpha_{eff} = \alpha_0 + \frac{\hbar\gamma^2 g^{\uparrow\downarrow}}{4\pi V[1 + (\sqrt{\epsilon}tanh(L/\lambda_{sd}))^{-1}]} \qquad (2.62)$$

The damping is then increased for $L \gg \lambda_{sd}$ and a large ϵ. Light metals with atomic numbers $Z \leq 50$ and heavy elements with only s electrons in the conducting channel would have $\epsilon \leq 10^{-2}$. These elements would be poor spin sinks. On the contrary, elements like Pt, Pd or Ta would be

---

[23]provided that the frequency of the precession and the spin flip rate in the ferromagnet are slower than the injection (into the ferromagnet).

much better spin sinks owing to the relatively large $\epsilon \leq 10^{-1}$. This is due to the high atomic number and/or p and d character of the conduction electrons. This trend in the effective enhancement of the Gilbert damping has been reported by Mizukami et.al.(124).

2.4 Ultrafast optical excitation of magnetic heterostructures

2.4.1 Ultrafast demagnetization
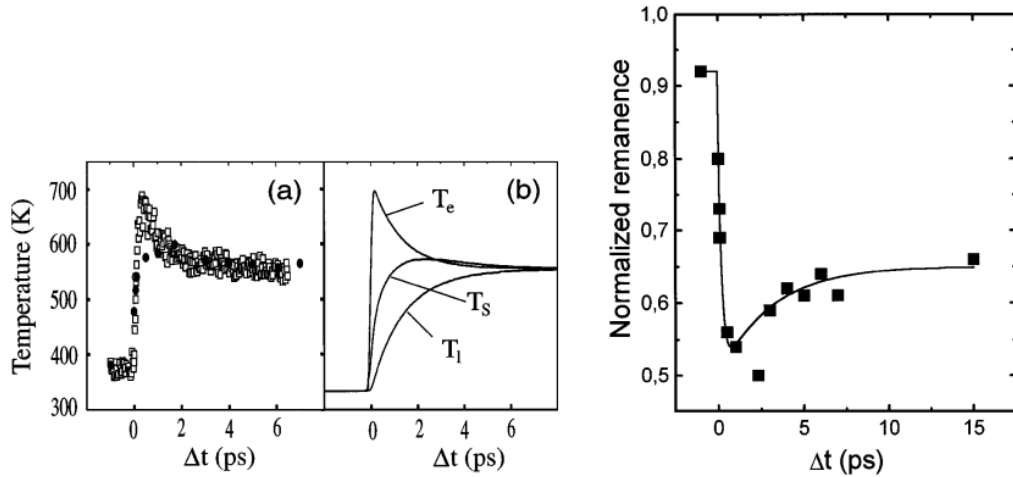
Figure 2.14: Ultrafast demagnetization in Ni. On the left hand side: (a) The time resolved experimentally deduced spin(full black circles) and electron (white squares) temperatures. (b) time evolution electron,lattice and spin temperatures during ultrafast demagnetization, according to the three temperature model. On the right hand side: time resolved remanant Magneto-Optical Kerr Effect (MOKE) signal of a 20nm Ni film with a laser fluence of $7mJ/cm^2$. The signal is normalized to the one without the pump beam.(modified from (1)).

Ultrafast optical excitation of magnetic materials is a field of intensive research and it offers a variety of fundamental science as well as technological opportunities. It allows to access the world of condensed matter down to the femtosecond time scale. More specifically the birth of the field of femtomagnetism started with a single experiment in 1996(1) that showed a surprising result. Bigot and Beaurepaire carried out this experiment by shining a 60 femtosecond laser pulse on a Ni thin film and measured subsequently the magneto-optical response using a pump and probe technique. Surprisingly, the magnetic order gets quenched down to 50% of its initial value in the sub-picosecond time scale followed then by a slow recovery that span over few tens of picoseconds. This ultafast demagnetization is generic and happens in multiple magnetic systems(125; 126; 127; 128; 129; 130). Moreover, Beaurepaire et.al. performed reflectivity measurements which probe the electronic temperature of the system. This ultrafast quenching has been further confirmed and observed with other techniques such as second harmonic generation(125). Moreover, time resolved and spin resolved two photon emission measurements registered a sub picosecond magnetic quenching on ultrathin Ni and Fe films ($\sim$1nm) with a

demagnetization time constant around 300-500 fs for both(126; 131). Later on time resolved x-ray circular dicroism (XMCD) has been carried out for a Ni film showing an ultrafast decrease of the spin and orbital moments with a similar time constant $\sim 130 \pm 40fs$(132). These latter experiments confirmed the actual loss of spin moment. This surprising result triggered intensive debates on the fundamental principles of ultrafast magnetism. Several mechanisms have been reported and will be reviewed shortly in this section. Before diving into the microscopic con-
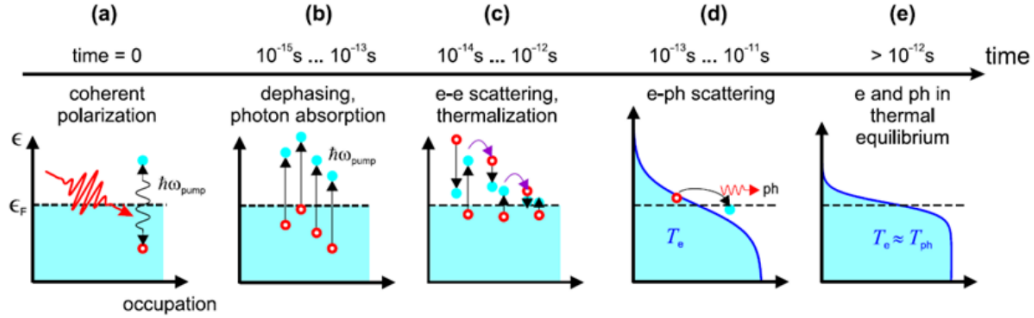
Figure 2.15: **Ultrafast processes after laser pulse excitation in a metal**(a) The photon energy is first transferred to the system creating a coherent polarization leading to a non thermal electron hole. The electrons redistribute their energies due to electron electron scatterings until thermalization at around 100fs. Then the electronic system transfer energy to the phononic system through electron phonon coupling processes at later times. After roughly 1ps, the electronic and phononic system are in equilibrium and share the same temperature $T_e \sim T_p$. (Taken from (133)).

didates for ultrafast demagnetization, we briefly review the ultrafast processes resulting from an optical laser pulse in metals. For a metal at equilibrium, the electronic system is in thermal equilibrium according the distribution of Fermi Dirac having a proper defined temperature T_e. At this equilibrium state, the lattice is also defined with its own temperature T_l and in equilibrium with electronic system ($T_e = T_l$). As illustrated in Fig. 2.15, when the metal absorbs the photon enegy deposited by the laser, the electronic system is excited to higher states lying in higher energy levels defined by the laser energy. These states lie above the Fermi level and the electronic system is driven out of equilibrium and its distribution deviates from an equilibrium Fermi Dirac one. These new electron states are called hot electrons. Due to electron electron scattering processes occurring in the first hundreds of femtosecond, the electronic system thermalizes and can be assigned its electronic temperature. In a longer time scale, in the picosecond regime, the difference between the lattice temperature and the electron temperature acts as a driving force to restore the equilibrium of the two systems with each other through electron-phonon scattering(134). In noble metals, the hot carriers occupying high energy sp states experience a ballistic transport with velocities $\sim 10^6 m/s$ just after their excitation and diffusive transport with velocities $\sim 10^4 m/s$ after the electron electron scattering takes place. For magnetic systems, the situation becomes more complicated since the spin degree of freedom plays a major role. In ferromagnets, the density of states are spin split with the exchange energy ($\Delta_{ex} \sim 1eV$). For 3d transition metal ferromagnets, the excited states are different for both spin species. Indeed the lifetime and velocities of the excited states are spin dependent. The minority spins are excited to an unfilled d band with high scattering rates due to the

large density of states which results in a quicker thermalization of the electron system with the lattice and lower mobility which reduces the ballistic transport(135; 136). On the other hand, the mobility of the electrons in the sp band in a magnetic material is similar to that in noble metals. Spin dependent hot electron transport has been demonstrated in magnetic thin film heterostructures(137; 138; 139; 140). In the same perspective, Battiato et.al(4; 141). claim that this transport of spins accompanies the demagnetization and partly explains it. This is referred to as superdiffusive spin transport model and will be discussed later on in more details. Electron phonon coupling plays also a major role due to spin-orbit interaction. The electron can flip its spin due to Elliot-Yafet like type of scattering at the sub-picosecond time scale. Another important ingredient that needs to be considered in ferromagnetic materials is thermal magnons which offer also a channel of spin flips(142).
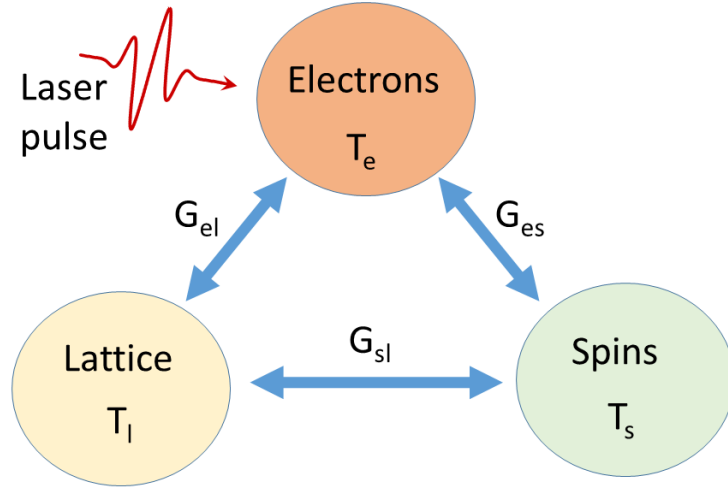
Figure 2.16: Schematic illustration of the three temperature model. All electronic, lattice and spin subsystems have well defined temperatures and are coupled to each other. The laser pulse deposits energy directly in the elctronic system.

Before we review few of the microscopic candidate mechanisms for the ultrafast demagnetization, we present here a phenomenological model developed by Beaurepaire(1) where he used T_s as the temperature of the spin system considered as a heat bath.[24] This model couples the electron, spin and lattice heat baths with ad-hoc coupling constants relating the relative temperature differences which acts as a driving force for angular momentum transfer between the subsystems (see Fig. 2.16):

$$C_e \frac{dT_e}{dt} = -G_{el}(T_e - T_l) - G_{es}(T_e - T_s) + P(t)$$
$$C_s \frac{dT_s}{dt} = -G_{es}(T_s - T_e) - G_{sl}(T_s - T_l) \qquad (2.63)$$
$$C_s \frac{dT_l}{dt} = -G_{el}(T_l - T_e) - G_{sl}(T_l - T_s)$$

---

[24]This temperature has been introduced in 1991 by Vaterlaus(143)

Where C_i is the heat capacity of the heat bath i and G_{ij} is the coupling constant between two heat baths i and j. $P(t)$ here represents the energy deposited by the laser. This model can be used to fit the data and shows the different channels for energy exchange in the non equilibrium regime but certainly lacks a physical and meaningful description of the processes responsible for such dynamics. Moreover, it assumes the thermalization of the heat baths at all times which is not necessarily the case.

In the following, we will introduce briefly few of the competing microscopic mechanisms suggested to account for the ultrafast demagnetization:

1. electron phonon coupling(144; 145; 146; 147; 148; 149): One of the most followed theory for the ultrafast quenching of the magnetization is one that considers a spin flip channel in the ultrafast time scale. The majority channel flips its spin transfering the angular to the lattice through an ultrafast Elliot Yafet mechanism. As we saw earlier, due to SOC the spin states are mixed and the probablity that a spin gets flipped depends on $|b_{sf}|$ which can be 25 times larger for the case of the transition metal ferromagnets compared to the one of Cu for example.

2. SOC mediated spin flips(150; 151): This process is different from the previous one for it transfer the spin angular momentum to the orbital channel which dissipates it almost immediately to the lattice due to the interaction of the itinerant electrons with the field potential of the nuclei. Based on ab-initio time dependent density function theory (TDDFT) calculations, Elliot et.al.(152) claim that the spin flip process can take action in a very fast time scale down to $15fs$. Tows and Pastor(150) also used a many body theory where the angular momentum exchanged between the spin system and the orbital system is transferred directly to the lattice through the electronic hopping which is responsible for dynamical orbital quenching. This effect is almost instantaneous and happens in the time scale of $< 1fs$.[25] The orbital system is not an angular momentum reservoir and here acts only as a mediator for enegry transfer. This is in agreement with XMCD measurement where the orbital and spin angular momentum have been measured simultaneously and both show rapid quenching with a slightly faster dynamics for the orbital system(132). Nevertheless, the angular momentum is not accumulated in the orbital degree of freedom.

3. electron magnon spin flips(153; 154): In this case, the electrons would flip their spins due to electron magnon scattering. It is argued that the system would conserve overall the total spin angular momentum, but with the action of SOC, the magnon moment would differ from the difference of the spin momenta caused by the spin flip(155).[26]Therefore, the total magnetic moment is allowed to decrease. In a second step, it is believed that magnon would transfer its momentum to the lattice for the same reasons evoked earlier.

2.4.2 Superdiffusive spin transport

This process is rather different from the previous mentioned processes as it doesn't include spin flip processes where the magnetization is locally altered. It states that the magnetic

---

[25]This time is characteristic of the orbital character itself and for an electron in the d band, this time is approximately $\sim \hbar/W_d \approx 0.1fs$ where $W_d \approx 6eV$ is the width of the d band.

[26]Spin up and spin down are mixed and are not completely disentangled quantities.
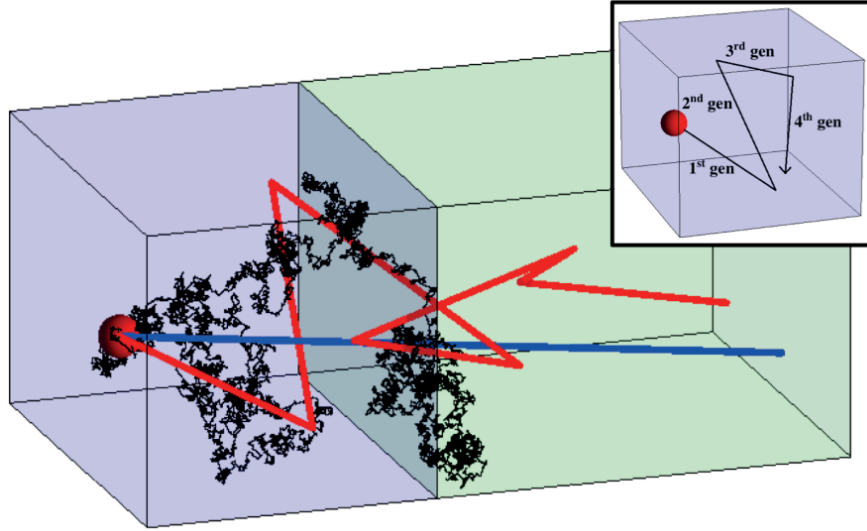
Figure 2.17: **Superdiffusive spin transport:** In the sketch, the three different regimes are illustrated: The black line represents the movement of an electron in the standard diffusive regime with almost infinte amount of scatterings, the blue line the ballistic regime with no scattering and the red line the superdiffusive regime with a certain number of scatterings. (Taken from (156)).

moment is driven away from the excited region. We will focus in detail on this approach as it constitutes the driving engine for the ultrafast currents generated in thim film magnetic heterostructures throughout this thesis. Upon laser excitation, as we saw earlier, an electron hole pair forms where the electron is excited to high energies defined by the photon energy. Battiato was interested in solving the diffusion problem of the excited particles in a film with a thickness compared to the mean free path of the excited particles which is around tens of nanometer[27], also the same range of values for the optical skin depth in metals. This case is an intermediate state between the ballistic motion where no scattering event happens (i.e. the lifetime can be viewed infinite) and the diffusive motion consequence of a random walk with an infinite scattering events. Due mostly to electron electron scattering, the excited electron oust another from below the Fermi level and scatters as a result to a lower level of energy closer to Fermi level. The second excited electron generated would be called second generation electron. Battiato solved this dynamical problem by summing over all ballistic parts of the whole trajectory considering the distribution of the previous ballistic walk as the starter for the next generation. For a particle with a lifetime equal to $\tau \approx 10fs$, the evolution of the process starts ballistically for time $t < \tau$ and becomes diffusive at times around $100fs$. The diffusion process in between is anomalous and called superdiffusive process. These regimes are characterized by the exponent of the time variable with which the variance of displacement varies with time:

$$\sigma^2 \propto t^{2/d_w} \tag{2.64}$$

---

[27]The lifetime of excited particles is around tens of nanometers and in the ballistic regime the velocity is around 1nm/fs.

Where d_w is called anomalous diffusion exponent and we have ballistic and standard diffusion
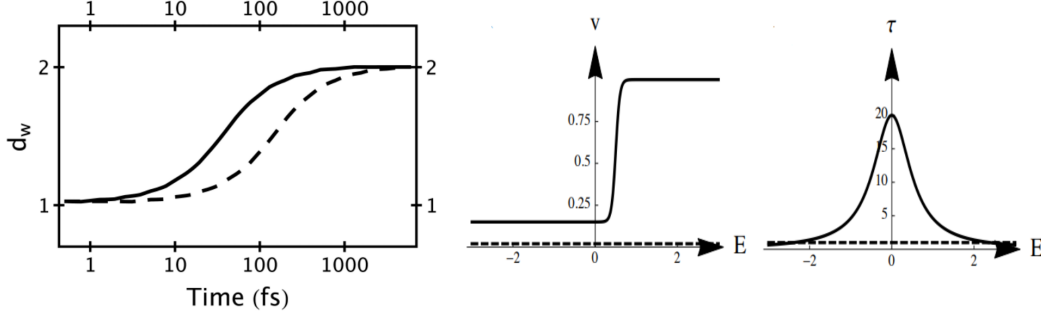
Figure 2.18: **Superdiffusive spin transport:** (a) time dependence of the anomalous diffusion exponent for a particle moving with a constant velocity. The black line is calculated for a particle lifetime $\tau = 10fs$ and the dashed one is for $\tau = 40fs$. Energy and spin dependent velocity(b) and lifetime (c) of electrons and holes in an ideal material. The spin up channel is represented with black line and the spin down channel with the dashed line. (Taken from (156)).

regimes for $d_w = 1$ and $d_w = 2$ respectively. Superdiffusive transport is for $d_w > 1$. For a typical 3d ferromagnet, both spin channels experience different transport because of the spin dependent density of states. In Fig. 2.18, we show calculations of the spin dependent velocity and lifetime[28] of quasiparticles(electrons and holes) in an ideal ferromagnet where spin up quasiparticle[29] lies in a very dispersive band above the Fermi level and less below and the minority remain in localized bands below and above the Fermi level. This is a simplified case but captures the physics of the transport. Yet, it has some similarities with real systems. for example, lifetimes are similar for both spin channel in Fe, the velocities are very asymmetric approaching the behaviour of the one in the Figure. This contrasts with the case of Ni where the asymmetry is pronounced in the lifetimes. In both cases, this leads to a superdiffusive spin dependent current vehiculating spins away of the absorption region. Nonetheless, it is important to mention that sofar the role of the holes has been neglected due to their low energies[30], which is the case until local thermal equilibrium. Consequently after electon electron scattering processes the electron and hole energies both approach the Fermi level and the gap between their velocities and lifetimes closes up. Therefore, the diffusion of holes starts contributing and counters the spin current transported by electrons. This explains the fact that the demagnetization peaks at around hundreds of femtoseconds and does not prolong longer. Other processes are also responsible for this at longer time scales namely due to electron phonon coupling. Battiato considered also a bilayer consisting of a 3d ferromagnet and a normal metal. In this case, the demagnetization is even enhanced due the diffusion of the spin current to the normal layer which acts then as spin sink. This phenomena came to be the source of spintronic THz emitters.

Q

FM

NM

$\mu^{(\uparrow)}$

$\mu^{(\uparrow)}$

$\Delta\mu$

λ_F λ_N
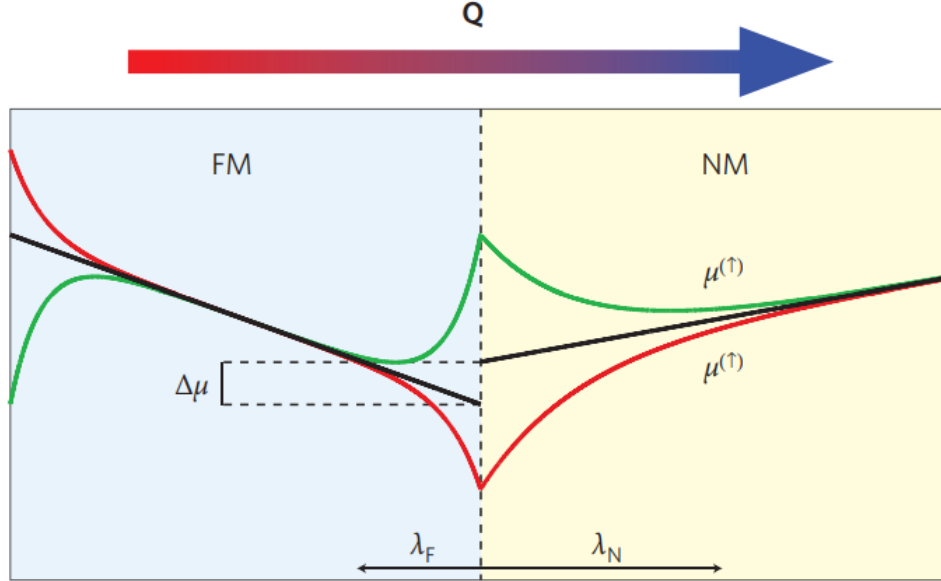
Figure 2.19: **Schematic illustration of the SDSE:** A temperature gradient leads to a discontinuity of the charge chemical potential between the FM and the NM. This is the charge Seebeck effect. The chemical potential is split around the interface due to different Seebeck coefficients for both spin channels generating a spin accumulation driving a spin current that decays in each layer away from the interface with a spin diffusion length $_F$ and $_N$ for both FM and NM respectively. This is the SDSE. (Taken from (157)).

2.4.3 Thermal-based processes

As mentioned before, when a metal is excited with a laser pulse, the temperatures of its electronic, spin and phononic subsystems change subsequently with different time scales depending on their intercoupling. Therefore, thermal processes based on temperature gradients between the species within or between the subsystems can act as a driving force for spin current generation. Two main thermal mechanisms are responsible for spin current generation which are briefly presented below:

Spin-dependent Seebeck effect: As predicted by Silsbee and Johnson(158)[31], this effect is the spin resolved version of the normal conventional charge Seebeck effect. Imaginatively, same as in a thermocouple where a temperature gradient generates a chemical potential gradient, a ferromagnet can be considered as a single unit combining two thermocouples for both spin channels(157). The property defining the amount of current generated is quantified by the

---

[28]includes electron phonon coupling, defect and impurity scatterings.

[29]The holes carry the spin current in the opposite direction to the one carried by electrons. In the early stage of ultrafast transport, their contribution is neglected due to their lower velocities until their energies approach the Fermi level, same as for the case of electrons. Their dynamics cannot be neglected then. This gradually decreases the spin current.

[30]Hence a lower mobility in this case.

[31]Originally called spin Seebeck effect when it was observed experimentally by Uchida et.al.(159) The spin Seebeck effect now refers to magnonic Seebeck effect as will be seen in the next paragraph.

Seebeck coefficient which in in the linear response regime[32] could be expressed as :

$$S = -eL_0 T \frac{\partial ln\sigma(\epsilon)}{\partial \epsilon}|_{\epsilon_F} \tag{2.65}$$

Where L_0 is called the Lorenz constant. In a ferromagent, both spin species possess different scattering rates and different density of states at the Fermi level. Therefore, they possess different Seebeck coefficients rendering their responses to the temperature gradient to be different. This difference is imprinted in the change in their respective chemical potentials which is by definition a spin voltage μ_s[33]. The gradient of this spin voltage is consequently a spin current flowing along the temperature gradient direction. When interfaced with a metal, a heat current can be generated at the interface, for example by resistive heating of the ferromagnet or by asymmetry in the absorption of the laser power between the two adjacent materials. This heat current drives consequently a spin accumulation μ_s at the interface, which can be treated as before in the framework of the Valet-Fert spin diffusion equation. In this sens, the superdiffusive spin current model could be seen as a non thermal version of the SDSE.
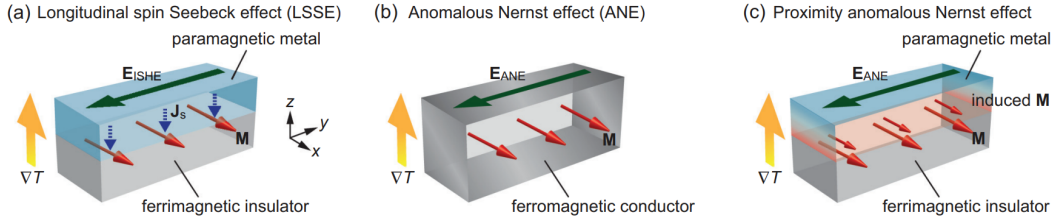
Figure 2.20: **Schematic illustration of electromotive thermal processes**. (a) SSE: a temprature gradient perpendicular to the FM/NM interface generates a spin current in the same direction which is converted to a charge current in the third orthogonal direction in the NM due to ISHE. (b) ANE: a temperature gradient accross a FM, with $\nabla T \perp M$, creates a charge current in a direction perpendicular to both the magnetization and the temperature gradient. (c) Proximity induced ANE: a temperature gradient perpendicular to the FM/NM interface induces an ANE charge current in the NM due to the induced magnetic moments in the NM. (Modified from (161)).

Spin Seebeck effect: Even though the spin Seebeck effect(162) is a general term pointing to the generation of a spin voltage under the influence of a temperature gradient, it actually refers to the generation of a magnonic voltage at the interface between a ferromagnet and a metal. The temperature difference between the electronic temperature of the metal and the magnonic temperature of the ferromagnet acts as a driving force for pumping spin current. The SSE is fundamentally different from the SDSE. In the former, similar to spin pumping, the magnonic excitations in the FM transfer spin angular momentum at the interface to the adjacent layer via the electron magnon coupling mediated by the s-d exchange. This creates a spin current carried by the electrons in the normal metal. Whereas, in the latter case, the spin current is generated from the difference of thermoelectric power of electrons in the FM itself. For this

---

[32]This is a derivation of Mott's law(9) using Sommerfeld approximation dictating that the conductivity can be expressed linearly as an expansion of $k_b T$ terms.

[33]In the literature, there is still some confusion on the nomenclature(160) on whether the spin current $j_s \propto S^\uparrow - S^\downarrow$ or $j_s \propto \frac{S^\uparrow \sigma^\uparrow - S^\downarrow \sigma^\downarrow}{\sigma^\uparrow + \sigma^\downarrow}$

reason, the SSE can be also observed in insulating FMs(163). The spin current can then be expressed :

$$j_s = S(T_m^{FM} - T_e^N) \tag{2.66}$$

Where S is the Seebeck coefficient. T_e^N and T_m^{FM} are the electronic temperature and the magnonic temperature of the non magnetic metal and the ferromagnet respectively. Usually both SDSE and SSE are detected electrically once the spin current is converted to a charge current via the ISHE. Another thermal based electromotive contribution has to be taken into account as it overlaps with these two effects: the Anomalous Nernst effect.

Anomalous Nernst effect: The anomalous Nersnt effect (ANE)(164; 165; 166) is the generation of a transverse charge current driven by a temperature gradient in a conducting ferromagnet. It has its origin in the Berry curvature and is therefore an intrinsic property of the material. In other words, it represents the thermal version of the AHE. When the ferromagnet is interfaced with a normal metal, the latter can acquire an induced magnetism at the interface. In this case, when the ferromagnet is insulating for example, ANE can still occur in the non magnetic metal due to the proximity effect. This is refered to as proximity ANE as depicted in Figure 2.20.

2.4.4 Spintronic THz generation
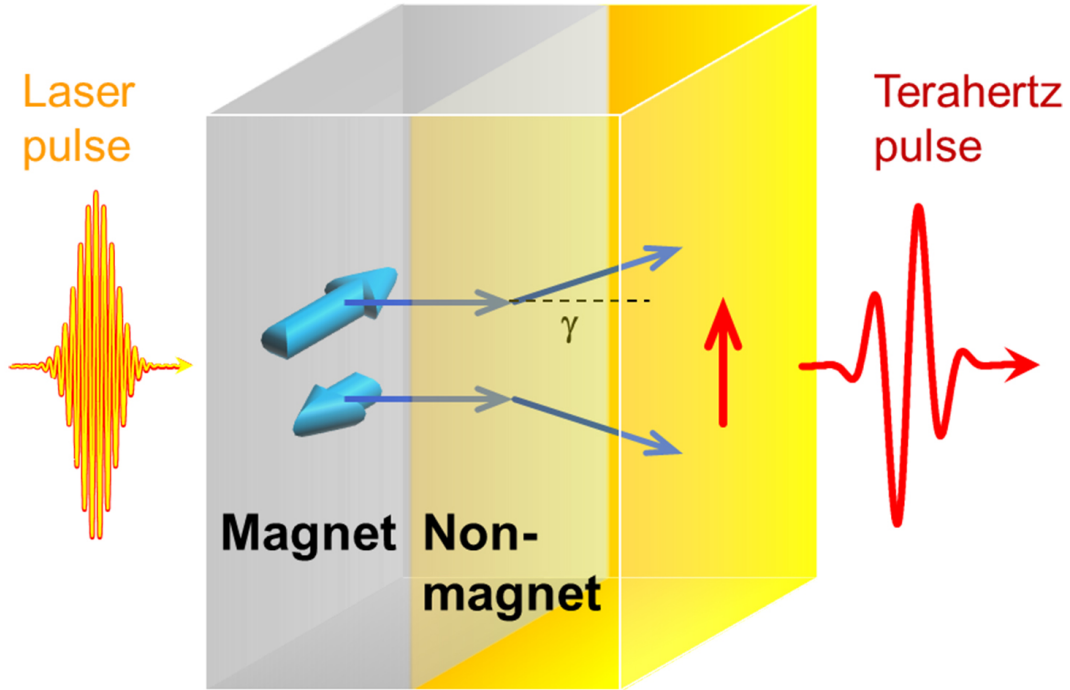
Figure 2.21: Illustration of the broadband THz generation in a spintronic emitter. A femtosecond laser pulse induces ulrafast demagnetization in the ferromagnet, launching an ultrafast spin current directed from the FM to the HM where it gets converted to a transient charge current, owing to the SHE of the material. This charge current radiates an electromagnetic wave which extends in the THz regime.

One of the big technological prowess of ultrafast spintronics is the development of highly

efficient, broadband and scalable THz emitters(167). As noted in the earlier sections, ultrafast demagnetization is accompagnied by a transient spin current. In a metallic FM/NM bilayer structure, this spin polarized current diffuses to the NM layer where it gets converted to a charge current due a spin galvanic effect inherent to the interface or the NM layer itself such as IREE or ISHE respectively. This charge current carries the same symmetry as the spin current pulse itself[34]. The converted spin current radiates a THz pulse with a broad coverage band of the frequency domain extending from 1 to 40 THz. The charge current originating from the bilayer comprises few different contributions and can be optimized. It contains radiation coming from the dynamics of magnetic dipoles, the anomalous Nernst effect, the photogalvanic spin effects at the interface and ISHE in the bulk of the NM layer. With a careful choice of materials, the THz signal[35] can be further increased to large values exceeding those of available traditional THz sources in the market such as ZnTe crystals. Indeed, the ISHE depends on the material and its strength is evaluated by the spin Hall conductivity or the spin Hall angle. A clear correlation exists between the SHC and the THz peak signal(5). The THz transient can be detected using THz time domain spectroscopy as we will see in the next chapter. The radiated THz electric field can be expressed in the following manner:

$$E_{THz} \propto \frac{P_{abs}}{d_F + d_N} \tanh\left(\frac{d_F - d_0}{2\lambda_{pol}}\right) \tanh\left(\frac{d_N}{2\lambda_N}\right) \frac{1}{n_{air} + n_{sub} + Z_0(\sigma_F d_F + \sigma_N d_N)} e^{-\left(\frac{d_F + d_N}{s_{THz}}\right)}$$

(2.67)

Where here P_{abs} is the absorbed laser power. d_F,σ_F and d_N and σ_N are the thicknesses and conductivities of the ferromagnet and the normal layer respectively. d_0 is an effective thickness below which the ferromagnet loses its ferromagnetism. λ_{pol} is a characteristic length for the saturation of the spin polarization in the ferromagnet and λ_N is the spin diffusion length in the normal layer. n_{air}, n_{sub} and Z_0 are the refractive indexes of ambiant air and of the substrate and impedence of vacuum respectively. Finally, s_{THz} characterizes the attenuation of the THz radiation in metallic medium. The first term represents the energy absorbed by the layers. The second term quantifies the generation of the spin current flowing in the ferromagnet. The third term represents the diffusion of the spin accumulation in the normal metal layer. The fourth term takes into account the total impedence of the layers and the reflections of the THz wave between the interfaces of the air medium and the substrate. The last term corresponds effectively to the attenuation of the THz wave in the metallic layers(5; 170).

---

[34]The spin current pulse can be mostly considered as unipolar. Yet, theoretical calculation within the framework of the Boltzmann transport formalism shows a bipolar shape of the current with a fast contribution arising solely from the mobile majority spin electrons followed by a small slower contrbution with the opposite spin polarization(168; 169).

[35]arising mostly from the ISHE of the NM, when it has a large spin Hall conductivity.

Chapter 3

Experimental Methods

In this Chapter, all experimental means and methods used in this thesis are presented. In the first part, the main film growth method is introduced followed by a brief review on the techniques needed for the deposited film characterization. Then, two main investigation techniques of spin dynamics, depending on the excitation method, are introduced: namely the ferromagnetic resonance driven spin pumping technique and the femtosecond laser pulse induced magnetization dynamics measured with a pump and probe scheme.

3.1 Sample fabrication and characterization

3.1.1 Film deposition: magnetron Sputtering

Film deposition consists of techniques used in laboratories as well as industry to manifacture well defined atomic multilayers with controlled interface roughness below $1nm$ and even controlled layer by layer growth depending on the process used. Here we present mainly the magnetron sputtering technique which is the most used film deposition method throughout this thesis.

Sputtering is the most common and used technique in industry and is relevant for nowadays semiconductor industry. In addition to its low cost, ease and flixibility with the materials of interest, it offers high controllable deposition rates, density, stocheometry and purity of the film of interest and is suitable for multilayers with roughnesses down to 2Å.

To discuss the fundamental principle of a sputter system, we consider the simplest sputter apparatus which is called a DC diode consisting of two plates: the anode and cathod, sitting a vacuum chamber(172). The anode is attached to the substrate holder where the film of interest is bound to *grow* and the cathod is attached to the material *targeted* for this process. Therefore, the latter is referred to as a target. An inert gas, called sputtering gas, usually argon gas (Ar) is introduced to the chamber. By applying a voltage between the plates above a certain threshold, electrons are ejected and collide sufficiently with Ar gas resulting in its ionization forming a plasma. The resulting Ar ions are positively charged and are attracted to the cathod. The electrons with a lighter mass form a so called sheath layer next to the cathod and result in a large potential drop, called the cathod drop. This mechanism amplifies the ionization process even further as the heavier Ar^+ ions are accelerated through the cathod potential drop creating secondary electrons from the cathod which in turn are accelerated and
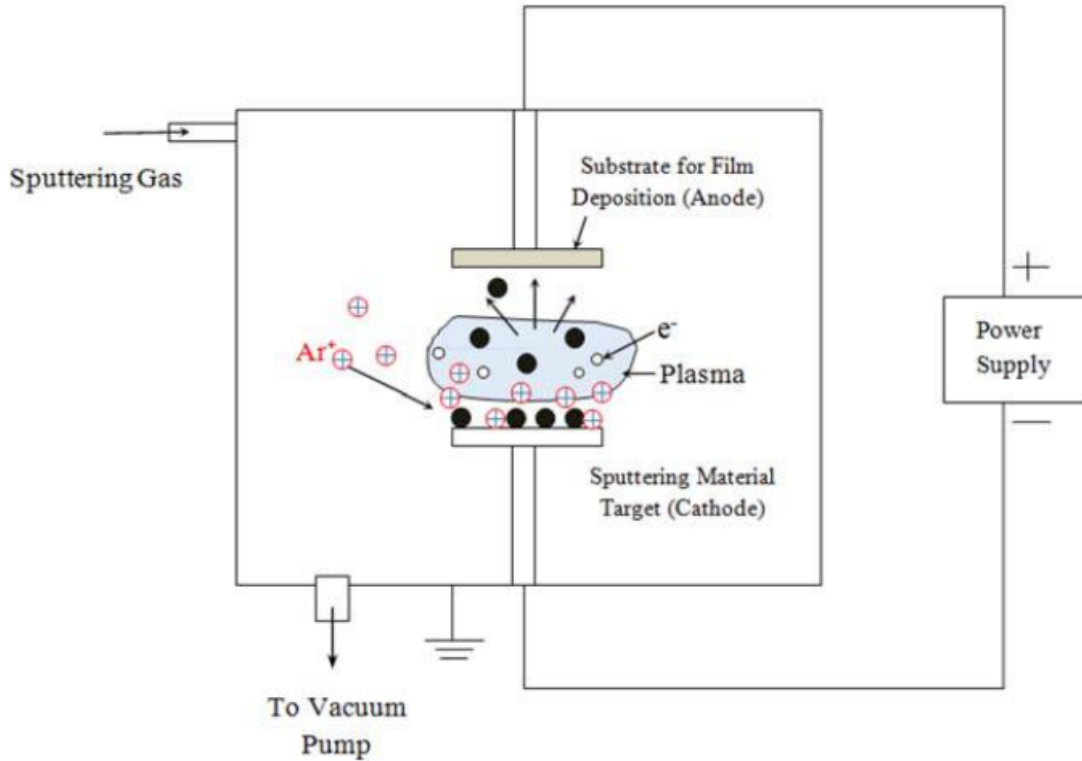
Figure 3.1: **DC diode sputtering**. Schematics of a typical DC diode sputtering.(taken from (171))

contribute to the plasma through Ar-electron collisions and electron electron scatterings. This yields the condition for a self sustaining plasma with a constant plasma current. Due to the fact that secondary electrons can be lost to the anode, this simple sputtering technique is no longer used and has been replaced by magnetron sputtering in the 1970s(173).

Indeed, magnetron sputtering provides a better efficiency of the ionization process through a confinement scheme. Permanent magnets are added to the cathod enabling trapping of the secondary electrons owing to the Lorenz force in cycloidal motion parallel to the target surface. This increases greatly the ionization process in the vicinity of the target. Once the Ar^+ ions current hits the target, their energies is transferred to the atoms at the surface ejecting a certain number of atoms that are accelerated to the anode where they adhere to the substrate. The efficiency of this process is quantified by the sputter yield defined as the ratio between the number of ejected atoms and the number of incident ions.

In our magnetron sputter apparatus[1], the Ar mass flow is kept constant at 55sccm[2] and the deposition Ar pressure is usually kept at 3mTorr. The base pressure of the chamber during deposition is less than 3.10^{-9} Torr. All metallic relevant targets (for example CoFeB, Pt, Ta, Co, Ni..) are fed with a DC power supply except for MgO which is powered with an RF power supply with a typical frequency of 13.56 MHz. This brings the advantage of longer residence

---

[1]Magnetron sputtering apparatus customized by AJA company.
[2]standard cubic centimeters per minute.
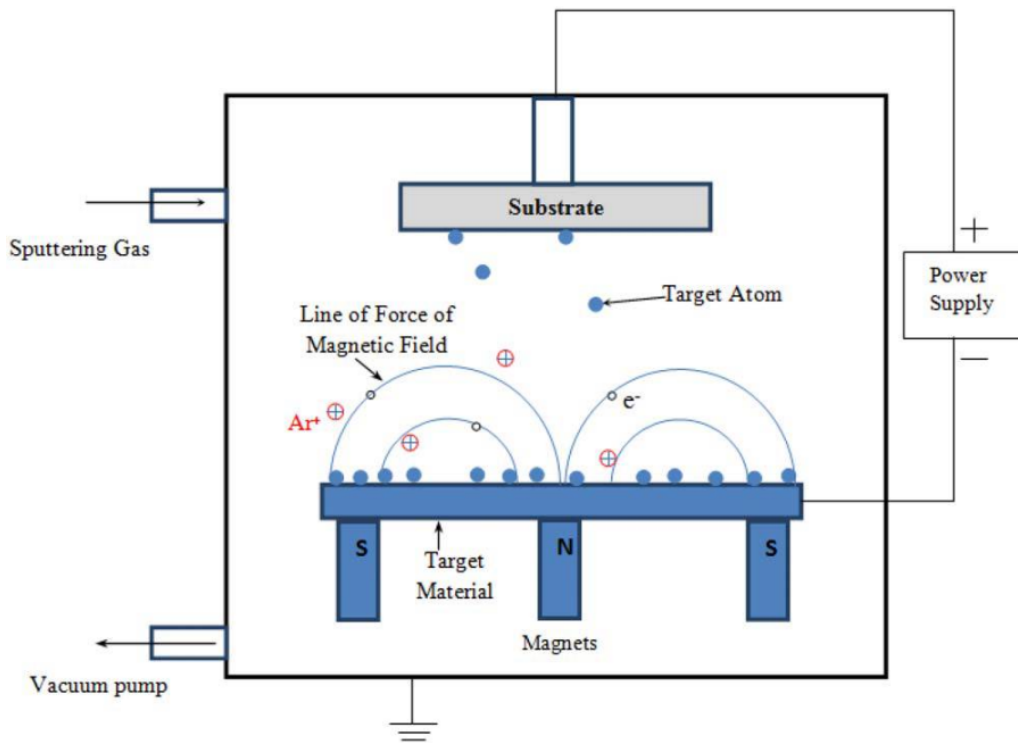
Figure 3.2: **Magnetron sputtering**. Schematics of a magnetron sputtering apparatus.(taken from (171))

times in the plasma and higher collision rates. Moreover, it is suitable for insulating targets such as MgO, since it prevents charge accumulation on the cathod surface. In our system, as can be seen in Fig. 3.3 , the MgO target sits at a right angle relative to the substrate holder and can be moved farther or closer with the use of an off-axis sputter gun motor. This brings the advantage of deposition optimization to insure that excess of oxygen ions are avoided during the deposition process leading to a better interface with the CoFeB layer compared to standard on-axis deposition.

3.1.2 X-ray diffractometer (XRD)

X-ray diffraction is a powerful technique used to investigate the crystal structure of thin films(175). This is possible owing to the matching between the atomic distances in a crystal and the x-ray wavelength. Let's consider a periodic structure, for example atomic planes with a fixed inter plane distance, and an x-ray beam incident with the certain angle θ relative to the surface. The incident beam experience a diffraction as the atomic arrangement acts as a three dimensional grating, generating well defined diffraction pattern spots called Von Laue/Bragg diffraction spots. The constructive interference condition came to be known as the
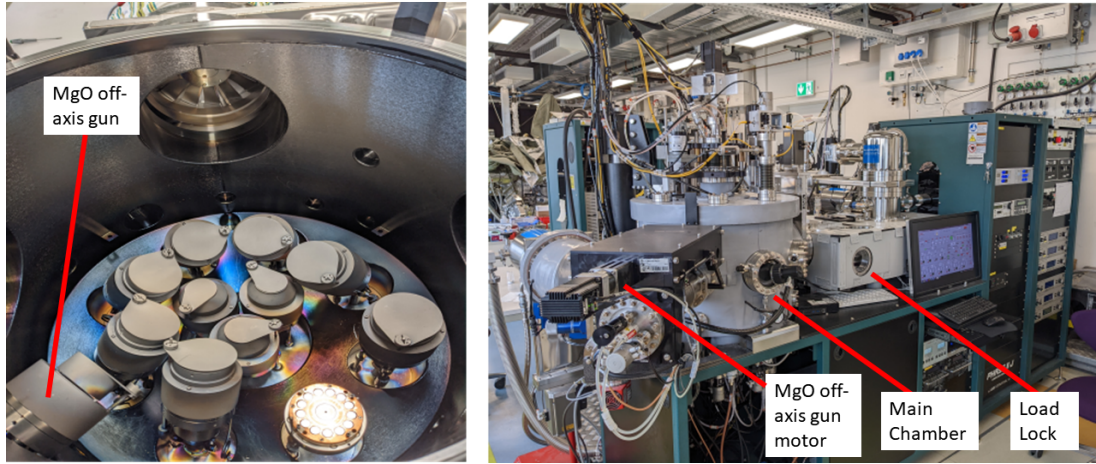
Figure 3.3: **Magnetron sputtering system**. Left hand side: targets inside the main chamber. Right hand side: view of the magnetron sputtering apparatus used in this thesis.
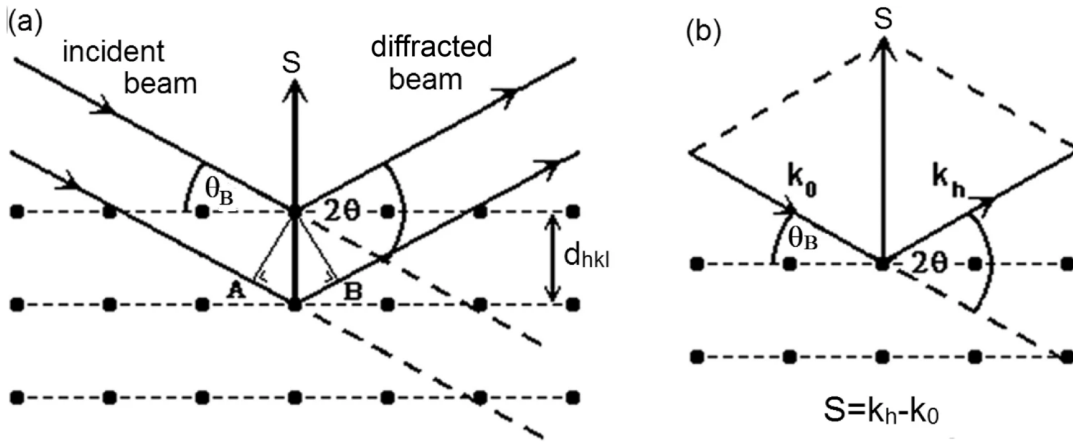
Figure 3.4: **XRD**.Bragg's law for (a) real space and (b) reciprocal space.(Taken from (174))

Bragg's law(10):

$$n\lambda = 2d_{hkl}sin(\theta) \tag{3.1}$$

Where n is an integer, λ is the wavelength of the x-ray, θ is the Bragg angle and d_{hkl} is the interplanar distance between (hkl) planes indexed with Miller indices.[3] For a cubic lattice for example with a lattice constant a_0, the interplanar spacing d_{hkl} is written as:

$$d_{hkl} = \frac{a_0}{\sqrt{h^2 + k^2 + l^2}} \tag{3.2}$$

---

[3]Bragg and Von Laue were awarded the Nobel price in 1915 for this discovery as it proved the regular atomic arrangement in solids.

An x-ray diffractometer (XRD) consists of a well defined x-ray source, a goniometer and a
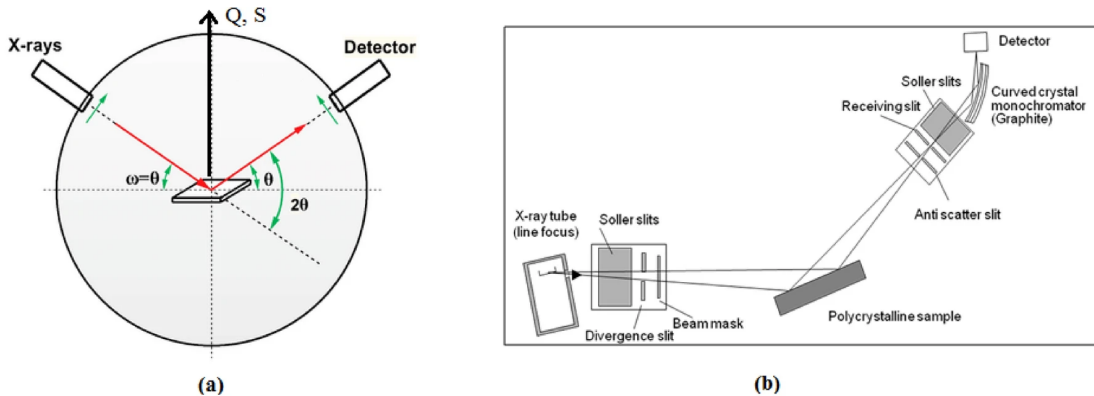
Figure 3.5: **XRD**. (a) Schematic of the powder X-ray diffraction geometry. (b) Experimental setup.(Taken from (174)).

detector. In the following, we will explain in more details the roles of the x-ray source and the goniometer in the powder XRD function mode(174):

1. **X-ray source**: Generation of x-rays is done in vacuum tube diodes. Subjected to a bias voltage of typically $-40kV$, electrons are ejected from the filament and accelerated in the direction of the anode kept at ground potential. Through a Bremstrahlung process, a process of inelastic scattering with atoms, the incident electron loses energy in a form of a radiation in the x-ray energy range. Usually, copper is the most used material for XRD with a characteristic wavelength of 1.5418Å, known as the $Cu\ K_\alpha$ radiation. Additional filter foils and monochromators and a slit are installed after the x-ray source to obtain a monochromatic continuous and a well spatially confined x-ray beam.

2. **Goniometer**: As evidenced by Bragg's law, for a certain sample orientation, sweeping the angle θ would result in diffraction peaks in the 2θ direction, relative to the incident angle. Therefore a precise control of the relative angle between the sample holder, source and detector is required. For this matter, the system is mounted on a goniometer with the sample stage at the center and the source and detector at the periphery. The goniometer controls precisely the azimuthal angleϕ of the sample, which is the rotation in the plane of the sample's surface as wel as the angle ω in the goniometer plane. These two angles are usually adjusted through rocking curves to get the sample crystallographic planes perpendicular to the plane of incidence. In the case of a sample with a random polycrystalline orientations, there are no preferred angles. The source and the detector are moved freely along the circumference. To insure good illumination of the sample, therefore better difftaction intensities, the x-ray beam is diverged from the x-ray source, diffracted at the sample and refocused at the detector. In Fig. 3.5, we show a $\theta - 2\theta$ scan where the source and the detector are moving accordingly to keep their relative angles constant. This geometry is refered to as the "Bragg-Brentano" geometry.
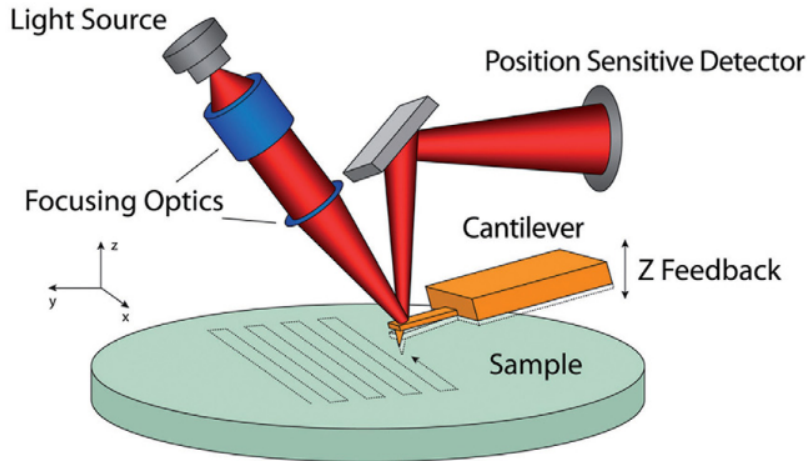
Figure 3.6: **Atomic force microscopy**. Schematics of a typical AFM intrument.(modified from (176))

3.1.3   Atomic Force Microscopy (AFM)

Unlike most common microscopy techniques, Atomic Force Microscopy (AFM), doesn't require the usage of any sort of beam, rather it is a highly precise force sensor(177). In a typical AFM apparatus, the sample is placed on a high precision piezoelectric stage that can be moved in all three directions. The AFM force sensor probe is a sharp tip of a conical shape with a certain apex curvature, defining its spatial imaging resolution (typically around few to tens of nanometers). It's usually made out of silicon or silicon nitride. The tip is mounted on a flexible cantilever which bends according to the force felt by the tip above the sample surface. Therefore measuring accurately the deflections of the cantilever translates into measuring the tip-sample interaction force. Usually, an optical approach[4] is used for this purpose with the laser beam directed onto the cantilever surface and reflected to a position sensitive photodiode. An intuitive understanding of the AFM would be to imagine the sample topography, as it is being scanned in x-y direction, modulates the force field acting on the tip. Therefore reconstructing this field equivalently determines the sample's topography. This is a simplified picture for the main forces acting on the tip are of two different natures. An attractive force due to Van der Waals interaction dominates if the distance between the sample and the tip is large enough whereas at lower distances, the repulsive electrostatic forces dominate. The interplay between these two forces in conjuction with the operation mode of the tip determines the interaction and thus the imaging process. Indeed, there are several modes of operation for the AFM categorized in static and dynamic modes. Here, we present shortly some of them:

1. **Contact mode**: In this static mode, the tip is brought to a distance of less than a few Ångström to the sample surface where the repulsive electrostatic forces are dominating. The feedback circuitry, keeps the tip close to the sample surface and drags it along the surface topography. In this case, the cantilever has a very small spring constant ($\leq$1N/m), to prevent the tip from wearing out. This mode suffers the lateral forces experienced by

---

[4]Some techniques use a tuning fork approach instead.

the tip as well as contamination on the sample surface.

2. **Noncontact mode**: In this dynamical mode, the tip is at typical distances of few tens to hundred Ångström experiencing the week Van der Waals forces (in the order of $10^{-12}N$) as compared to the contact mode. The tip is stiff and is coupling to a vibrational system near its resonant frequency with typical frequencies ranging from 100 to 400 kHz. The stiff tip resists the attractive forces with the help of the feedback system which maintains the vibrational frequency as well as the sample to tip distance to a constant level. This in return gives small signals and slower scans compared to the case of the contact mode. On the other hand, it is a non invasive technique with less risk of damaging the sample or the tip.

3. **Tapping mode**: The tapping is also a dynamical mode and similar to the noncontact mode, the cantilever is brought to vibrate near its resonant frequency. The difference between both is in the vibrational amplitude which is much larger for the tapping mode. As its name suggests, the tip (with spring constants in the range of 10-100N/m) is allowed to tap the sample surface during its oscillations. The forces acting on the tip are mainly the repulsive forces which are large enough to affect its oscillation motion. Therefore the feedback system is set to maintain the vibration amplitude constant. The tapping mode holds the advantages of the noncontact mode in addition to being more sensitive and provides faster scans.

3.1.4 Transmission Electron Microscopy (TEM)

Transmission Electron Microscopy(179) is a powerful technique for microstructural characterization of samples as well as resolving atomic resolution features of a specimen. It utilizes an electron beam which can be focused on the sample. The changes in intensity of the diffracted electron beam gives the so called diffraction contrast relevant to investigate specific regions of the material (defects, dislocations) and the phase of the diffracted beam can be used to reconstruct a high resolution image of the region of interest in the sample. We will explain briefly both phenomena in the following part.

TEM uses an electron gun which provides an electron beam that can be guided and focused using magnetic lenses onto the sample where it gets diffracted. The transmitted and diffracted electrons are then guided, once again through lenses, to a viewing screen(see Fig. 3.7). At this point no apparent contrast can be viewed. Indeed each point in the back focal point contains electronic rays coming from all points of the specimen. However, placing an objective aperture before the back focal can whether in one case block the transmitted (not diffracted) light, allowing only the diffracted electrons to pass or the other way around. In the first case, we call this type of imaging *Dark field* imaging (DF) and in the other case *Bright field* imaging (BF). Since their relative intensities are antagonist, blocking one mode of transmission increases the apparent intensity coming from the other mode. In other terms, regions of the sample "that diffract would appear bright in DF and dark in BF and regions that don't appear dark in DF and bright in BF". This is how the diffraction contrast is obtained.

More importantly for this thesis, the TEM is capable of reconstructing a high resolution image resolving the individual atoms in the specimen. This is called high resolution TEM
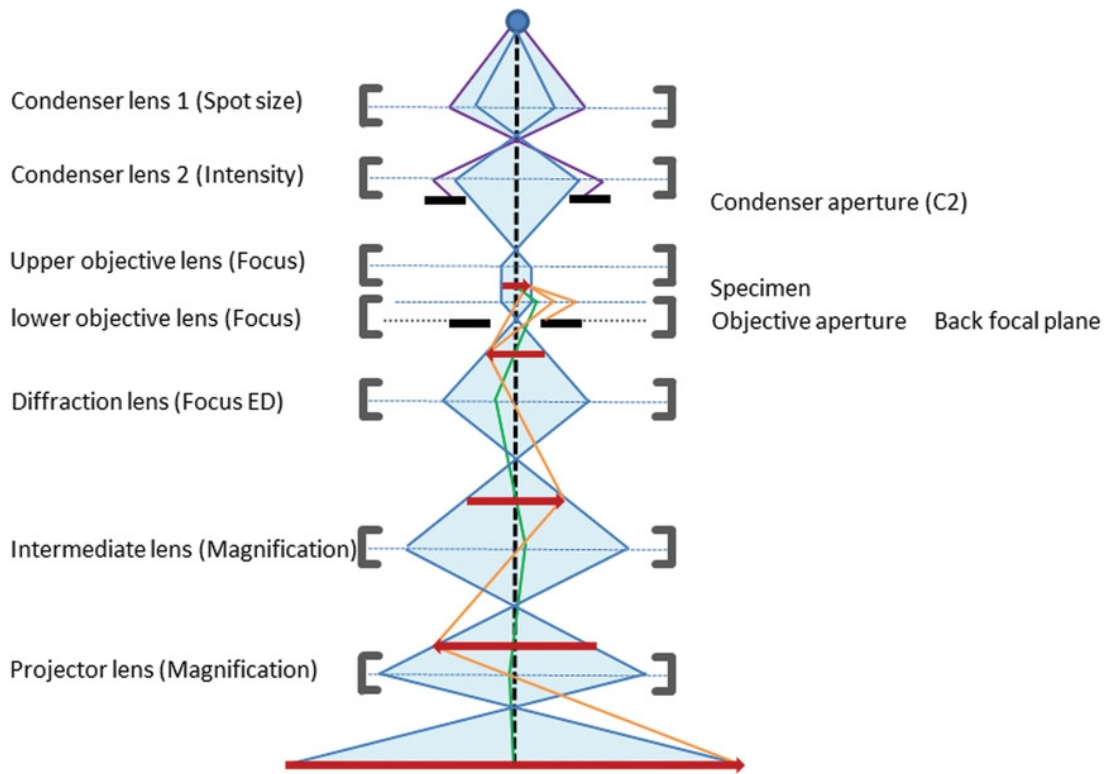
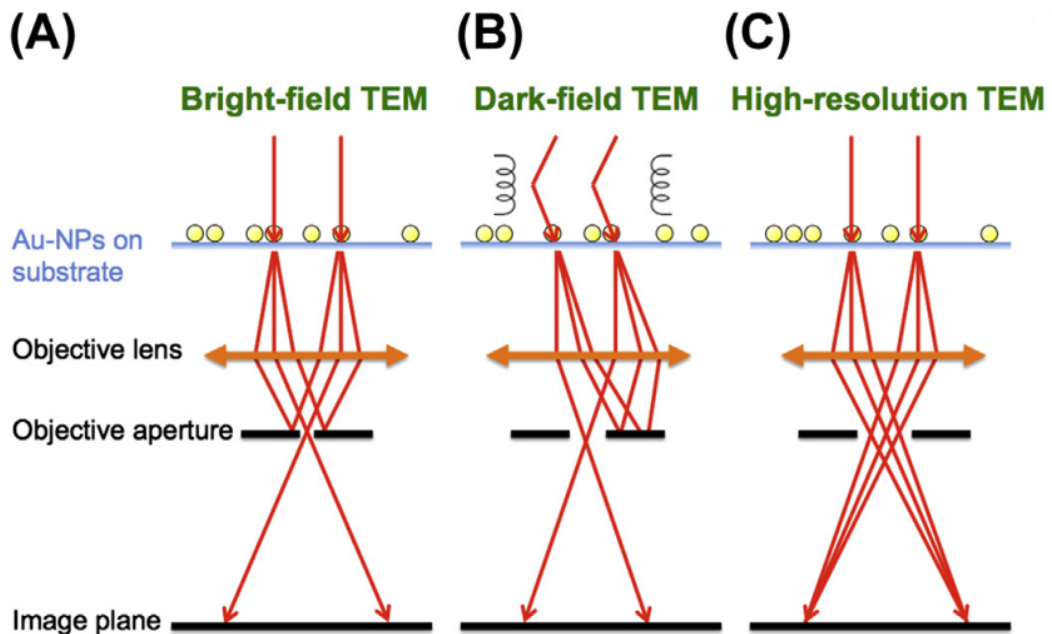Figure 3.7: **TEM**. Schematics of a typical TEM instrument.(modified from (178))

Figure 3.8: **TEM**. Illustration of Bright field, Dark field and High-resolution TEM.(modified from (180))

(HRTEM). To explain its working principle, let's consider a spherical waveform of electrons

diffracted from the specimen, the waveform of the electronic wave experiences a phase shift traversing the material until it falls on the viewing screen. The diffracted wavefunction $\psi(\Delta k)$ is the Fourier transform of the scattering factor in the material $f(r)$. Δk is the scattering wavevector. $f(r)$ is expressed as follows:

$$f(r) = \frac{1}{2\pi} \int_{-\infty}^{\infty} \psi(\Delta k) e^{-i\Delta k.r} d^3(\Delta k) \tag{3.3}$$

In order to reconstruct $f(r)$, a clear access to $\psi(\Delta k)$ as well as a certain large coverage of Δk is needed. This selection would define the spatial resolution of the microscope according to $\delta x \simeq \frac{2\pi}{\delta k}$. Therefore, placing an objective aperture as in the case of DF or BF imaging trancates the Δk range and hinders the spatial resolution needed for atomic imaging. A larger aperture[5] is then placed to allow the transmitted or "forward scattered" electrons and only one diffracted beam to pass. The first beam acts as a reference and the resulting wavefunction at the screen is an interference pattern between the reference and the diffracted beam giving then access to $f(r)$ which contains all the information about the atomic arrangement in the specimen. Reconstruction of the image requires sofisticated computer simulations to fit the experimental images. Moreover, another important parameter needed for HRTEM imaging of ultrathin multilayers is the defocus of the objective lens which can enhance greatly the contrast and enable even resolving the interface between similar atomic layers (in terms of their atomic number Z).

3.1.5   Vibrating Sample Magnetometry (VSM)

Vibrating Sample Magnetometry(182) or VSM is a technique that enables the measurement of the magnetic moment of a sample in an external magnetic field(183). The magnetic sample is mounted on a holder, usually in the form of a tube, in between the poles of an electromagnet. Depending on the type of measurement, the sample is attached accordingly to perform in plane or out plane magnetic measurements. The advantage of the VSM is that it is a non invasive technique. It can measure signals down to 10^{-6}emu.

As depicted in Fig. 3.9, the sample holder vibrates perpendicularly to the external magnetic field at a fixed frequency. For a fixed sample position, due to Faraday's induction law, the magnetic flux of the sample is picked up as an AC voltage by two coils placed near the electromagnet poles. The magnetic signal can be filtered out with a Lock-in amplifier. When the magnetic field is swept, changes in the magnetic signal are recorded and the hysteresis loop is registered.

---

[5]A maximum range of Δk is obtained without placing any aperture but the waves which are the most tilted from the optical axis, i.e. with the largest Δk would suffer spherical aberration of the obejective lens. Therefore, there is a certain compromise between the size of the aperture and the spherical aberation. It was not until around the year 2005, owing to computer processing and better optics which improved the spherical aberration, that the resolution of the HRTEM was boosted to around 0.8Å.
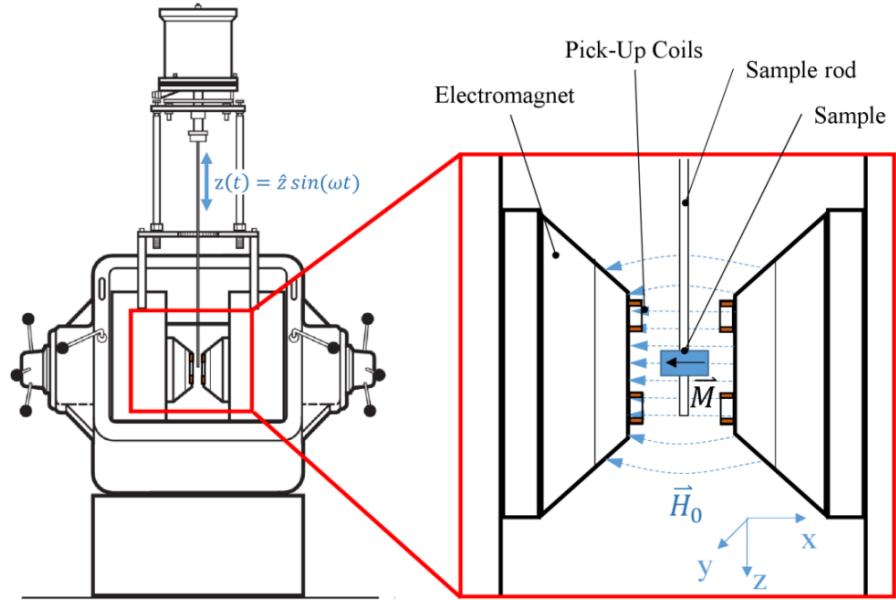
Figure 3.9: **VSM**. Schematics of a typical VSM intrument.(modified from (181))

3.2 Ferromagnetic resonance driven spin pumping
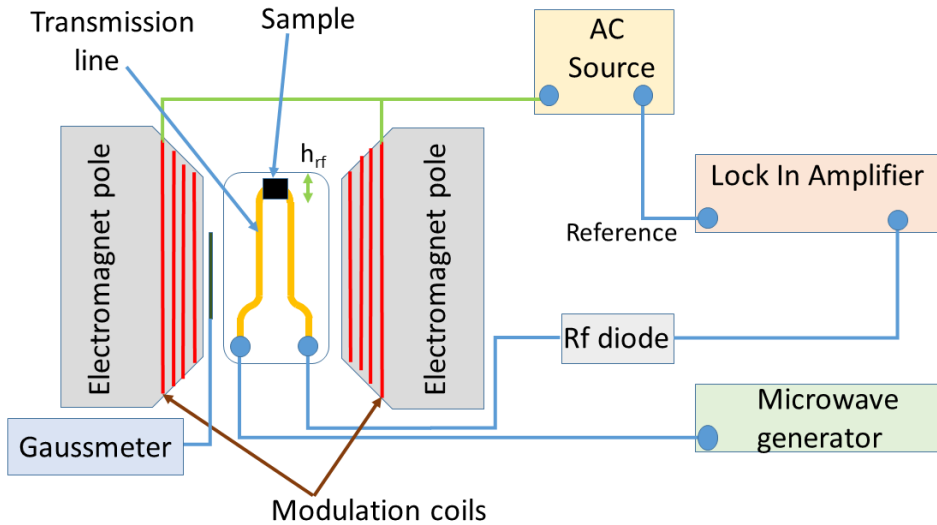
Figure 3.10: **FMR**. Schematics of the FMR setup.

Ferromagnetic resonance is a widely used measurement technique that measures the absorption spectrum by feeding a microwave to the sample of interest under the FMR condition. The FMR condition which denotes the coherent precession of the magnetization of the magnetic sample happens in the GHz regime, i.e. can be triggered by microwaves. For a certain external magnetic field, the FMR condition is reached and the absorption spectrum registers a peak.

The microwave is fed to the sample through a coplanar waveguide as depicted in Fig. 3.10. The sample of interest is cut to a size of around 2x3 mm^2 and placed face down on top of the transmission line of the waveguide sitting on a holder between the poles of an electromagnet. A signal generator is used to provide a radio frequency current to the waveguide. The frequency span covers frequencies up to 20 GHz. Furthermore, a modulation of the external field is used by setting additional coils around the poles of the electromagnet. Frequencies around 50-100 Hz are used and the rf out signal of the transmission line of the waveguide is fed into a Lock-in amplifier. The magnitude of the oscillating magnetic field can be tuned to typical values around $500\mu T$.
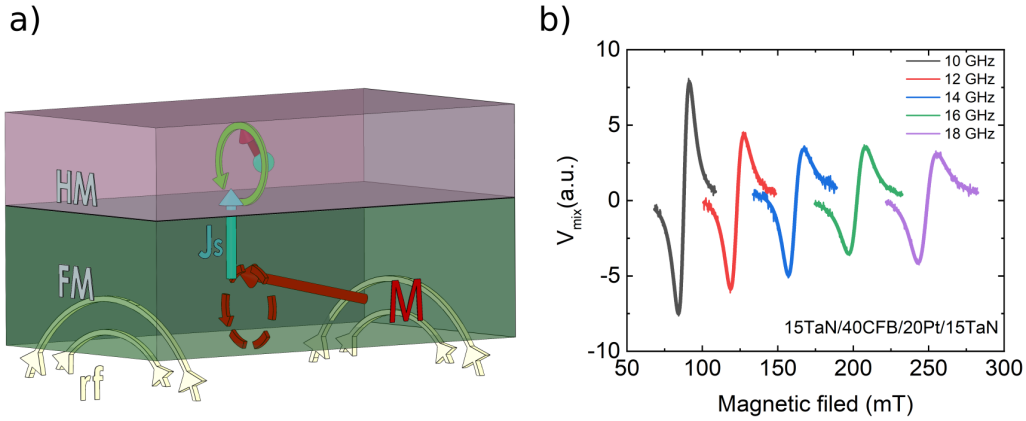
Figure 3.11: (a) Schematics of FMR spin pumping in a typical FM/HM bilayer. The spin current is pumped to the HM which acts as a spin sink, therefore effectively increasing the damping of the FM. (b) Magnetic field dependence of the absorption spectra at the FMR condition for various microwave frequencies.

As was discussed in details in Section 2.3.5, the FMR absorption spectrum is proportional to the imaginary part of the microwave susceptibility χ'' which is a function of the external field H_{ext}. Taking the modulation field $h_m e^{i\omega_0 t}$ into account and considering that $h_m \ll H_{ext}$, we can use Taylor expansion of the susceptibility with respect to time. We then obtain:

$$\chi(H_{ext} + h_m e^{i\omega_0 t}) \simeq \chi(H) + i\omega_0 h_m e^{i\omega_0 t} \frac{d\chi}{dH_{ext}} \qquad (3.4)$$

Therefore using the lock-in signal, locked at the frequency ω_0, retrieves only the $\frac{d\chi}{dH_{ext}}$ component of the susceptibility. ω_0 being the frequency of the modulation field which is different from ω used as the frequency of the microwave exciting the sample.
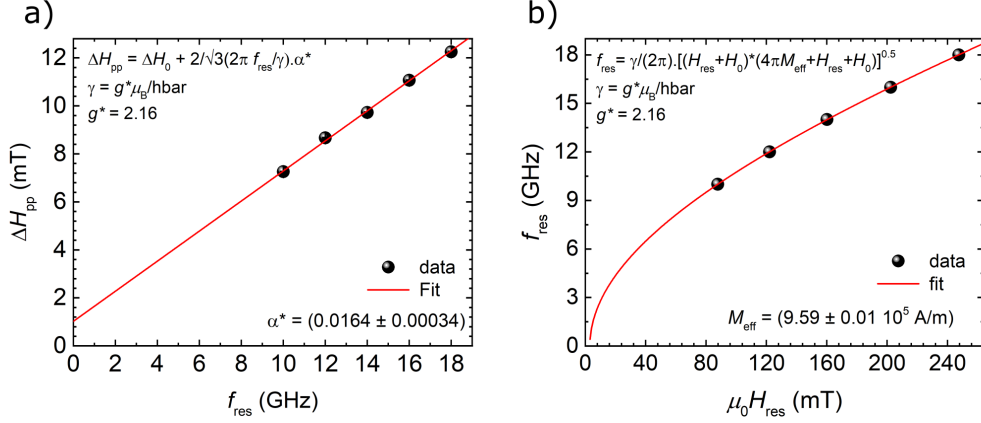
Figure 3.12: (a) Frequency dependence of the FMR linewidth. The linear fit is used to extract the effective Gilbert damping. (b) The resonance field dependence of the microwave frequency fitted using Kittel's formula.

In Section 2.3.5, we mentioned that the fitting of the FMR spectra leads to the extraction of two parameters : the resonance field H_{res} and the linewidth ΔH_{pp}. The first one is fitted with the Kittel formula and therefore one can extract the g-factor and the effective magnetization M_{eff} which gives information about the magnetic anisotropy field through:

$$M_{eff} = M_S - H_k \tag{3.5}$$

where H_k is the anisotropy field and M_S is the saturation magnetization. The second parameter of importance is the linewidth related to the Gilbert damping through :

$$\Delta H_{pp} = \Delta H_0 + \frac{2}{\sqrt{3}} \frac{\alpha \omega}{\gamma} \tag{3.6}$$

Here ΔH_0 is called the inhomogeneous broadening and ideally should tend to zero. Its value is correlated to the irregularities and defects of the sample.

Next, we show an example of FMR results of a simple case study. The sample is a bare CoFeB(4nm)/Pt(2nm) bilayer sandwiched between two TaN thin layers. In Fig. 3.11, the FMR spectra is shown for frequencies ranging from 10 GHz to 18 GHz. The corresponding resonances and linewidths are extracted and plotted in Fig. 3.12, where we also show the corresponding values of M_{eff} and the effective Gilbert damping α of the system.

3.3 Short laser pulses and THz detection techniques

Laser amplified pulses in the femtosecond time scale are used throughout all the experiments described in this thesis. In the first part, we will review the fundamental key points to achieve such pulses and their characteristics. To access the ultrafast response signal of a sample, we employ a time resolved pump and probe method. Once the pump laser pulse hits the sample, ultrafast response is triggered.

Various methods based on the pump and probe process can be used to detect the transient response of the system. In a first appraoch, we use the an rf probe connected to a fast sampling

oscilloscope to measure the transient response whether on-chip or in free space. This is the mainly used detection method in this thesis. The two next approaches use a probe laser pulse and electro-optic sampling to reconstruct the signal. One detects the free space radiation and the second detects the on-chip transient.

Herein, we review the amplification process of laser pulses, discuss the pump and probe measurement scheme and briefly introduce the various THz response detection techniques.

3.3.1 Amplified femtosecond laser pulses
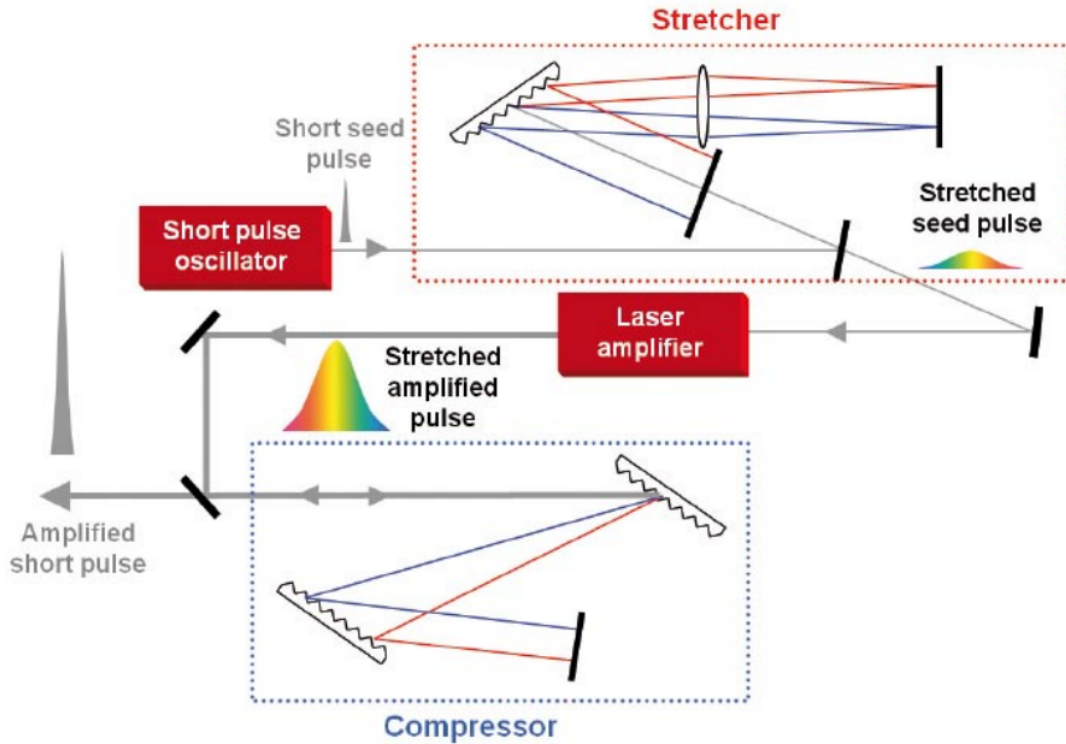
Figure 3.13: Schematics of a chirped pulsed amplification laser system. (Taken from (184)).

LASER is an acronym for Light Amplification Stimulated Emission Radiation. As specified in the name, a laser is a cavity enclosed within two mirrors (one of which is partly transmittive to couple out the radiation) containing a gain medium. Usually, electrons in the gain medium are excited to higher levels constantly, before feeding the cavity with the light beam that needs to be amplified for it to "lase". This is called population inversion and is a necessary condition for the amplification of the light which happens on the basis of the stimulated emission discovered by Einstein. The light inside the cavity bounces back and forth and more photons are generated during each round trip. At this stage the amplification outcomes the losses in the cavity and the former is reduced with the amount of photons generated in contrast to the latter, until they fully compensate each other. This is the operating condition of a laser with certain conditions for the light to sustain itself. Indeed, it has to interfere constructively with itself creating a coherent oscillating light inside the cavity. This is an important feature for the laser as it

is primarily a resonant cavity with a gain medium. Several modes satisfy this condition and they are called longitudinal modes. In the frequency domain, these modes are separated by $\Delta\nu = c/2l$, where c is the speed of light and l is the length of the cavity.

In order to achieve pulse operation, modulating the phases of the longitudinal modes of the laser, i.e. *Mode Locking* is required. In our case, It is passive mode locking which requires an optical Kerr effect medium. This means that the light Gaussian beam intensity modulates the refrative index of the medium itself which in turn acts as a lens, called a Kerr lens. With the combined action of the chirped mirrors needed to compensate for the group velocity dispersion, this acts in favour of reducing the pulse length until stable femtosecond pulses regime is achieved. At this stage, the oscillator is delivering ultrashort pulses of a pulse width around ~ 100fs at a high repetition rate of 80MHz, with a pulse energy in the nJ range.

The next step is to obtain ultarashot femtosecond pulses with energies in the μJ-mJ range. For this, Chirped Pulse Amplification(185) is needed[6]. Schematics of this technique are shown in Fig. 4.13. The oscillator laser pulses are stretched to the nanosecond time scale and fed to the regenerative amplifier, which in our case consists of a Yb:KGW lasing medium with a central wavelength characteristics of 1028 nm. The medium is pumped with "high brightness diode bar modules delivering up to 60W of power"(188). Pockels cells pulse pickers transmit pulses after a certain amount of passes of the seeded pulse for amplification. This reduces the repetition rate to 100 kHz in our case. The pulses then are compressed again in time reaching a pulse duration of around 280 fs and a pulse energy up to 2mJ and average power of 8W(188). The PHAROS[7] oscillator can be locked to an external clock. This feature will be utilized in our sampling oscilloscope detection technique, discussed in more details further below.

3.3.2 Pump and probe technique

The pump and probe technique is a powerful technique that provides access to ultrafast dynamics. A typical pump and probe experiment involves a pump laser pulse powerful enough to excite a dynamical response in the sample. The probe pulse is usually a fraction (less than 5%) of the pump pulse as it should interact with the sample without altering the dynamics. It is delayed from the pump pulse in a controlled way. Usually a mechanical stage is used to induce such a delay. To provide a time resolved evolution of the response signal, the delay is incremented by a step at every pump pulse which hits the sample at a regular rate. The time resolution is affected by two parameters which are the pulse width and the mechanical step resolution provided by the delay stage.

Throughout this thesis, we are interested in probing ultrafast currents in the sample. These currents generate an electric field which can be radiated or guided through a waveguide. Three detection methods will be presented here below.

3.3.3 Sampling oscilloscope detection

The measurement setup is displayed in Fig. 3.15. The laser is providing a laser pulse as a pump at a rate of 100kHz. The pulse is guided and focused on the sample with spot size of around

---

[6]This technique was awarded half of the Physics Nobel prize in 2018(186; 187).
[7]Name of the laser from the Light and Conversion company.
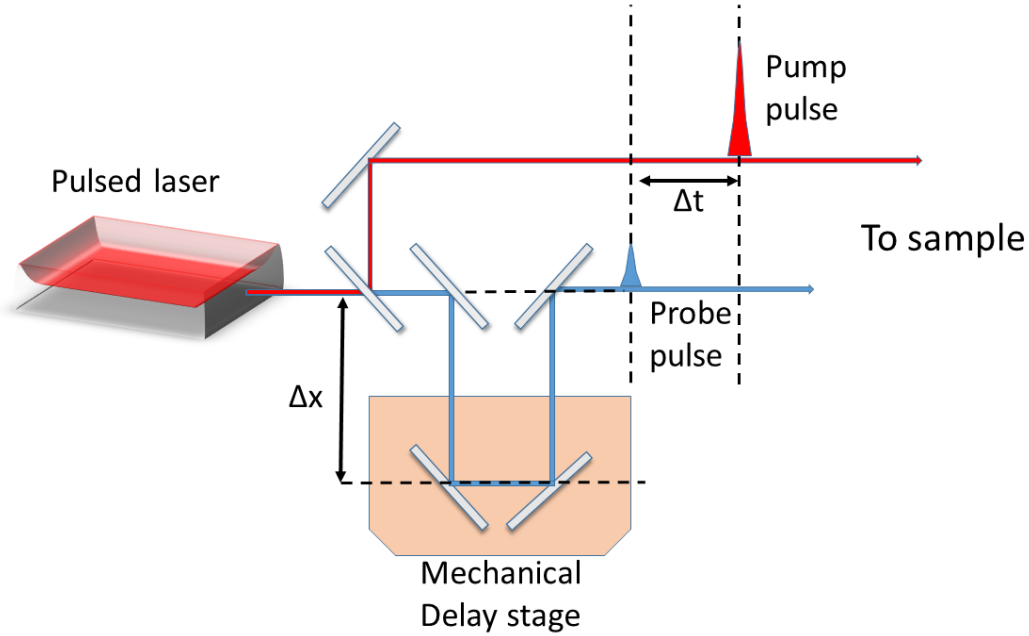
Figure 3.14: Illustration of a simple pump and probe scheme. The pump and probe pulses are delayed in time using a mechanical stage.

200-300μm. This detection technique involves an electrical probe detection enabled by an rf coplanar probe[8] connected to a sampling oscilloscope. In our case, we are using a Tektonix DSA 8200 with a sampling Time Domain Reflectometry (TDR) module(80E10) with a typical response width of 10ps and a bandwidth of 50GHz. The sampling oscilloscope trigger clock is sychronized with the laser with the seeding signal of 80MHz, the rate at which the light pulse comes out of the oscillator and therefore prior to the amplification stage. This adds a certain delay in the order of 30ns for the laser pulse to travel through the amplification stage until it reaches the sample generating the waveform of interest. The electrical trigger has a certain delay around 24ns which matches the delay of the light pulse, making the acquisition possible.

In Fig. 3.16, we illustrate the working principle of the sampling module. A trigger event is selected and the acquisition is delayed by a certain time intrinsic to the equipment, T_{int}. This time can be tuned over a certain range by adding a controllable delay T_{cnt}. The overall delay is then $T_{ds} = T_{int} + T_{cnt}$. The light pulse is delayed with a time T_{dl}. The repetition rate of the amplified laser stage is 100kHz. Therefore the waveform is generated every 10 μs. For the first acquisition point at $T_{ds} = T_{dl}$, the sampling oscilloscope is armed for the next event with a certain time around $T_{arm} \sim 25\,\mu$s and shifts the trigger delay by 1ps, time at which the next point of the waveform is acquired. This procedure is repeated until the generation of the entire waveform.

Two measurement schemes can be employed with this detection technique. Whether the rf probe tip is contacting the sample's surface or hovering above it with a certain distance as shown it Fig. 3.17(a) and Fig. 3.18(a) respectively. These two schemes are referred to as "Contact Mode"(CM) and "Noncontact Mode"(NCM) respectively. In the first scheme, the

_____
[8]The pitch between the two tips of the probe is around 100μm.

58
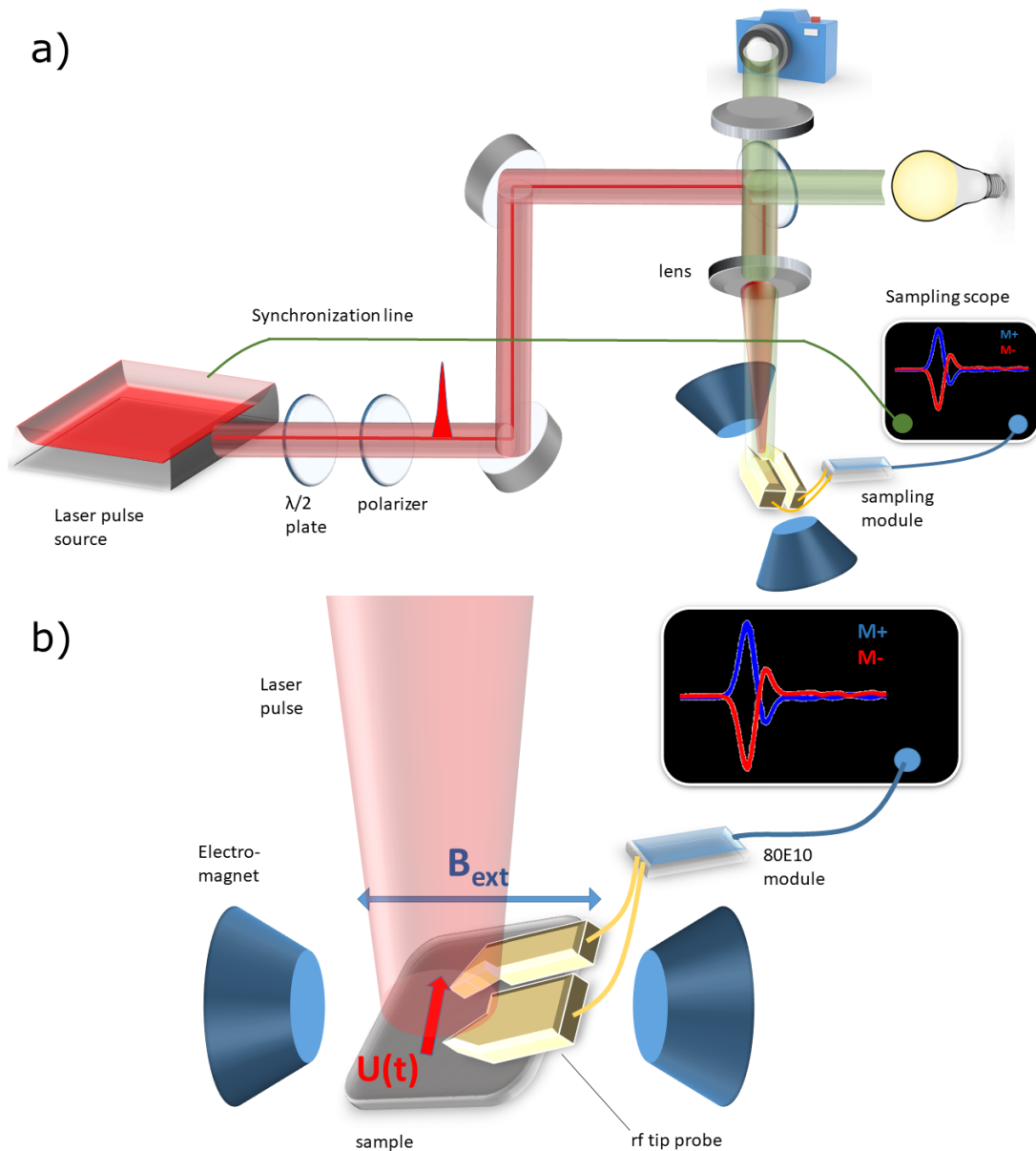
Figure 3.15: **Measurement scheme using rf probe-sampling oscilloscope detection technique**. (a)The laser source delivers a optical pulse with a central wavelength of 1030nm that is guided and focus on the sample's surface with an illumination spot covering the rf-probe pins' spacing. The probe is connected to the sampling module, which is connected to the oscilloscope. A synchronization line connects the laser system to the sampling oscilloscope allowing the waveform recontruction. (b) Zoom on the sample side. The sample is placed between the poles of an electromagnet generating a magnetic field perpendicular the voltage $U(t)$ measured by the rf-probe tip.

probe measures directly the current on the sample whereas in the second scheme the tip acts as an antenna, hence measuring the emitted free space radiation from the current flowing in the sample. In Fig. 3.17(b) and Fig. 3.18(b) , we show a typical time resolved waveform response for both measurement schemes. The free space measured voltage is proportional to the derivative of the current flowing in the sample. Both signals are shown in Fig. 3.19. The sample considered
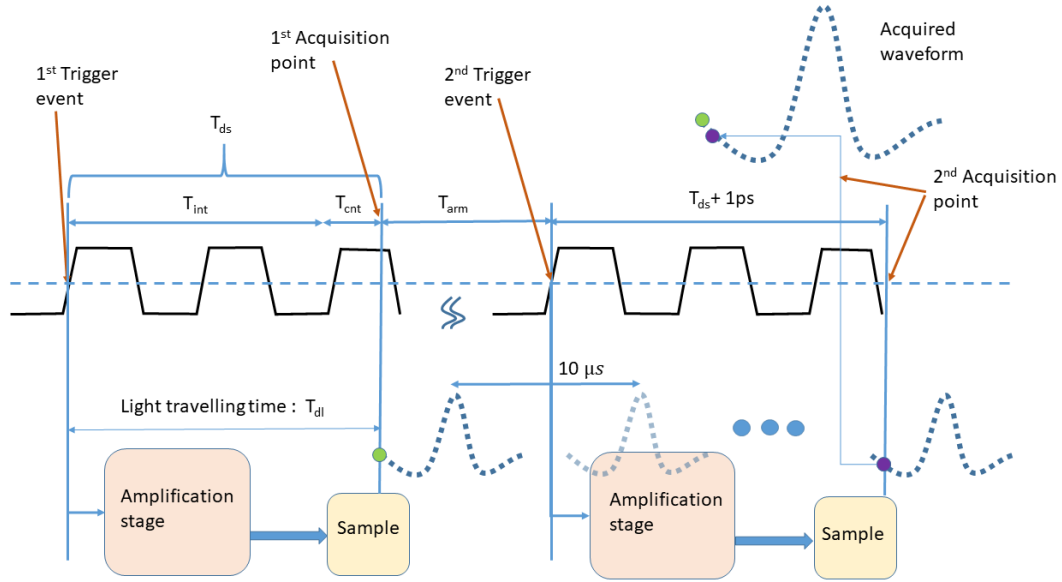
Figure 3.16: **Sampling oscilloscope working principle**. Illustration of a repeating waveform reconstruction for the first two acquisition points.

here is Sapphire/CoFeB(30)/Ta(20)/TaN(15). Thicknesses in parenthesis are in Å.
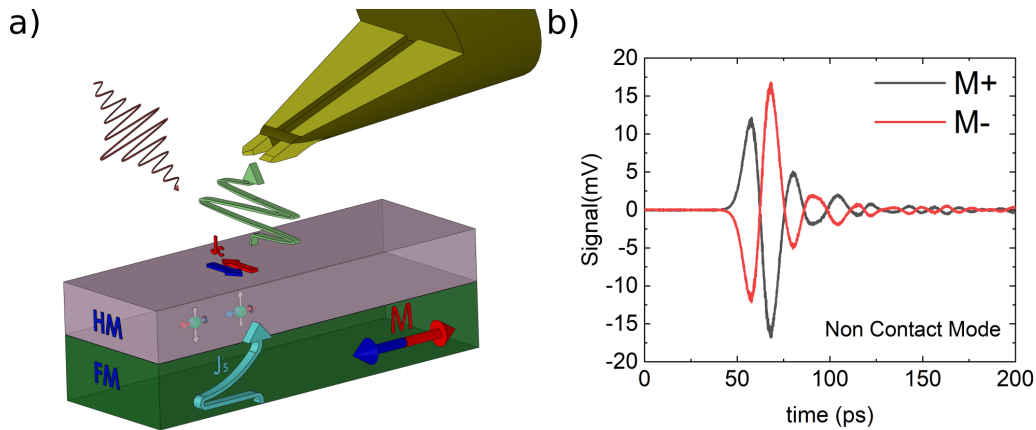
Figure 3.18: **Noncontact Mode (NCM)**. (a) Schematics of the NCM for a typical FM/HM bilayer sample. A laser pulse triggers a spin current oriented from the FM to the HM. The spin up and down electrons, depending of the Magnetization direction, move in opposite directions. The SHE in the HM converts the spin current into a charge current that radiates an electromagnetic wave which is measured by the rf-probe, hovering on top of the sample's surface. (b) time resolved measured signal for two magnetization orientations in the NCM.

Next, we present two detection techniques which involve a probe laser pulse and an electro-optic sampling detection technique[9]. One is used to measure the radiated THz electric field from the sample and the second measured the on-chip THz response.

---

[9]A comparative study between the sampling oscilloscope detection technique and the free space THz electro-optic sampling technique can be found here(189).
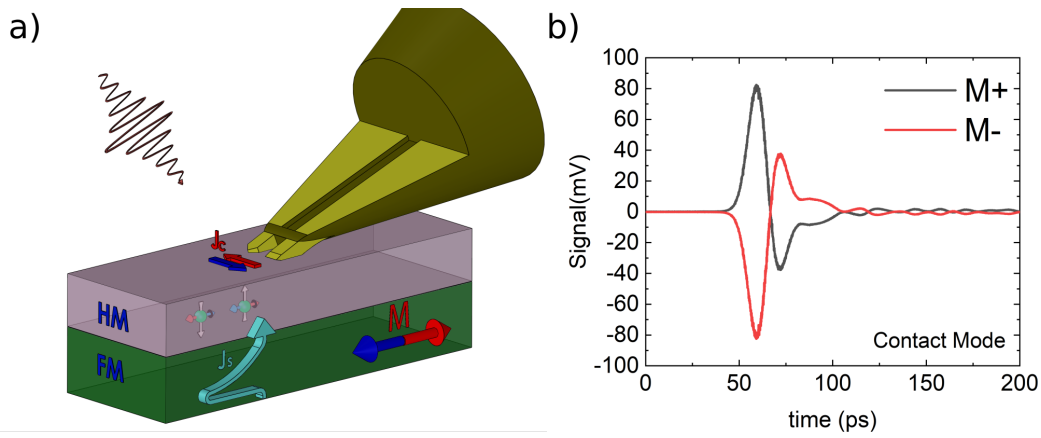
Figure 3.17: **Contact Mode (CM)**. (a) Schematics of the CM for a typical FM/HM bilayer sample. A laser pulse triggers a spin current oriented from the FM to the HM. The spin up and down electrons, depending of the Magnetization direction, move in opposite directions. The SHE in the HM converts the spin current into a charge current $\mathbf{J}_c$ that is measured by the rf-probe, in contact with the sample's surface. (b) time resolved measured signal for two magnetization orientations in the CM.
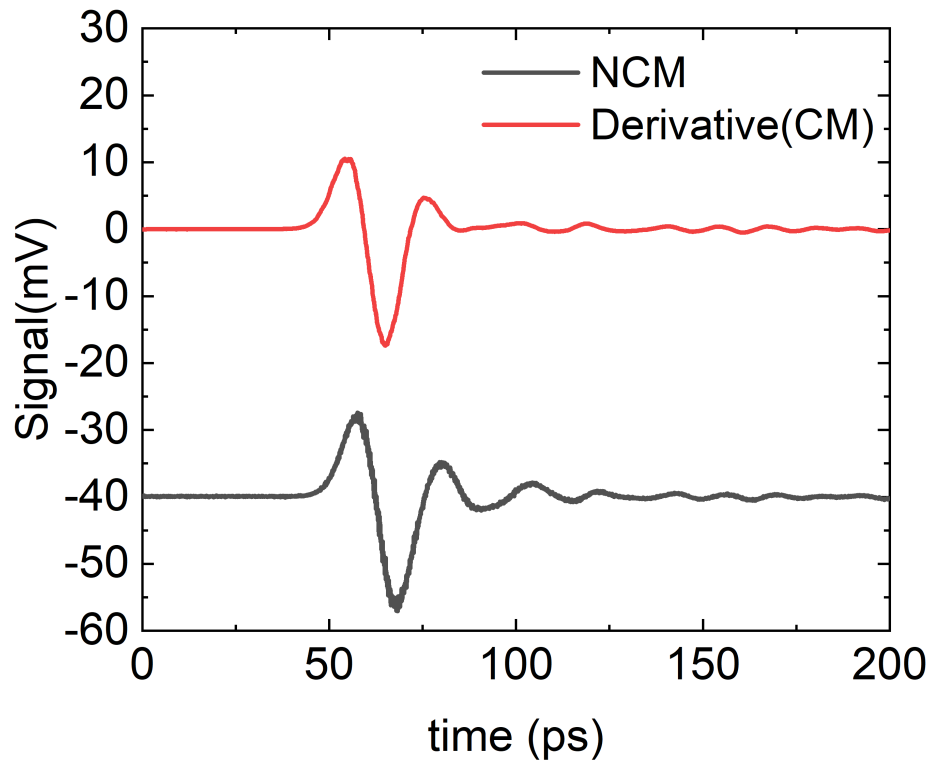
Figure 3.19: Comparison between the first derivative of the signal acquired from the CM and the one from the NCM.

3.3.4 Free space electro-optic sampling detection
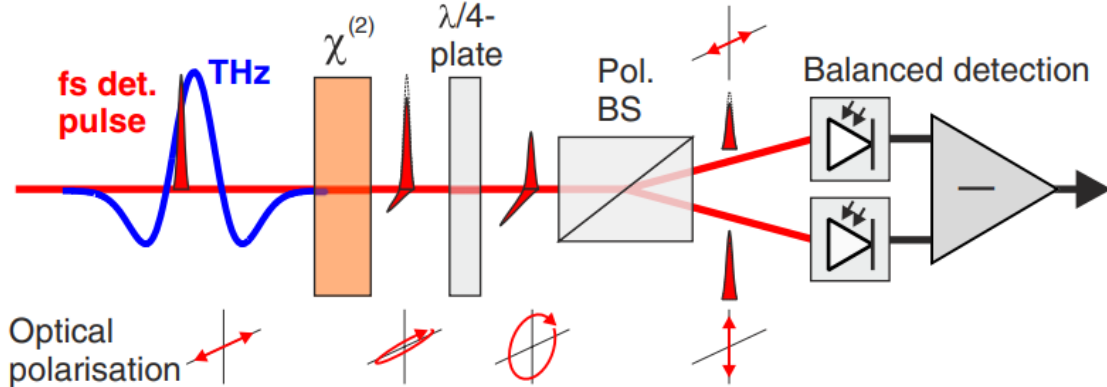
Figure 3.20: **Free space electro-optic time domain sampling detection scheme.** The incident THz transient falls on the nonlinear crystal. Due to the Pockel's effect, the probe pulse polarization is rotated with an amount proportional to the THz electric filed. Polarization optics and balanced photodetection are used to measure the s and p polarizations of the pulse. (Modified from (190)).

The free space detection aims at reconstructing the electric field radiated by the sample. For this matter, materials endowed with the linear electro-optic effect (Pockel's effect)[10] are used(191; 192). This effect denotes the change of the refractive index of the medium linearly with the electric field applied. This applies to certain metrials with broken inversion symmetry. Subjected to a certain electric field $E(t)$, the material develops a birefringence $\Delta n \propto E(t)$. Typical crystals are used such as ZnTe. The linearly polarized probe pulse then interacts with the birefringent medium experiencing an ellipticity change in its polarization. This ellipticity can be detected using a balanced detection scheme where it goes through a $\lambda/4$ plate and a polarizing beam splitter feeding then two beams to two photodetectors. The signal resulting from the subtraction of both detected signals is proportional to the ellipticity, therefore to the birefringence, which leads to the transient electric field of interest. Illustration of the measurement scheme is displayed in Fig. 3.20.

3.3.5 On-chip electro-optic sampling detection

Once the response is generated, subsequent to the laser pulse excitation, the ultrafast current can be guided through a metallic waveguide. One possible design is two have two golden stripes in contact with the two ends of the sample. These contacts extend in a parallel fashion. The transient current would create an electric field between the stripes. In this case, the substrate used is a linear electro-optic effect material with similar properties to the crystals used in the previous detection method. In this case, lithium niobate (LiNbO3) is the substrate of choice. Similar to the free space electro-optic sampling technque, the probe beam hits the region between the stripes and acquires an ellipticity after its propagation through the LiNbO3

---

[10]Such as ZnTe crystal.

substrate. The same detection method is used to access the ellipticity and from there reconstruct the transient electric field.

Chapter 4

Spin injection efficiency in Ferromagnet/heavy metal bilayer and spin transport across MgO

One important goal for the field of spintonics is the manipulation of magnetization through spin currents. For this matter, usually a nanomagnet is interfaced with another non magnetic layer responsible for the spin current(SC) generation through a charge to spin conversion mechanism, such as SHE. The spin current migrates through the bilayer's interface to the ferromagnet where it exerts a torque on the magnetization, thus enabling its switching. Consequently, a hunt for materials enabling larger spin currents is essential for a better performance. Yet, equally important is the transmittivity of the interface. In this Chapter, we show that for a typical transition metal $3d$ ferromagnet(FM) interfaced with a $5d$ heavy metal(HM), the spin injection through the interface can be limited and reduced due to $3d$-$5d$ orbital hybridization effects responsible for significant magnetic moment reduction at the interface. We conjecture that this effect should be present for all heavy metals with less than half filled d shell. Furthermore, we point to the insignificant spin-memory loss in our systems, therefore not needed to account for our results. We also demonstrate that this effect can be eliminated by atomic scale engineering with oxide interlayer(e.g. MgO interlayer). We further confirm the suppression of the spin current transmission after 1nm of MgO interlayer extracting a spin diffusion length of $\sim 2\text{Å}$.

4.1 Motivation

Generating spin currents is paramount for the field of Spintronics and has important technological implications. Indeed, the magnetization of the ferromagnetic element can be manipulated by the action of a torque excerted by individual spin momenta(93; 193; 94; 194). This generates a precession of the magnetization and in some conditions the total switching of the magnetization direction. This effect is present in various sprintronic fields such as magneto-random acess memories (MRAM) technology, displacement of spin textures such as chiral domain walls and skyrmions for racetrack applications(195; 196; 197; 198; 199) as well as spin

torque oscillators(200).

Generally, spin currents can be generated (1) by passing an electrical current through a ferromagnet. This method is usually used in a spin valve geometry where the ferromagnet of interest is interfaced with a non magnetic layer and another ferromagnetic layer that has its magnetization pinned. Indeed, by passing an electrical current through the structure, the electrons become spin polarized in the pinned layer and migrate through the non magnetic element to the ferromagnet of interest called free layer where they transfer their angular momenta to the local magnetization. This is called spin transfer torque. (2) Another method uses a layer with the property to convert charge currents into spin currents. Such materials exhibit a sizeable spin-orbit coupling(SOC) such as in heavy metals where the conversion process due to spin Hall effect(SHE)(201; 202; 82). Additionnally, the conversion process can take place at an interface endowed with SOC. Such a phenomenon is called a Rashba-Edelstein effect. When the spin generator layer is interfaced with the ferromagentic element, the spin current -generated via the Spin Hall effect or Rashba Edelstein effect- exerts a torque on the magnetization called spin orbit torque owing to its spin-orbit coupling origin.

Reciprocally, spins can be pumped from the FM into the HM where the SC is converted to a charge current via the inverse SHE (ISHE). This approach may be demonstrated via microwave induced precession of the magnetization(202; 203) or via ultrafast optical excitation(204; 5). The latter example is the basis of ultrabroadband and efficient terahertz (THz) emitters(5; 205; 189). To maximize the SC generation, the focus has been on the search for materials with a large spin to charge conversion property. For spin Hall materials, such a quantity is defined as the spin Hall angle and quantifies this conversion or equivalently the spin Hall conductivity for a given electrical conductivity of the material itself. Intense research has been carried out to maximize the former and minimize the latter.
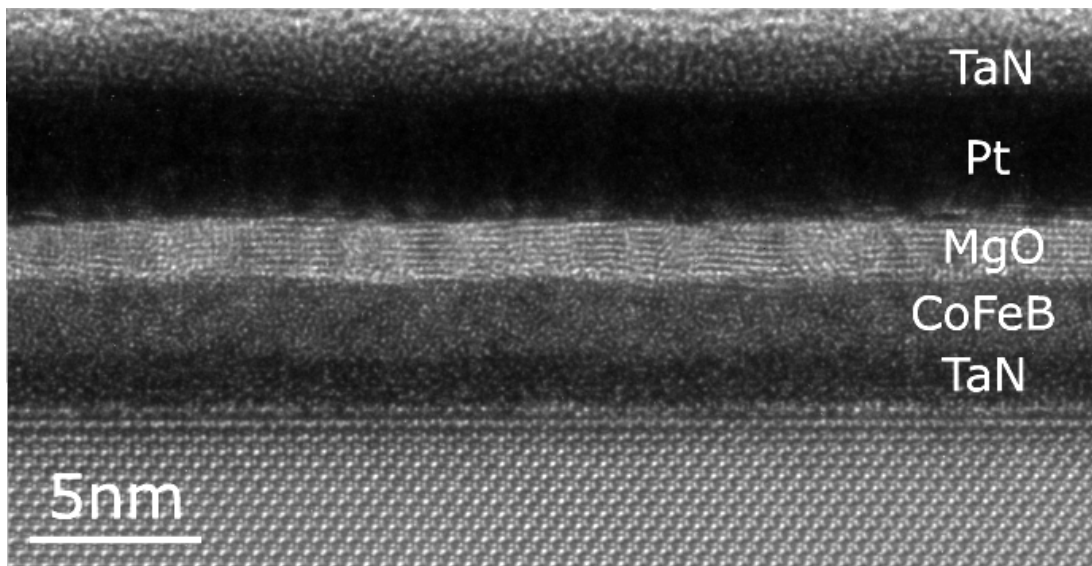

Figure 4.1: Transmission electron microscopy micrograph acquired at FEI TITAN 80-300 electron microscope showing the layered structure with Pt as a heavy metal and the MgO interlayer in its cubic phase with (001) orientation. From bottom to top: TaN(1.5), CoFeB(2), MgO(1.7), Pt(4), TaN(1.5). All thicknesses are in nm.

Equally important, the interface between the spin current source and the ferromagnet can potentially hinder significantly the transmission of the spin current. Electronic transparency (206)of the interface towards spin channels is of fundamental importance. Moreover, the spin degree of freedom is not conserved and can be subjected to spin mixing at the interface, therefore assigning it a quantity called the spin mixing conductance. This quantity has been used widely in ferromagnetic resonance spin pumping experiments to quantify the spin transparency of the interface(207). Additionally, it has been reported that interfaces can host phenomena responsible for the loss of the spin momentum and reports date from magneto-resistance measurements(208; 209). This effect is referred to as spin-memory loss (SML)(210; 211; 212; 213) and is responsible for limited spin current transmission through the interface. The origin of SML is still debatable, nonetheless, it has been claimed to depend of interfacial SOC(214; 215; 216; 213; 217), disorder(210; 218), lattice mismatch(210) and non collinear magnetization at the interface. In this regard, models have been developped where the interface is accounted for as a bulk material with its own spin resistance and spin diffusion length. Based on this phenomenological model, SML has been employed systematically to account for the discrepancies between different spin Hall angle measurements.

In this chapter, by utilizing two spin injection techniques, we are able to clearly disserrate the total amount of the spin current that gets generated compared to the spin current that gets converted in the heavy metal material via the ISHE. We demonstrate that depending on the heavy metal (whether Pt or Ta), the spin injection efficiency is unaltered in the first case and heavily reduced in the second. Ab-initio density functional theory combined with spin transport calculations demonstrate that due to $3d$-$5d$ orbital hybridization effects, the magnetic moment at the interface is significantly reduced when Ta is used as a heavy metal, thus limiting the spin polarization and consequently its transmission. This effect can be eliminated with the addition of atomic scale thin MgO interlayers. We further demonstrate that a small/inexistance SML is present in our systems and therefore is not needed to explain our results. Indeed, the spin interface transparency accounts totally for all spin conserving relevant parameters rendering it the figure of merit for quantifying the efficiency of the spin current transmission.

4.2   Samples

The ferromagnet of choice is $Co_{20}Fe_{60}B_{20}$(CoFeB). Two heavy metals, Pt and Ta, are considered. All the films are prepared on sapphire substrates using magnetron sputtering. The structure of the films is TaN(15)/CoFeB(20)/ MgO(t)/ Pt(40)/TaN(15) and TaN(15)/CoFeB(20)/ MgO(t)/Ta(30)/TaN(15) where t varies between 0 and 17Å. The thicknesses displayed in parenthesis are in Å. All the layers except for MgO have been grown using DC magnetron sputtering. For the MgO layer, rf sputtering is employed and an Off axis gun is used to facilitate the crystallinity of the layer on top of the CoFeB and eliminate the excess of the oxygen ions. A transmission electron micrograph of CoFeB/MgO(17Å)/Pt can be seen in Fig. 4.1, confirming the (001) orientation of the MgO crystal structure. Atomic Force Microscopy is carried out on all samples and the measured root mean square(rms) value of the roughness is less that 2Å. AFM graphs are provided in Fig. 4.2 and Fig. 4.3 for both Pt and Ta series respectively. Sheet resistance measurements using four point probe are performed on all samples and results are
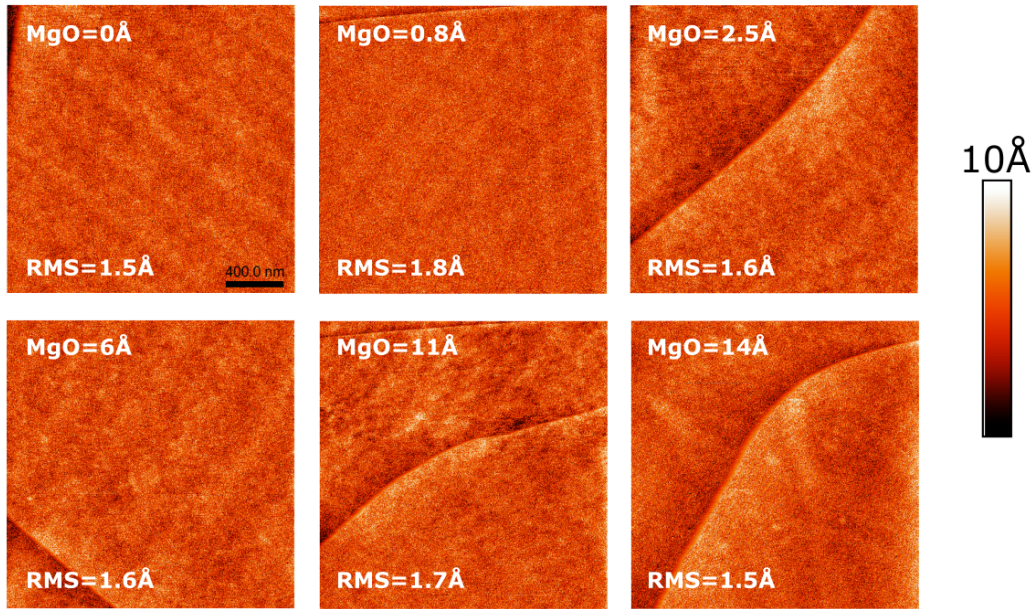
Figure 4.2: Atomic Force Microscopy scans of $2 \times 2\mu m^2$ areas the CoFeB/MgO/Pt samples for various MgO thicknesses. The root mean square roughness (RMS) is displayed for every micrograph.
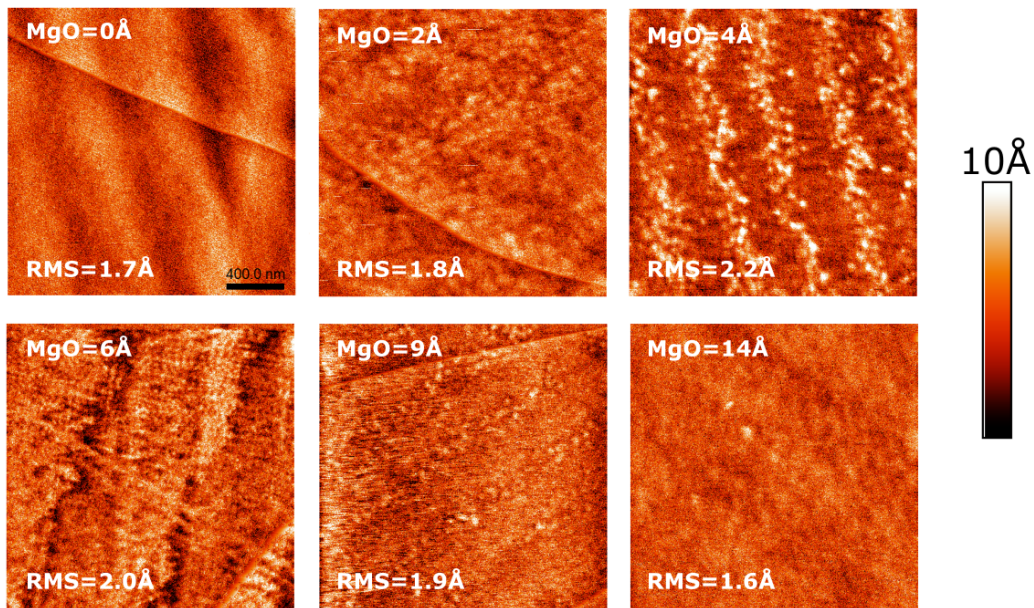
Figure 4.3: Atomic Force Microscopy scans of $2 \times 2\mu m^2$ areas the CoFeB/MgO/Ta samples for various MgO thicknesses. The root mean square roughness (RMS) is displayed for every micrograph.

shown in Fig. 4.4. Additionally, all samples display an in-plane magnetic anisotropy which is required for the experiments.
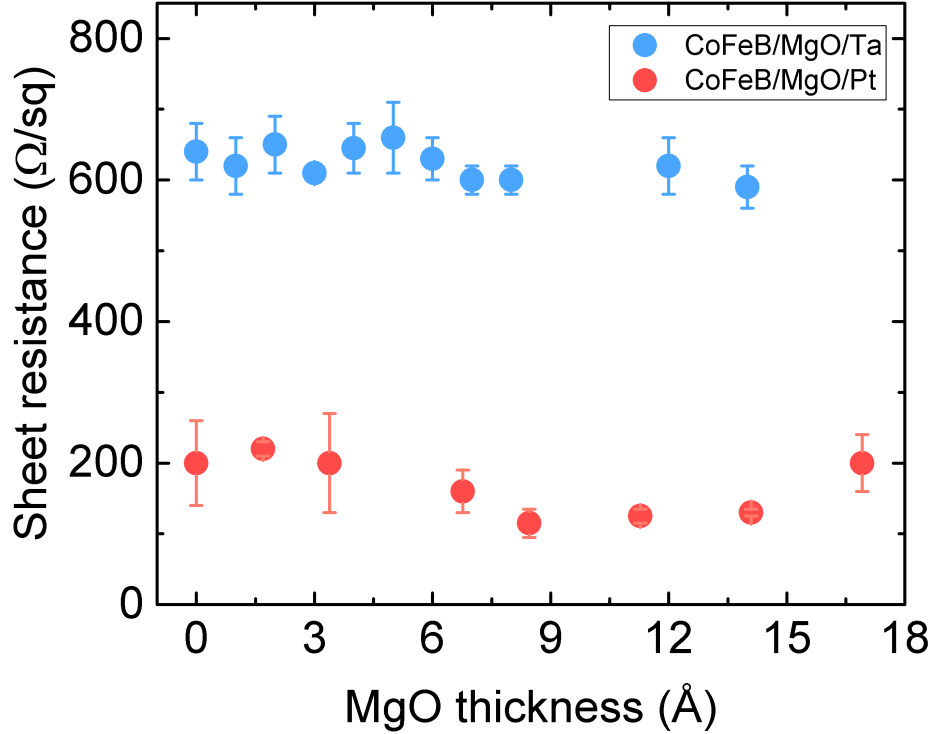
Figure 4.4: MgO thickness dependence of the sheet resistivity, measured with a 4 point probe method, for CoFeB/MgO/Ta and CoFeB/MgO/Pt.

4.3 Ultrafast optical spin injection

At first, we consider an ultrafast spin injection by utilizing femtosecond laser pulses. The laser pulse illuminates the whole film structure. The electronic temperature of ferromagnet is heated and non thermal hot electrons are generated which thermalize the in the sub picosecond regime(around 100fs). The majority electrons are excited to higher energy states where they earn an sp-orbital character responsible for more mobility than the minority counterpart which are less mobile due to their d orbital character. This asymmetry in electron's velocities leads to a superdiffusive spin current(4). This spin current pulse is directed towards the heavy metal where it gets converted via the inverse Spin Hall effect into a transient charge current. More details about this process are found in Section 2.4.2. This ultrafast charge current radiates an electric field with dynamics confined to the subpicosecond regime and its Fourier spectrum extends to the THz regime (up to 40 THz)(5). Usually, electro-optic sampling is used to access the real time signal with a a sufficiently high time resolution down to a few tens of femtosecond. Details on this detection technique are found in Section 3.3.4. In our experiment, we access the sub-THz current on the sample with an rf tip connected to a fast sampling oscilloscope limited to 50 GHz bandwidth. Details of the setup and its functionalities are explained in Section 3.3.3.

The laser photon energy is equal to 1.1eV and the laser fluence is set to around $0.5 \, \mathrm{mJ/cm^2}$.
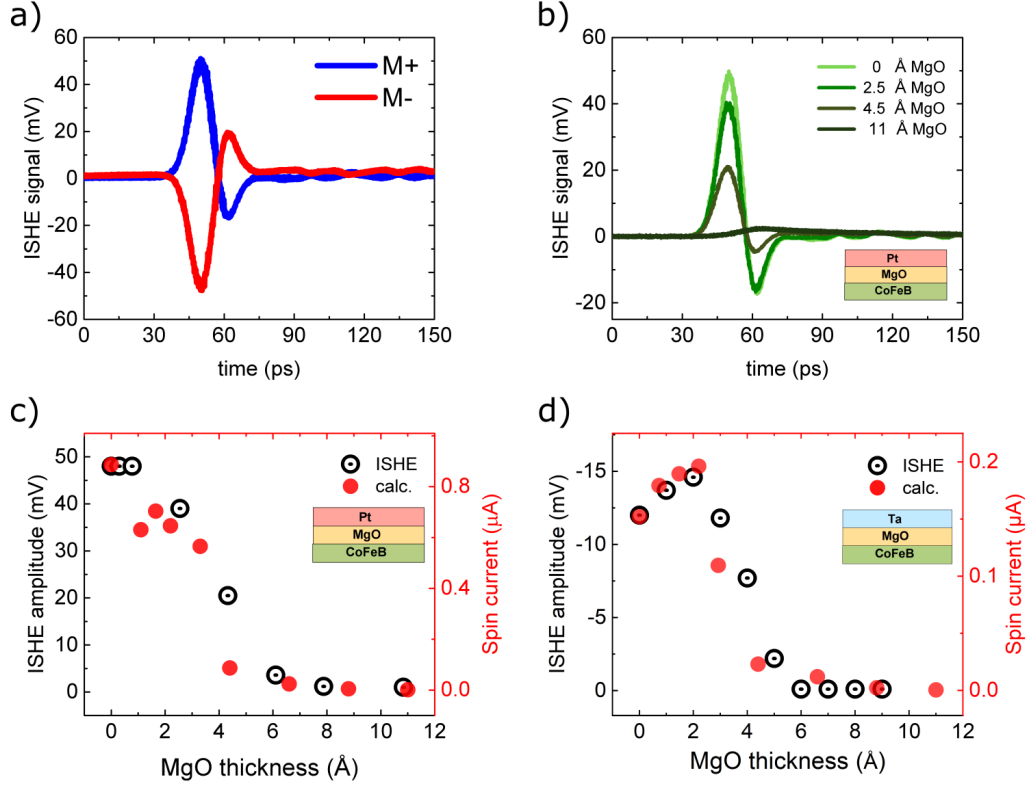
Figure 4.5: **Ultrafast ISHE measurements.** (a) Time-resolved ISHE signal for opposite magnetization directions. (b) Time-resolved ISHE signal for the HM=Pt sample with different MgO thicknesses ranging from 0 to 17Å.(c),(d) MgO-thickness dependence of the ISHE signal amplitude and the calculated spin-current transmission per unit cell for HM=Pt and HM=Ta, respectively. Note that for HM=Ta, the ISHE signal has negative values due to the negative sign of the spin Hall angle of Ta.

An external magnetic field with a value around 50mT is applied to saturate the magnetic film in plane. In Fig. 4.5(a), we show a typical time dependent signal response for both opposite magnetic field directions. As can be seen, the waveforms are symmetrical confirming their magnetic origin. From here on, the difference signal is considered, since it filters all non magnetic related components.

Next, we examine the behaviour of the signal with the insertion of MgO. In Fig. 4.5(b), we show the ISHE signals for various MgO thicknesses for the case of the 'P' batch. The signal is decreasing gradually with increasing MgO thickness. The peak value is taken as the ISHE signal amplitude. In Fig. 4.5(c) and (d), we show the MgO thickness dependence of the ISHE signal amplitude for both heavy metals. In the case of HM=Pt, the signal exhibits a small plateau (extending according to the fit to almost one effective thickness of one monolayer(ML) of MgO) and then the signal decreases, vanishing after ~8Å of MgO thickness, with a decay length of ~2Å according to the exponential fit. We note that free space THz field detection has been performed and results are shown in Fig. 4.6. Both techniques show the same behaviour of the MgO thickness dependence of the signal amplitude. The same experiment is repeated for the case Hm=Ta. In contrast to the case HM=Pt, the ISHE signal amplitude is enhanced
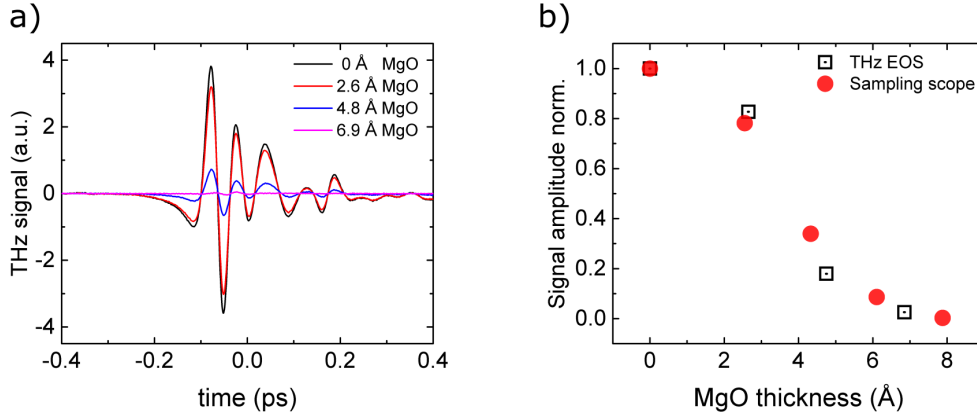
Figure 4.6: (a) Time resolved THz signals measured on CoFeB(20Å)/MgO/Pt(20Å) for different MgO thicknesses. (b) MgO thickness dependence of the root mean square value of the free space electro-optic sampling THz signals in comparison with the fast sampling scope technique used in our study for CoFeB/MgO/Pt.
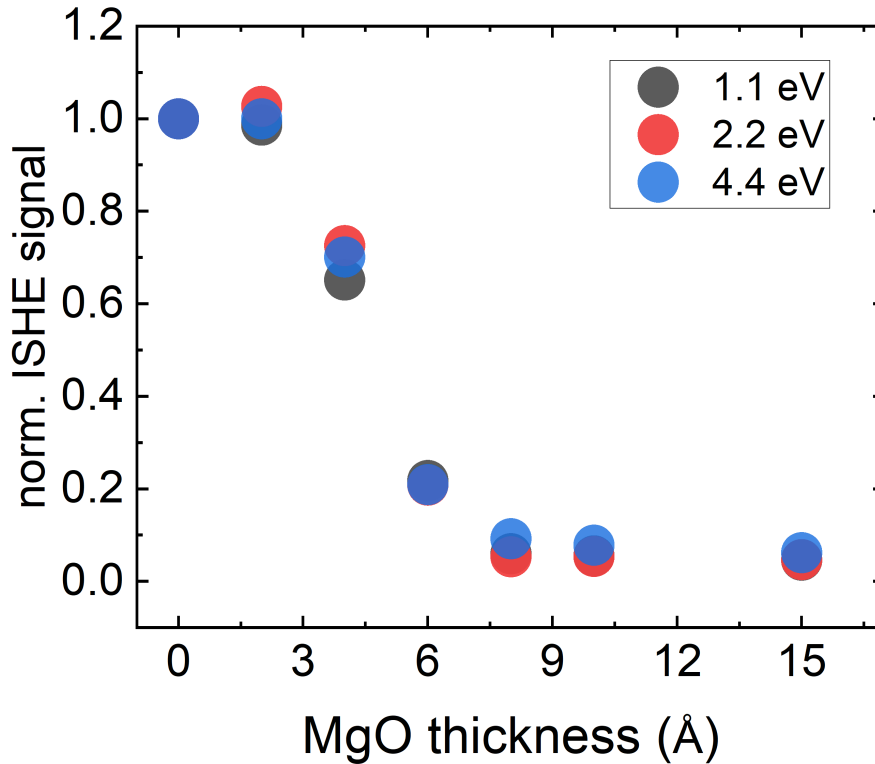
Figure 4.7: MgO thickness dependence of the normalized ISHE signal for various photon energies: 1.1eV, 2.2eV and 4.4eV.

by ~20% with a maximum at around 2Å of MgO and followed by a similar decay as for the case of HM=Pt. Note that in this case case, the signal has a negative value, i.e. opposite sign compared to the one of Pt. This is due to the negative sign of the spin Hall angle of Ta which

confirms the spin Hall origin of the signal.

Moreover, the same experiments for the case of HM=Pt are repeated with different photon energies of 2.2 and 4.4 eV with comparable laser fluences. The results are shown in Fig. 4.7. No noticeable difference is found for the MgO thickness dependence of the ISHE signal for the different photon energies.

4.4   Theoretical calculations
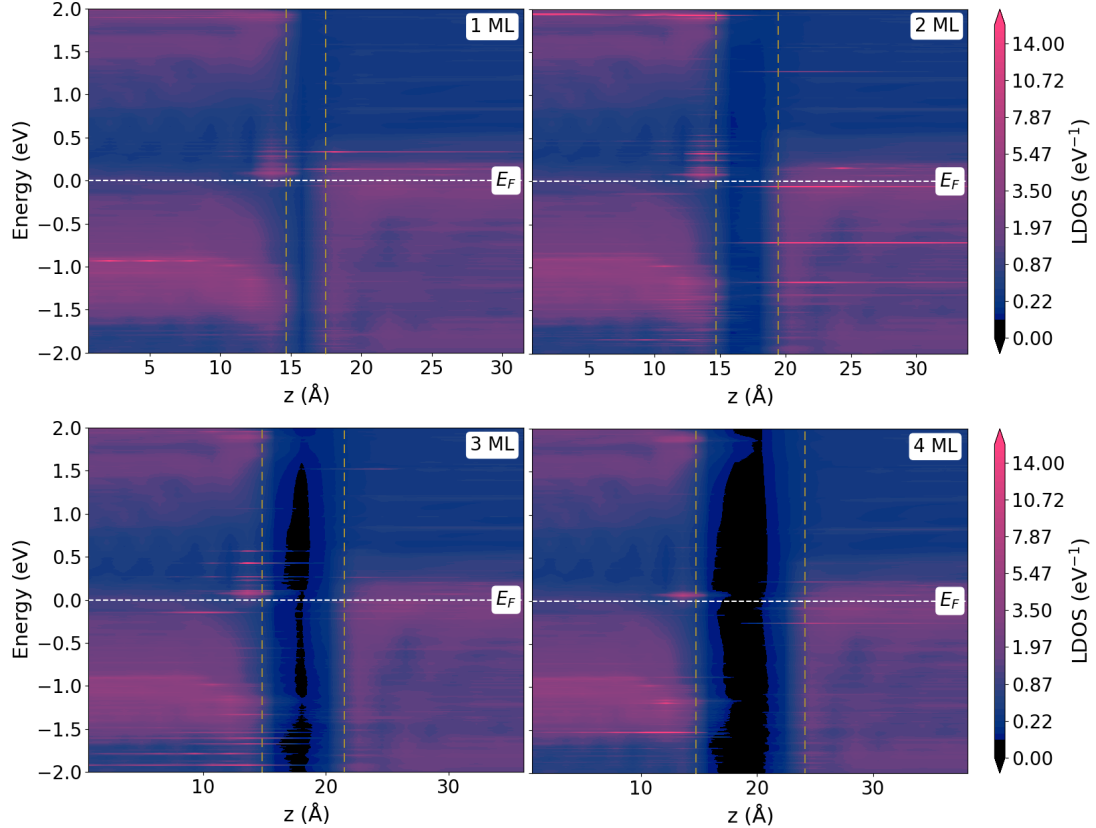
Figure 4.8: The zero-bias projected local density of states (LDOS) of the Fe/MgO/Ta junction for different monolayers of MgO barrier. The horizontal white dashed lines indicate the Fermi level. The vertical dashed lines denote the interface between Fe(left), MgO(middle) and Ta(right).

Ab initio calculation based on density functional theory have been performed and fed to transport calculations based on the Landauer Buttiker formalism[1]. To model our system, we use interface builder in the QuantumATK package to construct a common unit cell for Fe/MgO/HM trilayers. The MgO matches well the bcc Fe in its (001) orientation where the oxygen atoms face directly the Fe atoms. We consider HM=Pt and HM=Ta. For the case of Pt, we consider it in its body centered tetragonal structure giving a mismatch of 3% with bcc Fe. As for the case of Ta, We build a 1×3 supercell of Ta (110) in its body centered cubic phase. The MgO has been varied until 6MLs and to account for effective thicknesses less than one ML,

[1]Calculations have been performed by Dr. Ersoy Şaşıoğlu.
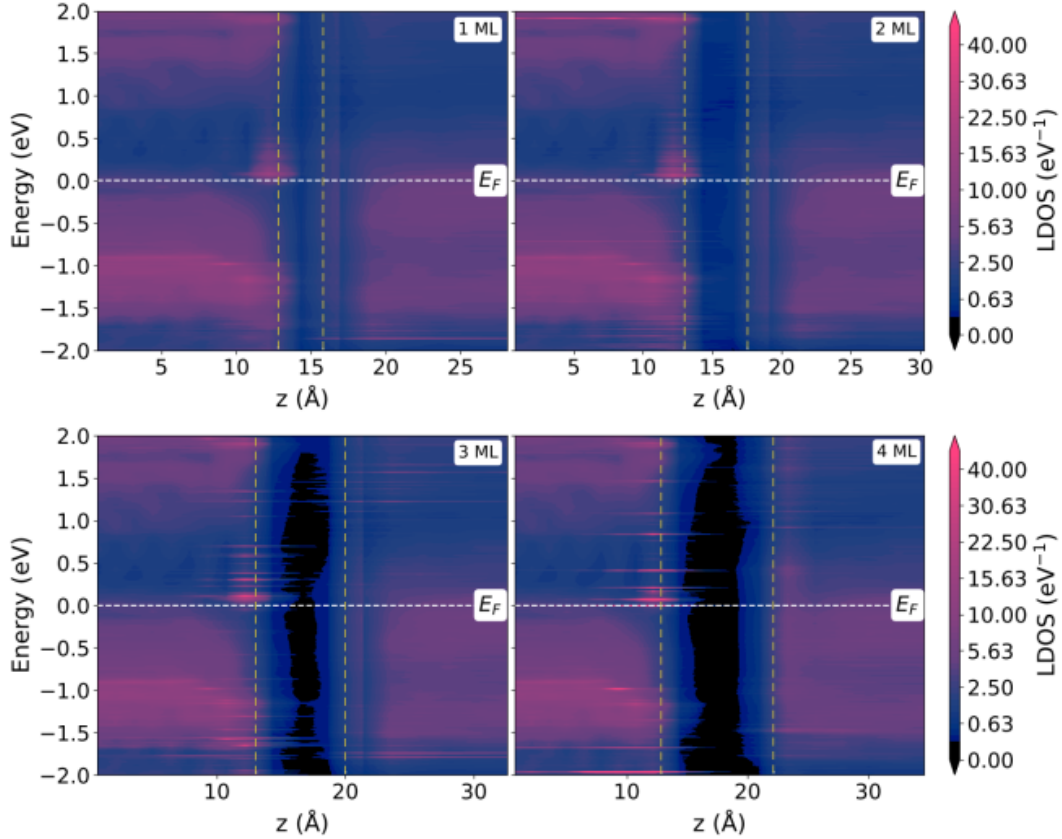
Figure 4.9: The zero-bias projected local density of states (LDOS) of the Fe/MgO/Pt junction for different monolayers of MgO barrier. The horizontal white dashed lines indicate the Fermi level. The vertical dashed lines denote the interface between Fe(left), MgO(middle) and Pt(right).

we consider intermixing between the first Fe and HM ML at the interface and MgO. A sketch of the device structure with 4 ML of MgO and Ta as a HM is shown in supplementary Fig. 4.10(a). Ground-state electronic structure calculations are carried out using DFT, implemented in the QuantumATK R-2020.09 package (219) with Perdew-Burke-Ernzerhof (PBE) parametrization of the generalized gradient approximation for the exchange-correlation (XC) functional (220). We use PseudoDojo pseudopotentials (221) and LCAO basis sets. A dense $20 \times 20 \times 1$ ($20 \times 7 \times 1$) **k**-point grid for Pt case (Ta case) and a density mesh cut-off of 120 hartree are used. The total energy and forces converge to at least 1×10^{-4} eV and 0.01 eV/ Å, respectively. The transport calculations are carried out using DFT combined with the nonequilibrium Green's function method (NEGF). We use a $20 \times 20 \times 172$ ($20 \times 7 \times 172$) **k**-point grid for Pt and Ta case in self-consistent DFT-NEGF calculations. The current is calculated within a Landauer approach [57], where $I(V) = \frac{2e}{h} \sum_\sigma \int T^\sigma(E,V) \left[f_L(E,V) - f_R(E,V)\right] \mathrm{d}E$. Here V denotes the bias voltage, $T^\sigma(E,V)$ is the spin-dependent transmission coefficient for an electron with spin σ and $f_L(E,V)$ and $f_R(E,V)$ are the Fermi-Dirac distributions for the left and right leads which translates here to FM and HM, respectively. We assume that the electronic system is thermalized and thus temperature effects on transport properties can be taken into account via the Fermi-Dirac distribution function. The transmission coefficient $T^\sigma(E,V)$ is calculated
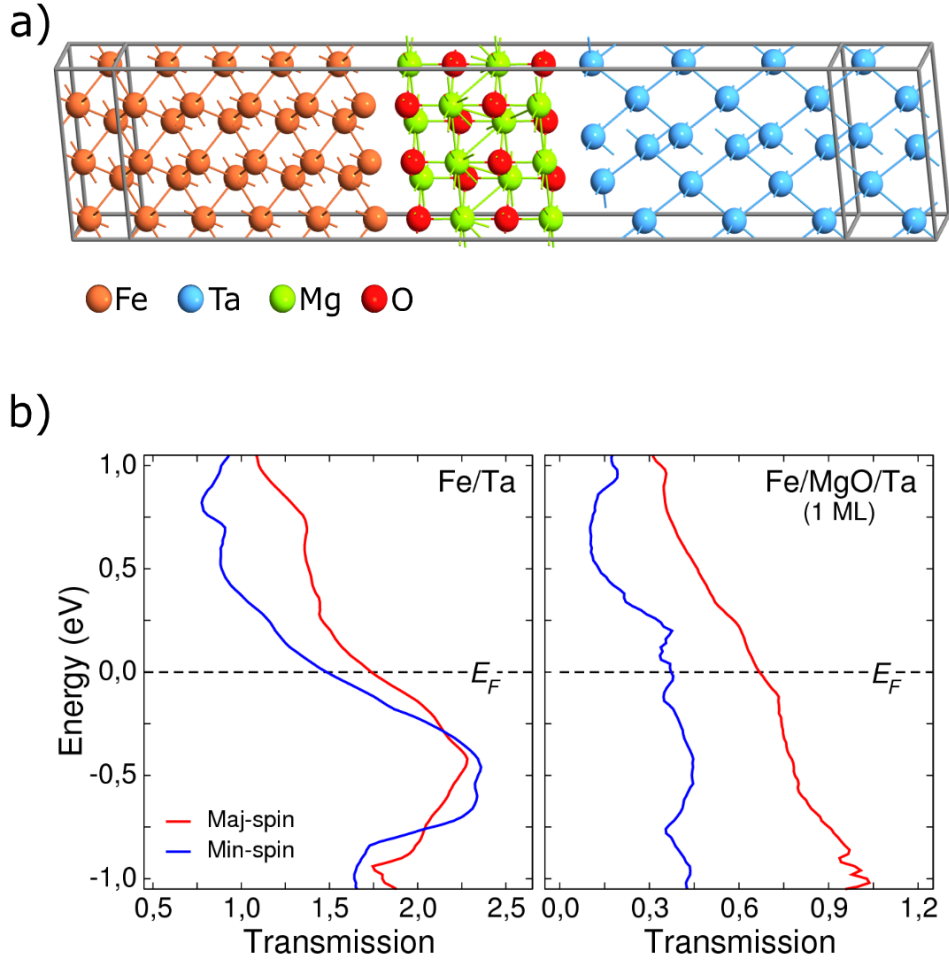
Figure 4.10: (a) The atomic structure of the Fe/MgO/Ta junction. (b) Spin-resolved transmission spectra for Fe/Ta and Fe/MgO/Ta junctions with one monolayer of MgO. Inset: voltage bias dependence of the ratio of the spin current transmission for Fe/MgO(1ML)/Ta compared to Fe/Ta

using a 100×100 (100×34) **k**-point grid for the Pt and Ta cases.

In order to reveal the mechanism responsible for the enhanced ISHE signal in samples with MgO interlayer and HM =Ta, ab-initio transport calculations are combined with density functional theory (DFT). Fig. 4.5(c) and (d) show the calculated MgO thickness dependence of the SC for a small bias voltage of 50~mV. Clearly, for both Pt and Ta as HM the calculated SC well reproduces well the corresponding experimental ISHE data. For the case of Pt, the spin current decreases monotonously with the MgO thickness after showing a plateau behavior up to 2Å. By contrast when Ta is used as HM, one first finds an increase of the SC for 1 ML of MgO followed by a rapid decay matching well the experimental results.

To understand the origin of the overall rapid decay of the SC with MgO thickness, we consider the projected local density of states (LDOS) for both systems, where the thickness t of MgO barrier varies from 1 ML to 4 MLs. The results are shown in Fig. 4.8 and Fig. 4.9 for both HM=Pt and HM=Ta respectively. Interestingly, the MgO layer is actually metallic for

73

a thickness of up to 2 MLs and only starts opening a band gap for thicknesses larger than 3 ML. With increasing MgO barrier thickness the transport mechanism changes gradually from a metallic transport to a tunneling behavior and thus, as expected the SC drops exponentially with a decay length close to 2Å as shown in Fig. 4.5(c) and (d).

Fig. 4.10(b) shows the spin- and energy-dependent transmission spectrum for the case of Fe/Ta and Fe/MgO(1ML)/Ta. One finds that around the Fermi level the transmission is reduced by more than 50% for both spin channels when 1 ML of MgO is inserted at the Fe/Ta interface. However, this reduction is larger for the spin-down channel (minority-spin), which leads to an enhancement of the overall SC, i.e., the absolute value of the $T^{\uparrow} - T^{\downarrow}$ at the Fermi level for Fe/MgO(1ML)/Ta is about 30% larger than the corresponding value in Fe/Ta case (see Fig. 4.10(b)). This enhancement of the SC is linked to the recovery the magnetic moment of Fe(Co) and hence the spin polarization at the Fe/Ta (CoFeB/Ta) interface.

4.5   Magnetic moment reduction at the interface

	Fe(B)	Fe/Ta		Fe/MgO/Ta		Fe/Pt		Fe/MgO/Pt	
		Fe	Ta	Fe	Ta	Fe	Pt	Fe	Pt
Magnetic moment(μ_B)	2.3	0.80	-0.16	2.92	-0.002	2.92	0.2	2.89	-0.06
		0.57	-0.22	2.92	-0.03				
		1.13	-0.21	2.91	-0.03				

Table 4.1: Calculated magnetic moments for interfacial and bulk(B) layers in Fe/HM with and without one ML of MgO. For the case of Ta as a heavy metal, three atoms per layer are considered.

It is known that when elementary 3d ferromagnets are interfaced with transition metals with less than half filled 5d shell such as Hf, Ta, or W the magnetic moment at the interface is reduced (222). In some cases (e.g. $Ni_{81}Fe_{19}$) this effect can even give rise to formation of a magnetically dead layer (223). This suppression of the magnetic moment can be qualitatively explained on the basis of the Stoner model by considering the density of states at the Fermi level $N(E_F)$ (see Fig. 4.11 and Fig. 4.13(a)) and the Stoner parameter.
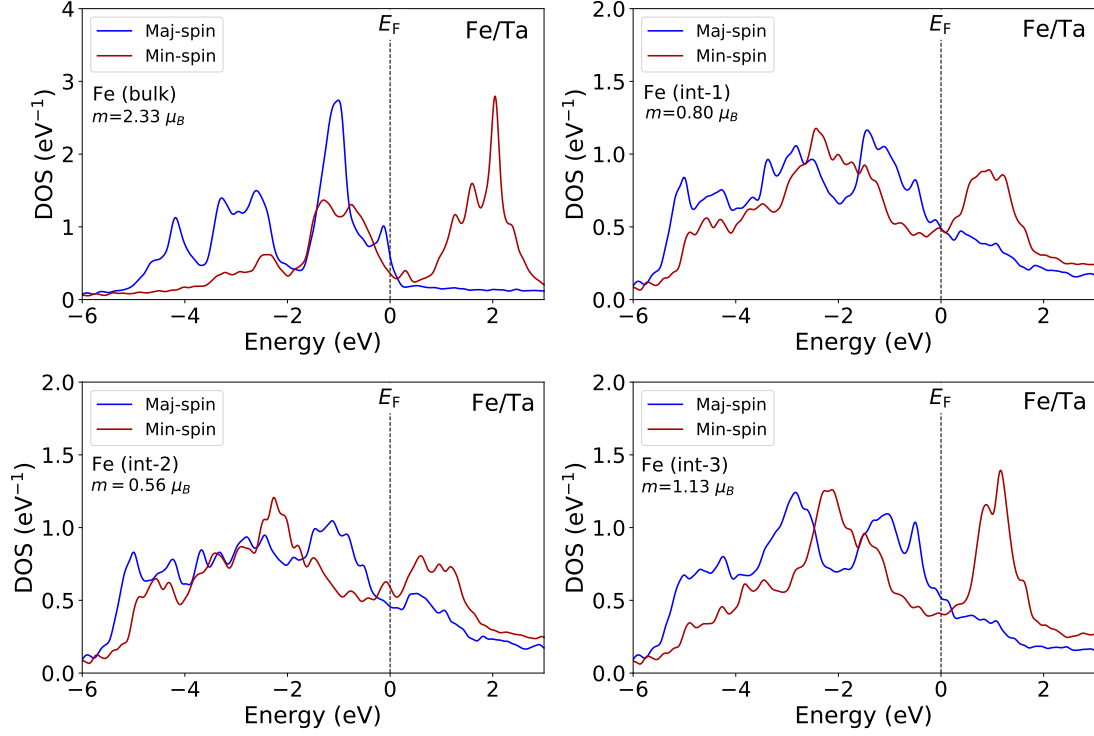
Figure 4.11: DOS for majority and minority spin for bulk Fe and the three different interfacial Fe atoms at Fe/Ta interface. The magnetic moment is shown for all cases.
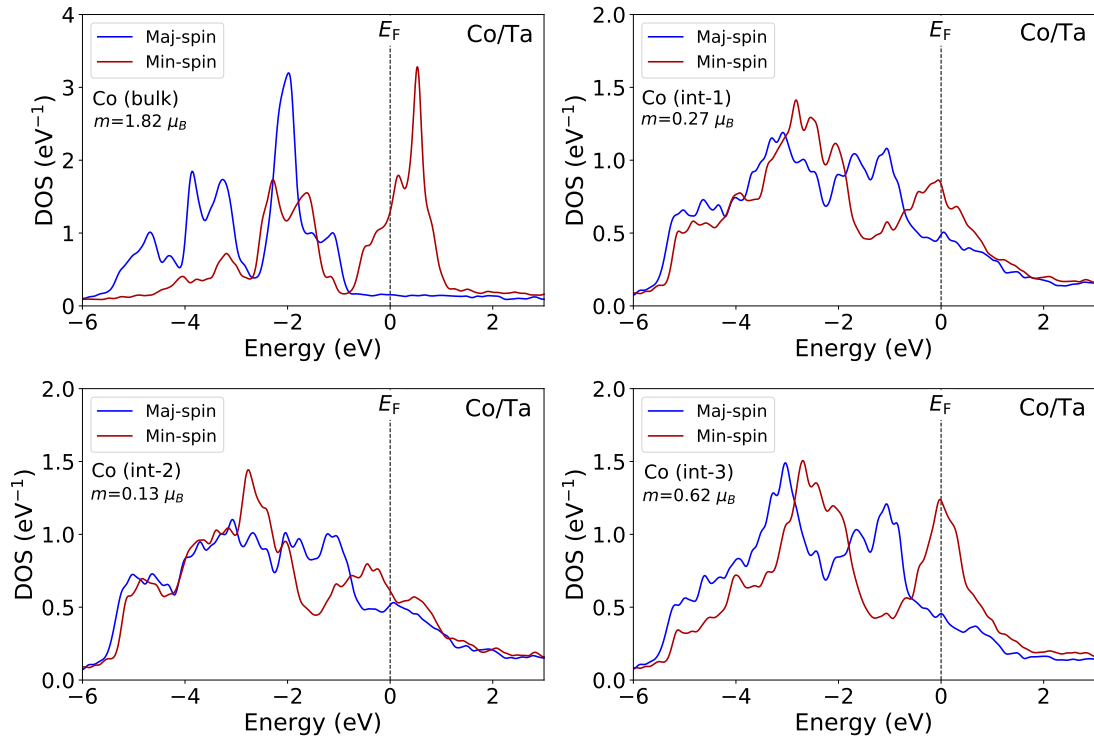
Figure 4.12: DOS for majority and minority spin for bulk Co and the three different interfacial Co atoms at Co/Ta interface. The magnetic moment is shown for all cases.
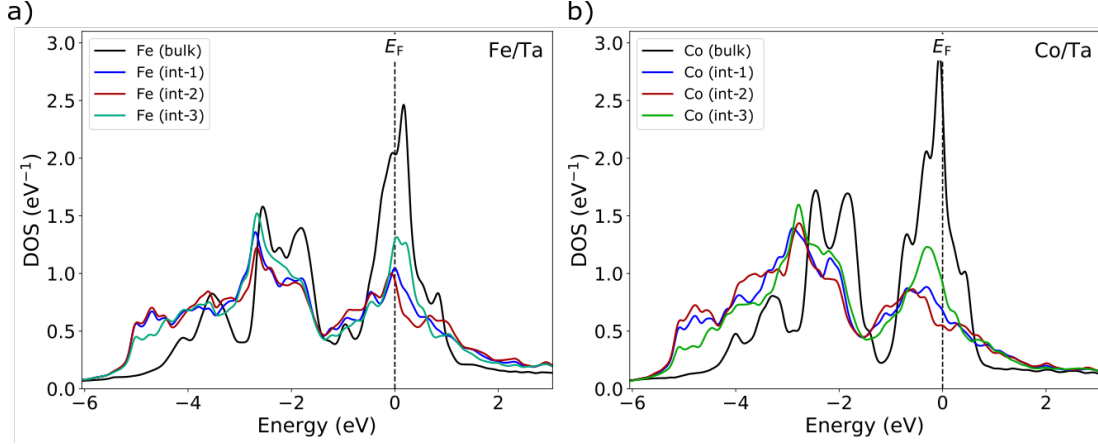
Figure 4.13: Non magnetic DOS for bulk Fe, the three interfacial Fe atoms at Fe/Ta interface, bulk Co and the three interfacial Co atoms at Co/Ta interface.
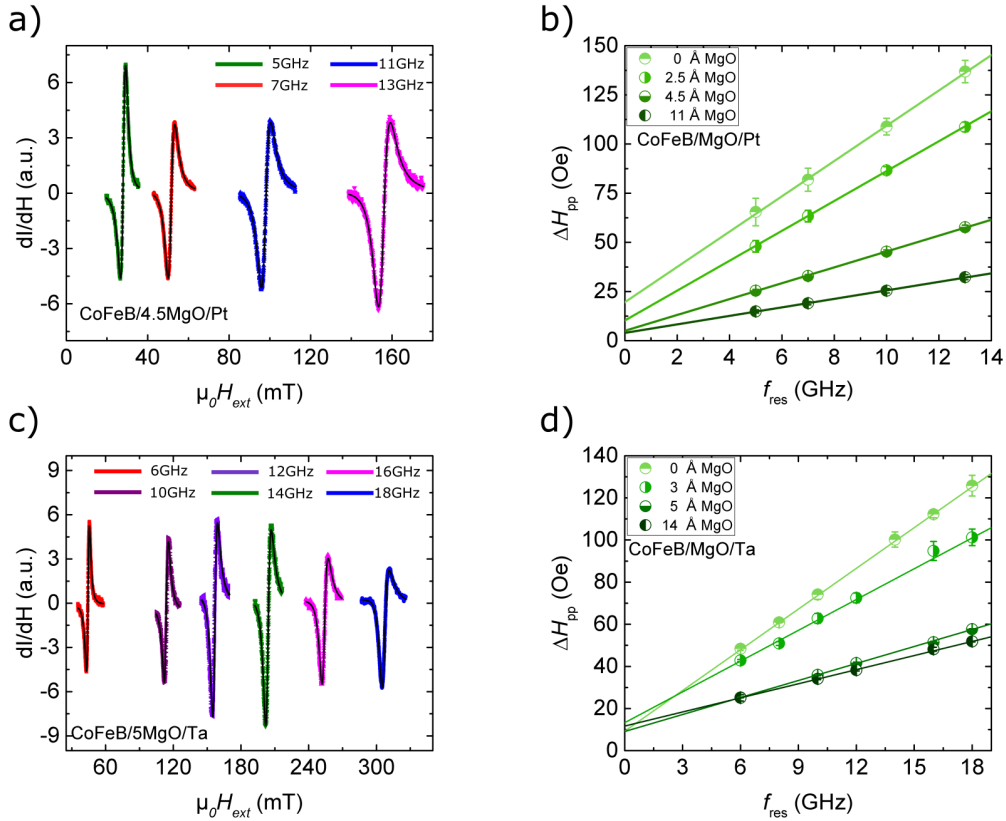
Figure 4.14: (a) and (c) Magnetic field dependence of the absorption spectra at the ferromagnetic resonance for various rf excitation frequencies for CoFeB/4.5MgO/Pt and CoFeB/5MgO/Ta respectively. (b) and (d) Frequency dependence of the ferromagnetic resonance linewidth for CoFeB/MgO/Pt and CoFeB/MgO/Ta respectively with various MgO thicknesses.

Due to extended $5d$ orbitals of the early transition metals the strong Fe($3d$)-Ta($5d$) hybridization at the interface transfers the Fe-$3d$ weight around the Fermi level to lower energies

and thus $N(E_F)$ is substantially reduced. Therefore, the Stoner criterion for the Fe atoms at the interface is hardly satisfied. Note, that for simplicity only Fe atoms are considered in the calculations. However, we want to point out that for Co atoms at the interface the reduction of $N(E_F)$ is even larger than for the Fe case as illustrated in Fig. 4.12 and Fig. 4.13(b). Thus the Co magnetic moments at the interface with Ta are also strongly suppressed. As one moves from the left to the right within the row of Elements in the Periodic Table, the nuclear charge of the HM increases causing the d-wave functions to contract. This reduces the hybridization between Fe($3d$)-Pt($5d$) orbitals and causes an enhancement of the Fe magnetic moments at the Fe/Pt interface.

The calculated DFT values of interface magnetic moments are presented in Table 4.1 and show that the spin magnetic moment of the Fe atoms at the interface layer are reduced to an average value of $0.8\mu_B$, which only corresponds to 30% of the Fe bulk magnetic moment. The reduced spin polarization at the interface layer also leads to a reduced spin current transmission. Interestingly, the insertion of 1 ML MgO at Fe/Ta junction causes the recovery of magnetic moment of Fe at the interface, resulting in an enhancement of the spin dependent transmission and SC in agreement with experimental data.

4.6   Spin pumping via ferromagnetic resonance
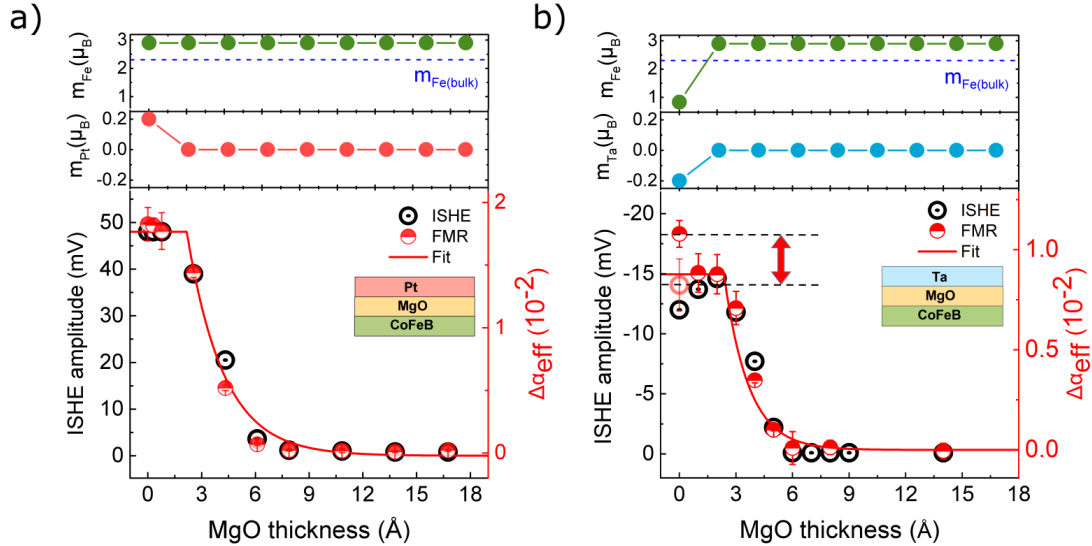
Figure 4.15:   **ISHE signals, enhanced damping and interface magnetic moments**. MgO-thickness dependence of the ISHE signal amplitude and the enhanced damping due to spin pumping for (a) HM=Pt and (b) HM=Ta. The top panels of (a) and (b) show the calculated magnetic moment per atom at the interface for (a) Fe and Pt and (b) Fe and Ta. The red open circle in panel (b) represents the corrected enhanced damping by considering the reduced magnetic moment as determined by the VSM measurement. The red fit is a function of a plateau up to 2.2 ± 0.1 Å followed by an exponential decay with a decay length of 2 ± 0.2 Å.

Here we consider spin pumping from the ferromagnet by ferromagnetic resonance technique. For this, the samples are placed on top of a coplanar waveguide enabling a microwave excitation.

For each frequency of the microwave, the external in plane magnetic field is swept and the total microwave absorption is registered at the ferromagnetic resonance. The additional damping caused by the MgO/HM capping layers due to spin pumping can be extracted (see Fig. 4.14). More details about the technique are found in Section 3.2. This effect is sensitive to the total spin current emitted by the ferromagnet, while the electrically measured ISHE signal is only sensitive to the fraction of the spin current pumped into the HM layer.

We emphasize here that, despite the difference in the excitation energies between the two techniques, the relevant electronic transport occurs in a small energy window close to the Fermi level. It has been recently demonstrated that ultrafast laser excitation leads to a generalized spin voltage driving the spin current(224). This notion is supported by measurements where the spin current does not depend on the photon energy from 0.8 to 1.5 eV(225). Here, we extend this range by showing results between 1.1 and 4.4 eV (see Fig. 4.7). We find no notable difference of the ISHE signal for the three different photon energies as a function of the MgO barrier thickness.
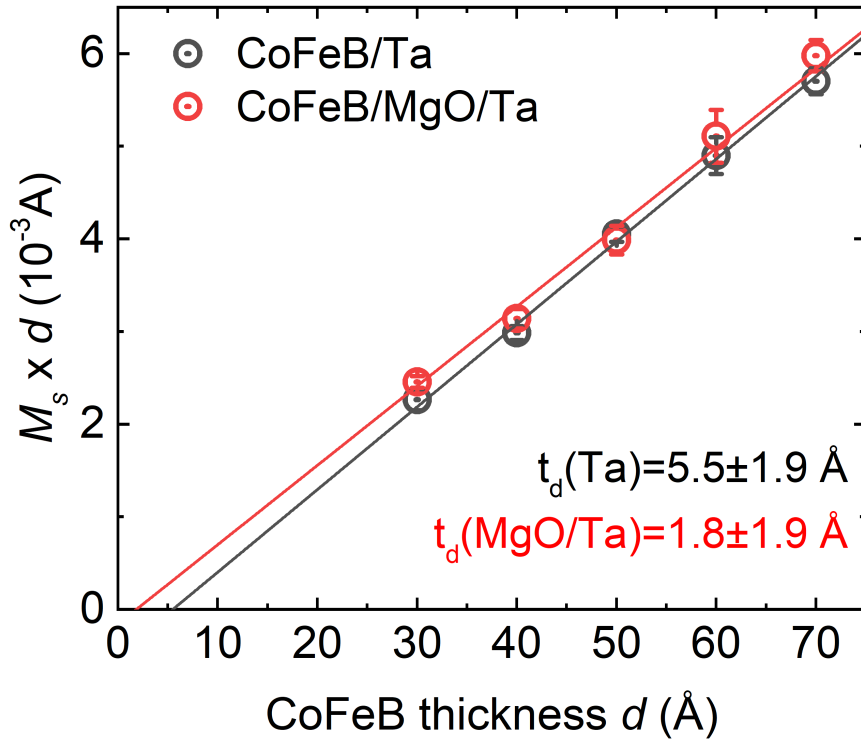
Figure 4.16: CoFeB thickness dependence of the saturation magnetization per area for CoFeB/20Ta and CoFeB/2MgO/20Ta. All thicknesses are in Å. The fit is a linear function used to extract the effective thickness of the non magnetic interface layer.

In Fig. 4.15, we show the enhanced damping $\Delta\alpha$ due to the proximity of the HM layer as a function of the MgO interlayer thickness and compare it to the thickness dependence of the corresponding inverse SHE signal. For the case of HM=Pt, the ISHE signal and the additional damping exhibit the same MgO thickness dependence as shown in Fig. 4.15(a). In contrast,

for the HM=Ta case, the enhancement of the SC transmission for thin MgO interlayers is not observed for the additional damping as shown in Fig. 4.15(b). Instead the damping due to spin pumping reduces in a similar fashion as observed for HM=Pt. This implies, that part of the spin current pumped in the HM=Ta case is not delivered to the HM layer. However, one needs to consider the magnetic moment suppression at the FM/Ta interface. From the calculations (which correspond to zero temperature) one expects only one atomic layer with reduced magnetization. At 300 K thermal fluctuations enhance the thickness range of the suppressed moment to about 3 atomic layers. This effect is often referred to as magnetically dead interface layer (226; 227; 228; 229) and was confirmed for the present samples using vibration sample magnetometry(VSM) as shown in Fig. 4.16. For a 2 nm thick CoFeB layer the depolarization of 3 atomic layers corresponds to a reduction the magnetic moment by about 25%. Since the enhanced damping scales inversely with the magnetic moment per interface area as $1/(M_s d)$, where d is the thickness of the magnetic layer (230; 122) one can expect an increase of the enhanced damping by 25% when the MgO spacer layer is absent.
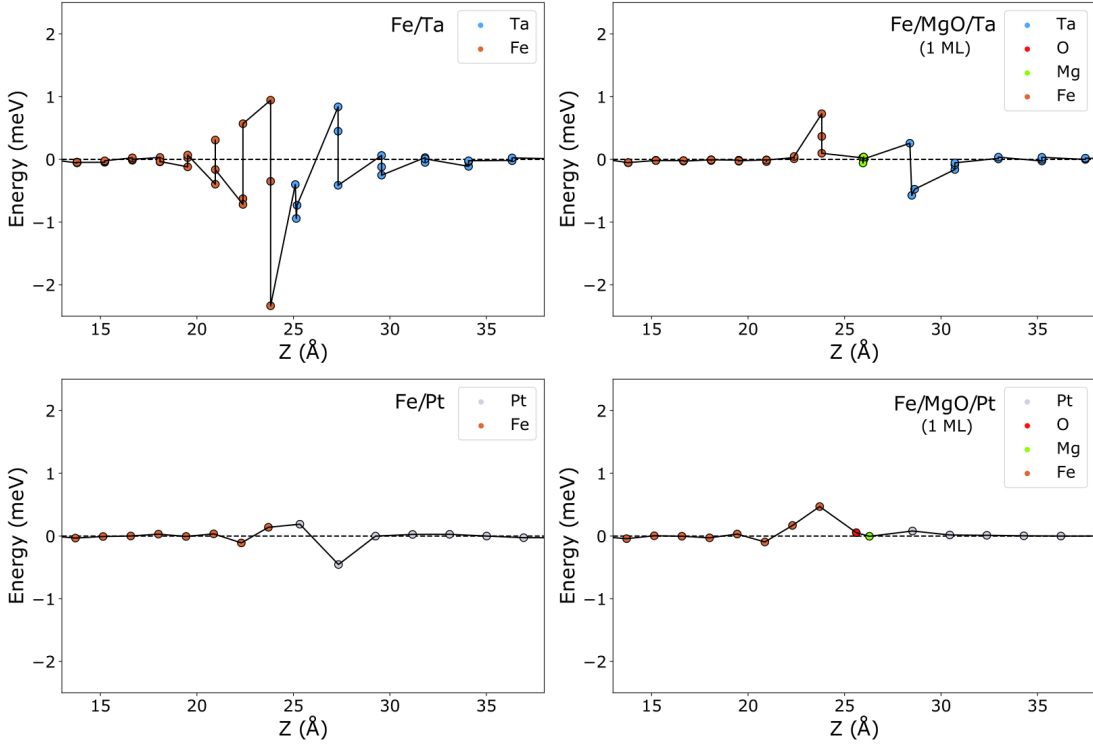
Figure 4.17: Local magnetic anisotropy energy for both heavy metals without MgO and with one ML of MgO.

Hence most of the deviation between enhanced damping and ISHE amplitudes can be explained by this effect. In the following we discuss the relevance of spin memory loss (SML) for the experiments above. SML can be quantified by the parameter δ as follows:

$$J_s^{HM} = (1 - \delta)J_s. \tag{4.1}$$

Here, J_s^{HM} is the spin current on the HM side, and J_s is the total spin current pumped from the

FM side. In the case of HM=Pt, there is very close correspondence between the ISHE voltage and the enhanced damping due to spin pumping implying that SML is a small effect at the Pt/CoFeB interface with $\delta_{Pt} \leq 0.05$. For HM=Ta, the results imply that $\delta_{Ta} \leq 0.10$ is needed to account for the remaining difference between enhanced damping and ISHE signals. With the insertion of 1 ML of MgO, the magnetic moment recovery at the interface enhances the spin current transmission and simultaneously suppresses the enhanced damping as well as the SML (see Fig. 4.15(b)). We want to point out that SOC is neglected in the transport calculations. To estimate the impact of SOC at the various interfaces, we calculate the layer-resolved magnetic anisotropy energy (MAE) (see Fig. 4.17). At the Fe/Ta interface, MAE is enhanced by more than a factor of 5 compared to the Fe/Pt or the Fe/MgO interface. This is in line with the experiments indicating enhanced spin relaxation for the FM/Ta interface.

4.7 Heavy metal Ta thickness dependence
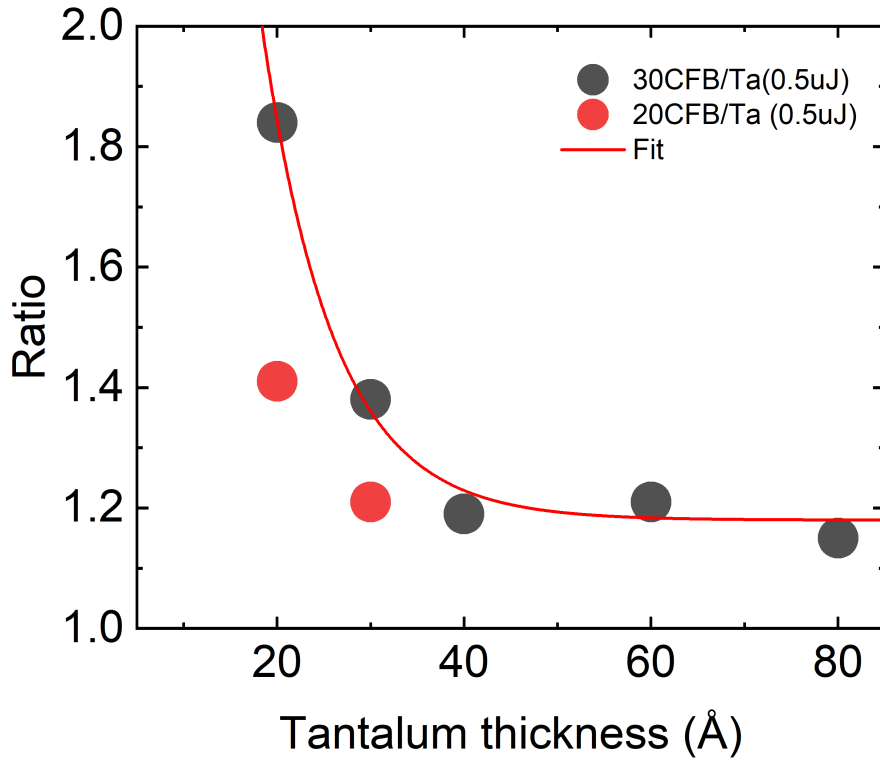
Figure 4.18: Tantalum thickness dependence of the relative increase of the ISHE signal for the case of CoFeB/MgO(2Å)/Ta compared to the reference samples without MgO.

In the following section, we monitor the recovery of the spin polarization at the interface for different Ta thicknesses by evaluating the ratio of the ISHE signal's amplitude with and without thin MgO interalyer. The results are shown in Fig. 4.18.For a certain thickness of the FM, the ratio decreases exponentially with the Ta thickness and saturates at around 20% increase for

Ta thickness of 40Å. For thinner Ta, around 20Å, the increase can reach values up to 85%. This could be due to the induced magnetic moments in Ta.

4.8   Discussion and conlusion

Inserting MgO interlayers between FM and HM layers suppresses the spin current transmission exponentially with a decay length of ≈ 2 Å. This effect can be well explained by the calculated spin-current transmission. By combining ISHE and spin-pumping measurements as a function of MgO thickness, we demonstrated a connection between reduced magnetic moments at the HM/FM interface and potentially a small SML contribution at the CoFeB/Ta interface. Based on calculations of the electronic structure, we conjecture that the effect interface moment reduction occurs for all $5d$ heavy metals with less than half-filled d-shells(222) and when interfaced with $3d$ ferromagnets. The insertion of an atomically thin MgO interlayer is sufficient to recover the interface polarization of the ferromagnet. We demonstrated that spin current transmission for two highly relevant HM/FM interfaces can be well modeled without considering spin relaxation (such as SML). Hence we conclude that it is physically more reasonable to discuss the incomplete spin current transmission across these interfaces by a transmitivity parameter (related to matching of the electronic bands) rather than attributing it to SML.

In summary, we demonstrated that the orbital hybridization between FM and HM layers at the interface can lead to two effects which need to be avoided for efficient spin injection: (1) reduced spin polarization of the FM and (2) enhanced spin relaxation. We show, an MgO interlayer with a thickness of 2 Å leads to optimum results for the spin injection at Ta/CoFeB interfaces. We believe that chemical control of the interface hybridization at the atomic scale (e.g. by ultrathin oxide layers) as demonstrated here is a promising approach to tune and enhance the interface spin transmission and thereby improve the efficiency of many spintronic devices.

Chapter 5

On-chip optimized THz spintronic emitter

A huge advance in THz wave generation has been enabled by spintronic THz emitters (STE) owing to their spin to charge conversion (S2C) feature reaching and even surpassing the performance of the conventional ZnTe crystal. Efforts have been focused to enhance their performance as radiative emitters mainly by optimizing the materials and the efficiency of the S2C conversion. In this letter, we demonstrate that stacking STEs seperated by MgO insulating barrier layers greatly enhances their on-chip performance compared to the free space radiation output.

5.1 Motivation

THz frequency range (0.1-30 THz) covers the electromagnetic spectrum lying between the microwave and the far-infrared bands. The generation of THz pulses(231; 232) has been a first great achievement that enabled THz-time domain spectroscopy. This provided numerous advantages and applications(233; 234) ranging from non invasive and non destructive imaging(235; 236), chemical species identification(237; 238), biomedical applications(239; 240), probing dynamics and properties of the four states of matter(241; 242), and even ultrafast magnetometry(65). This frequency range is less utilized than its microwave counterpart due to the limitation of efficient and intense THz sources and adequate detectors.

The most common ways to generate a THz pulse is by femtosecond laser pulse induced photocurrent generation by electrons and holes in photoconductive semiconductors(243; 244; 245) such as GaAs and InAs as well as by optical rectification in electro-optic nonlinear crystals(246; 247; 192) such as ZnTe, GaP. These emitters suffer a limited bandwidth in some cases. Additionally, generating intense pulses has been enabled by using liquid(248), plasma or gaseous media(249; 250; 251). However, this would require intense laser pumps in the order of 0.1-1 mJ. All the aforementioned emitters rely on the electron's charge used as a source.

Another way, which opened a new possibility to generate THz pulses is through the manipulation of the spin degree of freedom. This spintronic emitter, indeed, proved to generate low cost, ultra broadband, efficient, highly flexible and scalable THz sources(204; 5). Indeed, shining a femtosecond laser pulse on a simple ferromagnet (FM) and normal metal (NM) bi-

layer generates a THz pulse. The laser generates an ultrafast spin current pulse pointing from the FM to the NM. At the stage where the spin current is generated, the key mechanism that enables the THz generation is the S2C conversion feature which depends mainly on the NM and also on the interface. The main mechanism for S2C is the inverse spin Hall effect(ISHE), which is a property of the material and whose strength is quantified by the spin Hall angle. Thus, improving the performance of these STEs translates to enhancing the spin Hall conductivity of the NM.

Some other attempts to increase the radiation output were implemented by dielectric cavity implementation(252) or by stacking STEs separated by dielectrics(253) or by an insulating barriers(254; 255). In this latter case, the radiation increases slightly indeed but drops after few repeats.

In this work, by optically exciting a typical CoFeB/Pt bilayer we probe the performance of its signal using a fast sampling oscilloscope limited to the GHz regime. We show that by stacking several STEs seperated by MgO as thin as 7Å increases drastically the efficiency of the on-chip THz response, until saturation for a certain number of repeats. We confirm that the behaviour is different for the free space radiation THz output where the signal decreases with the number of repeats. We further explain these results with a simple model based on the impedance of the medium of the THz wave.

5.2   Samples and experimental setup

The full structure of the films consist of Sapphire (substrate)/TaN(15)/[Pt(20)/ CoFeB(15) /MgO(7)]$_N$/ TaN(15) with n an integer being the number of repeats. The layer thicknesses noted in the parenthesis are in Å. All the layers are grown using magnetron sputtering following the same procedure in Chapter 4. An external magnetic field is applied to saturate the magnetization in the plane of the film and the whole structure is excited with a femtosecond near infrared laser pulse with 1030 nm wavelength. This creates a net shift in the chemical potentials of both spin channels of the FM leading to a spin current moving perpendicular to the interface from the FM to the Pt layer. Due to its high S2C conversion ratio, the SC is converted to an ultrafast transient charge current, flowing in plane perpendicular to the magnetization.

When probed with electro-optic sampling detection technique, this current extends typically to a broad frequency range up to ~30 THz(167). In our experiment, we use an rf probe antenna connected to a sampling oscilloscope with a cut-off frequency of 50 GHz. More details of our experimental technique can be found in Section 3.3.3. The advantage of this technique is the ability to probe the current on the sample as well as the emitted radiation. Indeed, the former case is realized by contacting the rf probe antenna on the sample's surface and the latter by hovering it some distance away from the sample, as illustrated schematically in Fig. 5.1. We will refer to these two measurement schemes as 'contact mode'(CM) and 'noncontact mode' (NCM) respectively. These modes are already explained in more details in Section 3.3.3.

For both measurement modes, the corresponding time resolved ISHE signals are displayed in Fig. 5.2, for one single CoFeB/Pt bilayer (i.e. N=1). For either measurement scheme, the waveform is inverted with the inversion of the external magnetic field as expected from the symmetry of the SHE since the spin polarization is inverted. To additionally eliminate any
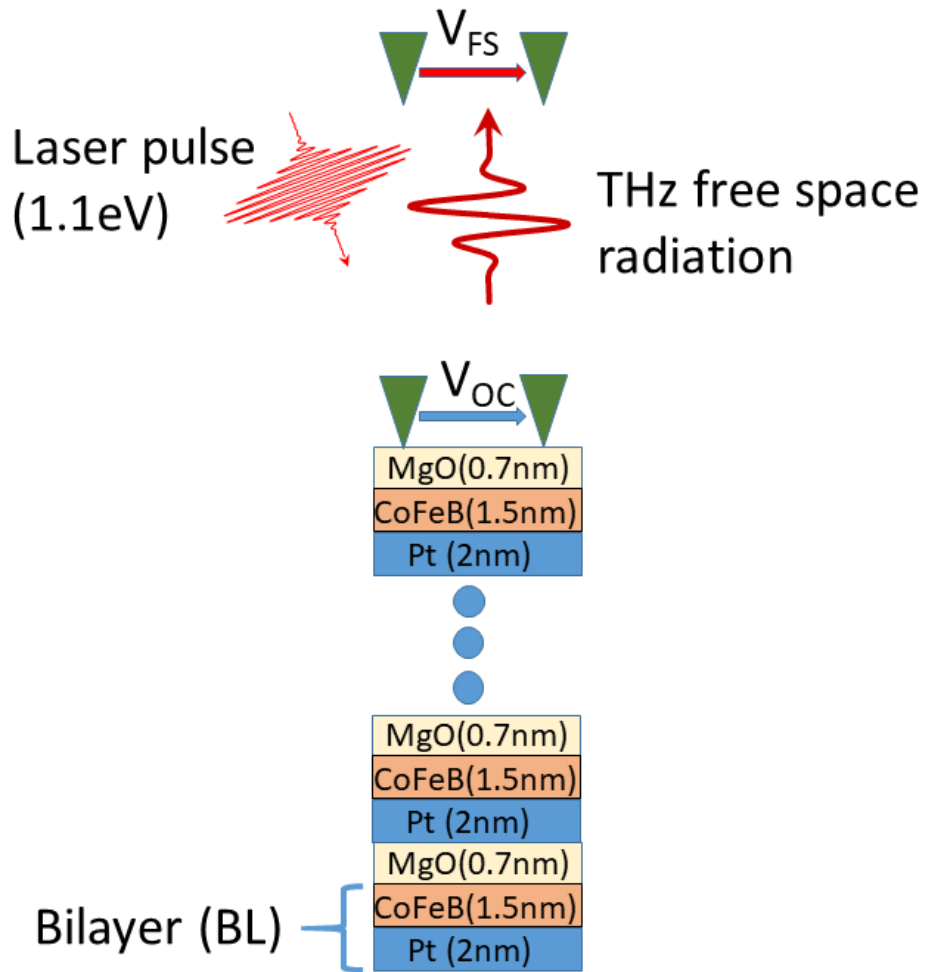
Figure 5.1: Schematics of the Spintronic emitter multilayer displaying the CM and the NCM measurement schemes for on-chip and free space radiation voltages. The laser pulse has a perpendicular incidence on the sample surface. Yet, for illustration purposes, the pulse is here tilted from real angle of incidence.

non magnetic contribution to the signals, the difference between the two waveforms, for both magnetic field directions, is considered and its amplitude value is defined as the absolute value of the peak amplitude.

We note V_{OC} and V_{FS} the signal amplitudes for the on-chip CM and the free space NCM ISHE signals respectively. In the NCM, the signal amplitude depends strongly on the distance between the sample and the antenna, as shown in Fig. 5.3. The distance is kept constant for all the samples considered. However, in order to minimize additional errors in the measurements due to, for example slight height differences in the considered substrates, the following NCM measurements are taken at a distance of $55 \mu m$ away from the sample. This distance offers a good trade-off between the amplitude of the signal and the signal to noise ratio.
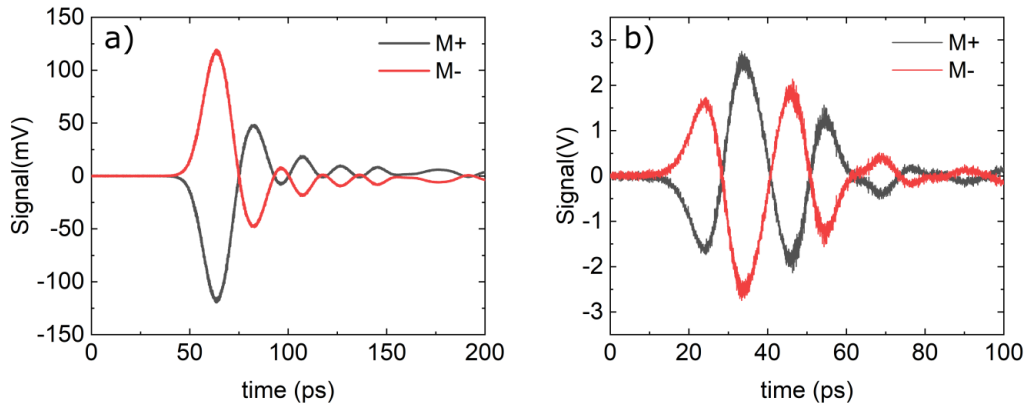
Figure 5.2: (a) and (b) time resolved measured on-chip and free space radiation voltages for both CM and NCM respectively.
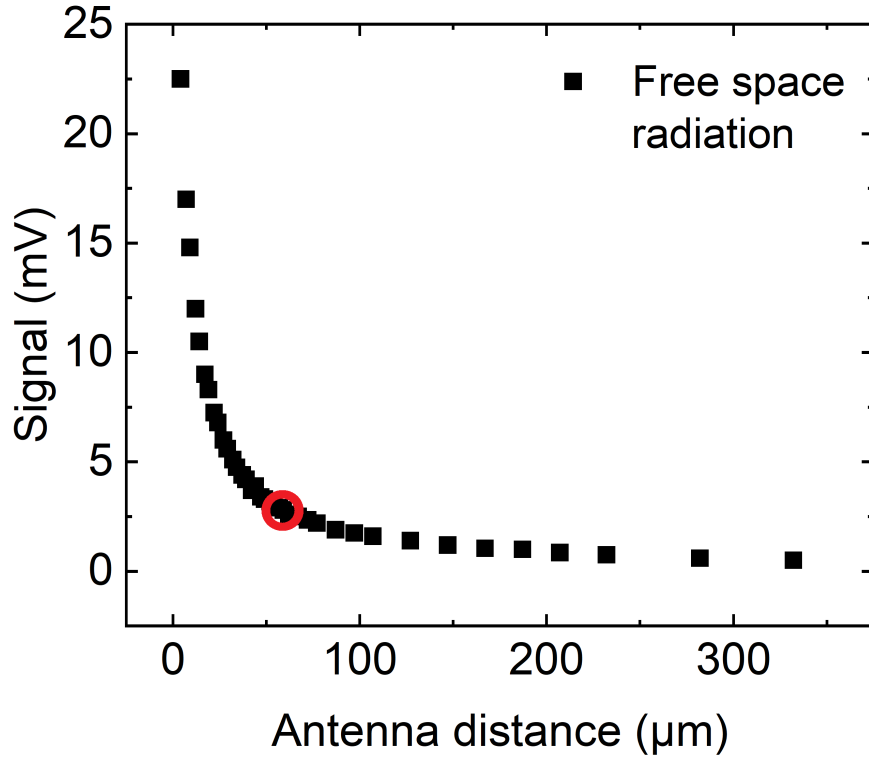
Figure 5.3: Free space radiation signal's amplitude with the rf-probe (antenna) sample distance.

5.3 Laser fluence measurements

In Fig. 5.4, the laser fluence dependence of the signal amplitude for both CM and NCM is shown for N=1..6 repeats. Interestingly, the on-chip saturation voltage keeps increasing with the number of repeats whereas the free space saturation voltage increases for N=2 and then starts decreasing for N≥3. This is better illustrated in Fig. 5.5 where only the saturation
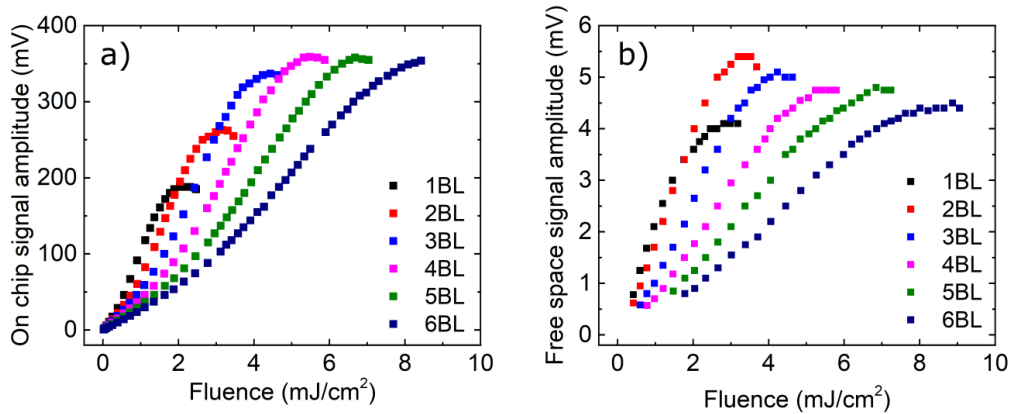
Figure 5.4: (a) and (b) fluence dependence of the on-chip and free space radiation signal's amplitudes V_{OC} and V_{FS} respectviely.

voltage for both cases is normalized to the one of a single BL (i.e. N=1). For the CM case, the normalized on-chip saturation voltage increases drastically and saturates at a value equal to ~ 1.9 for N=4. On the other hand, the normalized free space saturation voltage increases to a value of ~ 1.3 for N=2 and then starts decreasing reaching a value of ~ 1.1 for N=6.
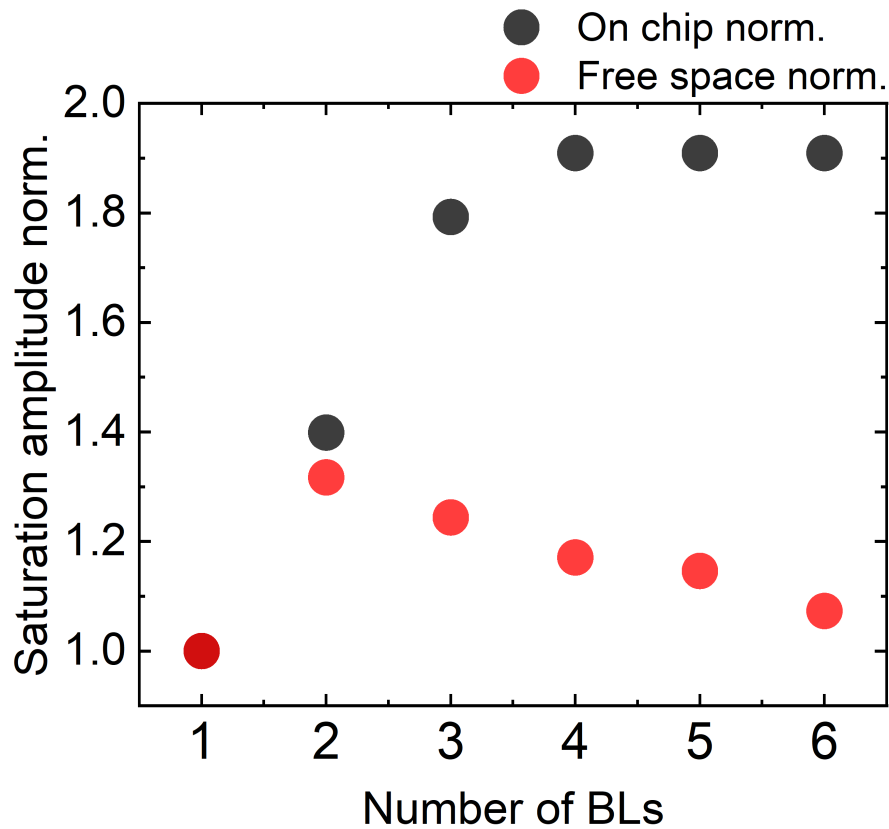
Figure 5.5: Number of bilayers (repeats) dependence of V^{sat} for both CM and NCM respectively.

5.4 Model

To better understand this behaviour, let's consider the charge current density j_c^n flowing in each bilayer n. This current radiates an electric field E^n. Our film stacks considered here are much thinner than the wavelength and attenuation length of the THz wave. Therefore, we can assume a constant electric field in each bilayer as well as a constant effective attenuation length s of the THz wave traversing each bilayer. In this case, the electric field generated from a certain bilayer n can be expressed as:

$$E^n \propto Z_{BL}(\omega) j_c^n e^{\frac{-nd}{s}}$$
$$\frac{1}{Z_{BL}(\omega)} = \int_{BL} dz\sigma(z',\omega) \tag{5.1}$$

Where d is the total thickness of a single BL. $Z_{BL}(\omega)$ is the impedance of a single BL and is inversely equal to $\int_{BL} dz\sigma(z',\omega)$ which is the corresponding sheet conductivity. For the following calculations, the measured DC sheet conductivity will be considered instead.
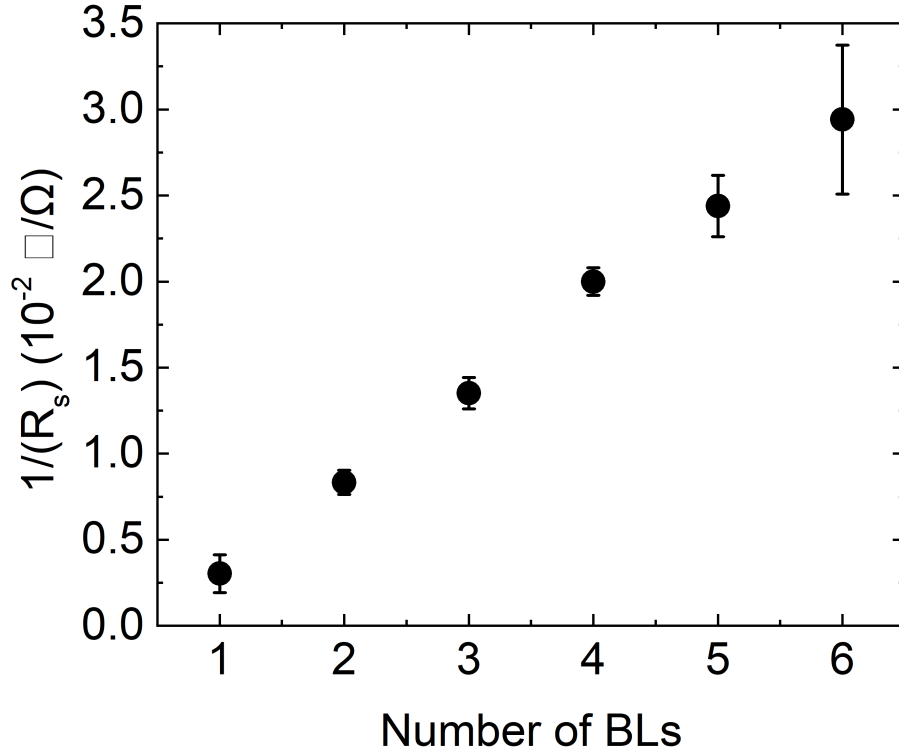
Figure 5.6: Number of bilayers dependence of the sheet resistance of the samples.

The main difference between both measurement schemes is the total impedance of the system which depends on the medium of propagation of the THz wave. In the NCM, the THz wave has to propagate through the multilayer and air. As specified in (204; 5; 170), the effective length s is expected to be larger than the bilayer thickness, since the THz wave experience multiple

reflections at the metal/dielectric interfaces. This leads to further simplifications of the total impedance of system (formula shown in Section 2.4.4). After summing all the contributions of the electric fields E^n, the total electric field after the sample can be written as:

$$E_{tot}^{FS} \propto \frac{\sum_{n=1}^{N} j_c^n e^{-\frac{nd}{s}}}{\frac{n_{air}+n_{sub}}{Z_0} + S(N)} = \frac{j_c e^{-\frac{(N+2)d}{2s}}}{\left[\frac{n_{air}+n_{sub}}{Z_0} + S(N)\right]} \frac{\sinh\left(\frac{Nd}{2s}\right)}{\sinh\left(\frac{d}{2s}\right)} \tag{5.2}$$

Where n_{sub} and n_{air} are the refractive indices of the substrate and air respectively. $Z_0 = 377\Omega$ is the impedance of the vacuum. S(N) is the measured DC sheet conductivity of the multilayer with N bilayers, shown in Fig. 5.6.

As for the case of the on-chip voltage, the same summation over the THz waves propagating within the sample is considered. The THz charge current flows in the multilayer in contact to the rf probe. Ohm's law can be applied to the system considering that the probe has an internal impedance of $Z_{50} = 50\Omega$. A simple voltage divider gives:

$$E_{tot}^{OC} \propto \frac{\sum_{n=1}^{N} j_c^n e^{-\frac{nd}{s}}}{\frac{1}{Z_{50}} + S(N)} = \frac{j_c e^{-\frac{(N+2)d}{2s}}}{\left[\frac{1}{Z_{50}} + S(N)\right]} \frac{\sinh\left(\frac{Nd}{2s}\right)}{\sinh\left(\frac{d}{2s}\right)} \tag{5.3}$$

The calculated saturation fields based on this model are compared to the experimental values in Fig. 5.7. Despite the simplicity of the model, it fits quantitatively well the data with a single fitting parameter s =196Å. This value satisfies the condition $(s \gg d)$ and is in agreement with previous works(167; 170).
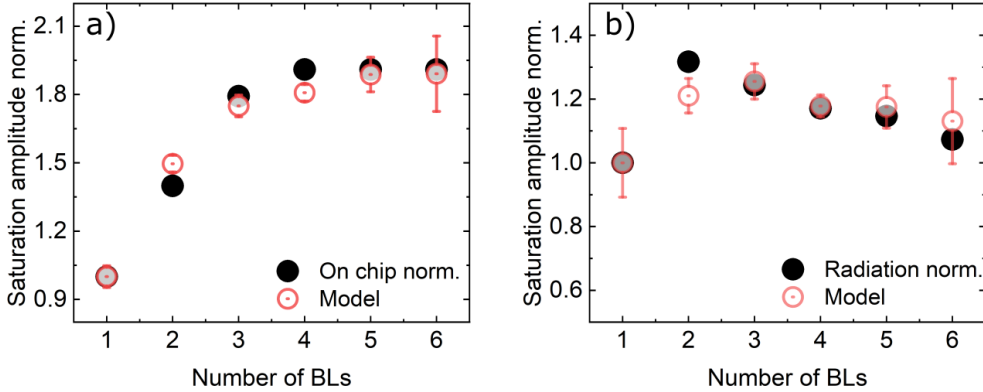
Figure 5.7: (a) and (b) Number of bilayers (repeats) dependence of the normalized V^{sat} and the corresponding normalized signal calculated from the model, for both CM and NCM measurement schemes respectively.

The saturation of the signal with the number of repeats is reproduced. The model then confirms that this is indeed due to the attenuation of the THz wave within the multilayers. Also, the main difference between the two cases is the impedance difference between those of the probe, air and multilayer. For radiative case, as the number of the repeat increases, the sheet conductance of the multilayer becomes much bigger than the shunt conductance, and the Eq. (5.2) reduces to a simple Ohm's law, therefore following the trend of the sheet resistance. As for the CM case, the sheet conductance of the multilayer is smaller than the standard

conductance of the probe, equals it at N=3, and is slightly above it for 4≤N. This explains qualitatively the behaviour of the data points.

5.5   Discussion and Conclusion

As demonstrated in the previous Chapter, 7Å of MgO is thick enough to suppress the spin current flowing from one bilayer to the next bilayer. The coupling between these bilayers is only due to dipolar fields. Therefore, this choice of MgO is valid and further demonstrated by comparing two stacks having only two repeats with MgO thicknesses of 7Å and 10Å (data not shown).

Stacking multiple STEs separated by an MgO interlayer enhances the THz wave generated. This enhancement has however an upper limit. Indeed, due to reflections at the interfaces and attenuation of the THz wave in the metallic layers, the THz wave's amplitude is bound to saturate after a certain number of repeats. We have demonstrated that this enhancement is different for the radiated THz wave as well as for the on-chip THz current flowing in the sample. Indeed, in the latter case, the THz output is almost doubled and, in the former case, increases slightly and starts decreasing again.

Such a multilayer of $[CoFeB/Pt/MgO]_N$ repeats was fabricated and measured with an electro-optic sampling detection technique(255) and agrees well with our results qualitatively and quantitatively, even though our detection method is limited to 50GHz in frequency. The reason for this decrease, is the impedance mismatch between the air medium to where the THz wave is emitted and the sheet resistance of the multilayer stack. On the other hand, the on-chip THz wave keeps increasing further with the number of repeats as the impedance of the structure and the standard impedance of 50Ω of our rf probe are closer in values. Therefore our STE multilayer is more suited for on-chip technology integration.

Chapter 6

Spin transport across TaN

In this study, we consider tantalum nitride (TaN) first as a spin sink and secondly as an interlayer between a ferromagnet(FM) and a heavy metal(HM). By considering ultrafast optical excitation and electrique detection technique, we show that a small spin Hall effect (SHE) is present in TaN extracting a spin diffusion length l_{sd} ∼10Å. When used as an interlayer, the spin current transmission decreases differently depending on the heavy metal used. For the case of Ta as a heavy metal, depending on the stacking order, few Angtroems of TaN can enhance substantially the signal to values exceeding 80%. A decay length in the range of 10-20Å is extracted depending on the stacking order. As for the case of Pt used as a heavy metal, the spin current transmission through thin TaN is unaltered for low laser fluences and is reduced with increasing the fluence. A decay length in the same range of 10-20Å is also extracted. Moreover, considering ferromagnetic resonance spin pumping for the case of Pt as a heavy metal, the enhanced damping decays with a characteristic length of∼6Å.

6.1   Ultrafast spin injection in CoFeB/TaN

All the layers in this study are grown using magnetron sputtering on Sapphire substrates. First, we consider a layer stack consisting of CoFeB(30)/TaN(t=0..200). The thicknesses in parenthesis are in Å. Resistivity measurements are conducted using a standard 4 point probe setup. The sheet resistance(R_s) of the bilayer can be expressed in the following manner:

$$\frac{1}{R_s} = \frac{d_{FM}}{\rho_{FM}} + \frac{d_N}{\rho_N} \tag{6.1}$$

where d_{FM} and d_N are the thicknesses of the ferromagnetic layer and the TaN layer respectively. Similarly, ρ_{FM} and ρ_N are the resistivities of the ferromagnetic layer and the TaN layer respectively. In Fig. 6.1(a), the resistivity of the bilayer is shown and fit with Eq. (6.1). The extracted values for the resistivities are $\rho_{FM} = 540\mu\Omega$.cm and $\rho_N = 1100\mu\Omega$.cm. A test sample consisting of Sapphire//CoFeB(30Å)/MgO(60Å) gives a resistivity $\rho_{FM} = 580\mu\Omega$.cm which agrees well with the extracted value from the model.

The ultrafast spin current injection is realized by a femtosecond laser pulse with a central wavelength of $1030nm$. The signal is subsequently measured with an rf coplanar probe con-
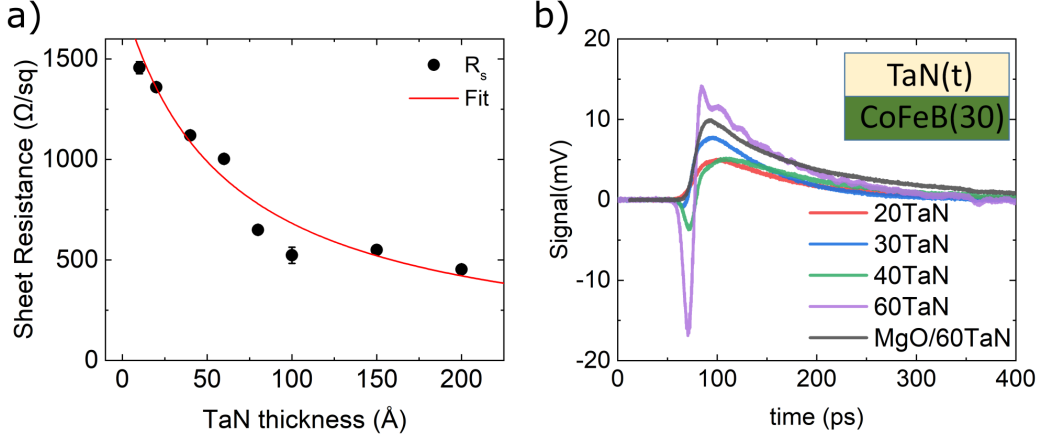
Figure 6.1: (a) TaN thickness dependence of the sheet resistance of the CoFeB/TaN stack. (b) Time resolved ISHE signal for different thicknesses of the TaN layer.

nected to a sampling oscilloscope module with a 50 GHz cut-off frequency. The magnetic field is set in both directions with a field amplitude of 50mT high enough to saturate the film in plane. By switching the magnetic field, the signal reverses and the difference between the two traces is considered. In Fig. 6.1(b), we present the time resolved measured signal for different thicknesses of the TaN capping layer for a laser fluence of ~1.7mJ/cm^2. Depending on the thickness, the signal can feature a fast contribution prior to a slow one happening later in time. The slow contribution is attributed to the recovery of the magnetization in the ferromagnet and doesn't affect the faster contribution which is of interest here. We note the peak value of the signal of this contribution for the different TaN thicknesses and plot it against the thickness for different fluences in Fig. 6.2. The amplitude rises significantly for a thickness of TaN ≥ 50Å. Two scenarios are possible: whether the signal originates from ISHE in the TaN or from the ferromagnet due to Anomalous Nernst effect. For this purpose, we insert MgO(10Å) between the FM and TaN(60Å). The time resolved signal is shown in Fig. 6.1(b). The ultrafast contribution disappears, which is a clear indication that the signal is indeed originating from the TaN layer.

Following the procedure in (5; 170), we fit the corresponding signal obtained with:

$$E \propto \tanh\left(\frac{d_N - d_0}{2l_{sd}}\right) R_s e^{-\left(\frac{d_{FM} + d_N}{s}\right)} \tag{6.2}$$

Where the d_N and l_{sd} are the thickness and the spin diffusion length of the TaN layer. d_0 is introduced here as a shift to make the fitting possible. s is the effective attenuation length of the THz wave in the heterostructre. We use the fit function R_s^{fit} used to fit the experimental resistivity R_s data. The results are shown in Fig. 6.3. The fit reproduces very well the data and the extracted parameters are shown in Table 6.1.

91

Figure 6.2: **ISHE signal amplitudes in CoFeB/TaN for different fluences**. TaN thickness dependence of the ISHE signal amplitude in CoFeB/TaN for various laser fluences. The red line is the fit considered using Eq. (6.2).

Fluence (mJ/cm^2)	l_{sd}(Å)	s(Å)	d_0(Å)
0.42	9.2	292	41.8
0.69	9.2	292	39.2
1.01	9.6	261	38.5
1.42	10.7	237	37.5

Table 6.1: Extracted values of spin diffusion length l_{sd}, THz attenuation length s and d_0 for various laser fluences.

The ranges of the values for s agree with those in the literature(5; 170). The spin diffusion length extracted increases slightly with the laser fluence.

6.2 Ultrafast spin injection across TaN with Ta as a heavy metal

6.2.1 Results

In this section, TaN is used as interlayer between the ferromagnet CoFeB and heavy metal Ta. The film structure consists of CoFeB(30)/TaN(t)/Ta(20)/TaN(15) grown by magnetron sputtering on Sapphire substrates. The thicknesses in parenthesis are in Å. Various TaN thicknesses, ranging from 0 to 50Å, are considered.
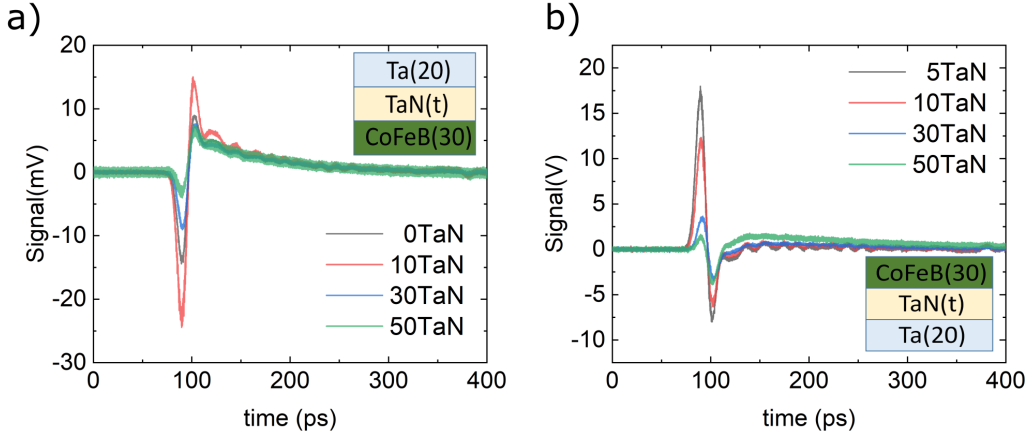
Figure 6.3: Time resolved ISHE signal for different thicknesses of the TaN layer in CoFeB/TaN/Ta (a) and Ta/TaN/CoFeB (b).

The same experiment is repeated for this samples. In Fig. 6.3(a), we show typical time resolved waveform of the signal registered for different TaN thicknesses for the CoFeB/TaN/Ta. The laser fluence considered is $\sim$1.0mJ/cm^2. The peak amplitude of the waveform quantifies the strength of the ISHE current. In Fig. 6.4, the dependence of the ISHE signal's amplitude on the TaN thickness is shown for various laser fluences. The signal has a sharp increase reaching a maximum for TaN thickness of 10Å and starts decaying exponentially for larger thicknesses of the TaN layer. An exponential fit is used for all traces starting from a TaN thickness of 15Å. The measurements are acquired for laser fluences ranging from 0.02 to $\sim$1.5mJ/cm^2. In Fig. 6.5(a), we present the laser fluence dependence of the decay length extracted from the fit. We note that the intrinsic contribution of the TaN to the ISHE signal is subtracted in order to extract the corresponding decay length. The decay length increases slightly from 17Å for low fluences to around 19Å for high fluences.

Next, the same experiments are repeated for the reversed stacking order. The behaviour is surprisingly different. In Fig. 6.3(b), we show the time resolved waveforms of the signals for various TaN thicknesses. In Fig. 6.4, the TaN thickness dependence of the signal amplitude is shown for various laser fluences. In this case, an increase is registered as well but for a TaN thickness of 5Å for low laser fluences. The signal decays exponentially in these series as well and an exponential fit is used starting from a TaN thickness of 5Å. In Fig. 6.5(a), the laser fluence dependence of the decay length is shown. In this case, the decay also shows a slight tendency to increase with laser fluence and can be averaged to a value of 13±2Å.

93
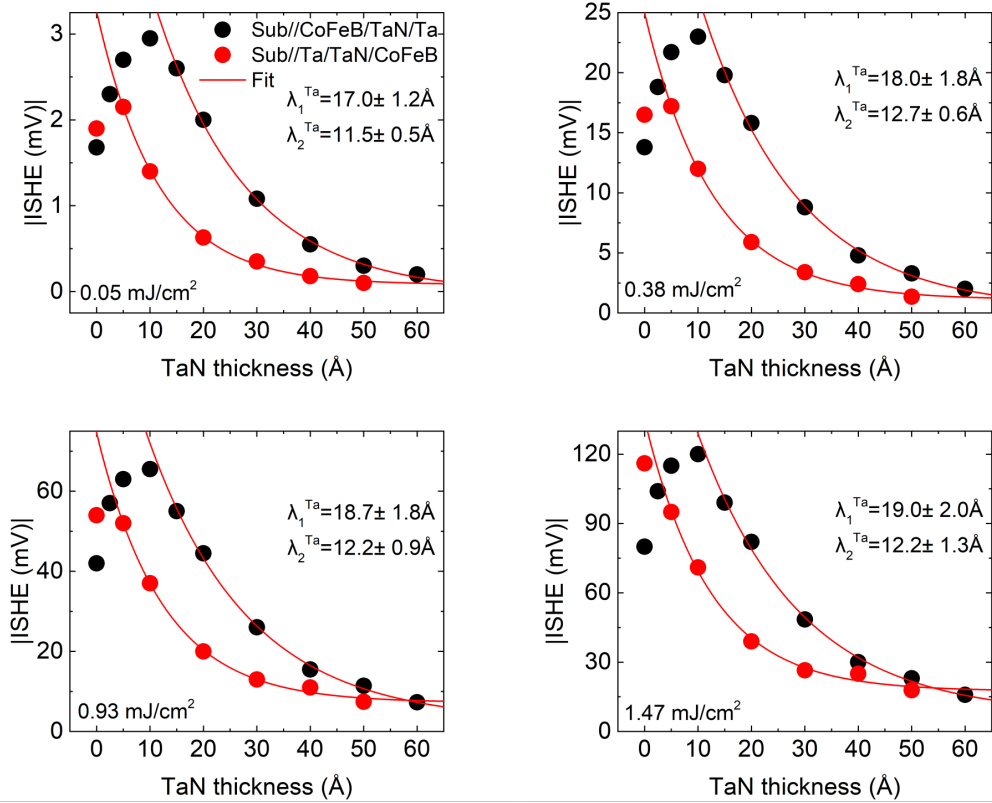
Figure 6.4: **Absolute value of the ISHE signal amplitudes in CoFeB/TaN/Ta and Ta/TaN/CoFeB for different fluences**. TaN thickness dependence of the ISHE signal amplitude in CoFeB/TaN/Ta and Ta/TaN/CoFeBfor various laser fluences. The red line is an exponential fit, used to extract the decay length λ_1^{Ta} and λ_2^{Ta}. These decay lengths are assigned to CoFeB/TaN/Ta and Ta/TaN/CoFeB respectively.
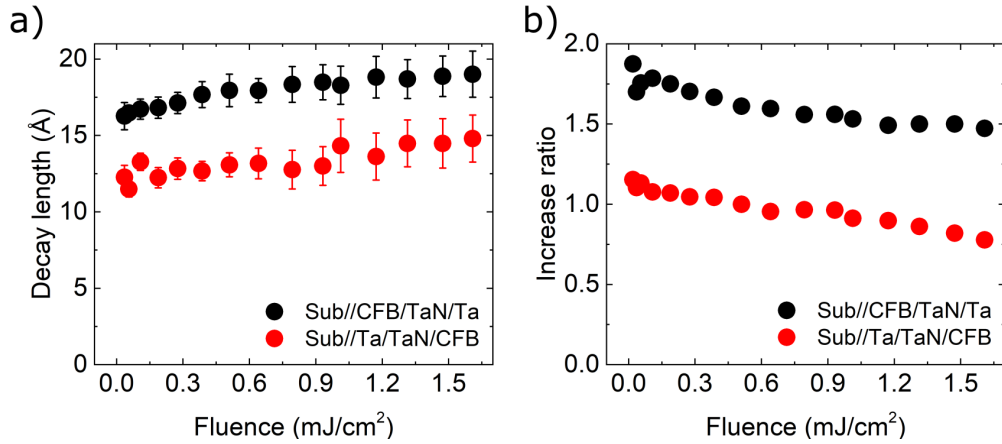
Figure 6.5: (a) Fluence dependence of the decay length for both CoFeB/TaN/Ta and Ta/TaN/CoFeB series. (b) Fluence dependence of the maximum increase ratio for both stacking orders.

6.2.2 Discussion

Both series show an exponential decay of the ultrafast ISHE signal with the TaN thickness. In the CoFeB/TaN/Ta case however, a sharp increase for thin TaN thicknesses, peaking at 10Å, is found. For the other reversed stacking order, a smaller increase is found for low fluences and lower TaN thickness of 5Å. The increase for both cases is fluence dependent. Indeed, in Fig. 6.5(b), we note the ratio between the maximum peak due to the TaN interlayer and the sample of reference, i.e. without the TaN interlayer. Both traces show a monotonous decrease of the ratio. In the case of CoFeB/TaN/Ta, the increase can reach values up to 80% at low fluences.

As evidenced in Chapter 4, the $3d$-$5d$ orbital hybridization at the interface between the Ta atoms and either the Fe or the Co atoms reduces significantly the magnetic moment at the interface. This effect generates a magnetic dead layer which can be eliminated with the insertion of the TaN layer. In this case, the interaction between the Ta and the FM is reduced and the magnetic moment at the interface is recovered. Comparing the apparent enhancement of the signal for both stacking orders entails that the magnetic moment suppression is larger in CoFeB/TaN/Ta. In this stacking order, the Ta layer is sputtered on top of the ferromagnet. In this condition, the Ta elements are heavy and therefore possess a high kinetic energy, which ensures their peneration in the ferromagnetic layer. However, in the reversed stacking order, the Co and Fe elements are lighter and therefore are sputtered on top of the Ta layer with less kinetic energy, yielding a less intermixing with the Ta atoms.

The fluence dependence of the decay length for both cases can be seen in Fig. 6.5(a). Interestingly, substantial difference between both cases is found. For CoFeB/TaN/Ta, the decay length can be averaged to a value of ~ 18Å contrasting a lower value of 13Å for the reversed stack case.

6.3 Spin injection across TaN with Pt as a heavy metal

6.3.1 Ultrafast spin injection

In this section, TaN is used as an interlayer and Pt as a heavy metal. The film stack consists of CoFeB(40)/TaN(t)/Pt(20)/TaN(15). The thicknesses in parenthesis are in Å. The TaN thickness ranges between 0 and 50Å.

The same experiments carried out for the HM=Ta case, are repeated for the case of Pt as a heavy metal. In Fig. 6.6, the TaN thickness dependence of the ISHE amplitude of the signal is shown for various laser fluences. The signal decays exponentially with increasing the TaN thickness. Interestingly, for TaN thickness of 5Å, the ISHE is unchanged compared to the one of the reference sample, i.e. without TaN, at low fluences and starts relatively decreasing with the laser fluence. After subtracting the ISHE contribution of the TaN, we extract the corresponding decay length for every laser fluence. The results are shown in Fig. 6.7. The decay length decreases monotonously with the laser fluence with values confined between 12 and 16Å, i.e. 12Å$< \lambda_N^{Pt,UF} <$16Å.
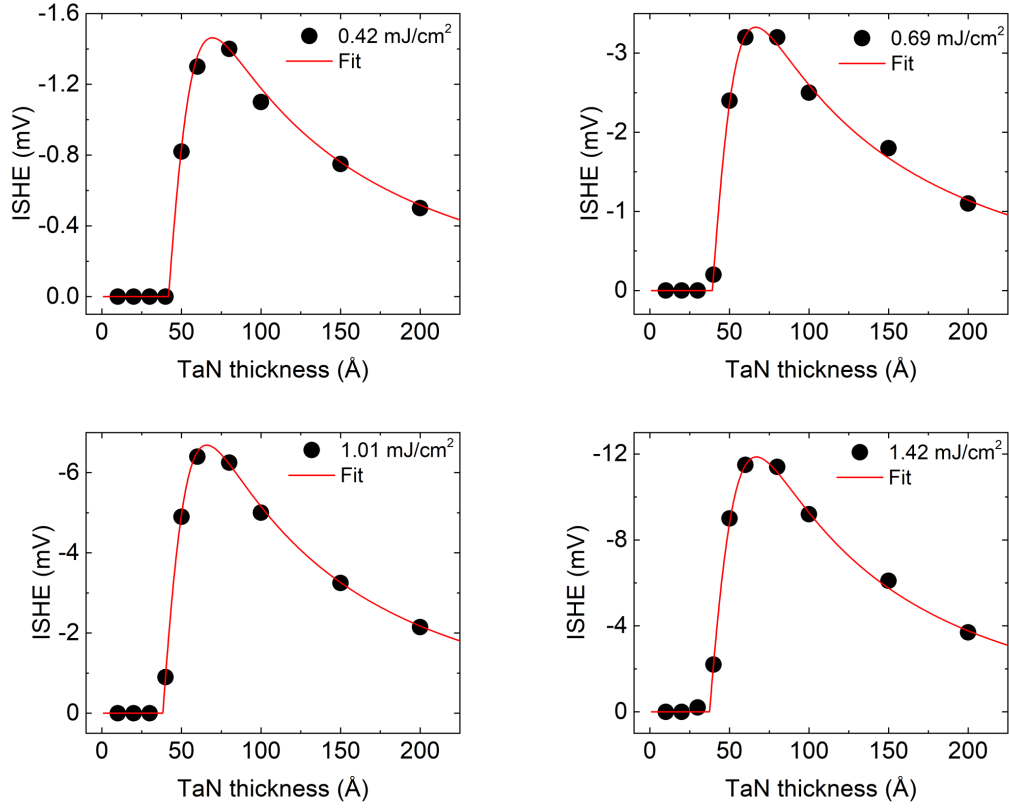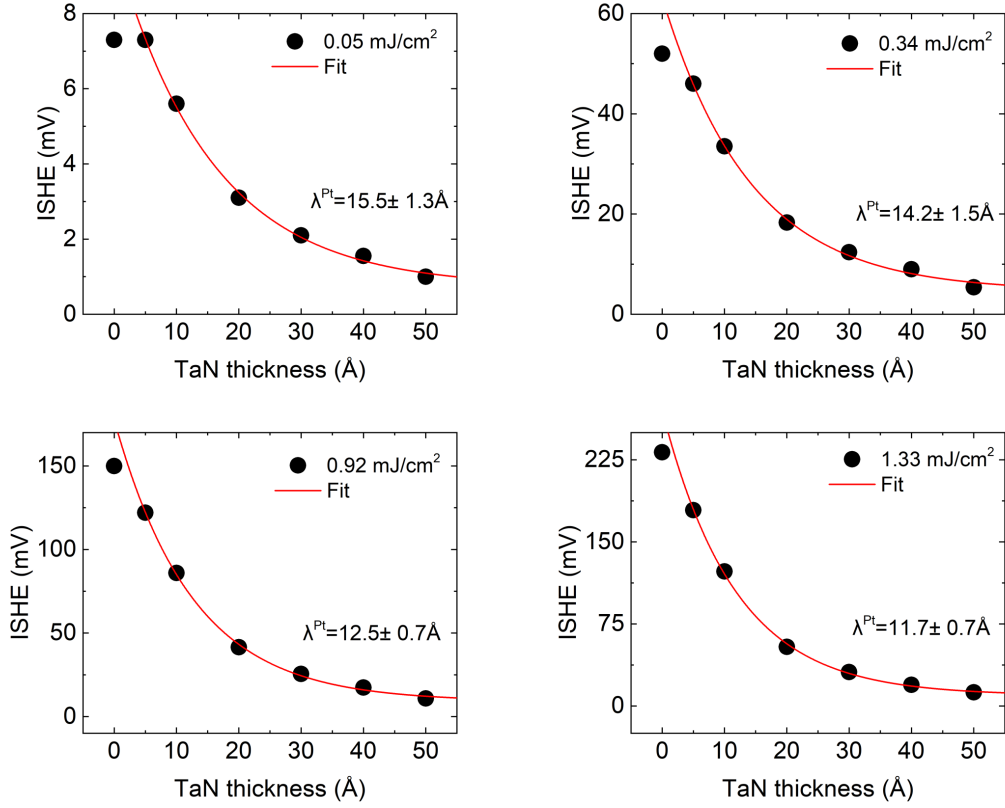
Figure 6.6: **ISHE signal amplitudes in CoFeB/TaN/Pt for different fluences**. TaN thickness dependence of the ISHE signal amplitude in CoFeB/TaN/Pt for various laser fluences. The red line is an exponential fit, used to extract the decay length λ^{Pt}.

6.3.2 FMR spin pumping

FMR spin pumping technique is herein conducted on the same samples with Pt as a heavy metal. The samples are placed on top of a broadband coplanar waveguide delivering continuous microwave with frequencies ranging from 8GHz to 18GHz. The absorption spectra is registred and the corresponding linewidth is extracted. The additional damping is deduced and plotted against the TaN thickness in Fig. 6.8. The damping is normalized to the case of CoFeB(40)/TaN(50), i.e. $\alpha_{eff} = \alpha_{FM/TaN/Pt} - \alpha_{FM/TaN}$. By considering an exponential fit of the decay part of the signal, we extract a decay length $\lambda_N^{Pt,FMR} = 6\text{Å}\pm0.8\text{Å}$.

6.3.3 Discussion

The insertion of TaN layer between CoFeB and Pt reduces the measured ISHE signal. For thin TaN thickness of 5Å, however, the signal is almost unchanged for low laser fluences, as compared to reference samples. With increasing the laser fluence, the ISHE signal of the sample with TaN starts decreasing compared to the one without. Moreover, the results are reproducible after reducing the laser fluence again. Therefore, structural changes due to the laser are ruled out.

This process means that the whether the spin current generation or the interface spin transmittance is laser fluence dependence. One possible explanation for this effect could be due
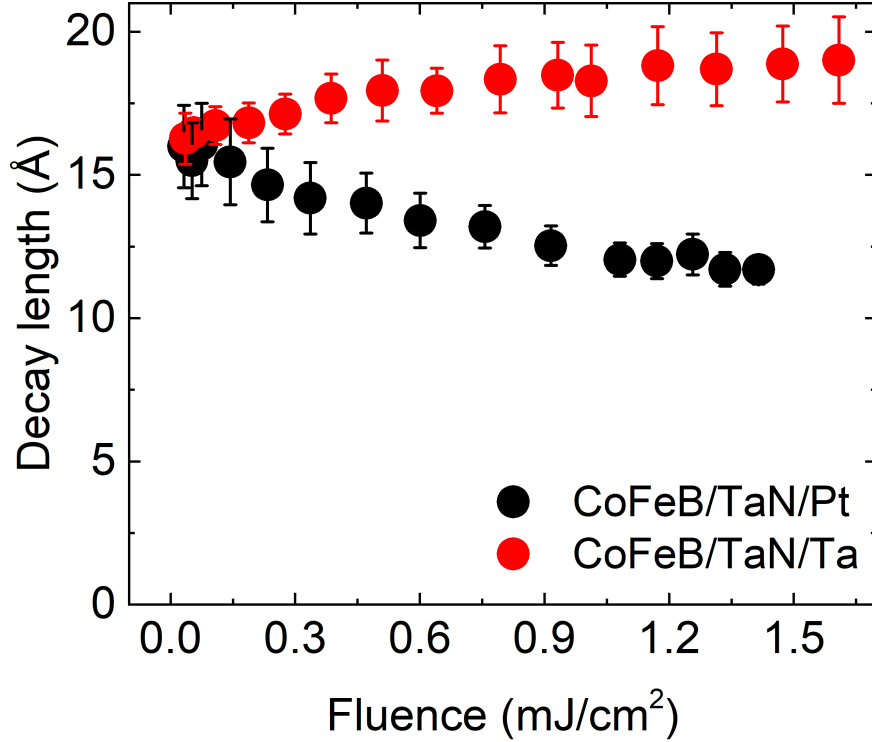
Figure 6.7: Fluence dependence of the decay length for both CoFeB/TaN/Pt and CoFeB/TaN/Ta series.

to the induced magnetism in the Pt layer.

As evidenced by density functional theory calculations in Chapter 4, the orbital hybridization at the interface between the CoFeB layer and the Pt layer induces a small net magnetic moment in the order of ∼$0.2\mu_B$ in the Pt layer. In the Stoner model, this translates into a shift between the majority and minority density of states of the Pt interfacial layer. Therefore, the number of available states for both spin channels at the Fermi level differ from each other, which influences the amount of spin current generated. For the same arguments evoked in Chapter 4, the electronic system can be considered thermalized, hence obeying a Fermi Dirac distribution. With increasing the laser fluence, the temperature of the electronic system is increased which stretches the distribution tail above the Fermi level. The assymmetry in the occupancy of the density of states for both spin channels in the Pt increases further. However, with the insertion of the TaN layer, the induced magnetic moment in the Pt layer is suppressed which restores the symmetry between the density of states for both spin channels.

Moreover, the decay length extracted for both measurement techniques differs by at least a factor of 2. Two possible effects could be the reason for such a discrepancy.

(1) In FMR, the spin polarization at the interface follows the magnetization precession and therefore pumps spin angular momentum with two components parallel and perpendicular to the film plane. Whereas, in the ultrafast spin injection technique, the spin polarization is in plane. One could conjecture that the out of plane component of the spin polarization
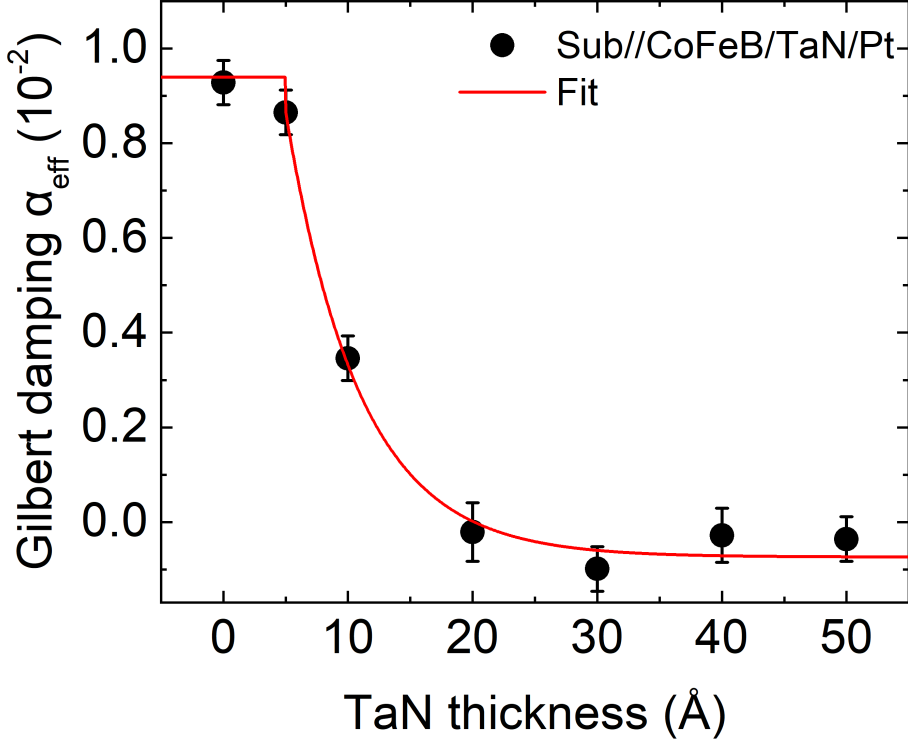
Figure 6.8: **FMR spin pumping in CoFeB/TaN/Pt**. TaN thickness dependence of the enhanced Gilbert damping in CoFeB/TaN/Pt.

experiences a different spin relaxation than its in plane counterpart.

(2) With the insertion of the TaN layer, the spin build up in the TaN/Pt generates a backflow of spin current which reduces with increasing the TaN layer thickness. This effect would result in a decay length in the order of $\frac{l_{sd}}{2}$, which is in the order of 5Å if we use the value of the spin diffusion length extracted from Section 6.1.

6.4   General discussion

The insertion of TaN between the ferromagnet and either heavy metal (Ta or Pt) yields a decay of the ISHE signal. The extracted decay lengths are similar for low laser fluences and start diverging from each other with increasing the laser fluence. While it is increasing with the laser fluence for the HM=Ta case, it decreases for the HM=Pt case.

For both cases, the extracted decay length is confined between 10Å and 20Å. These values constitute a lower bound to the spin diffusion length in TaN and agree with the value $l_{sd} \sim 10$Å, extracted from the ISHE measurements when TaN is used as a spin sink in Section 6.1.

These preliminary results need to be interpreted carefully with an adequate model in order to make claims about the relevant mechanisms taking place. For example, normalizing our ISHE signals by the sheet resistance of the samples leads to an enhanced decay length in the range of

25Å(data not shown). Indeed, the analysis is not straightforward when the resistivity of each sample needs to be taken into account. In this perspective, similar decay lengths in the range of 20Å-10Å are extracted with THz time domain spectroscopy on FM/Cu/HM(256; 257; 258) and FM/Au/HM(259) contrasting by at least one order of magnitude the spin diffusion lengths measured in these same materials by non local spin injection or GMR measurements(260; 261).

6.5   Conclusion and Outlook

We demonstrated a small spin Hall signal in TaN. Using the spin diffusion model, we extracted a spin diffusion length value of $\sim$10Å.

As a second step, we used TaN as an interlayer between the FM and a selected HM. In the case of Ta as a HM, thin TaN (thickness $\leq$ 10Å) enhances the measured ISHE. This behaviour is assigned to the recovery of the magnetic moment at the interface due to the $3d$-$5d$ orbital hybridization between the Ta and the ferromagnetic atoms. For thicker TaN, the ISHE signal decays in all systems with either HM. The decay length depends slightly on the laser fluence and span the range between 10Å and 20Å.

FMR spin pumping was also conducted for the case of Pt used as a HM and shows a decay length of $\sim$6Å which differs at least by a factor of 2 from the value extracted from the ultrafast laser induced spin injection.

We reckon that TaN could be a good candidate to investigate the mechanism of SHE as well as the related models to quantify it, relying mostly on FMR spin pumping and ISHE measurements. Indeed, for typical relevant HMs such as Pt or Ta, the values for the spin Hall angle span over one order of magnitude. Moreover, the spin relaxation processes dominating are still unclear. The difficulties in the analysis lies certainly in the modelling. For example, thickness independent resistivity of the HM and thickness dependence resistivity yield completely different conclusions about the mechanism governing the spin relaxation as well as the values of the relevant parameters.

In this regard, TaN offers tunability in its resistivity depending on the N_2 level. It can be tuned down to bare Ta resistivity in its β phase (around 100-200$\mu\Omega$.cm) to more than 1000$\mu\Omega$.cm for TaN. Seperation between the intrinsic and extrinsic contributions to the SHE, could be facilitated by theoretical calculations.

Chapter 7

Spin transport across insulating Antiferromagnet

In this chapter, by interfacing the well known half metallic ferromagnet(FM) $La_{0.67}Sr_{0.33}MnO_3$ with Pt, we demonstrate a femtosecond laser induced spin current generation in the bilayer, detected electrically as a charge current owing to the ISHE in Pt. We monitor then the transmission of the spin current by adding an insulating antiferromagnetic interlayer with various thicknesses. The antiferromagnet(AF) considered is $LaFeO_3$(LFO). A spin diffusion length of ~ 4nm is extracted, which is one order of magnitude larger than the one we demonstrated in MgO. This result demonstrate the relevance of the antiferromagnetic order in LFO for the long distance spin transport.

7.1   Motivation

Antiferromagnets are gaining further attention recently in the field of Spintronics as they hold fundamentally interesting different physics than their ferromagnet counterparts. AFs are inherently more suited for integration in spintronic devices since they produce no net magnetic field, therefore offer the advantage of robustness against stay magnetic fields. This is a very important feature since spintronic devices are scaled down to the nanometer size and crosstalk due to magnetic fields is a limiting factor that needs to be eliminated. Conseqeuntly, AFs would enable high density storage platform. Moreover, antiferromagnet exchange energy is two orders of magnitude higher than in ferromagnets, which shoots the dynamics of the Néel vector to the sub-THz up to the THz regime(262; 263; 264; 265). This feature would indeed allow the Néel staggered magnetization to be controlled, and potentially be switched within few picoseconds. An interesting breakthrough in the recent years showed the possibility to switch the orientation of the Néel vector electrically, on demand, between two orthogonal directions in CuMnAs(266; 267) as well as in Mn_2Au(268; 269). This is believed to be caused by the Néel spin-orbit torques mechanism predicted by Železný et.al.(270).

One more advantage of AFs is their abundance in the insulating phase. Not only Joule related effects are eliminated but they are also endowed with low magnetic dissipation. Besides the potential of utilizing AFs as a main write/read spintronic device, they offer a new platform

of transporting spin information. Indeed, it has been discovered recently that AF insulator α-Fe_2O_3 can transport steady state spin currents over long distances up to few microns(271). This interesting result triggered further theoretical and experimental works in order to unravel the possible scenarios behind this phenomenon. It is believed that antiferromagnetic magnons are the vectors responsible for the spin transport. Other materials have also been considered such as NiO(272; 273; 274) and CoO(275; 276; 273). Their corresponding spin diffusion lengths(SDL) have been evaluated. Conversely, the values of SDL can differ from study to the other, being scattered over two orders of magnitude from few nanometers(277; 278; 279; 280; 281; 272; 273; 274) to hundreds of nanometers(282). This is inherent to the material considered as well as the technique used. For example, in α-Fe_2O_3, non local geometry measurements, using dc spin current injection and detection through Pt wires, is used(271; 283). Another way to measure the dissipation of spin currents in AFs, is through the usage of a ferromagnet,as the spin source, and a non magnetic normal metal(NM), endowed with a spin to charge conversion property (e.g. SHE). The AF is then sandwiched in between with various thicknesses. Exciting a spin current in the structure generates a magnon current in the AF which propagates towards the NM where it can get detected as a charge current. In this configuration, it is claimed that the SDL can be affected by two magnon scattering process in the ferromagnet(282). It was also shown that the SDL is also affected by domain walls which act as spin scatterers(284). Moreover, it is suggested that a spin current pumped at a FM/AF interface is transported through the AF by two evanescent antiferromagnetic modes(285; 286).

In this study, we consider a similar approach to evaluate the spin dissipation in the insulating AF LFO. As a ferromagnet, we use the half metal LSMO and for the NM, Pt is used. We use femtosecond laser pulses to generate a spin current in the LSMO/Pt structure, which we detect electrically as a transient charge current owing to the ISHE in Pt. We monitor then the signal with the insertion of the LFO layer with various thicknesses. The signal is enhanced by $\sim 20\%$ for LFO thickness of 3nm and then decays with a decay length of $\sim$4nm.

7.2 $La_{0.67}Sr_{0.33}MnO_3$(LSMO)

$La_{0.67}Sr_{0.33}MnO_3$ or simply LSMO is a doped perovskite manganite of the form $A_{1-x}B_xMnO_3$ where A is a trivalent rare earth element and B is a divalent alkaline rare earth element(287). It is a ferromagnet that has one of the largest Curie temperature with $T_C \sim 350K$(288; 289) among its group. The ferromagnetic order in LSMO is established due to the double exchange interaction between the Mn atoms. Moreover it is a half metal, i.e. showing metallic behaviour for the majority spin channel with 3d character lying at the Fermi level and an insulating behaviour for the minority spin channel. The Fermi level lies consequently in the pseudo gap of the minority channel. This material attracts a lot of interest in the field of Spintronics for it provides nearly 100% spin polarization at the Fermi level showing Colossal Magnetoresistance(290) in magnetic tunnel junctions(291; 292).
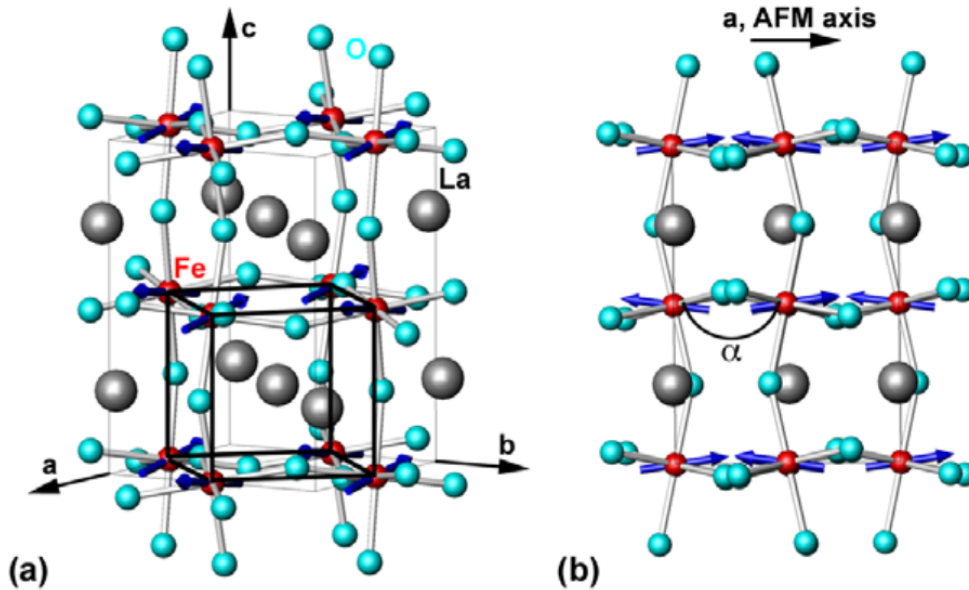
Figure 7.1: **LFO unit cell** (a) Schematic illustration of the LFO unit cell, with Fe spins pointing along the a-axis of the orthorhombic unit cell. (b) View of the buckling angle α mediated by the Fe-O-Fe superexchange coupling. (Taken from (293)).

7.3 LaFeO$_3$(LFO)

LaFeO$_3$ or LFO is a G-type antiferromagnet(294) oxide with the highest reported Néel temperature in the orthoferrite family approaching $T_N \sim 740K$(293). It has a disorted perovskite structure of the form ABO$_3$ which favours either cubic or orthorombic crystal structure depending on the substrate(295). The AF order is established through the superexchange coupling of the iron atoms through the π orbitals of the oxygen atoms. As can be seen in Fig. 7.1(b), the Fe-O-Fe bonds have a buckling angle $\alpha < 180°$. This is responsible for the enhancement of Néel temperature. As a consequence, this tilting of the FeO$_6$ octahedral is responsible for a staggered Dzyaloshinskii-Moriya (DMI), i.e. alternating sign from one atom to the other, between neighbouring spins showing even weak ferromagnetism in the bulk(296). In its bulk form, the spins are aligned along the orthorhombic a-axis(297) due to the magnetocrystalline anisotropy. In the thin film limit, the anisotropy decreases and the spins would lie in plane in the [001] and [010] pseudo cubic directions(298).

7.4 Samples

Our LSMO/LFO heterostructures were fabricated on (001)-oriented SrTiO$_3$(STO) substrates using pulsed laser deposition (248 nm excimer) during the growth[1]. Stoichiometric LSMO and LFO targets were ablated at a laser energy density of approximately $1\,\mathrm{J/cm^2}$ and a repetition rate of 5 Hz for the growth. The thickness of LFO and LSMO thin films were controlled by the pulse number of laser. During growth of LFO and LSMO, the substrate temperature was

---

[1]This process has been carried out by Dr. Chuanshou Wang.

maintained at 750 and 700 ℃ respectively at an oxygen environment of 0.13 mbar. Afterwards, the films were cooled to room temperature at 0.1 atm of oxygen with a cooling rate of 15°C/min. The LSMO is grown first with a fixed thickness of 40nm. Next, the LFO layer is grown. Multiple samples with different LFO thicknesses up to 13nm are fabricated. The Pt layer however is grown using magnetron sputtering. In this case, everytime the vacuum is broken to take out each sample of the Pulsed Layer Deposition chamber, it is immediately stored in a separate small vacuum chamber and later on, within the day, transferred to the sputtering system. The same procedure is repeated for all samples. A 4nm Pt layer is deposited on all of them. In Fig. 7.2(a), we show an XRD graph confirming the (001) orientation of both eiptaxial LSMO(30) and LFO(60) grown layers. Thicknesses are in nm. In Fig. 7.2(b), an AFM micrograph is shown for the same sample.
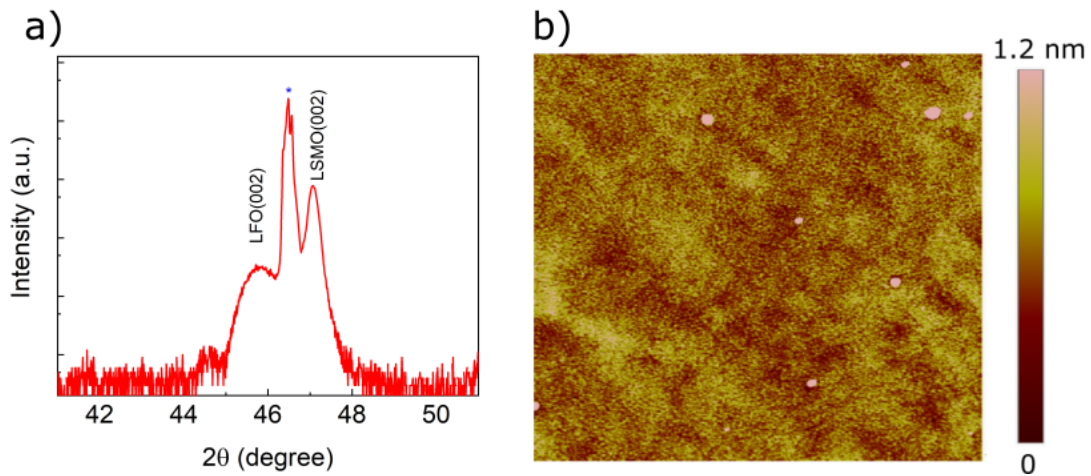
Figure 7.2: **X-ray diffraction (XRD) and Atomic force microscopy(AFM) for STO/LSMO/LFO**. $2\theta - \omega$ XRD scan of the LSMO/LFO structure grown on (001) oriented STO substrate. Two distinct peaks of LSMO(002) and LFO(002) indicate the epitaxial growth of the structure.
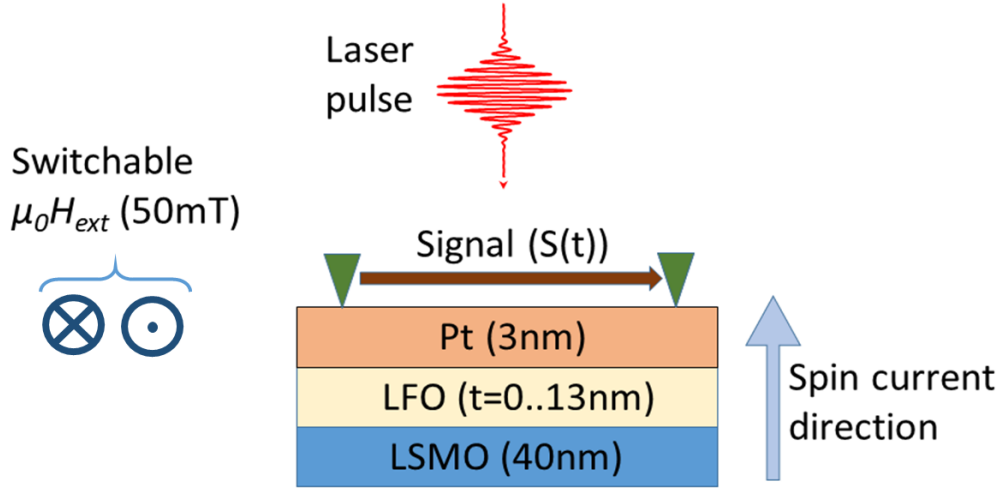
Figure 7.3: **Laser pulse excitation of the LSMO/LFO/Pt structure**. Schematics of the laser pulse excitation of the LSMO/LFO/Pt trilayer. A magnetic field is applied in plane and the rf-probe tip is positioned in contact with the sample surface conformally to ISHE symmetry.

7.5 Ultrafast laser excitation

Under a fixed external magnetic field value of 50mT, the trilayer is excited with a laser pulse with a central wavelength of 1030 nm as can be seen in the sketch in Fig. 7.3. The LSMO ferromagnet is subsequently demagnetized. This launches a spin current pulse oriented from the LSMO towards the Pt layer where it gets converted to a charge current pulse owing to the SHE in Pt. This current is measured as a voltage using coplanar rf probe connected to a sampling scope. Details about the setup are provided in Section 3.3.3.

We switch the external magnetic field direction and we note the two symmetric traces of the resultant measured charge current, shown in Fig. 7.4. We take the average difference between the two traces and show in Fig. 7.5(a) the corresponding traces for the samples with LFO as interlayer. As the LFO thickness increases, the signal amplitude is reduced. The peak amplitude is considered and in Fig. 7.5(b) is plotted against the LFO thickness. For small LFO thickness of 3nm, the signal is first enhanced by almost $\sim20\%$ and then starts decaying for larger thicknesses. An exponential fit is used and a decay length of $3.9 \pm 0.5nm$ is extracted. The fluence dependence of the amplitudes for all samples is shown in Fig. 7.6(a). Similarly, the decay length of the signal with the LFO thickness is extracted for various fluences. The result is shown in Fig. 7.6(b). The decay length increases slightly with the fluence. The same experiment has been repeated for additional photon energies of 2.2 eV and 4.4 eV. The results are qualitatevely almost unchanged. For 4.4 eV however, the increase at 3nm LFO is higher and reaches almost 40% of the reference signal. Results are shown in Fig. 7.7.

To confirm the crucial role of the antiferromagnet, the LFO interlayer has been replaced with a 3nm thick $SrTiO_3$(STO) layer and no signal has been observed. This is expected since, STO
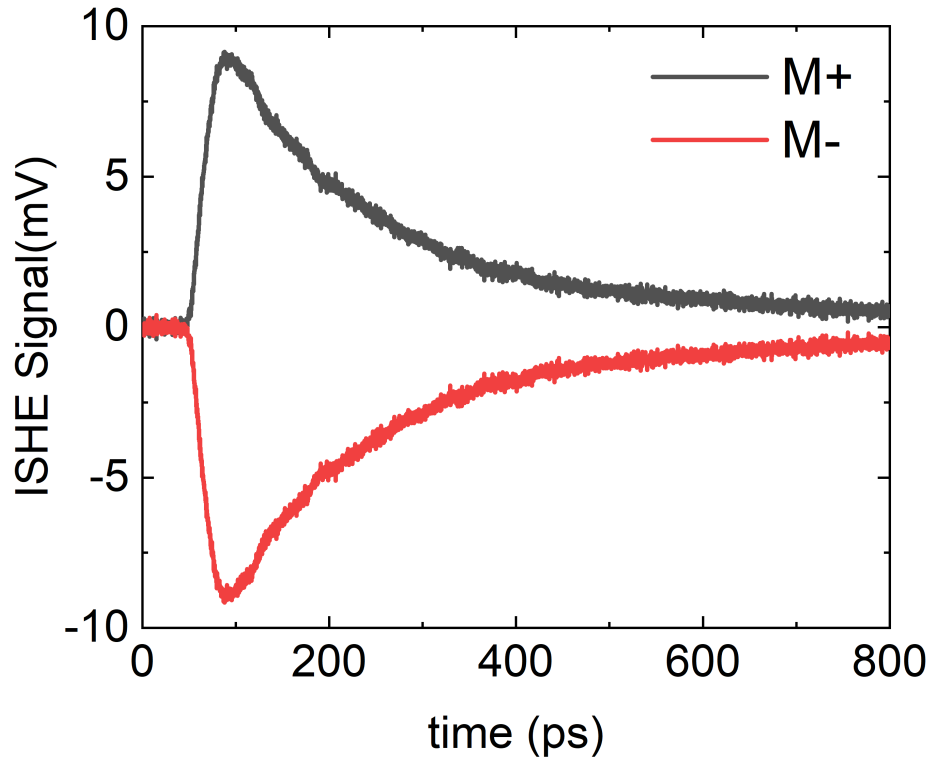
Figure 7.4: **ISHE signals in LSMO/Pt**. Time resolved ISHE signals of the LSMO/Pt reference sample for two magnetic field directions.
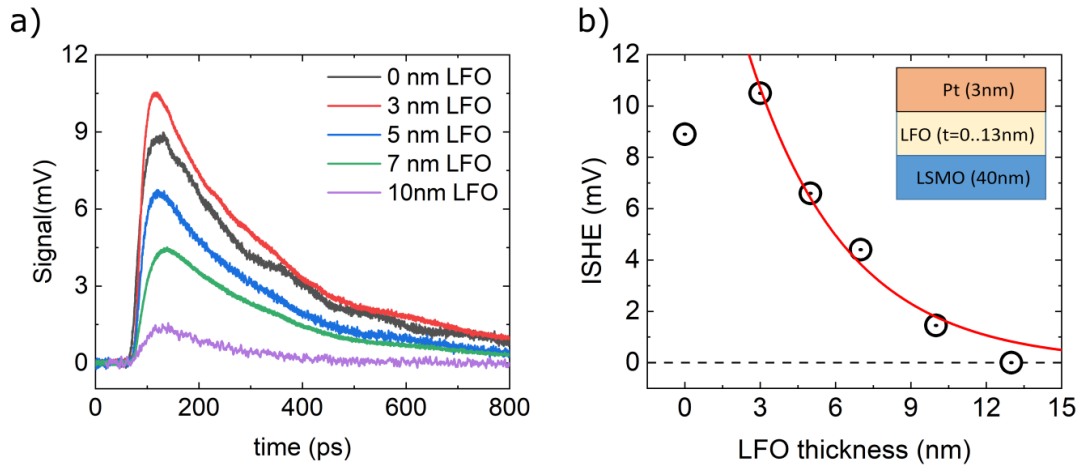
Figure 7.5: **ISHE signals in LSMO/LFO/Pt**. (a) Time resolved ISHE signals for different LFO thicknesses. (b) LFO thickness dependence of the amplitude of the measured voltage.

is an insulating oxide offering no channel of transmission for the spin current, thus suppressing its transmission.

THz time domain spectroscopy using free space electro-optic sampling detection has been conducted on all samples. Interestingly, no magnetic signal is observed. A very small signal
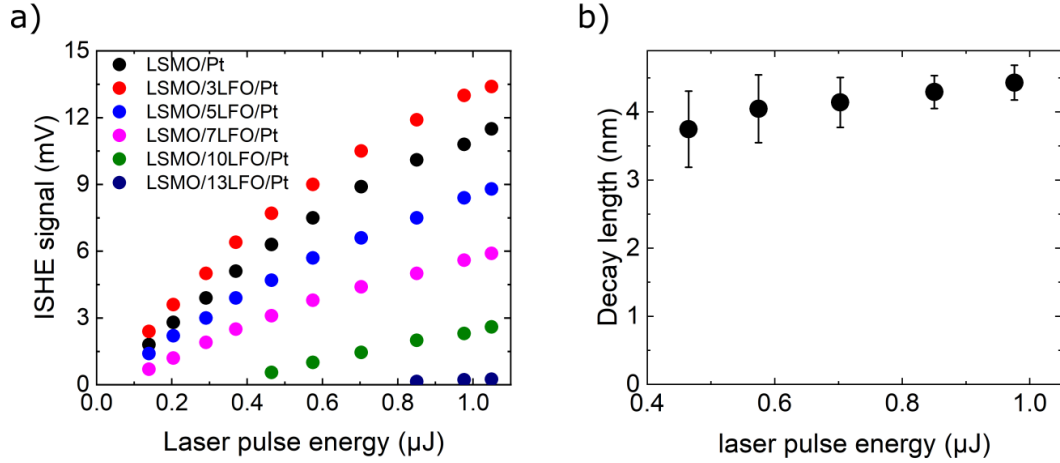
Figure 7.6: (a) Laser pulse energy dependence of the signal's amplitude for different LFO thicknesses. (b) Laser pulse energy dependence of the extracted decay length of the measured signal for LSMO/LFO/Pt.
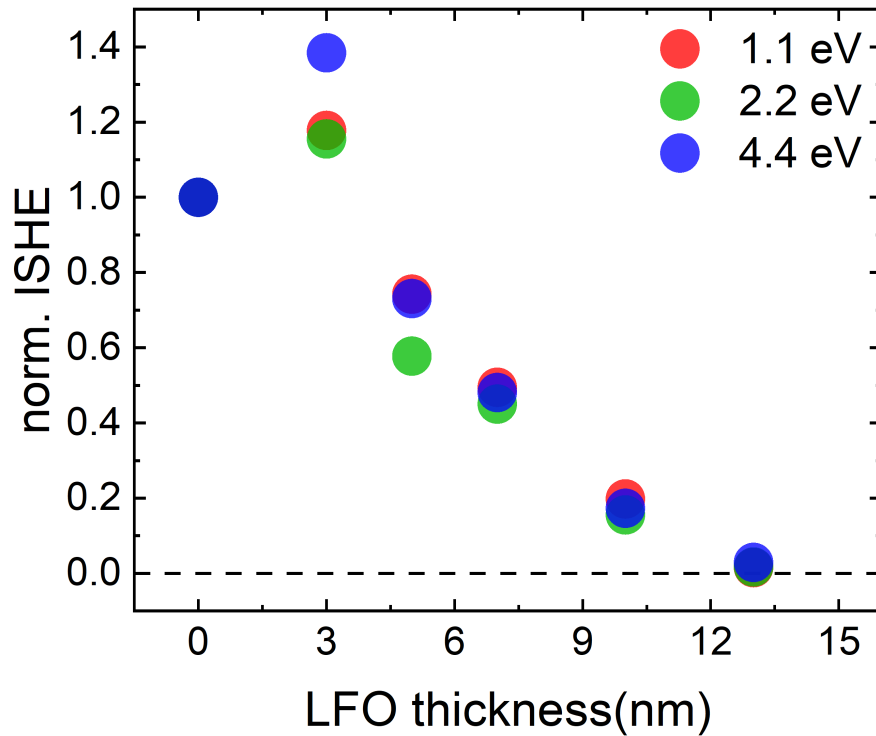
Figure 7.7: **Normalized ISHE signal amplitude in LSMO/LFO/Pt for different laser photon energies**. LFO thickness dependence of the normalized ISHE signal amplitude for different photon energies (1.1, 2.2 and 4.4 eV).

has been measured and doesn't reverse with the external magnetic field (data not shown).

7.6 Magnetometry measurements
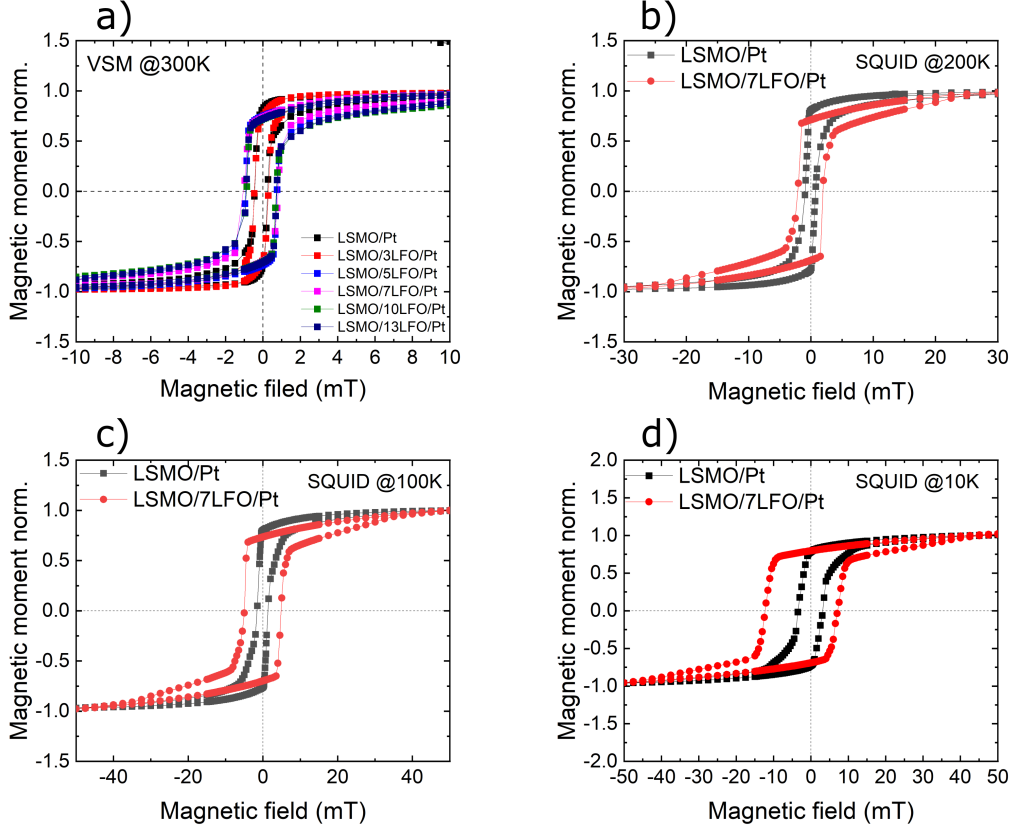
Figure 7.8: **VSM and SQUID results for LSMO/LFO/Pt**. (a) VSM normalized magnetic hysteresis loops for different thicknesses of LFO. Comparatif of SQUID normalized magnetic hysteresis loops for the reference sample without LFO and with 7nm LFO at 200K(b), 100K(c) and 10K(d).

Moreover, room temperature VSM has been carried out for all the samples and results are shown in Fig. 7.8(a). The coercive field for the reference sample is the same as the one with 3nm LFO. For higher thicknesses of the LFO layer, the coercive field is increased which could be indicative of interfacial coupling between the FM and AF. Superconducting Quantum Interference Device (SQUID) magnetometry is also conducted on LSMO/Pt and LSMO/LFO(7nm)/Pt at 200K, 100K and 10K. The results are shown in Fig. 7.8(b), (c) and (d) respectively. Both coercive fields increase with decreasing temperature. At 10K, the sample with the LFO interlayer shows a clear exchange bias.

7.7 Discussion

From earlier reports on ultrafast demagnetization in half metallic systems, it has been observed that a two step demagnetization process takes place(299; 300; 301). In the first step, subpicosecond fast demagnetization takes place. Its microscopic origin is still debatable, same as in the case of transition metals. Nevertheless, it could involve high energy electronic excitation

responsible for ultrafast spin currents (i.e. non local spin transport) or local phonon/magnon or both spin flip scatterings mediated by SOC. Upon equilibration of the electronic system via electron electron scattering, at a time scale below 1ps, the system relaxes back to dynamics governed at the Fermi level where the density of states for the minority channel is heavily reduced. Therefore, spin flips, due to intermixing between the two spin channels such as in Elliot Yafet scattering mechanism, are not allowed(300). This means that the coupling between the electron system and the spin system is effectively suppressed. According to the three temperature model, the spin system is, as a result, only coupled to the lattice and the spin dynamics are governed by spin lattice coupling which constitutes the second step of the demagnetization process with a time constant in the order of hundreds of picoseconds.

The fact that no THz signal was observed in our experimets, rules out the spin current generation originating from the first step of the demagnetization process. This leaves the second step, where it is believed that the spin system is quenched due to SOC mediated spin flip scattering(302; 303).

Interestingly, one can wonder about the spin current generation process. Indeed, this generation process is taking place in the second step of the demagnetization and therefore cannot be assigned to the non local ballistic, diffusive or superdiffusive electronic transport. Moreover, this is in line with our photon dependent energy measurements. Also, if the spin degree of freedom is transferred only to the lattice via spin phonon scattering, then no mechanism for spin current generation is possible. Another coupling channel is therefore needed.

One possible channel of spin transport is through the magnonic system. Indeed, the laser pulse excites magnons through the ultrafast spin Seebeck effect. The electronic temperarture of the Pt layer and the magnonic temperature difference acts as a driving force for the generation of the spin current at the interface:

$$j_s = K(T_e^{Pt} - T_m^{LSMO}) \tag{7.1}$$

Where K is the spin Seebeck coefficient.

With the insertion of the AF LFO layer, we note a larger coercive field compared to the reference sample, without the LFO layer. This agrees well with earlier reports(304; 305) and is indicative of the exchange coupling between the AF and FM. Upon coupling to temperatures around 10K, a clear exchange bias is observed, in agreement with the results in(304).

Furthermore, we confirm the long distance transport of spin current. Indeed, the SDL is found to be around 4nm which goes beyond the limit of what can be expected from a bare insulating material, as demonstrated in Chapter 4. This is further confirmed with a control sample where LFO is replaced by a 3nm layer of STO. In this case, no signal is observed proving the suppression of the spin current transmission. However, the 4nm value of the SDL differs from what has been reported in bulk α-Fe$_2$O$_3$(271; 283) crystal as well as thin films. However it agrees well with reported values for CoO(275) or NiO(279; 280; 281). As aforementioned, the SDL in insulating antiferromagnets depends highly on their magnetic domain structure as domain walls can scatter spin waves and therefore effectively reduce the propagation length of the spin current(284). Hence, more knowledge about the magnetic structure of our system is needed.

It is well established that the LSMO/LFO bilayer system exhibit a spin flop coupling at

the interface(306; 305; 307; 308; 304; 309), i.e. the magnetic moment of the FM is 90°oriented relative to the Néel vector of the AF. Additional measurements with rotating sample azimuthal angle does not alter the ISHE results. This would be expected if such a spin flop coupling is in fact present in our samples. This points to the fact that the magnetization of the ferromagnet and the Néel vector could be locked together. Furthermore, it is well known that, in the bulk LFO, a small spin canting due to the Dzyaloschinski Moriya interaction (DMI)(296) is present. In the thin film limit, it has been already reported that this canting could be stronger and responsible for an exchange bias(304). In our structure, if the ferromagnet's magnetization is saturated along the [001] direction, then the Néel vector points in the [010] direction. The DMI would induce a small rotation around the (001) axis, resulting in a canting of the spins, hence acquiring a small component on the [001] direction. All these points need to be addressed and probed to have a better understanding of the spin current transmission at the interface as well as in the antiferromagnetic layer.

Moreover, the enhancement of the ISHE signal has been reported several times in the literature for the AF NiO(273; 272; 280; 277; 278) for similar thicknesses as the one reported in our study. (285) claims that this is indeed an amplification of the spin current, i.e. more spins are pumped out of the lattice, which happens for a certain thickness of the AF.

7.8 Conclusion and Outlook

We have demonstrated the ultrafast spin current generation in the half metallic ferromagnet LSMO, when interfaced with the SHE heavy metal Pt. This spin current generation process is not trivial as it doesn't take place in the subpicosecond time scale. It definitively accompanies the second step of the demagnetization, where the spin and the electronic subsystems are believed to be decoupled. This leaves the spin Seebeck effect giving rise to elementary exciations of the magnetic system, called magnons. To the best of our knowledge, no such spin current generation in this *slow* demagnetization regime (in comparison to the one in the subpicosecond time scale) has been reported so far.

As a next step, we demonstrated the spin current dissipation in LFO extracting a SDL of ∼4nm. We also reported an enhancement of the measured ISHE signal for an LFO thickness of 3nm.

The coupling between the LSMO and LFO layers at the interface is still unknown in our system. Nonetheless, we report a uniaxial exchange bias at low temperatures.

As a next step, it is needed to determine the Néel vector orientation using x-ray magnetic linear dichroism for all samples. This would give insights on the FM/AF coupling at the interface and therefore more information about the coupling process between the ferromagnetic magnons and the magnon current in the AF.

Chapter 8

Conclusion and future perspectives

8.1 Summary

- Chapter 4: A typical transition metal FM CoFeB interfaced with a 5d HM is considered. An MgO interlayer is inserted at the FM/HM interface and different samples with various MgO thicknesses were fabricated using magnetron sputtering. Two samples series with either Pt or Ta as a HM were considered. By performing ultrafast optical spin injection and ISHE electrical detection, we showed that MgO reduces substantially the spin current transmission with a spin diffusion length of 2Å. Moreover, for ultrathin MgO layers ~ 2Å, we showed a significant enhancement of the ISHE signal for the case when Ta is used as a HM. This effect is absent when Pt is used as a HM. By performing DFT calculations in conjunction with Landauer Bütticker transport formalism, we calculated the spin currents in Fe/MgO/Pt and Fe/MgO/Ta. The calculated currents reproduce well the ISHE data. Moreover, we were able to elucidate the origin of the apparent enhancement of the ISHE signal in the case of HM=Ta. Indeed, we found that due to 3d-5d orbital hybridization effects, the magnetic moment at the interface is heavily reduced. This effect is present for all 5d elements with a less than half filled d shell. By performing FMR spin pumping, we proved that considering a certain magnetic dead layer accounts for all our results and therefore no SML is needed. Furthermore, the striking correspondence between the ISHE and FMR data for the case of HM=PT strengthens the argument that no notable SML is present in our system.

- Chapter 5: We optimized the on-chip performance of a typical STE. We considered a CoFeB/Pt bilayer as a standard STE. We fabricated a multilayer with different repeats of the bilayer separated by thin MgO layers. We performed ultrafast optical excitation of the multilayers driving spin currents in each bilayer. These spin currents are converted to transient charge currents. We have conducted two different measurement schemes where we measure the on-chip electric current and the free space radiation. With increasing the number of repeats, we demonstrated that the on-chip signal is enhanced up by a factor

110

of two until saturation for a number of repeats N=4. Whereas, the free space radiation signal slightly increases by 30% for two repeats and starts decreasing continuously with increasing further the number of repeats. Based on a model, we confirmed that this difference is accounted for by the impedance mismatch between the multilayer and the medium of the propagation for the THz wave.

- Chapter 6: We fabricated samples consisting of CoFeB/TaN bilayers with various thicknesses of TaN. By performing laser induced ultrafast spin injection and subsequent electrical detection, we showed that the TaN layer exhibit a small ISHE signal measurable for TaN thicknesses exceeding 50Å for nominal laser fluences. From thickness dependent measurements of the ISHE, we extracted a spin diffusion length equal to ~10Å. Next, TaN is considered as an interlayer inserted between CoFeB and two choices of HMs: Pt and Ta. The measured ISHE is then monitored with changing the thickness of TaN. For the case of Ta=HM, ultrathin TaN layer with a thickness ≤10Å enhances the signal significantly up to 80%. We believe that this enhancement is due to the magnetic moment recovery at the interface, also reported and explained based on theoretical consideration in Chapter 4. For the case of HM=Pt, no such effect is present which confirms further the aforementioned argument. With increasing the TaN thickness, the ISHE signal eventually decays for both systems with a characteristic length confined between 10Å and 20Å. These values constitute a lower bound for the spin diffusion length in TaN. Interestingly, the decay lengths are slightly different between the two systems where only the heavy metal is changed. Moreover, they show opposite trends of the laser fluence dependence of their corresponding decay lengths. Interestingly, the TaN thickness dependence of FMR spin pumping data, conducted on the samples with HM=Pt, shows a similar decay of the enhanced effective damping but with a smaller value ~6Å.

- Chapter 7: We performed femtosecond laser pulse excitation with electrical detection on the half metal ferromagnet LSMO interfaced with a Pt layer. Using a sampling oscilloscope with temporal resolution of 20ps, we clearly measured a signal that switches with the magnetic field confirming the spin current generation process in the half metal. Since no signal was detected using free space electro-optic detection technique, we confirmed that the spin current generation process should take place in the second slower step of the demagnetization of the LSMO. Next, we monitor the behaviour of the ISHE signal with the insertion of the antiferromagnetic insulator LFO. The ISHE signal is enhanced at an LFO thickness of 3nm and starts decaying with increasing the thickness. We extracted a spin diffusion length of ~4nm. This value is one order of magnitude higher than the one of MgO. This confirms that the antiferromagnetic ordering is responsible for long distance spin transport.

8.2   General remarks and future perspectives

- A typical FM/HM bilayer is at the heart of spintronics applications. Both layers can exchange spin angular momentum via spin currents. Besides the intrinsic properties of the materials to generate or convert spin currents, the interface is of crucial importance

for efficient spin current transmission or equivalently spin transfer via spin torque. We have indeed shown that orbital hybridization effects at the interface can alter the spin polarization and as a result the spin current transmission. We therefore point out to the interface transparency as a figure of merit rather than ascribing the limitation of spin current to SML. Consequently, as we have shown, orbital hybridization related phenomena results in a significant discrepancy between the FMR spin pumping data and ISHE measurements, which are two techniques widely used, simultaneously, to characterize spin Hall materials via thickness dependent measurements. In this case, SML is usually accounted for to properly fit the data leading to the extraction of relevant parameters such as spin Hall angle and spin diffusion length(310; 211). However, the resistivity is also a crucial parameter for such an analysis(311). For example, the same analysis with a thickness dependent resistivity yields an SML factor $\delta \sim 2\%$ in β-Ta(312), which is one order of magnitude less than in(310).

Depending for example on the dominating spin relaxation mechanism, the spin diffusion length scales differently with the resistivity (Elliot-Yafet or D'yakonov Perel). Even for the case of Pt, which is the most extensively studied spin Hall material, it is still unclear if one of the above mechanisms is dominating or both are present(311; 313; 314; 315; 316). Therefore, considering a constant(i.e. grain boundaries and surface scattering are neglected) or thickness dependent resistivity yields a constant or thickness dependent spin diffusion length. Along this perspective, it has been suggested recently that the spin diffusion length in Pt depends on its out of plane resistivity(316). To point out further the importance of the resistivity of the layers, let's consider the systems studied in this thesis.

Inserting oxide layer such as MgO at the FM/HM interface doesn't alter the sheet resistance of the studied samples and therefore we don't have to make extra assumptions for our analysis. However, in the case of TaN as an interlayer, the resistivity of the stack changes with the TaN thickness and the analysis becomes more complicated. Surprisingly, the MgO thickness dependence of the FMR and ISHE data, for the CoFeB/MgO/Pt, match very well. However, a large discrepancy is found when TaN is used an interlayer. This difference hints into the relevance of the resistivity which correlates directly to the spin relaxation mechanism in place.

The usage of TaN as an interlayer offers a great advantage of tuning its resistivity by changing the N_2 level. Performing FMR and ISHE measurements on different TaN_x layers would shed light on the differences between the mechanisms involved in the two techniques.

So far the FMR spin pumping performed throughout this thesis has been in the in-plane geometry. It would be interesting to conduct out-of-plane FMR spin pumping measurements. The main difference between its in-plane counterpart is the directions of the magnetization components that are "pumped" through the interface. In the out-of-plane geometry, all the pumped components are in plane, in contrast to the in-plane configuration where one out-of-plane component is present. This could confirm whether there is any difference between the out-of-plane and in-plane spin relaxation rates.

- In the last chapter, we demonstrated clearly spin current generation in the LSMO/Pt bilayer on a time scale of hundred of picoseconds. Conversely, sub-picosecond THz emission has been shown in both half metals $Co_2FeAl(317)$ and $Fe_3O_4(318)$ interfaced with Pt. These materials exhibit less half metallicity than LSMO and as demonstrated by Müller et.al.(300), the demagnetization time depends on the spin polarization at the Fermi level. It would be then required to perform time resolved magneto-optical Kerr effect and reflectvity measurements on our LSMO/Pt bilayer in order to gain insights about the demagnetization behaviour.

  Confirming that the spin current generation is linked to the second long step of the demagnetization translates to confirming the link between magnon excitations and SOC mediated spin lattice coupling. This goes in line with a suggested mechanism of ultrafast demagnetization combining the simultaneous action of electron phonon and electron magnon scattering(155). Our results show the advantage of using electric detection of subsequent ultrafast demagnetization induced spin currents for half metallic systems. A promising route is to explore, using our technique, Heusler half metallic materials which offer a big range of tunability of the spin polarization at the Fermi level(301), hence the demagnetization time. This could act as a switch turning on and off the sub picosecond processes.

- We have also clearly demonstrated a nanometer scale transport of spin currents in the antiferromagnetic insulator LFO. Even though the coupling between between the LSMO and LFO is still unknown, one first step is to use x-ray linear magnetic dichroism to resolve such a coupling. Another route worth exploring, is to anneal the samples in the presence of a magnetic field which has been reported to give a handle on the exchange bias(304). Therefore, investigation of the strength of the exchange bias and its correlation with the spin transport could be realized. Furthermore, Raman spectroscopy can be used to determine the magnon modes in our samples. This could potentially shed light on the evanescent magnon modes responsible for the spin transport.

Bibliography

[1] E. Beaurepaire, J.-C. Merle, A. Daunois, and J.-Y. Bigot, "Ultrafast spin dynamics in ferromagnetic nickel," *Physical review letters*, vol. 76, no. 22, p. 4250, 1996.

[2] S. R. Tauchert, M. Volkov, D. Ehberger, D. Kazenwadel, M. Evers, H. Lange, A. Donges, A. Book, W. Kreuzpaintner, U. Nowak, *et al.*, "Polarized phonons carry angular momentum in ultrafast demagnetization," *Nature*, vol. 602, no. 7895, pp. 73–77, 2022.

[3] C. Dornes, Y. Acremann, M. Savoini, M. Kubli, M. J. Neugebauer, E. Abreu, L. Huber, G. Lantz, C. A. Vaz, H. Lemke, *et al.*, "The ultrafast einstein–de haas effect," *Nature*, vol. 565, no. 7738, pp. 209–212, 2019.

[4] M. Battiato, K. Carva, and P. M. Oppeneer, "Superdiffusive spin transport as a mechanism of ultrafast demagnetization," *Physical review letters*, vol. 105, no. 2, p. 027203, 2010.

[5] T. Seifert, S. Jaiswal, U. Martens, J. Hannegan, L. Braun, P. Maldonado, F. Freimuth, A. Kronenberg, J. Henrizi, I. Radu, E. Beaurepaire, Y. Mokrousov, P. M. Oppeneer, M. Jourdan, G. Jakob, D. Turchinovich, L. M. Hayden, M. Wolf, M. Münzenberg, M. Kläui, and T. Kampfrath, "Efficient metallic spintronic emitters of ultrabroadband terahertz radiation," Nature Photonics, vol. 10, pp. 483–488, Jul 2016.

[6] P. M. Chaikin, T. C. Lubensky, and T. A. Witten, *Principles of condensed matter physics*, vol. 10. Cambridge university press Cambridge, 1995.

[7] S. Blundell, "Magnetism in condensed matter," 2003.

[8] J. Stöhr and H. C. Siegmann, "Magnetism," *Solid-State Sciences. Springer, Berlin, Heidelberg*, vol. 5, p. 236, 2006.

[9] N. W. Ashcroft and N. D. Mermin, "Solid state physics (saunders college, philadelphia, 1976)," *Appendix N*, vol. 166, p. 87, 2010.

[10] C. Kittel and P. McEuen, *Kittel's Introduction to Solid State Physics*. John Wiley & Sons, 2018.

[11] J. M. Coey, *Magnetism and magnetic materials*. Cambridge university press, 2010.

[12] G. T. Rado and H. Suhl, *Magnetism: A Treatise on Modern Theory and Materials. Exchange Interactions Among Itinerant Electrons/by Conyers Herring*. Academic Press, 1966.

114

[13] J. Kübler, *Theory of itinerant electron magnetism*, vol. 106. Oxford University Press, 2017.

[14] L. Sagnotti, *Magnetic Anisotropy*, pp. 717–729. Dordrecht: Springer Netherlands, 2011.

[15] R. C. O'handley, *Modern magnetic materials: principles and applications*. Wiley, 2000.

[16] A. Hubert and R. Schäfer, *Magnetic domains: the analysis of magnetic microstructures*. Springer Science & Business Media, 2008.

[17] W. Thomson, "Xix. on the electro-dynamic qualities of metals:—effects of magnetization on the electric conductivity of nickel and of iron," *Proceedings of the Royal Society of London*, no. 8, pp. 546–550, 1857.

[18] I. Campbell and A. Fert, "Transport properties of ferromagnets," *Handbook of Ferromagnetic Materials*, vol. 3, pp. 747–804, 1982.

[19] A. Fert and F. N. Van Dau, "Spintronics, from giant magnetoresistance to magnetic skyrmions and topological insulators," *Comptes Rendus Physique*, vol. 20, no. 7-8, pp. 817–831, 2019.

[20] M. N. Baibich, J. M. Broto, A. Fert, F. N. Van Dau, F. Petroff, P. Etienne, G. Creuzet, A. Friederich, and J. Chazelas, "Giant magnetoresistance of (001)fe/(001)cr magnetic superlattices," *Phys. Rev. Lett.*, vol. 61, pp. 2472–2475, Nov 1988.

[21] G. Binasch, P. Grünberg, F. Saurenbach, and W. Zinn, "Enhanced magnetoresistance in layered magnetic structures with antiferromagnetic interlayer exchange," *Phys. Rev. B*, vol. 39, pp. 4828–4830, Mar 1989.

[22] S. S. P. Parkin, R. Bhadra, and K. P. Roche, "Oscillatory magnetic exchange coupling through thin copper layers," *Phys. Rev. Lett.*, vol. 66, pp. 2152–2155, Apr 1991.

[23] S. Parkin, X. Jiang, C. Kaiser, A. Panchula, K. Roche, and M. Samant, "Magnetically engineered spintronic sensors and memory," *Proceedings of the IEEE*, vol. 91, no. 5, pp. 661–680, 2003.

[24] H. Van den Berg, R. Coehoorn, M. Gijs, P. Grünberg, T. Rasing, and K. Röll, *Magnetic multilayers and giant magnetoresistance: fundamentals and industrial applications*, vol. 37. Springer Science & Business Media, 2013.

[25] E. Hirota, E. Hirota, H. Sakakima, K. Inomata, and K. Inomata, *Giant magnetoresistance devices*, vol. 40. Springer Science & Business Media, 2002.

[26] S. Parkin, K. Roche, M. Samant, P. Rice, R. Beyers, R. Scheuerlein, E. O'sullivan, S. Brown, J. Bucchigano, D. Abraham, *et al.*, "Exchange-biased magnetic tunnel junctions and application to nonvolatile magnetic random access memory," *Journal of Applied Physics*, vol. 85, no. 8, pp. 5828–5833, 1999.

[27] W. Pratt Jr, S.-F. Lee, J. Slaughter, R. Loloee, P. Schroeder, and J. Bass, "Perpendicular giant magnetoresistances of ag/co multilayers," *Physical review letters*, vol. 66, no. 23, p. 3060, 1991.

[28] P. M. Tedrow and R. Meservey, "Spin-dependent tunneling into ferromagnetic nickel," *Physical Review Letters*, vol. 26, no. 4, p. 192, 1971.

[29] P. Tedrow and R. Meservey, "Spin polarization of electrons tunneling from films of fe, co, ni, and gd," *Physical Review B*, vol. 7, no. 1, p. 318, 1973.

[30] R. Meservey and P. Tedrow, "Surface relaxation times of conduction-electron spins in superconductors and normal metals," *Physical Review Letters*, vol. 41, no. 12, p. 805, 1978.

[31] R. Meservey and P. Tedrow, "Spin-polarized electron tunneling," *Physics reports*, vol. 238, no. 4, pp. 173–243, 1994.

[32] S. Parkin, "Origin of enhanced magnetoresistance of magnetic multilayers: Spin-dependent scattering from magnetic interface states," *Physical review letters*, vol. 71, no. 10, p. 1641, 1993.

[33] N. F. Mott, "The resistance and thermoelectric properties of the transition metals," *Proceedings of the Royal Society of London. Series A-Mathematical and Physical Sciences*, vol. 156, no. 888, pp. 368–382, 1936.

[34] N. F. Mott, "Electrons in transition metals," *Advances in Physics*, vol. 13, no. 51, pp. 325–422, 1964.

[35] S. Fukami, T. Anekawa, C. Zhang, and H. Ohno, "A spin–orbit torque switching scheme with collinear magnetic easy axis and current configuration," *nature nanotechnology*, vol. 11, no. 7, pp. 621–625, 2016.

[36] M. Julliere, "Tunneling between ferromagnetic films," *Physics letters A*, vol. 54, no. 3, pp. 225–226, 1975.

[37] J. S. Moodera, L. R. Kinder, T. M. Wong, and R. Meservey, "Large magnetoresistance at room temperature in ferromagnetic thin film tunnel junctions," *Physical review letters*, vol. 74, no. 16, p. 3273, 1995.

[38] T. Miyazaki and N. Tezuka, "Giant magnetic tunneling effect in fe/al2o3/fe junction," *Journal of magnetism and magnetic materials*, vol. 139, no. 3, pp. L231–L234, 1995.

[39] S. Yuasa, T. Nagahama, A. Fukushima, Y. Suzuki, and K. Ando, "Giant room-temperature magnetoresistance in single-crystal fe/mgo/fe magnetic tunnel junctions," *Nature materials*, vol. 3, no. 12, pp. 868–871, 2004.

[40] S. Yuasa, A. Fukushima, T. Nagahama, K. Ando, and Y. Suzuki, "High tunnel magnetoresistance at room temperature in fully epitaxial fe/mgo/fe tunnel junctions due to coherent spin-polarized tunneling," *Japanese Journal of Applied Physics*, vol. 43, no. 4B, p. L588, 2004.

[41] S. S. Parkin, C. Kaiser, A. Panchula, P. M. Rice, B. Hughes, M. Samant, and S.-H. Yang, "Giant tunnelling magnetoresistance at room temperature with mgo (100) tunnel barriers," *Nature materials*, vol. 3, no. 12, pp. 862–867, 2004.

[42] X. Zhang and W. Butler, "Band structure, evanescent states, and transport in spin tunnel junctions," *Journal of Physics: Condensed Matter*, vol. 15, no. 41, p. R1603, 2003.

[43] W. H. Butler, "Tunneling magnetoresistance from a symmetry filtering effect," *Science and Technology of Advanced Materials*, vol. 9, no. 1, p. 014106, 2008.

[44] W. Butler, X.-G. Zhang, T. Schulthess, and J. MacLaren, "Reduction of electron tunneling current due to lateral variation of the wave function," *Physical Review B*, vol. 63, no. 9, p. 092402, 2001.

[45] W. Butler, X.-G. Zhang, T. Schulthess, and J. MacLaren, "Spin-dependent tunneling conductance of fe— mgo— fe sandwiches," *Physical Review B*, vol. 63, no. 5, p. 054416, 2001.

[46] J. MacLaren, X.-G. Zhang, W. Butler, and X. Wang, "Layer kkr approach to bloch-wave transmission and reflection: Application to spin-dependent tunneling," *Physical Review B*, vol. 59, no. 8, p. 5470, 1999.

[47] "Ucl spintronics group." `https://www.ucl.ac.uk/spintronics/`. Accessed: 2022-03-05.

[48] J. C. Slonczewski, "Current-driven excitation of magnetic multilayers," *Journal of Magnetism and Magnetic Materials*, vol. 159, no. 1-2, pp. L1–L7, 1996.

[49] L. Berger, "Emission of spin waves by a magnetic multilayer traversed by a current," *Physical Review B*, vol. 54, no. 13, p. 9353, 1996.

[50] Y. B. Bazaliy, B. Jones, and S.-C. Zhang, "Modification of the landau-lifshitz equation in the presence of a spin-polarized current in colossal-and giant-magnetoresistive materials," *Physical Review B*, vol. 57, no. 6, p. R3213, 1998.

[51] M. Tsoi, A. Jansen, J. Bass, W.-C. Chiang, M. Seck, V. Tsoi, and P. Wyder, "Excitation of a magnetic multilayer by an electric current," *Physical Review Letters*, vol. 80, no. 19, p. 4281, 1998.

[52] E. Myers, D. Ralph, J. Katine, R. Louie, and R. Buhrman, "Current-induced switching of domains in magnetic multilayer devices," *Science*, vol. 285, no. 5429, pp. 867–870, 1999.

[53] J. Z. Sun, "Spin-current interaction with a monodomain magnetic body: A model study," *Physical Review B*, vol. 62, no. 1, p. 570, 2000.

[54] X. Waintal, E. B. Myers, P. W. Brouwer, and D. Ralph, "Role of spin-dependent interface scattering in generating current-induced torques in magnetic multilayers," *Physical Review B*, vol. 62, no. 18, p. 12317, 2000.

[55] M. D. Stiles and A. Zangwill, "Anatomy of spin-transfer torque," *Physical Review B*, vol. 66, no. 1, p. 014407, 2002.

[56] K. Bussmann, G. Prinz, S.-F. Cheng, and D. Wang, "Switching of vertical giant magnetoresistance devices by current through the device," *Applied physics letters*, vol. 75, no. 16, pp. 2476–2478, 1999.

[57] J. Katine and E. E. Fullerton, "Device implications of spin-transfer torques," *Journal of Magnetism and Magnetic Materials*, vol. 320, no. 7, pp. 1217–1226, 2008.

[58] Z. Zeng, G. Finocchio, and H. Jiang, "Spin transfer nano-oscillators," *Nanoscale*, vol. 5, no. 6, pp. 2219–2231, 2013.

[59] Y. K. Kato, R. C. Myers, A. C. Gossard, and D. D. Awschalom, "Observation of the spin hall effect in semiconductors," *science*, vol. 306, no. 5703, pp. 1910–1913, 2004.

[60] J. Wunderlich, B. Kaestner, J. Sinova, and T. Jungwirth, "Experimental observation of the spin-hall effect in a two-dimensional spin-orbit coupled semiconductor system," *Phys. Rev. Lett.*, vol. 94, p. 047204, Feb 2005.

[61] V. M. Edelstein, "Spin polarization of conduction electrons induced by electric current in two-dimensional asymmetric electron systems," *Solid State Communications*, vol. 73, no. 3, pp. 233–235, 1990.

[62] E. Rashba, "Symmetry of energy bands in crystals of wurtzite type. 1. symmetry of bands disregarding spin-orbit interaction," *Soviet Physics-Solid State*, vol. 1, no. 3, pp. 368–380, 1959.

[63] E. Rashba and V. Sheka, "Symmetry of energy bands in crystals of wurtzite type ii. symmetry of bands with spin-orbit interaction included," 2015.

[64] L. Fu and C. L. Kane, "Topological insulators with inversion symmetry," *Physical Review B*, vol. 76, no. 4, p. 045302, 2007.

[65] W. Zhang, P. Maldonado, Z. Jin, T. S. Seifert, J. Arabski, G. Schmerber, E. Beaurepaire, M. Bonn, T. Kampfrath, P. M. Oppeneer, *et al.*, "Ultrafast terahertz magnetometry," *Nature communications*, vol. 11, no. 1, pp. 1–9, 2020.

[66] E. H. Hall *et al.*, "On a new action of the magnet on electric currents," *American Journal of Mathematics*, vol. 2, no. 3, pp. 287–292, 1879.

[67] E. H. Hall, "Xviii. on the "rotational coefficient" in nickel and cobalt," *The London, Edinburgh, and Dublin Philosophical Magazine and Journal of Science*, vol. 12, no. 74, pp. 157–172, 1881.

[68] R. Karplus and J. Luttinger, "Hall effect in ferromagnetics," *Physical Review*, vol. 95, no. 5, p. 1154, 1954.

[69] M. V. Berry, "Quantal phase factors accompanying adiabatic changes," *Proceedings of the Royal Society of London. A. Mathematical and Physical Sciences*, vol. 392, no. 1802, pp. 45–57, 1984.

[70] R. Kubo, "Statistical-mechanical theory of irreversible processes. i. general theory and simple applications to magnetic and conduction problems," *Journal of the Physical Society of Japan*, vol. 12, no. 6, pp. 570–586, 1957.

[71] N. Nagaosa, J. Sinova, S. Onoda, A. H. MacDonald, and N. P. Ong, "Anomalous hall effect," *Reviews of modern physics*, vol. 82, no. 2, p. 1539, 2010.

[72] F. Haldane, "Berry curvature on the fermi surface: Anomalous hall effect as a topological fermi-liquid property," *Physical review letters*, vol. 93, no. 20, p. 206602, 2004.

[73] J. Smit, "The spontaneous hall effect in ferromagnetics i," *Physica*, vol. 21, no. 6-10, pp. 877–887, 1955.

[74] J. Smit, "The spontaneous hall effect in ferromagnetics ii," *Physica*, vol. 24, no. 1-5, pp. 39–51, 1958.

[75] L. Berger, "Influence of spin-orbit interaction on the transport processes in ferromagnetic nickel alloys, in the presence of a degeneracy of the 3d band," *Physica*, vol. 30, no. 6, pp. 1141–1159, 1964.

[76] J. Hirsch, "Spin hall effect," *Physical review letters*, vol. 83, no. 9, p. 1834, 1999.

[77] J. Sinova, S. O. Valenzuela, J. Wunderlich, C. Back, and T. Jungwirth, "Spin hall effects," *Reviews of Modern Physics*, vol. 87, no. 4, p. 1213, 2015.

[78] A. Hoffmann, "Spin hall effects in metals," *IEEE transactions on magnetics*, vol. 49, no. 10, pp. 5172–5193, 2013.

[79] J. Wunderlich, B. Kaestner, J. Sinova, and T. Jungwirth, "Experimental discovery of the spin-hall effect in rashba spin-orbit coupled semiconductor systems," *arXiv preprint cond-mat/0410295*, 2004.

[80] S. Murakami, N. Nagaosa, and S.-C. Zhang, "Dissipationless quantum spin current at room temperature," *Science*, vol. 301, no. 5638, pp. 1348–1351, 2003.

[81] J. Sinova, D. Culcer, Q. Niu, N. Sinitsyn, T. Jungwirth, and A. H. MacDonald, "Universal intrinsic spin hall effect," *Physical review letters*, vol. 92, no. 12, p. 126603, 2004.

[82] J. Sinova, S. O. Valenzuela, J. Wunderlich, C. H. Back, and T. Jungwirth, "Spin hall effects," Rev. Mod. Phys., vol. 87, pp. 1213–1260, Oct 2015.

[83] F. Bloch, "Nuclear induction," *Physical review*, vol. 70, no. 7-8, p. 460, 1946.

[84] H. C. Torrey, "Bloch equations with diffusion terms," *Physical review*, vol. 104, no. 3, p. 563, 1956.

[85] D. Pines and C. P. Slichter, "Relaxation times in magnetic resonance," *Physical Review*, vol. 100, no. 4, p. 1014, 1955.

[86] V. Andreev and V. Gerasimenko, "On the theory of paramagnetic resonance and paramagnetic relaxation in metals," *SOVIET PHYSICS JETP*, vol. 35, no. 8, 1959.

[87] C. P. Slichter, *Principles of magnetic resonance*, vol. 1. Springer Science & Business Media, 2013.

[88] R. . J. Elliott, "Theory of the effect of spin-orbit coupling on magnetic resonance in some semiconductors," *Physical Review*, vol. 96, no. 2, p. 266, 1954.

[89] Y. Yafet, "g factors and spin-lattice relaxation of conduction electrons," in *Solid state physics*, vol. 14, pp. 1–98, Elsevier, 1963.

[90] M. Dyakonov and V. Perel, "Spin relaxation of conduction electrons in noncentrosymmetric semiconductors," *Soviet Physics Solid State, Ussr*, vol. 13, no. 12, pp. 3023–3026, 1972.

[91] M. D'yakonov and V. Perel', "Soy. phys. jetp 33, 1053 (1971); sov," *Phys. Solid State*, vol. 13, p. 3023, 1972.

[92] I. Žutić, J. Fabian, and S. Das Sarma, "Spintronics: Fundamentals and applications," Rev. Mod. Phys., vol. 76, pp. 323–410, Apr 2004.

[93] I. M. Miron, K. Garello, G. Gaudin, P.-J. Zermatten, M. V. Costache, S. Auffret, S. Bandiera, B. Rodmacq, A. Schuhl, and P. Gambardella, "Perpendicular switching of a single ferromagnetic layer induced by in-plane current injection," Nature, vol. 476, pp. 189–193, Aug 2011.

[94] L. Liu, C.-F. Pai, Y. Li, H. W. Tseng, D. C. Ralph, and R. A. Buhrman, "Spin-torque switching with the giant spin hall effect of tantalum," Science, vol. 336, no. 6081, pp. 555–558, 2012.

[95] S. Peng, D. Zhu, J. Zhou, B. Zhang, A. Cao, M. Wang, W. Cai, K. Cao, and W. Zhao, "Modulation of heavy metal/ferromagnetic metal interface for high-performance spintronic devices," *Advanced Electronic Materials*, vol. 5, no. 8, p. 1900134, 2019.

[96] A. Aronov, "Spin injection in metals and polarization of nuclei," *ZhETF Pisma Redaktsiiu*, vol. 24, p. 37, 1976.

[97] M. Johnson and R. Silsbee, "Thermodynamic analysis of interfacial transport and of the thermomagnetoelectric system," *Physical Review B*, vol. 35, no. 10, p. 4959, 1987.

[98] M. Johnson and R. Silsbee, "Coupling of electronic charge and spin at a ferromagnetic-paramagnetic metal interface," *Physical Review B*, vol. 37, no. 10, p. 5312, 1988.

[99] P. Van Son, H. Van Kempen, and P. Wyder, "Boundary resistance of the ferromagnetic-nonferromagnetic metal interface," *Physical Review Letters*, vol. 58, no. 21, p. 2271, 1987.

[100] T. Valet and A. Fert, "Theory of the perpendicular magnetoresistance in magnetic multilayers," *Physical Review B*, vol. 48, no. 10, p. 7099, 1993.

[101] S. Hershfield and H. L. Zhao, "Charge and spin transport through a metallic ferromagnetic-paramagnetic-ferromagnetic junction," *Physical Review B*, vol. 56, no. 6, p. 3296, 1997.

[102] G. Schmidt, D. Ferrand, L. Molenkamp, A. Filip, and B. Van Wees, "Fundamental obstacle for electrical spin injection from a ferromagnetic metal into a diffusive semiconductor," *Physical Review B*, vol. 62, no. 8, p. R4790, 2000.

[103] E. Rashba, "Theory of electrical spin injection: Tunnel contacts as a solution of the conductivity mismatch problem," *Physical Review B*, vol. 62, no. 24, p. R16267, 2000.

[104] E. I. Rashba, "Diffusion theory of spin injection through resistive contacts," *The European Physical Journal B-Condensed Matter and Complex Systems*, vol. 29, no. 4, pp. 513–527, 2002.

[105] P. Van Son, H. van Kempen, and P. Wyder, "van son, van kempen, and wyder reply," *Physical Review Letters*, vol. 60, no. 4, p. 378, 1988.

[106] M. Büttiker, Y. Imry, R. Landauer, and S. Pinhas, "Generalized many-channel conductance formula with application to small rings," *Physical Review B*, vol. 31, no. 10, p. 6207, 1985.

[107] M. Büttiker, "Four-terminal phase-coherent conductance," *Physical review letters*, vol. 57, no. 14, p. 1761, 1986.

[108] A. Barman and A. Haldar, "Chapter one - time-domain study of magnetization dynamics in magnetic thin films and micro- and nanostructures," vol. 65 of *Solid State Physics*, pp. 1–108, Academic Press, 2014.

[109] L. Landau and E. Lifshitz, "On the theory of the dispersion of magnetic permeability in ferromagnetic bodies," in *Perspectives in Theoretical Physics*, pp. 51–65, Elsevier, 1992.

[110] T. L. Gilbert, "A phenomenological theory of damping in ferromagnetic materials," *IEEE transactions on magnetics*, vol. 40, no. 6, pp. 3443–3449, 2004.

[111] O. Yalçın, *Ferromagnetic Resonance: Theory and Applications*. BoD–Books on Demand, 2013.

[112] C. P. Poole, "Electron spin resonance: a comprehensive treatise on experimental techniques," 1996.

[113] Z. Celinski, K. Urquhart, and B. Heinrich, "Using ferromagnetic resonance to measure the magnetic moments of ultrathin films," *Journal of Magnetism and Magnetic Materials*, vol. 166, no. 1-2, pp. 6–26, 1997.

[114] B. Heinrich and J. Cochran, "Ultrathin metallic magnetic films: magnetic anisotropies and exchange interactions," *Advances in Physics*, vol. 42, no. 5, pp. 523–639, 1993.

[115] C. Kittel, "On the theory of ferromagnetic resonance absorption," *Phys. Rev.*, vol. 71, p. 270, 1947.

[116] K. Ando, S. Takahashi, J. Ieda, Y. Kajiwara, H. Nakayama, T. Yoshino, K. Harii, Y. Fujikawa, M. Matsuo, S. Maekawa, and E. Saitoh, "Inverse spin-hall effect induced by spin pumping in metallic system," *Journal of Applied Physics*, vol. 109, no. 10, p. 103913, 2011.

[117] R. H. Silsbee, A. Janossy, and P. Monod, "Coupling between ferromagnetic and conduction-spin-resonance modes at a ferromagnetic—normal-metal interface," *Phys. Rev. B*, vol. 19, pp. 4382–4399, May 1979.

[118] Y. Tserkovnyak *et al.*, "A, brataas, and gew bauer," *Phys. Rev. Lett*, vol. 88, p. 117601, 2002.

[119] Y. Tserkovnyak, A. Brataas, and G. E. Bauer, "Spin pumping and magnetization dynamics in metallic multilayers," *Physical Review B*, vol. 66, no. 22, p. 224403, 2002.

[120] Y. Tserkovnyak, A. Brataas, G. E. Bauer, and B. I. Halperin, "Nonlocal magnetization dynamics in ferromagnetic heterostructures," *Reviews of Modern Physics*, vol. 77, no. 4, p. 1375, 2005.

[121] P. Brouwer, "Scattering approach to parametric pumping," *Physical Review B*, vol. 58, no. 16, p. R10135, 1998.

[122] Y. Tserkovnyak, A. Brataas, and G. E. W. Bauer, "Enhanced gilbert damping in thin ferromagnetic films," *Phys. Rev. Lett.*, vol. 88, p. 117601, Feb 2002.

[123] A. Brataas, Y. Tserkovnyak, G. E. Bauer, and B. I. Halperin, "Spin battery operated by ferromagnetic resonance," *Physical Review B*, vol. 66, no. 6, p. 060404, 2002.

[124] S. M. S. Mizukami, Y. A. Y. Ando, and T. M. T. Miyazaki, "The study on ferromagnetic resonance linewidth for nm/80nife/nm (nm= cu, ta, pd and pt) films," *Japanese journal of applied physics*, vol. 40, no. 2R, p. 580, 2001.

[125] J. Hohlfeld, E. Matthias, R. Knorren, and K. Bennemann, "Nonequilibrium magnetization dynamics of nickel," *Physical review letters*, vol. 78, no. 25, p. 4861, 1997.

[126] A. Scholl, L. Baumgarten, R. Jacquemin, and W. Eberhardt, "Ultrafast spin dynamics of ferromagnetic thin films observed by fs spin-resolved two-photon photoemission," *Physical review letters*, vol. 79, no. 25, p. 5146, 1997.

[127] G. Ju, A. Vertikov, A. Nurmikko, C. Canady, G. Xiao, R. Farrow, and A. Cebollada, "Ultrafast nonequilibrium spin dynamics in a ferromagnetic thin film," *Physical Review B*, vol. 57, no. 2, p. R700, 1998.

[128] U. Conrad, J. Güdde, V. Jähnke, and E. Matthias, "Ultrafast electron and magnetization dynamics of thin ni and co films on cu (001) observed by time-resolved shg.," *Applied Physics B: Lasers & Optics*, vol. 68, no. 3, 1999.

[129] J. Güdde, U. Conrad, V. Jähnke, J. Hohlfeld, and E. Matthias, "Magnetization dynamics of ni and co films on cu (001) and of bulk nickel surfaces," *Physical Review B*, vol. 59, no. 10, p. R6608, 1999.

[130] B. Koopmans, M. Van Kampen, J. Kohlhepp, and W. De Jonge, "Femtosecond spin dynamics of epitaxial cu (111)/ni/cu wedges," *Journal of Applied Physics*, vol. 87, no. 9, pp. 5070–5072, 2000.

[131] A. Weber, F. Pressacco, S. Guenther, E. Mancini, P. M. Oppeneer, and C. Back, "Ultrafast demagnetization dynamics of thin fe/w (110) films: Comparison of time-and spin-resolved photoemission with time-resolved magneto-optic experiments," *Physical Review B*, vol. 84, no. 13, p. 132412, 2011.

[132] C. Boeglin, E. Beaurepaire, V. Halté, V. López-Flores, C. Stamm, N. Pontius, H. Dürr, and J.-Y. Bigot, "Distinguishing the ultrafast dynamics of spin and orbital moments in solids," *Nature*, vol. 465, no. 7297, pp. 458–461, 2010.

[133] T. Kampfrath, *Charge-Carrier Dynamics in Solids and Gases Observed by Time-Resolved Terahertz Spectroscopy.* PhD thesis, 2006.

[134] E. G. Gamaly, *Femtosecond laser-matter interaction: theory, experiments and applications.* Jenny Stanford Publishing, 2011.

[135] M. Aeschlimann, M. Bauer, S. Pawlik, W. Weber, R. Burgermeister, D. Oberli, and H. Siegmann, "Ultrafast spin-dependent electron dynamics in fcc co," *Physical review letters*, vol. 79, no. 25, p. 5158, 1997.

[136] J. Hohlfeld, S.-S. Wellershoff, J. Güdde, U. Conrad, V. Jähnke, and E. Matthias, "Electron and lattice dynamics following optical excitation of metals," *Chemical Physics*, vol. 251, no. 1-3, pp. 237–258, 2000.

[137] A. Melnikov, I. Razdolski, T. O. Wehling, E. T. Papaioannou, V. Roddatis, P. Fumagalli, O. Aktsipetrov, A. I. Lichtenstein, and U. Bovensiepen, "Ultrafast transport of laser-excited spin-polarized carriers in Au/Fe/MgO(001)," *Phys. Rev. Lett.*, vol. 107, p. 076601, Aug 2011.

[138] A. Alekhin, I. Razdolski, N. Ilin, J. P. Meyburg, D. Diesing, V. Roddatis, I. Rungger, M. Stamenova, S. Sanvito, U. Bovensiepen, and A. Melnikov, "Femtosecond spin current pulses generated by the nonthermal spin-dependent seebeck effect and interacting with ferromagnets in spin valves," *Phys. Rev. Lett.*, vol. 119, p. 017202, Jul 2017.

[139] I. Razdolski, A. Alekhin, N. Ilin, J. P. Meyburg, V. Roddatis, D. Diesing, U. Bovensiepen, and A. Melnikov, "Nanoscale interface confinement of ultrafast spin transfer torque driving non-uniform spin dynamics," *Nature communications*, vol. 8, no. 1, pp. 1–5, 2017.

[140] T. Kampfrath, M. Battiato, P. Maldonado, G. Eilers, J. Nötzold, S. Mährlein, V. Zbarsky, F. Freimuth, Y. Mokrousov, S. Blügel, *et al.*, "Terahertz spin current pulses controlled by magnetic heterostructures," *Nature nanotechnology*, vol. 8, no. 4, pp. 256–260, 2013.

[141] M. Battiato, K. Carva, and P. M. Oppeneer, "Theory of laser-induced ultrafast superdiffusive spin transport in layered heterostructures," *Physical Review B*, vol. 86, no. 2, p. 024404, 2012.

[142] E. G. Tveten, A. Brataas, and Y. Tserkovnyak, "Electron-magnon scattering in magnetic heterostructures far out of equilibrium," *Physical Review B*, vol. 92, no. 18, p. 180412, 2015.

[143] A. Vaterlaus, T. Beutler, and F. Meier, "Spin-lattice relaxation time of ferromagnetic gadolinium determined with time-resolved spin-polarized photoemission," *Physical review letters*, vol. 67, no. 23, p. 3314, 1991.

[144] B. Koopmans, G. Malinowski, F. Dalla Longa, D. Steiauf, M. Fähnle, T. Roth, M. Cinchetti, and M. Aeschlimann, "Explaining the paradoxical diversity of ultrafast laser-induced demagnetization," *Nature materials*, vol. 9, no. 3, pp. 259–265, 2010.

[145] D. Steiauf and M. Fähnle, "Elliott-yafet mechanism and the discussion of femtosecond magnetization dynamics," *Physical Review B*, vol. 79, no. 14, p. 140401, 2009.

[146] C. Illg, M. Haag, and M. Fähnle, "Ultrafast demagnetization after laser irradiation in transition metals: Ab initio calculations of the spin-flip electron-phonon scattering with reduced exchange splitting," *Physical Review B*, vol. 88, no. 21, p. 214404, 2013.

[147] B. Mueller, A. Baral, S. Vollmar, M. Cinchetti, M. Aeschlimann, H. Schneider, and B. Rethfeld, "Feedback effect during ultrafast demagnetization dynamics in ferromagnets," *Physical review letters*, vol. 111, no. 16, p. 167204, 2013.

[148] D. Steiauf, C. Illg, and M. Fähnle, "Extension of yafet's theory of spin relaxation to ferromagnets," *Journal of magnetism and magnetic materials*, vol. 322, no. 6, pp. L5–L7, 2010.

[149] M. Fähnle and C. Illg, "Electron theory of fast and ultrafast dissipative magnetization dynamics," *Journal of Physics: Condensed Matter*, vol. 23, no. 49, p. 493201, 2011.

[150] W. Töws and G. M. Pastor, "Many-body theory of ultrafast demagnetization and angular momentum transfer in ferromagnetic transition metals," *Phys. Rev. Lett.*, vol. 115, p. 217204, Nov 2015.

[151] J. Dewhurst, S. Shallcross, P. Elliott, S. Eisebitt, C. v. K. Schmising, and S. Sharma, "Angular momentum redistribution in laser-induced demagnetization," *Physical Review B*, vol. 104, no. 5, p. 054438, 2021.

[152] P. Elliott, N. Singh, K. Krieger, E. Gross, S. Sharma, and J. Dewhurst, "The microscopic origin of spin-orbit mediated spin-flips," *Journal of Magnetism and Magnetic Materials*, vol. 502, p. 166473, 2020.

[153] B. Y. Mueller, T. Roth, M. Cinchetti, M. Aeschlimann, and B. Rethfeld, "Driving force of ultrafast magnetization dynamics," *New Journal of Physics*, vol. 13, no. 12, p. 123010, 2011.

[154] E. Carpene, E. Mancini, C. Dallera, M. Brenna, E. Puppin, and S. De Silvestri, "Dynamics of electron-magnon interaction and ultrafast demagnetization in thin iron films," *Physical Review B*, vol. 78, no. 17, p. 174422, 2008.

[155] M. Haag, C. Illg, and M. Fähnle, "Role of electron-magnon scatterings in ultrafast demagnetization," *Physical Review B*, vol. 90, no. 1, p. 014417, 2014.

[156] M. Battiato, *Superdiffusive spin transport and ultrafast magnetization dynamics*. PhD thesis, Ph. D Thesis, 2013.

[157] G. E. Bauer, E. Saitoh, and B. J. Van Wees, "Spin caloritronics," *Nature materials*, vol. 11, no. 5, pp. 391–399, 2012.

[158] M. Johnson and R. H. Silsbee, "Interfacial charge-spin coupling: Injection and detection of spin magnetization in metals," *Physical review letters*, vol. 55, no. 17, p. 1790, 1985.

[159] K. Uchida, S. Takahashi, K. Harii, J. Ieda, W. Koshibae, K. Ando, S. Maekawa, and E. Saitoh, "Observation of the spin seebeck effect," *Nature*, vol. 455, no. 7214, pp. 778–781, 2008.

[160] L. Yi, D. Yang, M. Liu, H.-H. Fu, L. Ding, Y. Xu, B. Zhang, L. Pan, and J. Q. Xiao, "Concepts of spin seebeck effect in ferromagnetic metals," *Advanced Functional Materials*, vol. 30, no. 38, p. 2004024, 2020.

[161] T. Kikkawa, K. Uchida, S. Daimon, Y. Shiomi, H. Adachi, Z. Qiu, D. Hou, X.-F. Jin, S. Maekawa, and E. Saitoh, "Separation of longitudinal spin seebeck effect from anomalous nernst effect: Determination of origin of transverse thermoelectric voltage in metal/insulator junctions," *Physical Review B*, vol. 88, no. 21, p. 214403, 2013.

[162] H. Adachi, K.-i. Uchida, E. Saitoh, and S. Maekawa, "Theory of the spin seebeck effect," *Reports on Progress in Physics*, vol. 76, no. 3, p. 036501, 2013.

[163] K.-i. Uchida, J. Xiao, H. Adachi, J.-i. Ohe, S. Takahashi, J. Ieda, T. Ota, Y. Kajiwara, H. Umezawa, H. Kawai, *et al.*, "Spin seebeck insulator," *Nature materials*, vol. 9, no. 11, pp. 894–897, 2010.

[164] A. W. Smith, "The transverse thermomagnetic effect in nickel and cobalt," *Physical Review (Series I)*, vol. 33, no. 4, p. 295, 1911.

[165] T. Miyasato, N. Abe, T. Fujii, A. Asamitsu, S. Onoda, Y. Onose, N. Nagaosa, and Y. Tokura, "Crossover behavior of the anomalous hall effect and anomalous nernst effect in itinerant ferromagnets," *Physical review letters*, vol. 99, no. 8, p. 086602, 2007.

[166] Y. Pu, D. Chiba, F. Matsukura, H. Ohno, and J. Shi, "Mott relation for anomalous hall and nernst effects in ga 1- x mn x as ferromagnetic semiconductors," *Physical review letters*, vol. 101, no. 11, p. 117208, 2008.

[167] T. Seifert, S. Jaiswal, U. Martens, J. Hannegan, L. Braun, P. Maldonado, F. Freimuth, A. Kronenberg, J. Henrizi, I. Radu, *et al.*, "Efficient metallic spintronic emitters of ultra-broadband terahertz radiation," *Nature photonics*, vol. 10, no. 7, pp. 483–488, 2016.

[168] D. M. Nenno, B. Rethfeld, and H. C. Schneider, "Particle-in-cell simulation of ultrafast hot-carrier transport in fe/au heterostructures," *Physical Review B*, vol. 98, no. 22, p. 224416, 2018.

[169] D. M. Nenno, R. Binder, and H. C. Schneider, "Simulation of hot-carrier dynamics and terahertz emission in laser-excited metallic bilayers," *Physical Review Applied*, vol. 11, no. 5, p. 054083, 2019.

[170] G. Torosyan, S. Keller, L. Scheuer, R. Beigang, and E. T. Papaioannou, "Optimized spintronic terahertz emitters based on epitaxial grown fe/pt layer structures," *Scientific reports*, vol. 8, no. 1, pp. 1–9, 2018.

[171] N. K. Jain, M. S. Sawant, S. H. Nikam, S. Jhavar, and L. Shohet, "Metal deposition: Plasma-based processes," *Encyclopedia of Plasma Technology*, pp. 722–740, 2016.

[172] P. J. Kelly and R. D. Arnell, "Magnetron sputtering: a review of recent developments and applications," *Vacuum*, vol. 56, no. 3, pp. 159–172, 2000.

[173] J. T. Gudmundsson and D. Lundin, "1 - introduction to magnetron sputtering," in *High Power Impulse Magnetron Sputtering* (D. Lundin, T. Minea, and J. T. Gudmundsson, eds.), pp. 1–48, Elsevier, 2020.

[174] A. Pandey, S. Dalal, S. Dutta, and A. Dixit, "Structural characterization of polycrystalline thin films by x-ray diffraction techniques," *Journal of Materials Science: Materials in Electronics*, vol. 32, no. 2, pp. 1341–1368, 2021.

[175] A. Segmüller, I. Noyan, and V. Speriosu, "X-ray diffraction studies of thin films and multilayer structures," *Progress in crystal growth and characterization*, vol. 18, pp. 21–66, 1989.

[176] N. A. Geisse, "Afm and combined optical techniques," *Materials Today*, vol. 12, no. 7, pp. 40–45, 2009.

[177] F. J. Giessibl, "Advances in atomic force microscopy," *Rev. Mod. Phys.*, vol. 75, pp. 949–983, Jul 2003.

[178] L. E. Franken, K. Grünewald, E. J. Boekema, and M. C. A. Stuart, "A technical introduction to transmission electron microscopy for soft-matter: Imaging, possibilities, choices, and technical developments," *Small*, vol. 16, no. 14, p. 1906198, 2020.

[179] D. B. Williams and C. B. Carter, "The transmission electron microscope," in *Transmission electron microscopy*, pp. 3–17, Springer, 1996.

[180] C. Kranz and B. Mizaikoff, "Chapter 6 - microscopic techniques for the characterization of gold nanoparticles," in *Gold Nanoparticles in Analytical Chemistry* (M. Valcárcel and Ángela I. López-Lorente, eds.), vol. 66 of *Comprehensive Analytical Chemistry*, pp. 257–299, Elsevier, 2014.

[181] "Vibrating sample magnetometry m106." `https://www.tf.uni-kiel.de/servicezentrum/neutral/praktika/anleitungen/m106`. Accessed: 2022-04-22.

[182] S. Foner, "Versatile and sensitive vibrating-sample magnetometer," *Review of Scientific Instruments*, vol. 30, no. 7, pp. 548–557, 1959.

[183] R. E. Camley, Z. Celinski, and R. L. Stamps, *Magnetism of surfaces, interfaces, and nanoscale materials.* Elsevier, 2015.

[184] I. Jovanovic, "Chirped-pulse amplification: Ultrahigh peak power production from compact short-pulse laser systems," *Optik & Photonik*, vol. 5, no. 4, pp. 30–33, 2010.

[185] C. Zhou, "Chirped pulse amplification: review and prospective from diffractive optics," *Chinese Optics Letters*, vol. 18, no. 11, p. 110502, 2020.

[186] D. Strickland and G. Mourou, "Half of nobel prize in physics honors the inventors of chirped pulse amplification," *Physics Today*, 2018.

[187] M. C. Asplund, J. A. Johnson, and J. E. Patterson, "The 2018 nobel prize in physics: optical tweezers and chirped pulse amplification," *Analytical and bioanalytical chemistry*, vol. 411, no. 20, pp. 5001–5005, 2019.

[188] "Light conversion pharos." https://www.lastek.com.au/1658-light-conversion-pharos-ybkgw-utrafast-lasers. Accessed: 2022-03-22.

[189] W. Hoppe, J. Weber, S. Tirpanci, O. Gueckstock, T. Kampfrath, and G. Woltersdorf, "On-chip generation of ultrafast current pulses by nanolayered spintronic terahertz emitters," ACS Applied Nano Materials, vol. 4, no. 7, pp. 7454–7460, 2021.

[190] W. Zouaghi, M. Thomson, K. Rabia, R. Hahn, V. Blank, and H. Roskos, "Broadband terahertz spectroscopy: principles, fundamental research and potential for industrial applications," European Journal of Physics, vol. 34, no. 6, p. S179, 2013.

[191] P. U. Jepsen, D. G. Cooke, and M. Koch, "Terahertz spectroscopy and imaging–modern techniques and applications," Laser & Photonics Reviews, vol. 5, no. 1, pp. 124–166, 2011.

[192] T. Löffler, T. Hahn, M. Thomson, F. Jacob, and H. Roskos, "Large-area electro-optic znte terahertz emitters," Optics express, vol. 13, no. 14, pp. 5353–5362, 2005.

[193] I. Mihai Miron, G. Gaudin, S. Auffret, B. Rodmacq, A. Schuhl, S. Pizzini, J. Vogel, and P. Gambardella, "Current-driven spin torque induced by the rashba effect in a ferromagnetic metal layer," Nature Materials, vol. 9, pp. 230–234, Mar 2010.

[194] L. Liu, O. J. Lee, T. J. Gudmundsen, D. C. Ralph, and R. A. Buhrman, "Current-induced switching of perpendicularly magnetized magnetic layers using spin torque from the spin hall effect," Phys. Rev. Lett., vol. 109, p. 096602, Aug 2012.

[195] S. S. P. Parkin, M. Hayashi, and L. Thomas, "Magnetic domain-wall racetrack memory," Science, vol. 320, no. 5873, pp. 190–194, 2008.

[196] K.-S. Ryu, L. Thomas, S.-H. Yang, and S. Parkin, "Chiral spin torque at magnetic domain walls," Nature Nanotechnology, vol. 8, pp. 527–533, Jul 2013.

[197] A. Fert, V. Cros, and J. Sampaio, "Skyrmions on the track," Nature Nanotechnology, vol. 8, pp. 152–156, Mar 2013.

[198] J. Iwasaki, M. Mochizuki, and N. Nagaosa, "Current-induced skyrmion dynamics in constricted geometries," Nature Nanotechnology, vol. 8, pp. 742–747, Oct 2013.

[199] J. Sampaio, V. Cros, S. Rohart, A. Thiaville, and A. Fert, "Nucleation, stability and current-induced motion of isolated magnetic skyrmions in nanostructures," Nature Nanotechnology, vol. 8, pp. 839–844, Nov 2013.

[200] V. E. Demidov, S. Urazhdin, H. Ulrichs, V. Tiberkevich, A. Slavin, D. Baither, G. Schmitz, and S. O. Demokritov, "Magnetic nano-oscillator driven by pure spin current," Nature Materials, vol. 11, pp. 1028–1031, Dec 2012.

[201] A. Hoffmann, "Spin hall effects in metals," IEEE Transactions on Magnetics, vol. 49, no. 10, pp. 5172–5193, 2013.

[202] E. Saitoh, M. Ueda, H. Miyajima, and G. Tatara, "Conversion of spin current into charge current at room temperature: Inverse spin-hall effect," Applied Physics Letters, vol. 88, no. 18, p. 182509, 2006.

[203] K. Ando, S. Takahashi, J. Ieda, Y. Kajiwara, H. Nakayama, T. Yoshino, K. Harii, Y. Fujikawa, M. Matsuo, S. Maekawa, and E. Saitoh, "Inverse spin-hall effect induced by spin pumping in metallic system," Journal of Applied Physics, vol. 109, no. 10, p. 103913, 2011.

[204] T. Kampfrath, M. Battiato, P. Maldonado, G. Eilers, J. Nötzold, S. Mährlein, V. Zbarsky, F. Freimuth, Y. Mokrousov, S. Blügel, M. Wolf, I. Radu, P. M. Oppeneer, and M. Münzenberg, "Terahertz spin current pulses controlled by magnetic heterostructures," Nature Nanotechnology, vol. 8, pp. 256–260, Apr 2013.

[205] O. Gueckstock, L. Nádvorník, M. Gradhand, T. S. Seifert, G. Bierhance, R. Rouzegar, M. Wolf, M. Vafaee, J. Cramer, M. A. Syskaki, G. Woltersdorf, I. Mertig, G. Jakob, M. Kläui, and T. Kampfrath, "Terahertz spin-to-charge conversion by interfacial skew scattering in metallic bilayers," Advanced Materials, vol. 33, no. 9, p. 2006281, 2021.

[206] W. Zhang, W. Han, X. Jiang, S.-H. Yang, and S. S. P. Parkin, "Role of transparency of platinum–ferromagnet interfaces in determining the intrinsic magnitude of the spin hall effect," Nature Physics, vol. 11, pp. 496–502, Jun 2015.

[207] K. Xia, P. J. Kelly, G. E. W. Bauer, A. Brataas, and I. Turek, "Spin torques in ferromagnetic/normal-metal structures," Phys. Rev. B, vol. 65, p. 220401, May 2002.

[208] J. Bass and W. P. Pratt, "Spin-diffusion lengths in metals and alloys, and spin-flipping at metal/metal interfaces: an experimentalist's critical review," Journal of Physics: Condensed Matter, vol. 19, p. 183201, apr 2007.

[209] C. Galinon, K. Tewolde, R. Loloee, W.-C. Chiang, S. Olson, H. Kurt, W. P. Pratt, J. Bass, P. X. Xu, K. Xia, and M. Talanana, "Pd/ag and pd/au interface specific resistances and interfacial spin flipping," Applied Physics Letters, vol. 86, no. 18, p. 182502, 2005.

[210] K. Gupta, R. J. H. Wesselink, R. Liu, Z. Yuan, and P. J. Kelly, "Disorder dependence of interface spin memory loss," Phys. Rev. Lett., vol. 124, p. 087702, Feb 2020.

[211] J.-C. Rojas-Sánchez, N. Reyren, P. Laczkowski, W. Savero, J.-P. Attané, C. Deranlot, M. Jamet, J.-M. George, L. Vila, and H. Jaffrès, "Spin pumping and inverse spin hall effect in platinum: The essential role of spin-memory loss at metallic interfaces," Phys. Rev. Lett., vol. 112, p. 106602, Mar 2014.

[212] K. D. Belashchenko, A. A. Kovalev, and M. van Schilfgaarde, "Theory of spin loss at metallic interfaces," Phys. Rev. Lett., vol. 117, p. 207204, Nov 2016.

[213] K. Dolui and B. K. Nikolić, "Spin-memory loss due to spin-orbit coupling at ferromagnet/heavy-metal interfaces: Ab initio spin-density matrix approach," Phys. Rev. B, vol. 96, p. 220403, Dec 2017.

[214] L. Zhu, D. C. Ralph, and R. A. Buhrman, "Effective spin-mixing conductance of heavy-metal–ferromagnet interfaces," Phys. Rev. Lett., vol. 123, p. 057203, Aug 2019.

[215] L. Zhu, D. C. Ralph, and R. A. Buhrman, "Spin-orbit torques in heavy-metal–ferromagnet bilayers with varying strengths of interfacial spin-orbit coupling," Phys. Rev. Lett., vol. 122, p. 077201, Feb 2019.

[216] G. G. B. Flores, A. A. Kovalev, M. van Schilfgaarde, and K. D. Belashchenko, "Generalized magnetoelectronic circuit theory and spin relaxation at interfaces in magnetic multilayers," Phys. Rev. B, vol. 101, p. 224405, Jun 2020.

[217] M. Zeng, B. Chen, and S. T. Lim, "Interfacial electric field and spin-orbitronic properties of heavy-metal/cofe bilayers," Applied Physics Letters, vol. 114, no. 1, p. 012401, 2019.

[218] R. J. H. Wesselink, K. Gupta, Z. Yuan, and P. J. Kelly, "Calculating spin transport properties from first principles: Spin currents," Phys. Rev. B, vol. 99, p. 144409, Apr 2019.

[219] S. Smidstrup, D. Stradi, J. Wellendorff, P. A. Khomyakov, U. G. Vej-Hansen, M.-E. Lee, T. Ghosh, E. Jónsson, H. Jónsson, and K. Stokbro, "First-principles Green's-function method for surface calculations: A pseudopotential localized basis set approach," Phys. Rev. B, vol. 96, no. 19, p. 195309, 2017.

[220] J. P. Perdew, K. Burke, and M. Ernzerhof, "Generalized gradient approximation made simple," Phys. Rev. Lett., vol. 77, no. 18, pp. 3865–3868, 1996.

[221] M. J. Van Setten, M. Giantomassi, E. Bousquet, M. J. Verstraete, D. R. Hamann, X. Gonze, and G.-M. Rignanese, "The PseudoDojo: Training and grading a 85 element optimized norm-conserving pseudopotential table," Comput. Phys. Commun., vol. 226, pp. 39–54, 2018.

[222] Y. Miura, M. Tsujikawa, and M. Shirai, "A first-principles study on magnetocrystalline anisotropy at interfaces of fe with non-magnetic metals," Journal of Applied Physics, vol. 113, no. 23, p. 233908, 2013.

[223] M. Kowalewski, W. H. Butler, N. Moghadam, G. M. Stocks, T. C. Schulthess, K. J. Song, J. R. Thompson, A. S. Arrott, T. Zhu, J. Drewes, R. R. Katti, M. T. McClure, and O. Escorcia, "The effect of ta on the magnetic thickness of permalloy ($ni_8 1fe_1 9$) films," Journal of Applied Physics, vol. 87, pp. 5732–5734, May 2000.

[224] R. Rouzegar, L. Brandt, L. Nadvornik, D. A. Reiss, A. L. Chekhov, O. Gueckstock, C. In, M. Wolf, T. S. Seifert, P. W. Brouwer, G. Woltersdorf, and T. Kampfrath, "Laser-induced terahertz spin transport in magnetic nanostructures arises from the same force as ultrafast demagnetization," vol. arXiv:2103.11710 [cond-mat.mes-hall], 2021. https://arxiv.org/abs/2103.11710 (last accessed 25.02.2022).

[225] R. I. Herapath, S. M. Hornett, T. S. Seifert, G. Jakob, M. Kläui, J. Bertolotti, T. Kampfrath, and E. Hendry, "Impact of pump wavelength on terahertz emission of a cavity-enhanced spintronic trilayer," Applied Physics Letters, vol. 114, no. 4, p. 041107, 2019.

[226] J. Sinha, M. Hayashi, A. J. Kellock, S. Fukami, M. Yamanouchi, H. Sato, S. Ikeda, S. Mitani, S.-h. Yang, S. S. P. Parkin, and H. Ohno, "Enhanced interface perpendicular magnetic anisotropy in ta—cofeb—mgo using nitrogen doped ta underlayers," Applied Physics Letters, vol. 102, no. 24, p. 242405, 2013.

[227] L. Cuchet, B. Rodmacq, S. Auffret, R. C. Sousa, and B. Dieny, "Influence of magnetic electrodes thicknesses on the transport properties of magnetic tunnel junctions with perpendicular anisotropy," Applied Physics Letters, vol. 105, no. 5, p. 052408, 2014.

[228] N. Sato, K. P. O'Brien, K. Millard, B. Doyle, and K. Oguz, "Investigation of extrinsic damping caused by magnetic dead layer in ta-cofeb-mgo multilayers with perpendicular anisotropy," Journal of Applied Physics, vol. 119, no. 9, p. 093902, 2016.

[229] S.-H. Shen, D.-S. Lee, C.-W. Cheng, W.-J. Chan, and G. Chern, "The correlation between magnetic dead layer and perpendicular magnetic anisotropy in mgo/cofeb/ta top structure," IEEE Transactions on Magnetics, vol. 55, no. 2, pp. 1–5, 2019.

[230] R. Urban, G. Woltersdorf, and B. Heinrich, "Gilbert damping in single and multilayer ultrathin films: Role of interfaces in nonlocal spin dynamics," Phys. Rev. Lett., vol. 87, p. 217204, Nov 2001.

[231] D. H. Auston, K. Cheung, J. Valdmanis, and D. Kleinman, "Cherenkov radiation from femtosecond optical pulses in electro-optic media," Physical Review Letters, vol. 53, no. 16, p. 1555, 1984.

[232] C. Fattinger and D. Grischkowsky, "Point source terahertz optics," Applied Physics Letters, vol. 53, no. 16, pp. 1480–1482, 1988.

[233] M. Tonouchi, "Cutting-edge terahertz technology," Nature photonics, vol. 1, no. 2, pp. 97–105, 2007.

[234] D. M. Mittleman, "Perspective: Terahertz science and technology," Journal of Applied Physics, vol. 122, no. 23, p. 230901, 2017.

[235] K. Kawase, Y. Ogawa, Y. Watanabe, and H. Inoue, "Non-destructive terahertz imaging of illicit drugs using spectral fingerprints," Optics express, vol. 11, no. 20, pp. 2549–2554, 2003.

[236] W. L. Chan, J. Deibel, and D. M. Mittleman, "Imaging with terahertz radiation," Reports on progress in physics, vol. 70, no. 8, p. 1325, 2007.

[237] J. Kindt and C. Schmuttenmaer, "Far-infrared dielectric properties of polar liquids probed by femtosecond terahertz pulse spectroscopy," The Journal of Physical Chemistry, vol. 100, no. 24, pp. 10373–10379, 1996.

[238] B. Ferguson and X.-C. Zhang, "Materials for terahertz science and technology," Nature materials, vol. 1, no. 1, pp. 26–33, 2002.

[239] E. Pickwell and V. Wallace, "Biomedical applications of terahertz technology," Journal of Physics D: Applied Physics, vol. 39, no. 17, p. R301, 2006.

[240] A. G. Davies, A. D. Burnett, W. Fan, E. H. Linfield, and J. E. Cunningham, "Terahertz spectroscopy of explosives and drugs," *Materials today*, vol. 11, no. 3, pp. 18–26, 2008.

[241] B. Kolner, R. Buckles, P. Conklin, and R. Scott, "Plasma characterization with terahertz pulses," *IEEE Journal of Selected Topics in Quantum Electronics*, vol. 14, no. 2, pp. 505–512, 2008.

[242] R. Ulbricht, E. Hendry, J. Shan, T. F. Heinz, and M. Bonn, "Carrier dynamics in semiconductors studied with time-resolved terahertz spectroscopy," *Reviews of Modern Physics*, vol. 83, no. 2, p. 543, 2011.

[243] D. H. Auston, K. P. Cheung, and P. R. Smith, "Picosecond photoconducting hertzian dipoles," *Applied physics letters*, vol. 45, no. 3, pp. 284–286, 1984.

[244] M. Tani, K. Yamamoto, E. S. Estacio, C. T. Que, H. Nakajima, M. Hibi, F. Miyamaru, S. Nishizawa, and M. Hangyo, "Photoconductive emission and detection of terahertz pulsed radiation using semiconductors and semiconductor devices," *Journal of Infrared, Millimeter, and Terahertz Waves*, vol. 33, no. 4, pp. 393–404, 2012.

[245] S. Lepeshov, A. Gorodetsky, A. Krasnok, E. Rafailov, and P. Belov, "Enhancement of terahertz photoconductive antenna operation by optical nanoantennas," *Laser & Photonics Reviews*, vol. 11, no. 1, p. 1600199, 2017.

[246] X.-C. Zhang, Y. Jin, and X. Ma, "Coherent measurement of thz optical rectification from electro-optic crystals," *Applied physics letters*, vol. 61, no. 23, pp. 2764–2766, 1992.

[247] A. Rice, Y. Jin, X. Ma, X.-C. Zhang, D. Bliss, J. Larkin, and M. Alexander, "Terahertz optical rectification from¡ 110¿ zinc-blende crystals," *Applied physics letters*, vol. 64, no. 11, pp. 1324–1326, 1994.

[248] Q. Jin, Y. E, K. Williams, J. Dai, and X.-C. Zhang, "Observation of broadband terahertz wave generation from liquid water," *Applied Physics Letters*, vol. 111, no. 7, p. 071103, 2017.

[249] K. Reimann, "Table-top sources of ultrashort thz pulses," *Reports on Progress in Physics*, vol. 70, no. 10, p. 1597, 2007.

[250] X. Lu and X.-C. Zhang, "Generation of elliptically polarized terahertz waves from laser-induced plasma with double helix electrodes," *Physical Review Letters*, vol. 108, no. 12, p. 123903, 2012.

[251] W.-M. Wang, P. Gibbon, Z.-M. Sheng, and Y.-T. Li, "Tunable circularly polarized terahertz radiation from magnetized gas plasma," *Physical review letters*, vol. 114, no. 25, p. 253901, 2015.

[252] R. I. Herapath, S. M. Hornett, T. Seifert, G. Jakob, M. Kläui, J. Bertolotti, T. Kampfrath, and E. Hendry, "Impact of pump wavelength on terahertz emission of a cavity-enhanced spintronic trilayer," *Applied Physics Letters*, vol. 114, no. 4, p. 041107, 2019.

[253] Z. Feng, R. Yu, Y. Zhou, H. Lu, W. Tan, H. Deng, Q. Liu, Z. Zhai, L. Zhu, J. Cai, *et al.*, "Highly efficient spintronic terahertz emitter enabled by metal–dielectric photonic crystal," *Advanced Optical Materials*, vol. 6, no. 23, p. 1800965, 2018.

[254] D. Yang, J. Liang, C. Zhou, L. Sun, R. Zheng, S. Luo, Y. Wu, and J. Qi, "Powerful and tunable thz emitters based on the fe/pt magnetic heterostructure," *Advanced Optical Materials*, vol. 4, no. 12, pp. 1944–1949, 2016.

[255] R. Schneider, M. Fix, J. Bensmann, S. Michaelis de Vasconcellos, M. Albrecht, and R. Bratschitsch, "Composition-dependent ultrafast thz emission of spintronic cofe/pt thin films," *Applied Physics Letters*, vol. 120, no. 4, p. 042404, 2022.

[256] Y. Wu, M. Elyasi, X. Qiu, M. Chen, Y. Liu, L. Ke, and H. Yang, "High-performance thz emitters based on ferromagnetic/nonmagnetic heterostructures," *Advanced Materials*, vol. 29, no. 4, p. 1603031, 2017.

[257] G. Li, R. Mikhaylovskiy, K. Grishunin, J. Costa, T. Rasing, and A. Kimel, "Laser induced thz emission from femtosecond photocurrents in co/zno/pt and co/cu/pt multilayers," *Journal of Physics D: Applied Physics*, vol. 51, no. 13, p. 134001, 2018.

[258] T. S. Seifert, N. M. Tran, O. Gueckstock, S. M. Rouzegar, L. Nadvornik, S. Jaiswal, G. Jakob, V. V. Temnov, M. Muenzenberg, M. Wolf, *et al.*, "Terahertz spectroscopy for all-optical spintronic characterization of the spin-hall-effect metals pt, w and cu80ir20," *Journal of Physics D: Applied Physics*, vol. 51, no. 36, p. 364003, 2018.

[259] W. Hoppe, "Fast screening of laser-induced THz current pulses in metallic bilayers," Master's thesis, Martin-Luther-Universität Halle-Wittenberg, Von-Danckelmann-Platz 3, 06120 Halle, Germany, 2020.

[260] F. J. Jedema, A. Filip, and B. Van Wees, "Electrical spin injection and accumulation at room temperature in an all-metal mesoscopic spin valve," *Nature*, vol. 410, no. 6826, pp. 345–348, 2001.

[261] J. Bass and W. P. Pratt, "Spin-diffusion lengths in metals and alloys, and spin-flipping at metal/metal interfaces: an experimentalist's critical review," *Journal of Physics: Condensed Matter*, vol. 19, no. 18, p. 183201, 2007.

[262] T. Kampfrath, A. Sell, G. Klatt, A. Pashkin, S. Mährlein, T. Dekorsy, M. Wolf, M. Fiebig, A. Leitenstorfer, and R. Huber, "Coherent terahertz control of antiferromagnetic spin waves," *Nature Photonics*, vol. 5, no. 1, pp. 31–34, 2011.

[263] T. Jungwirth, X. Marti, P. Wadley, and J. Wunderlich, "Antiferromagnetic spintronics," *Nature nanotechnology*, vol. 11, no. 3, pp. 231–241, 2016.

[264] V. Baltz, A. Manchon, M. Tsoi, T. Moriyama, T. Ono, and Y. Tserkovnyak, "Antiferromagnetic spintronics," *Reviews of Modern Physics*, vol. 90, no. 1, p. 015005, 2018.

[265] R. Cheng, D. Xiao, and A. Brataas, "Terahertz antiferromagnetic spin hall nano-oscillator," *Physical review letters*, vol. 116, no. 20, p. 207603, 2016.

[266] P. Wadley, B. Howells, J. Železný, C. Andrews, V. Hills, R. P. Campion, V. Novák, K. Olejník, F. Maccherozzi, S. Dhesi, *et al.*, "Electrical switching of an antiferromagnet," *Science*, vol. 351, no. 6273, pp. 587–590, 2016.

[267] K. Olejník, V. Schuler, X. Martí, V. Novák, Z. Kašpar, P. Wadley, R. P. Campion, K. W. Edmonds, B. L. Gallagher, J. Garcés, *et al.*, "Antiferromagnetic cumnas multi-level memory cell with microelectronic compatibility," *Nature communications*, vol. 8, no. 1, pp. 1–7, 2017.

[268] S. Y. Bodnar, L. Šmejkal, I. Turek, T. Jungwirth, O. Gomonay, J. Sinova, A. Sapozhnik, H.-J. Elmers, M. Kläui, and M. Jourdan, "Writing and reading antiferromagnetic mn2au by néel spin-orbit torques and large anisotropic magnetoresistance," *Nature communications*, vol. 9, no. 1, pp. 1–7, 2018.

[269] M. Meinert, D. Graulich, and T. Matalla-Wagner, "Electrical switching of antiferromagnetic mn 2 au and the role of thermal activation," *Physical Review Applied*, vol. 9, no. 6, p. 064040, 2018.

[270] J. Železný, H. Gao, K. Výborný, J. Zemen, J. Mašek, A. Manchon, J. Wunderlich, J. Sinova, and T. Jungwirth, "Relativistic néel-order fields induced by electrical current in antiferromagnets," *Physical review letters*, vol. 113, no. 15, p. 157201, 2014.

[271] R. Lebrun, A. Ross, S. Bender, A. Qaiumzadeh, L. Baldrati, J. Cramer, A. Brataas, R. Duine, and M. Kläui, "Tunable long-distance spin transport in a crystalline antiferromagnetic iron oxide," *Nature*, vol. 561, no. 7722, pp. 222–225, 2018.

[272] H. Wang, C. Du, P. C. Hammel, and F. Yang, "Antiferromagnonic spin transport from y 3 fe 5 o 12 into nio," *Physical review letters*, vol. 113, no. 9, p. 097202, 2014.

[273] W. Lin, K. Chen, S. Zhang, and C. Chien, "Enhancement of thermally injected spin current through an antiferromagnetic insulator," *Physical review letters*, vol. 116, no. 18, p. 186601, 2016.

[274] A. Prakash, J. Brangham, F. Yang, and J. P. Heremans, "Spin seebeck effect through antiferromagnetic nio," *Physical Review B*, vol. 94, no. 1, p. 014427, 2016.

[275] Y. Sasaki, G. Li, T. Moriyama, T. Ono, R. V. Mikhaylovskiy, A. V. Kimel, and S. Mizukami, "Laser stimulated thz emission from pt/coo/fecob," *Applied Physics Letters*, vol. 117, no. 19, p. 192403, 2020.

[276] Z. Qiu, J. Li, D. Hou, E. Arenholz, A. T. N'Diaye, A. Tan, K.-i. Uchida, K. Sato, S. Okamoto, Y. Tserkovnyak, *et al.*, "Spin-current probe for phase transition in an insulator," *Nature communications*, vol. 7, no. 1, pp. 1–6, 2016.

[277] L. Jin, K. Jia, D. Zhang, B. Liu, H. Meng, X. Tang, Z. Zhong, and H. Zhang, "Effect of interfacial roughness spin scattering on the spin current transport in yig/nio/pt heterostructures," *ACS applied materials & interfaces*, vol. 11, no. 38, pp. 35458–35467, 2019.

[278] C. Hahn, G. De Loubens, V. V. Naletov, J. B. Youssef, O. Klein, and M. Viret, "Conduction of spin currents through insulating antiferromagnetic oxides," *EPL (Europhysics Letters)*, vol. 108, no. 5, p. 57005, 2014.

[279] Y. Chen, E. Cogulu, D. Roy, J. Ding, J. B. Mohammadi, P. G. Kotula, N. A. Missert, M. Wu, and A. D. Kent, "Spin transport in an insulating ferrimagnetic-antiferromagnetic-ferrimagnetic trilayer as a function of temperature," *AIP Advances*, vol. 9, no. 10, p. 105319, 2019.

[280] L. Baldrati, C. Schneider, T. Niizeki, R. Ramos, J. Cramer, A. Ross, E. Saitoh, and M. Kläui, "Spin transport in multilayer systems with fully epitaxial nio thin films," *Physical Review B*, vol. 98, no. 1, p. 014409, 2018.

[281] T. Ikebuchi, T. Moriyama, H. Mizuno, K. Oda, and T. Ono, "Spin current transmission in polycrystalline nio films," *Applied Physics Express*, vol. 11, no. 7, p. 073003, 2018.

[282] H. Sakimura, A. Asami, H. Hayashi, T. Harumoto, Y. Nakamura, J. Shi, and K. Ando, "Intrinsic spin decay length in an antiferromagnetic insulator," *Physical Review Research*, vol. 1, no. 1, p. 013013, 2019.

[283] R. Lebrun, A. Ross, O. Gomonay, V. Baltz, U. Ebels, A.-L. Barra, A. Qaiumzadeh, A. Brataas, J. Sinova, and M. Kläui, "Long-distance spin-transport across the morin phase transition up to room temperature in ultra-low damping single crystals of the antiferromagnet α-fe2o3," *Nature communications*, vol. 11, no. 1, pp. 1–7, 2020.

[284] A. Ross, R. Lebrun, O. Gomonay, D. A. Grave, A. Kay, L. Baldrati, S. Becker, A. Qaiumzadeh, C. Ulloa, G. Jakob, *et al.*, "Propagation length of antiferromagnetic magnons governed by domain configurations," *Nano letters*, vol. 20, no. 1, pp. 306–313, 2019.

[285] R. Khymyn, I. Lisenkov, V. S. Tiberkevich, A. N. Slavin, and B. A. Ivanov, "Transformation of spin current by antiferromagnetic insulators," *Physical Review B*, vol. 93, no. 22, p. 224421, 2016.

[286] M. Dabrowski, T. Nakano, D. M. Burn, A. Frisk, D. G. Newman, C. Klewe, Q. Li, M. Yang, P. Shafer, E. Arenholz, *et al.*, "Coherent transfer of spin angular momentum by evanescent spin waves within antiferromagnetic nio," *Physical review letters*, vol. 124, no. 21, p. 217201, 2020.

[287] H. Boschker, M. Huijben, A. Vailionis, J. Verbeeck, S. v. van Aert, M. Luysberg, S. Bals, G. v. van Tendeloo, E. P. Houwman, G. Koster, *et al.*, "Optimized fabrication of high-quality la0. 67sr0. 33mno3 thin films considering all essential characteristics," *Journal of physics D: applied physics*, vol. 44, no. 20, p. 205001, 2011.

[288] J.-H. Park, E. Vescovo, H.-J. Kim, C. Kwon, R. Ramesh, and T. Venkatesan, "Magnetic properties at surface boundary of a half-metallic ferromagnet la 0.7 sr 0.3 mno 3," *Physical review letters*, vol. 81, no. 9, p. 1953, 1998.

[289] M. Bibes, J. E. Villegas, and A. Barthelemy, "Ultrathin oxide films and interfaces for electronics and spintronics," *Advances in Physics*, vol. 60, no. 1, pp. 5–84, 2011.

[290] J. O'donnell, A. Andrus, S. Oh, E. Colla, and J. Eckstein, "Colossal magnetoresistance magnetic tunnel junctions grown by molecular-beam epitaxy," *Applied Physics Letters*, vol. 76, no. 14, pp. 1914–1916, 2000.

[291] M. Bowen, M. Bibes, A. Barthélémy, J.-P. Contour, A. Anane, Y. Lemaıtre, and A. Fert, "Nearly total spin polarization in la 2/3 sr 1/3 mno 3 from tunneling experiments," *Applied Physics Letters*, vol. 82, no. 2, pp. 233–235, 2003.

[292] Y. Ogimoto, M. Izumi, A. Sawa, T. Manako, H. Sato, H. Akoh, M. Kawasaki, and Y. Tokura, "Tunneling magnetoresistance above room temperature in la0. 7sr0. 3mno3/srtio3/la0. 7sr0. 3mno3 junctions," *Japanese journal of applied physics*, vol. 42, no. 4A, p. L369, 2003.

[293] J. W. Seo, E. Fullerton, F. Nolting, A. Scholl, J. Fompeyrine, and J.-P. Locquet, "Antiferromagnetic lafeo3 thin films and their effect on exchange bias," *Journal of Physics: Condensed Matter*, vol. 20, no. 26, p. 264014, 2008.

[294] J. Lüning, F. Nolting, A. Scholl, H. Ohldag, J. W. Seo, J. Fompeyrine, J.-P. Locquet, and J. Stöhr, "Determination of the antiferromagnetic spin axis in epitaxial lafeo 3 films by x-ray magnetic linear dichroism spectroscopy," *Physical Review B*, vol. 67, no. 21, p. 214433, 2003.

[295] S. Manzoor, A. Somvanshi, and S. Husain, "Structural analysis of lafeo3 thin films grown on srtio3 and laalo3 substrates," in *AIP Conference Proceedings*, vol. 1942, p. 080011, AIP Publishing LLC, 2018.

[296] D. Treves, "Studies on orthoferrites at the weizmann institute of science," *Journal of Applied Physics*, vol. 36, no. 3, pp. 1033–1039, 1965.

[297] M. Eibschütz, S. Shtrikman, and D. Treves, "Mössbauer studies of fe 57 in orthoferrites," *Physical review*, vol. 156, no. 2, p. 562, 1967.

[298] E. Folven, A. Scholl, A. Young, S. Retterer, J. Boschker, T. Tybell, Y. Takamura, and J. Grepstad, "Effects of nanostructuring and substrate symmetry on antiferromagnetic domain structure in lafeo 3 thin films," *Physical Review B*, vol. 84, no. 22, p. 220410, 2011.

[299] Q. Zhang, A. Nurmikko, G. Miao, G. Xiao, and A. Gupta, "Ultrafast spin-dynamics in half-metallic cr o 2 thin films," *Physical Review B*, vol. 74, no. 6, p. 064414, 2006.

[300] G. M. Müller, J. Walowski, M. Djordjevic, G.-X. Miao, A. Gupta, A. V. Ramos, K. Gehrke, V. Moshnyaga, K. Samwer, J. Schmalhorst, *et al.*, "Spin polarization in half-metals probed by femtosecond spin excitation," *Nature Materials*, vol. 8, no. 1, pp. 56–61, 2009.

[301] A. Mann, J. Walowski, M. Münzenberg, S. Maat, M. J. Carey, J. R. Childress, C. Mewes, D. Ebke, V. Drewello, G. Reiss, *et al.*, "Insights into ultrafast demagnetization in pseudogap half-metals," *Physical Review X*, vol. 2, no. 4, p. 041008, 2012.

[302] W. Hübner and K. Bennemann, "Simple theory for spin-lattice relaxation in metallic rare-earth ferromagnets," *Physical Review B*, vol. 53, no. 6, p. 3422, 1996.

[303] T. Ogasawara, K. Ohgushi, Y. Tomioka, K. Takahashi, H. Okamoto, M. Kawasaki, and Y. Tokura, "General features of photoinduced spin dynamics in ferromagnetic and ferrimagnetic compounds," *Physical review letters*, vol. 94, no. 8, p. 087202, 2005.

[304] F. K. Olsen, I. Hallsteinsen, E. Arenholz, T. Tybell, and E. Folven, "Coexisting spin-flop coupling and exchange bias in lafe o 3/l a 0.7 s r 0.3 mn o 3 heterostructures," *Physical Review B*, vol. 99, no. 13, p. 134411, 2019.

[305] F. Y. Bruno, M. Grisolia, C. Visani, S. Valencia, M. Varela, R. Abrudan, J. Tornos, A. Rivera-Calzada, A. Ünal, S. Pennycook, *et al.*, "Insight into spin transport in oxide heterostructures from interface-resolved magnetic mapping," *Nature communications*, vol. 6, no. 1, pp. 1–9, 2015.

[306] E. Folven, A. Scholl, A. Young, S. T. Retterer, J. E. Boschker, T. Tybell, Y. Takamura, and J. K. Grepstad, "Crossover from spin-flop coupling to collinear spin alignment in antiferromagnetic/ferromagnetic nanostructures," *Nano letters*, vol. 12, no. 5, pp. 2386–2390, 2012.

[307] Y. Takamura, E. Folven, J. B. Shu, K. R. Lukes, B. Li, A. Scholl, A. T. Young, S. T. Retterer, T. Tybell, and J. K. Grepstad, "Spin-flop coupling and exchange bias in embedded complex oxide micromagnets," *Physical review letters*, vol. 111, no. 10, p. 107201, 2013.

[308] M. S. Lee, T. A. Wynn, E. Folven, R. V. Chopdekar, A. Scholl, S. T. Retterer, J. K. Grepstad, and Y. Takamura, "Temperature dependence of ferromagnet-antiferromagnet spin alignment and coercivity in epitaxial micromagnet bilayers," *Physical Review Materials*, vol. 1, no. 1, p. 014402, 2017.

[309] A. D. Bang, I. Hallsteinsen, F. K. Olsen, S. D. Slöetjes, S. T. Retterer, A. Scholl, E. Arenholz, E. Folven, and J. Grepstad, "Néel vector reorientation in ferromagnetic/antiferromagnetic complex oxide nanostructures," *Applied Physics Letters*, vol. 114, no. 19, p. 192403, 2019.

[310] X. Tao, Q. Liu, B. Miao, R. Yu, Z. Feng, L. Sun, B. You, J. Du, K. Chen, S. Zhang, L. Zhang, Z. Yuan, D. Wu, and H. Ding, "Self-consistent determination of spin hall angle and spin diffusion length in pt and pd: The role of the interface spin loss," Science Advances, vol. 4, no. 6, 2018.

[311] C. T. Boone, J. M. Shaw, H. T. Nembach, and T. J. Silva, "Spin-scattering rates in metallic thin films measured by ferromagnetic resonance damping enhanced by spin-pumping," *Journal of Applied Physics*, vol. 117, no. 22, p. 223910, 2015.

[312] R. Yu, B. Miao, L. Sun, Q. Liu, J. Du, P. Omelchenko, B. Heinrich, M. Wu, and H. Ding, "Determination of spin hall angle and spin diffusion length in β-phase-dominated tantalum," *Physical Review Materials*, vol. 2, no. 7, p. 074406, 2018.

[313] M.-H. Nguyen, D. Ralph, and R. Buhrman, "Spin torque study of the spin hall conductivity and spin diffusion length in platinum thin films with varying resistivity," *Physical review letters*, vol. 116, no. 12, p. 126601, 2016.

[314] R. Freeman, A. Zholud, Z. Dun, H. Zhou, and S. Urazhdin, "Evidence for dyakonov-perel-like spin relaxation in pt," *Physical review letters*, vol. 120, no. 6, p. 067204, 2018.

[315] J. Ryu, M. Kohda, and J. Nitta, "Observation of the d'yakonov-perel'spin relaxation in single-crystalline pt thin films," *Physical review letters*, vol. 116, no. 25, p. 256802, 2016.

[316] C. Gonzalez-Fuentes, R. Henríquez, C. García, R. K. Dumas, B. Bozzo, and A. Pomar, "Spin diffusion length associated with out-of-plane conductivity of pt in spin pumping experiments," *Physical Review B*, vol. 103, no. 22, p. 224403, 2021.

[317] R. Gupta, S. Husain, A. Kumar, R. Brucas, A. Rydberg, and P. Svedlindh, "Co2feal full heusler compound based spintronic terahertz emitter," *Advanced Optical Materials*, vol. 9, no. 10, p. 2001987, 2021.

[318] T. Seifert, U. Martens, S. Günther, M. Schoen, F. Radu, X. Chen, I. Lucas, R. Ramos, M. H. Aguirre, P. A. Algarabel, *et al.*, "Terahertz spin currents and inverse spin hall effect in thin-film heterostructures containing complex magnetic compounds," in *Spin*, vol. 7, p. 1740010, World Scientific, 2017.

Publication(s)

M. A. Wahada, E.Şaşıoğlu, W. Hoppe, X. Zhou, H. Deniz, R. Rouzegar, T. Kampfrath,I. Mertig, S. S. P. Parkin, and G. Woltersdorf, "Atomic scale control of spin currenttransmission at interfaces,"Nano Letters, Apr 2022.

Curriculum Vitae

Personal details

- **Name**: Mohamed Amine Wahada
- **Date of birth**: 07.07.1991
- **Place of birth**: Tunis, Tunisia

- **Gender**: Male

- **Email**: amine.wahada@gmail.com

Education

- 2017–2022: **Doctoral Candidate for Ph.D in Physics**
  Martin-Luther-University Halle-Wittenberg (Halle (Saale), Germany)

- 2015–2017: **Master in Electronics and Photonics and Research in Magnon Spintronics**
  Keio University (Tokyo, Japan)

- 2013–2015: **Engineering studies**
  Supélec (Gif-sur-Yvettes, France)

- 2014–2015: **First year of Master in Fundamental and Applied Physics**
  Paris-Sud University (Orsay, France)

- 2013–2014: **Bachelor in Fundamental and Applied Physics**
  Paris-Sud University (Orsay, France)

- 2010–2013: **Intensive preparation in Mathematics and Physics for highly competitive entrance exams to the French Grandes écoles**
  IPEST (La Marsa, Tunisia)

Merits

- 2015–2017: **Japanese government MEXT scholarship**

- 2013–2015: **Tunisian government scholarship**

Halle (Saale), 03.05.2022   Mohamed Amine Wahada

Eidesstattliche Erklärung (Statutory declaration)

Hiermit erkläre ich, Mohamed Amine Wahada, die vorliegende Arbeit, **Ultrafast spin transport through oxide and nitride barriers measured by inverse Spin Hall effect**, selbst ändig und ohne fremde Hilfe verfasst zu haben. Es wurden keine anderen als die von mir angegebenen Quellen und Hilfsmittel benutzt. Die den benutzten Werken wörtlich oder inhaltlich entnommenen Stellen sind als solche kenntlich gemacht worden. Ich erkläre, die Angaben wahrheitsgemäß gemacht, keine vergeblichen Promotionsversuche unternommen und keine Dissertation an einer anderen wissenschaftlichen Einrichtung zur Erlangung eines akademischen Grades eingereicht zu haben. Ich bin weder vorbestraft noch sind gegen mich Ermittlungsverfahren anhängig.

I, Mohamed Amine Wahada, hereby declare that I have written the present work, **Ultrafast spin transport through oxide and nitride barriers measured by inverse Spin Hall effect**, independently and without third-party help. No sources other than those cited by me were used. Elements quoting directly from, or making reference to, such sources have been identified as such. I declare that I have provided this information truthfully, that I have not made any previous unsuccessful attempts at doctoral studies, and that I have not submitted either the current version or another version of this thesis to another academic institution for the purpose of obtaining an academic degree. I do not have any prior criminal convictions, nor am I subject to any preliminary investigations.

Halle(Saale), 03.05.2022   Mohamed Amine Wahada